Ultrahigh Vacuum Studies of the Reaction Mechanisms of Ozone with Saturated and Unsaturated Self-Assembled Monolayers

Larry Richard Fiegland

Dissertation submitted to the faculty of the
Virginia Polytechnic Institute and State University
in partial fulfillment of the requirements for the degree of

DOCTOR OF PHILOSOPHY
In
Chemistry

John R. Morris, Chair
T. Daniel Crawford
Alan R. Esker
James E. McGrath
Brian M. Tissue

January 4th, 2008
Blacksburg, Virginia

Keywords: vinyl-terminated self-assembled monolayers, ozone, ultrahigh vacuum, atmospheric aerosols, ozonolysis

Ultrahigh Vacuum Studies of the Reaction Mechanisms of Ozone with Saturated and Unsaturated Self-Assembled Monolayers

Larry Richard Fiegland

(ABSTRACT)

Constructing a detailed understanding of the heterogeneous oxidation of atmospheric organic aerosols, both from a mechanistic and kinetic perspective, will enable researchers to predict the fate and lifetime of atmospheric gases and the particles with which they interact. In an effort to develop a more complete understanding of the interfacial reactions of ozone with vinyl-containing organic thin films, self-assembled monolayers that contain vinyl groups positioned precisely at the gas/surface interface were synthesized as model systems for atmospheric organic aerosols. To isolate the reactions of background gases with ozone or surface products, an ultrahigh vacuum surface analysis instrument was designed and constructed to explore the reactions of ozone with the atmospheric model systems. The surface reactions can be monitored in real-time with reflection absorption infrared spectroscopy (RAIRS) and mass spectrometry. The chemical identity of adsorbates on a surface can also be determined before or after a reaction with X-ray photoelectron spectroscopy (XPS). Disordering of the monolayers concurrent with the disappearance of the vinyl group was observed with RAIRS. New bands within the RAIR spectra were observed and assigned to carbonyl or carboxylic acids bound to the surface. Little oxidation of the sulfur head groups and no significant loss of carbon during the reaction was observed with XPS. A mechanism is proposed that includes the cross linking of the hydrocarbon chains within the monolayer, which impedes further oxidation of the sulfur head group and limits desorption of the chains. By RAIRS, the kinetics of the oxidation of the vinyl groups were tracked and an observed rate constant was determined by monitoring the changes in IR absorbance of the C=C bond. With the aid of the rate constant, an initial reaction probability for the collisions of ozone with vinyl groups positioned precisely at an interface was determined. The reaction probability is approximately three orders of magnitude greater than the reaction probability for an analogous gas-phase reaction, which demonstrates that the gas/surface interface plays an important role in this reaction. The results presented in this thesis should help develop a more detailed understanding of the interfacial reactions of pure ozone at surfaces.

Acknowledgments

First and foremost, I would like to thank Jesus Christ for my salvation and assurance of my eternal destiny. With His personal relationship, my life is more abundant. I am also extremely appreciative of my wife, Jessica, for her encouragement, patience, and understanding during the many long nights spent in my study in graduate school. She makes my life enjoyable. I would also like to thank my mom and dad for their support and encouragement to pursue my dreams. I am also grateful to my brother, sister, and brother-in-law for being great friends that are always available.

I would also like to thank the many people who made the daily grind of graduate school pleasant. In particular, I would like to acknowledge the past and present Morris group members: Gwen Davis, Melinda McPherson, Scott Day, James Lohr, Jeff Carter, Wesley Gordon, Josh Uzarski, Jessica Lu, Erin Davis, William Alexander, Steve Burrows, and Dimitar Panayotov.

I would also like to thank Tom Wertalik, Raymond Dessy, Scott Allen, John Miller, and Melvin Shaver. Their friendships and expertise are extremely appreciated. In addition, I am thankful to my committee members for their contributions to my education in chemistry. I would also like to thank Richard Gandour for his advice, guidance, and willingness to allow me to use his laboratory for organic synthesis.

And last, but certainly not least, I would like to offer my sincere thanks and gratitude to my advisor John Morris for being a valuable role-model for me to follow. John has taught me, by example, how to be an excellent research leader and teacher. His patience, guidance and support are extremely appreciated.

Table of Contents

List of Figures vii
List of Tables xiii
Index of Acronyms xiv

Chapter 1 1
Introduction and Motivation 1
Thesis Statement 1
1.1 Background 1
1.1.1 Aerosol Particles 1
1.1.2 Ozone 4
1.1.2.1 Ozone's History 4
1.1.2.2 Ozone's Properties 4
1.1.2.3 Ozone Chemistry in Organic Synthesis 5
1.2 Reactivity of Ozone at the Gas/Surface Interface 6
1.2.1 Reactions of Ozone with Liquid Interfaces 6
1.2.2 Reactions of Ozone with Unsaturated Surfaces 8
1.2.3 Reactions of Ozone with Fully Saturated Organics: Alkanethiol Monolayers 13
1.3 Ultrahigh Vacuum Experiments 17
1.4 Summary 20

Chapter 2 23
Instrumental Design and Experimental Approach 23
2.1. Background 23
2.2. Instrumental Design 24
2.2.1 Surface Analysis Chamber 24
2.2.1.1 Main Chamber 24
2.2.1.2 Load Lock Chamber 30
2.2.1.3 Detector Chamber 32
2.2.1.4 Ultrahigh Vacuum Chamber Assembly 33
2.2.2 Ultrahigh Vacuum Surface Analysis Chamber Interlock 35
2.2.2.1 LabView® Program 35
2.2.2.1.1 Pressure Readings 36
2.2.2.1.2 Pressure Set Points 37
2.2.2.1.3 Load Lock Chamber Alarm 38
2.2.2.1.4 FieldPoint™ Relays Update 38
2.2.2.1.5 Chamber Venting 39
2.2.2.1.6 Front Panel Update 40
2.2.2.2 Pressure Gauge Electronics 40
2.2.2.3 Fieldpoint ™ Relay Module 42
2. 3 Ozone Generation, Storage, and Exposure Monitoring 45
2. 3.1 Background 45
2.3.2 Ozone Generators 46
2.3.3 Ozone Purification and Storage System 48
2.3.4 Ozone Doser Design 52

2.4 Surface Analysis Instrumentation 53
2.4.1 Reflection-Absorption Infrared Spectroscopy 53
2.4.2 X-ray Photoelectron Spectroscopy 57
2.5 Summary 59

Chapter 3 61
The Reactions of Ozone with Alkanethiol Self-Assembled Monolayers:Mechanism and Kinetics 61
3.1. Introduction 61
3.1.1 Self-Assembled Monolayers 61
3.1.2 Monolayer Stability 63
3.2. Experimental Details 66
3.2.1 Materials 66
3.2.2 Ozone Synthesis and Storage 66
3.2.3 Synthesis of Self-Assembled Monolayers 68
3.2.4 Monolayer Exposure 68
3.2.5 Reflection-Absorption Infrared Spectroscopic Measurements 69
3.2.6 Infrared Spectrum Analysis 70
3.2.7 X-ray Photoelectron Spectroscopic Measurements 71
3.3 Results and Discussion 72
3.3.1 Monolayer Characterization 72
3.3.1.1 Reflection-Absorption Infrared Spectroscopic Data 72
3.3.1.2 X-ray Photoelectron Spectroscopic Data 76
3.3.2 Ozone Exposure 80
3.3.2.1 Reflection-Absorption Infrared Spectroscopic Data 80
3.3.2.2 X-ray Photoelectron Spectroscopic Data 97
3.3.2.3 Mechanistic Details 102
3.3.2.4 Kinetic Measurements 103
3.4 Summary 109

Chapter 4 111
Synthesis, Characterization, and In situ Monitoring of the Reactive Uptake of Gas-phase Ozone with Vinyl-terminated Self-assembled Monolayers 111
4.1 Introduction 111
4.2 Experimental Details 115
4.2.1 Materials 115
4.2.2 Synthesis of Thiols 116
4.2.2.1 Thiourea Reaction 116
4.2.2.2 Trimethylsilylthioxy-Dehalogenation Reaction 117
4.2.3 Synthesis of Monolayer 119
4.2.4 Monolayer Exposure 120
4.2.5 RAIRS Data Acquisition 120
4.2.6 XPS Measurements 121
4.3 Results 122
4.3.1 Monolayer Characterization 122
4.3.1.1 RAIRS 122

4.3.1.2 XPS 132
4.3.2 Ozone Exposure 138
4.3.2.1 RAIRS 138
4.3.2.2 XPS 148
4.4 Discussion 151
4.4.1 Ozone Exposure 152
4.4.1.1 Mechanism 152
4.4.1.2 Kinetics 155
4.5 Summary 160

Chapter 5 162
Summary and Concluding Remarks 162
5.1 Summary of Results 162
5.2 Atmospheric Implications 165
5.3 Future Research 166
5.4 Concluding Remarks 167

6. Appendix 168
6.1 Non-Linear Least Squares Fitting in Fortran 77 168
6.2 Ultrahigh Vacuum Chamber Interlock Program in Labview 171

References 188

Vita 194

List of Figures

Figure 1.1 A schematic demonstrating the four resonance contributors of ozone.……5

Figure 1.2 Proposed mechanism for the ozonolysis of terminal surface alkenes. For clarity, subscripts (s) and (g) represent surface and gas-phase products, respectively……..11

Figure 2.1 Top view of the main chamber with port numbers…….26

Figure 2.2 Sample receiver attached to the manipulator inside the UHV chamber equipped with heating and cryogenic cooling capabilities……..28

Figure 2.3 Devices for sample control: sample stub and transfer key……..32

Figure 2.4 Overview of the surface analysis chamber. The labeled components are: (1) IR detector box, (2) FTIR spectrometer, (3) magnetically levitated compound molecular pump, (4) manipulator, (5) glass-capillary array doser, (6) differentially pumped detector chamber (Extrel MS), (7) load-lock chamber, (8) linear/rotary magnetic manipulator, (9) manual gate valve, (10) hemispherical energy analyzer, (11) cryostat, (12) X-ray source, (13) residue gas analyzer, (14) cold-cathode gauge, (15) load-lock ion pump, (16) FullRange^{TM} gauge, (17) detector ion pump……34

Figure 2.5 Cut-away view of the surface analysis chamber demonstrating the sample alignment during RAIRS analysis and simultaneous dosing with the capillary array doser. The sample mount and manipulator have been omitted for clarity. The labeled components are: (1) FTIR spectrometer, (2) MCT detector box, (3) IR beam, (4) sample, (5) effusive ozone beam, (6) X-ray source, (7) entrance to hemispherical analyzer…….…… 35

Figure 2.6 An electrical schematic of the circuits in the gauge box used to monitor the pressures of the surface analysis chamber…….…. 41

Figure 2.7 An electrical schematic of the circuits in the Fieldpoint^{TM} relay box providing power to the individual load plugs…….……..44

Figure 2.8 Custom-made corona discharge ozone generator with cooling jacket…..……47

Figure 2.9 Ozone purification and storage system. The labeled components are: (1) mechanical stirrer, (2) silica gel trap, (3) capacitance monometer, (4) UV/Vis spectrometer, (5) profile controller, (6) ozone generator, (7) oxygen flow meter, (8) flame arrestor, (9) oxygen regulator, (10) research grade oxygen cylinder, (11) ultrahigh pure nitrogen cylinder, (12) nitrogen regulator, (13) nitrogen flow meter, (14) dry ice/acetone bath containing copper coils, (15) liquid nitrogen bath containing copper coils, (16) thermocouple feedback, (A-G) Teflon®-sealed glass valves described in the text……...49

Figure 2.10 A graph of the absorbance vs. time of the ozone in the UV/Vis spectrometer demonstrating the stability of the ozone storage system…….52

Figure 2.11 Drawing of the all-glass capillary array doser designed to deliver controlled fluxes of pure ozone. The following components are labeled: (A) Teflon®-sealed glass valve, (B) 0.08 mm glass capillary, (C) 2 ¾" Conflat® flange, (D) gas doser head……..53

Figure 2.12 Infrared radiation reflecting from a substrate at incident angles (φ) near grazing can be resolved into two components: perpendicular to the plane of incidence (E_s) and parallel to the plane of incidence (E_p)……55

Figure 2.13 A schematic representing the path of the IR radiation from the Bruker IFS 66v/S spectrometer. The labeled components are: (A) SiC globar source, (B) variable aperture wheel, (C) interferometer, (D) internal sample compartment, (E) internal detector housing (MCT and DTGS), (F) movable mirror, (G) sample within the external UHV chamber, (H) MCT detector……57

Figure 2.14 A schematic demonstrating the experimental setup of an X-ray photoelectron spectrometer containing an X-ray source, hemispherical energy analyzer, and single channel electron multiplier. The dashed lines represent the path of a photoelectron through the hemispherical analyzer. Only electrons with certain energy with pass through the field created by the charged hemispheres and be detected by the electron multiplier……...…58

Figure 2.15 Energy level diagram of an ejected photoelectron. E_k is the kinetic energy of the ejected photoelectron, Eb is the binding energy of the electron, and Φ is the work function of the instrument…….59

Figure 3.1 Schematic representation demonstrating the three components of self-assembled monolayers and how they bind to substrates……..62

Figure 3.2 Schematic representation of the three-fold hollow absorption sites of the sulfur atoms in an alkanethiol SAM on a Au(111) substrate with inter-chain spacing of ~5 Å……63

Figure 3.3 Reflection Absorption Infrared characterization of a series of n-alkanethiol SAMs, HS-$(CH_2)_nCH_3$(n=4,5,6,7,9,10,11,14,15,17), on polycrystalline Au substrates……...…...73

Figure 3.4 A schematic demonstrating the alignment of the transition dipole moments of the asymmetric and symmetric stretches for the methyl functional groups within self-assembled monolayers with an odd and even total number of carbons in the chains……....76

Figure 3.5 A representative X-ray photoelectron survey spectrum of methyl-terminated self-assembled monolayers……..77

Figure 3.6 High resolution X-ray photoelectron spectra of the S(2p), C(1s), O(1s), and Au(4f) regions of a methyl terminated self-assembled monolayers……....79

Figure 3.7 Reflection Absorption Infrared spectra showing the changes in reflectivity of a 16C CH_3 SAM after 0, 1.2×10^5, and 2.0×10^5 L of exposure to ozone.. ….81

Figure 3.8 Difference RAIR spectra of a 16C CH_3 SAM demonstrating the changes in reflectivity of the monolayer during exposure to ozone. Exposure increases from bottom to top ~7.7×10^3 L per scan. The upper-most spectrum is that of the monolayer before exposure to ozone with a clean Au reference spectrum……...87

Figure 3.9 A plot showing how the position of the band from the asymmetric methylene stretch for a 16C CH_3 SAM changes during exposure to ozone. This graph demonstrates that the monolayer transitions from an ordered system to a disorder system upon oxidation. The data becomes particularly noisy after ~1.5×10^5 L of exposure due to difficulties of the fitting procedure used in section 3.2.6 when fitting bands with very low intensities…….….90

Figure 3.10 A plot demonstrating the changes in the FWHM of the band from the asymmetric methylene stretch for a 16C CH_3 SAM during exposure to ozone. The increase of the FWHM is caused by disordering of the monolayer. The data becomes particularly noisy after ~1.5×10^5 L of exposure due to difficulties of the fitting procedure used in section 3.2.6 when fitting bands with very low intensities……..92

Figure 3.11 A graph indicating how the integrated area of the band from the asymmetric methylene stretch for alkanethiol self-assembled monolayers changes upon exposure to ozone. The area initially rises due to a disordering of the monolayer followed by a significant decrease in area caused by the direct removal of the aliphatic hydrocarbons during the oxidation……...…93

Figure 3.12 Plots of the changes in integrated area of the bands from the asymmetric CH_2 stretch (2919 cm^{-1}), asymmetric SO_2 stretch (1383 cm^{-1}), and symmetric SO_2 stretch (1192 cm^{-1}) of a 16C CH_3 SAM during exposure to pure ozone. No peak intensity above the noise was observed in the RAIR spectra at 1383 cm^{-1} between 0-5.0 × 10^4 L. The positions A, B, C, and D represent exposure times in which the monolayer was analyzed by XPS, see Figure 3.14 and text for details…….....96

Figure 3.13 High resolution X-ray photoelectron spectra of the S(2p), O(1s), and C(1s) regions of self-assembled monolayers a) before and b) after exposure to ozone……98

Figure 3.14 High resolution X-ray photoelectron spectra of the S(2p) binding energy region of methyl terminated monolayers: before exposure to ozone (A), after exposure to ozone but before any formation of a RAIR peak at 1383 cm^{-1} (~4.0 × 10^5 L of exposure) (B), after exposure to ozone but before any formation of a RAIR peak at 1192 cm^{-1} (~9.0 × 10^5 L of exposure) (C), after oxidation by ozone and formation of RAIR peaks at both 1383 and 1192 cm^{-1} (>2.0 × 10^6 L of exposure) (D)……..…101

Figure 3.15 Proposed mechanism demonstrating the changes that occur during the ozone oxidation of methyl-terminated self-assembled monolayers……....….103

Figure 3.16 Changes in the integrated peak area of the asymmetric methylene stretch during ozone exposure of methyl-terminated SAMs with differing numbers of methylene groups. The solid lines represent single exponential fits to the early exposure times of the individual monolayers, which demonstrate that the initial rate of disorder from ozone oxidation is dependent on chain length……..…106

Figure 3.17 The observed rate constant of the initial disordering from ozone oxidation vs. the total number of carbons in the exposed monolayers. The solid line is an exponential fit to the data (Y= 0.437 × EXP(-0.3707 × X))…….....107

Figure 3.18 A plot of the square of the reactodiffusion lengths vs the inverse of the observe rate constants for a series of n-alkanethiol self-assembled monolayers…….108

Figure 4.1 Nuclear magnetic resonance spectrum of the neat 17-octadecene-1-thiol….119

Figure 4.2 Reflection-absorption infrared spectrum with band positions of an 18C C=C SAM……...123

Figure 4.3 Reflection-absorption infrared spectra of 10,11,15, and 18C C=C SAMs. Spectra offset for clarity…….127

Figure 4.4 Reflection-absorption infrared spectra of 10,11,15, and 18C C=C SAMs in the hydrocarbon region of the spectrum……..…128

Figure 4.5 Schematic representation indicating the direction of the transition dipole moments for a vinyl terminated monolayer……...…130

Figure 4.6 A schematic representation of an odd chain length and even chain length vinyl terminated thiolate absorbed to an Au surface, demonstrating the direction relative to the surface normal of the transition dipole moments of the $\nu_a(CH_2)$ stretch…….131

Figure 4.7 X-ray photoelectron survey spectrum of an 18C C=C SAM……..…133

Figure 4.8 High-resolution X-ray photoelectron spectrum of the S(2p) region for a 18C C=C SAM. The raw XPS data (solid circles) have been fitted to a composite (thick solid line) of two spin-orbit doublets S(2p) Gaussian peaks and a linear baseline……..135

Figure 4.9 High-resolution X-ray photoelectron spectrum of the C(1s) region for a 18C C=C SAM. The raw XPS data (solid circles) have been fitted to a composite (thick solid line) of two C(1s) Gaussian peaks (dashed lines) and a linear baseline (thin solid line)…….136

Figure 4.10 High-resolution X-ray photoelectron spectrum of the O(1s) region for a 18C C=C SAM. The raw XPS data (solid circles) have been fitted to a composite (thick solid line) of a O(1s) Gaussian peak and a linear baseline (thin solid line). The small signal from oxygen is most likly due to the presence of a surface contamination (see text for details)……...…137

Figure 4.11 Reflection-absorption infrared difference spectra of an 18C C=C SAM during exposure to pure ozone. The bottom spectrum is the monolayer with no exposure to ozone, and the exposure increases ~1890 L per spectrum from bottom to top with the upper-most spectrum receiving a total dose of ~62,300 L of ozone……...…139

Figure 4.12 Reflection-absorption infrared spectra of an 18C C=C SAM before and after exposure to ozone. The bottom spectrum is that of the monolayer before exposure to ozone and the top spectrum is the monolayer after exposure to 62,300 L of ozone……..142

Figure 4.13 A graph of the position of the $\nu_a(CH_2)$ band versus the time of exposure to ozone…… .143

Figure 4.14 A graph of the ΔArea of the $\nu_a(CH_2)$ band (open circles) versus the time of exposure to ozone. The solid red line has been fitted to the data to determine observed rate constants (see text for details)……..…144

Figure 4.15 A graph of the intensity (open circles) of the ν(C=C) band at 1644 cm^{-1} versus the time of exposure to ozone. The solid red and black lines are fits to the data to determine observed rate constants (see text for details)…….147

Figure 4.16 High-resolution X-ray Photoelectron spectrum of the S(2p) region of an 18C C=C SAM after exposure to ~1.4×10^6 L of ozone. The raw XPS data (solid circles) have been fitted to a composite (thick solid line) of two spin-orbit doublets S(2p) Gaussian peaks and a linear baseline (see text for details)....149

Figure 4.17 High-resolution X-ray photoelectron spectrum of the C(1s) region for a 18C C=C SAM after exposure to ~1.4×10^6 L of ozone. The raw XPS data (solid circles) have been fitted to a composite (thick solid line) of two C(1s) Gaussian peaks (dashed lines) and a linear baseline (thin solid line)……....150

Figure 4.18 High-resolution X-ray photoelectron spectrum of the O(1s) region for a 18C C=C SAM after exposure to ~1.4×10^6 L of ozone. The raw XPS data (solid circles) have been fitted to a composite (thick solid line) of an O(1s) Gaussian peak and a linear baseline (thin solid line)……..…151

Figure 4.19 Overall scheme demonstrating the possible mechanistic pathways in which ozone can oxidize a terminal vinyl group bound to a surface. The subscripts (s) and (g) represent surface and gas-phase species, respectively…….153

List of Tables

Table 2.1 Main Chamber Dimensions…….26

Table 3.1 Selected spectral positions and vibrational mode assignments for methyl terminated self-assembled monolayers on Au……..……...…74

Table 4.1 RAIR band positions and assignments for SAMs made from 9-decene-1-thiol, 10-undecene-1-thiol, 14-pentadecene-1-thiol, and 17-octadecene-1-thiol....124

Index of Acronyms

ATR	Attenuated total reflection
CCN	Cloud condensation nuclei
DAQ	Data acquisition
FTIR	Fourier transform infrared
FWHM	Full width at half maximum
HPLC-EC	High performance liquid chromatography electrochemical detection
IR	Infrared
MBE	Molecular beam epitaxy
MCT	Mercury cadmium telluride
MS	Mass spectrometry
NMR	Nuclear magnetic resonance
RAIR	Reflection-absorption infrared
RAIRS	Reflection-absorption infrared spectroscopy
RGA	Residual gas analyzer
SAM	Self-assembled monolayer
SERS	Surface-enhanced Raman spectroscopy
STM	Scanning tunneling microscopy
THF	Tetrahydrofuran
TPD	Temperature program desorbtion
UHV	Ultrahigh vacuum
UV/Vis	Ultraviolet visible
XPS	X-ray photoelectron spectroscopy

Chapter 1

Introduction and Motivation

Thesis Statement

The objective of this research was to develop a fundamental understanding of the interfacial reactions between ozone and both methyl-terminated and vinyl-terminated organic thin films.

1.1 Background

1.1.1 Aerosol Particles

Heterogeneous reactions at gas/surface or gas/liquid interfaces of trace tropospheric gases have recently received significant attention in the chemical literature.[1-3] Understanding the interfacial reactions is important because they influence many atmospheric processes. Atmospheric chemistry has focused on many environmental issues including stratospheric ozone depletion, reactivity of aerosol particles, greenhouse gas buildup, and photochemical smog production.[1] Atmospheric particles can provide a reactive surface for many trace tropospheric gases, and the reactions can influence the particles' chemical composition and properties. For example, the hygroscopic character, optical property, or cloud condensation nuclei (CCN) activity of the particle[4-6] can be significantly changed during the reaction. Many atmospheric aerosols consist of dust particles coated with nitrates, sulfates, or organic materials.[7] The organic content of the aerosols can react with numerous oxidizing gases within the troposphere; however, the interfacial reaction of gas-phase species with aerosol particles is not well understood.[8] Oxidizing gases in the troposphere can include O_2, O^*, $\cdot OH$, O_3, SO_2, and NO_3.[3,5,9] All of

these gases can react with the organic material found within the aerosols and affect the particle's hygroscopic properties by forming -CO, -CHO, -COOH, and -OH functional groups. Therefore, understanding the products that form in the heterogeneous reaction of gas-phase oxidants with surface bound organic molecules is important in predicting the overall fate of the particles, as well as the gases, as they are processed in the environment. Furthermore, quantifying the reactive uptake of atmospheric oxidants by organic particles is an important step in understanding the lifetime of the atmospheric particle and the gas phase oxidant.

Field measurements have shown that atmospheric particles can contain significant amounts of organic matter.[10-12] A chemical model for organic aerosols in the form of an inverted micelle has been proposed by previous researchers.[5] The inverted micelle consists of an aqueous core that is encapsulated by a hydrophobic organic monolayer. Unsaturated hydrocarbons are organic substances that are prevalent in the troposphere.[13,14] Reactions of unsaturated hydrocarbons with oxidizing gases have been proposed to play a significant role in atmospheric chemistry.[13,14] Many studies have explored the reactions of ozone with unsaturated hydrocarbons both in the gas-phase and in solution.[13,15-17] Recently, the kinetics and mechanisms of the surface oxidation of unsaturated hydrocarbons in thin films or adsorbed on solid supports, used as models for organic aerosols, have received significant attention.[4,6,9,14,18-22] An underlying goal of these studies was to determine the reaction probability of ozone with the unsaturated hydrocarbons.[2] Reaction probabilities are parameters used in atmospheric modeling; however, the atmospheric models, in general, use reaction probabilities derived from gas-phase reaction data.[2] One common conclusion in the above mentioned experiments is

that ozone reacts more rapidly with surface bound alkenes relative to analogous gas-phase reactions. Therefore, using reaction probabilities from gas-phase reactions may not be appropriate when modeling atmospheric processes. Detailed studies should be performed to accurately determine the reaction probabilities for surface bound unsaturated hydrocarbons with oxidizing gases.

Ozone is one of the most important oxidizing gases and is the second most reactive oxidizer of atmospheric aerosols after the hydroxyl radical.[21] Ozone located in the stratosphere protects the surface of the earth from harmful ultra/violet radiation, but ozone is also present in the troposphere. In the troposphere, ozone is produced from the incomplete combustion of hydrocarbons and downward transport from the stratosphere.[3] In photochemical smog, ozone is a major pollutant found at concentrations as high as 0.4 parts per million (ppm) by volume.[23] Since unsaturated hydrocarbons are prevalent in the troposphere,[13] the reactions between ozone and unsaturated hydrocarbons are important processes within the troposphere. The reactions between ozone and unsaturated hydrocarbons have been thoroughly investigated in the gas and condensed phases, but few studies have explored the reactions of ozone at gas/surface or gas/liquid interfaces.[4,13]

Self-assembled monolayers (SAMs) have been used in numerous studies as proxies for organic aerosols.[4,6,9,19,24] SAMs provide the ability to control the functional group located precisely at the gas/surface interface and the ability to monitor changes to the interface before, during, and after the experiment. Due to their relative ease in preparation and reproducibility, alkanethiols on Au (111) surfaces are the most extensively studied self-assembled monolayer. In our studies, we use alkanethiol SAMs as proxies for

atmospheric aerosols. We are interested in understanding the interfacial reactions of ozone with the organic thin film, both from a mechanistic and kinetic perspective. The main research objective is to develop a fundamental understanding of the interfacial reactions of ozone with vinyl-terminated monolayers; however, to understand this reaction thoroughly, we must also understand how ozone reacts with a fully saturated SAM. The remainder of this chapter will discuss important properties of ozone and review relevant literature of experiments that explore the reaction of ozone at gas/liquid or gas/surface interfaces for unsaturated and saturated systems. Chapter 1 will be concluded with a brief discussion about surface science techniques and the design and construction of an UHV chamber for the experiments presented in this thesis.

1.1.2 Ozone

1.1.2.1 Ozone's History

The discovery of ozone as a chemical substance is generally credited to Christian Schönbein. In 1840, he gave the reactive compound the name "ozone", which is derived from the Greek word *ozein*, meaning "to smell."[25-27] During all of human history, ozone has been sensed after thunder storms by its odor. Mankind mimicked this method of making ozone (electrical discharge) in the first commercial ozone generator in 1857.[25]

1.1.2.2 Ozone's Properties

Although ozone was discovered in 1840, its chemical structure was not determined until nearly a century later, in the 1950's. Ozone is a highly reactive allotrope of oxygen, composed of three atoms. Using the microwave spectrum of ozone, Hughes[28] and Trambarulo[29] determined that the ozone molecule, in its ground state, had an obtuse angle of 116°45′ ± 35′. They also determined the O-O bond length to be 1.278 ± 0.003 Å.

Trambarulo[29] reported that ozone was not appreciably paramagnetic, and Hughes[28] reported that ozone had a dipole moment of 0.58 ± 0.05 Debye. Based on these findings, the structure of the ozone molecule can be described as a hybrid of the four resonance contributors in Figure 1.1.[25,29] Ozone is also toxic at concentrations above 1 ppm by volume, and has an odor threshold in air of 0.01–0.02 ppm.[30] Ozone is a colorless gas at low concentrations and a light-purple gas at extremely high concentrations at 25 °C. Ozone has a boiling point of -111.9 °C,[31] and forms a dark blue liquid. Ozone has a melting point of -193.5 ± 0.5 °C,[32] and forms a dark-violet solid. Due to ozone's high reactivity, ozone is extremely explosive. Ozone gas has a potential risk of explosion when the concentration of ozone is above 10% by volume at atmospheric pressure.[33-36] Below atmospheric pressure, ozone gas can be handled at higher concentrations. Ozone gas >99% has been produced in our laboratory at pressures less then 50 Torr without spontaneous detonation; however, explosive conversion of ozone to molecular oxygen can occur when triggered by a catalytic material, heat, mechanical vibrations, or organic substances.[34,37] *Therefore, extreme caution should be used when handling high concentrations of ozone.*

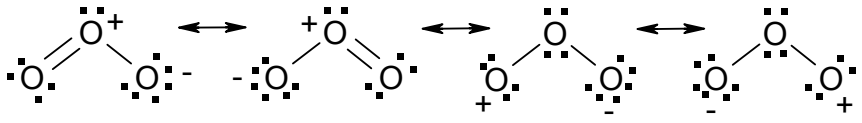

Figure 1.1. A schematic demonstrating the four resonance contributors of ozone.

1.1.2.3 Ozone Chemistry in Organic Synthesis

Ozone's discoverer, Schönbein, appears to be the first to explore the reactions of ozone with organic and inorganic substances.[25] Ozone is highly reactive with many

organic functionalities, especially unsaturated carbon–carbon bonds.[25] Because of its high reactivity with carbon–carbon double bonds, ozone has been used as a tool for structural determination of natural products.[26] By oxidizing ethylene, Schönbein performed the first ozonolysis reaction.[25,26,38] Professor R. Criegee is considered the father of modern ozone–organic chemistry, and he published his first major paper on the mechanism of ozonolysis in 1953.[25,39] Criegee speculated that ozone inserts into a double bond to form a primary ozonide. The primary ozonide is unstable and will decompose into a Criegee intermediate (zwitterion) and an aldehyde or ketone. Criegee suggested that the zwitterion could stabilize itself in one of four different ways: (a) reaction with an aldehyde or ketone to form a secondary ozonide; (b) reaction with itself to form a cyclic peroxide; (c) reaction with a protic, nucleophilic solvent molecule to form a C-O-O-H peroxide species; or (d) rearrangement to give "abnormal" ozonolysis products.[25] Knowledge of the ozonolysis mechanism in gas and condensed phase reactions provides a basis for understanding the heterogeneous oxidation of unsaturated hydrocarbons at gas/surface or gas/liquid interfaces.

1.2 Reactivity of Ozone at the Gas/Surface Interface

1.2.1 Reactions of Ozone with Liquid Interfaces

A model for atmospheric particles in the form of an inverted micelle has been proposed by previous researchers.[5] The inverted micelle consists of an aqueous core that is encapsulated by a hydrophobic organic monolayer. This chemical model has lead to studies with liquid and frozen liquid substrates as proxies for atmospheric organic aerosols. Moise and Rudich monitored the heterogeneous reactions between ozone and oleic and linoleic acid in liquid and frozen states in a flow reactor with electron impact

and chemical ionization mass spectrometry.[19] Oleic acid contains one unsaturation site while linoleic acid contains two unsaturation sites. Volatile reaction products were monitored and reactive uptake coefficients were determined. The authors observed a decrease in the reactive uptake coefficient by at least an order of magnitude upon freezing of both organic acids. Both reactions released long chain aldehyde gas-phase products. The reactive uptake coefficient for the mono-unsaturated acid was determined to be $(8.3 \pm 0.2) \times 10^{-4}$ in the liquid state and $(5.2 \pm 0.1) \times 10^{-5}$ in its frozen state. The authors suggested that the decrease in the reactive uptake coefficient upon freezing of the liquid indicates that solubility, diffusion, and reaction within the bulk liquid contribute substantially to the observed ozone uptake. This study suggests that the physical state of the unsaturated hydrocarbon plays an important role in its reactivity.

Pryor et al. studied the reactions of ozone with emulsions of oleic and linoleic acids in aqueous solutions by high-performance liquid chromatography with electrochemical detection (HPLC-EC).[40] Ozonolysis of the fatty acid emulsions were carried out by bubbling a stream of ozone in air at ppm levels through a fine capillary into the solutions. The reacted solutions were injected into an HPLC-EC system and the products of the reaction were analyzed. The authors reported that ozonolysis of emulsions of the unsaturated fatty acids yielded 1 mole of hydrogen peroxide per mole of ozone used. The researchers suggested a mechanism that involved the reaction of the fatty acid with ozone to form the Criegee intermediate. The Criegee intermediate reacted with H_2O to form a hydroxy hydroperoxide. The hydroxy hydroperoxide hydrolyzed to give hydrogen peroxide and an aldehyde.

Although the studies discussed above were able to determine products of the reactions of ozone with unsaturated interfaces, it is difficult to learn about the mechanisms of the reaction in such complicated systems. In an effort to simplify the systems, SAMs have been used as proxies for organic interfaces of aerosol particles.

1.2.2 Reactions of Ozone with Unsaturated Surfaces

The complexity and diversity of organic aerosols make the heterogeneous oxidation of organic aerosols by ozone a difficult reaction to explore.[8] Various models of organic aerosols have been used for the organic interface including actual aerosol particles, liquid/gas interfaces, organic thin-films at the liquid/gas interface of water, organosilane SAMs adsorbed to glass substrates, and alkanethiol SAMs adsorbed to Au substrates.[3,4,6,9,14,23,24] In general, each proxy is developed so that the essential features of the naturally occurring system are captured within the constraints of the analytical detection methods used.[41]

Moise and Rudich explored the reactions of ozone with two types of proxies for atmospheric aerosols: organic liquids and organosilane SAMs.[9] Both alkanes and vinyl-terminated alkenes were used. The monolayers were characterized before and after the reaction with infrared (IR) spectroscopy. Reactive uptake measurements were performed by means of a flow tube reactor coupled to a chemical ionization mass spectrometer. Ozone concentrations of 0.2-2 ppm in He were used. The researchers determined that the reaction of ozone with the double bond was the cause of the reactive uptake of ozone. They determined the reaction probability from the first-order rate loss of gas-phase ozone. When comparing the uptake probability between the organic liquid and a monolayer of the same chain length, Moise and Rudich determined that the monolayer's

uptake probability was an order of magnitude lower than that of the organic liquid. The authors attributed the increased reactivity of the liquid to solubility and reactions occurring in the bulk. Using IR, they saw a shifting of the bands assigned to the asymmetric and symmetric methylene stretches toward high wavenumbers, which was attributed to an increase in disorder of the system. While the study by Moise and Rudich provides useful information about the reactive uptake probabilities of vinyl-terminated monolayers compared to bulk liquids, neither products on the surface nor in the gas-phase were analyzed. Details about the products of the reaction are needed to determine the mechanisms of the reaction of ozone at vinyl terminated interfaces.

Gas-phase and surface-bound products were analyzed for the reaction of ozone with alkane and vinyl-terminated organosilane SAMs in the studies of Thomas et al.[6] In this study, the surfaces were characterized before and after the reaction with attenuated total reflection (ATR) IR spectroscopy, and the gas-phase products were determined by performing Fourier transform infrared (FTIR) spectroscopy directly above the reaction site. For the vinyl terminated monolayers, the authors observed the formation of carbonyls and carboxylic acids bound to the surface and formaldehyde, CO, and CO_2 in the gas phase. The alkane monolayers showed no reactivity toward ozone. ATR-IR spectroscopy showed a decrease in absorption from the C-H stretch associated with the terminal double bond and the formation of absorptions near 2660 cm^{-1} and 1705 cm^{-1}. These new peaks were assigned to carbonyl functional groups. Additional absorption features observed within the spectrum were assigned to C-H stretching of a newly formed methyl group. The researchers concluded that a combination of carboxylic acid and methyl groups were formed as products on the surface.

From their observations, the authors proposed a mechanism, shown in Figure 1.2, for the reaction of ozone with surface-bound terminal vinyl groups. Thomas et al. proposed that ozone reacts with the double bond to form a primary ozonide. The primary ozonide can decompose into two separate pathways. In one pathway, the primary ozonide decomposes into a diradical species (Criegee intermediate) on the surface releasing formaldehyde into the gas phase. The diradical species bound to the surface will rearrange leaving a carbonyl, carboxylic acid, or a methyl group bound to the surface. If the diradical rearranges to the methyl group, CO_2 is also released into the gas phase. Thomas et al. also proposed that the primary ozonide could decompose in a second pathway. This pathway leaves an aldehyde on the surface and a diradical species in the gas phase. The diradical species will rearrange to the products observed in the gas phase in their experiments. The experiments by Thomas et al. provided insight into the mechanism of the reactions of ozone with vinyl terminated monolayers as proxies for organic aerosols, but very few studies have provided information about the kinetics of this surface ozonolysis reaction.

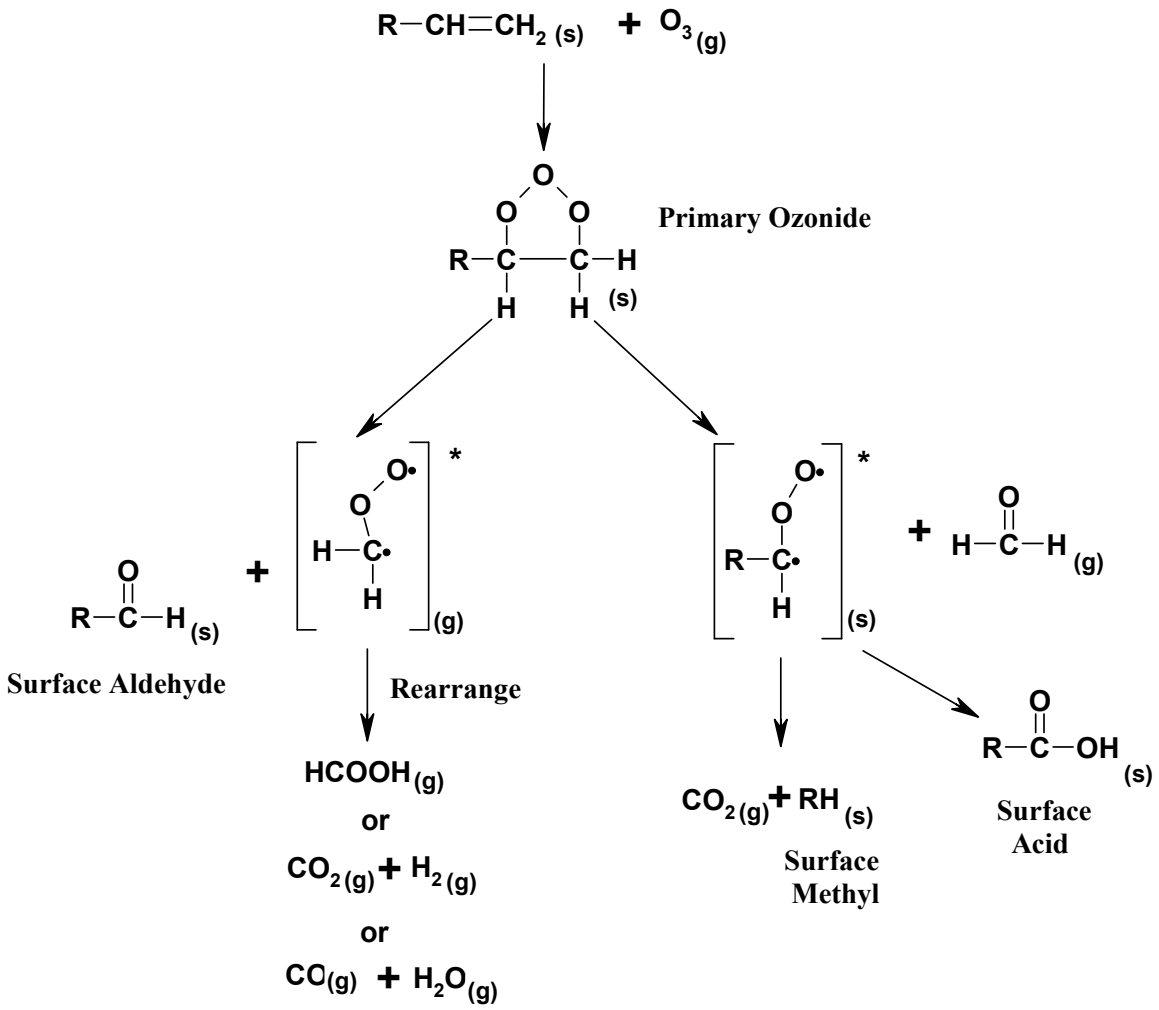

Figure 1.2. Proposed mechanism for the ozonolysis of terminal surface alkenes. For clarity, subscripts (s) and (g) represent surface and gas-phase products, respectively.

Dubowski et al. performed an experiment that monitored the products that formed in the gas-phase and bound to the surface, *and* they obtained kinetic measurements of the condensed phase oxidation in real time of alkylsilane SAMs with gas-phase ozone.[4] In this study, methyl and vinyl-terminated SAMs were adsorbed to the surface of an ATR crystal and the surfaces were monitored in real time with FTIR spectroscopy. The gas-phase products were also analyzed by infrared cavity ring-down spectroscopy. For the vinyl-terminated monolayers, ATR-FTIR spectroscopy showed loss of the double bond and formation of a carbonyl. Formaldehyde was observed as a product in the gas phase

by infrared cavity ring down spectroscopy. The kinetics of the formation of the carbonyl were shown to be consistent with a Langmuir–Hinshelwood mechanism in which ozone rapidly adsorbs to the surface and then reacts more slowly with the vinyl group. The author reported that the initial reaction probability is inversely and nonlinearly dependent on the ozone concentration when the concentration is in the range of 10^{12}–10^{16} molecules cm^{-3}. A second-order rate constant for the surface oxidation reaction was reported as $(2 \pm 1) \times 10^{-17}$ cm^2 $molecule^{-1}s^{-1}$. The authors report a residence time of ozone on the surface of ~7 s. This residence time raises an important question. Why is the residence time reported by Dubowski et al. (7 s) significantly different than the residence time suggested by the molecular dynamic simulations of Vieceli and coworkers (~17 ps)?[41]

Although SAMs provide useful models for atmospheric particles, SAMs have a few limitations. In the experiments discussed above, each monolayer system was developed from commercially available vinyl-terminated silanes. In an attempt to provide a more realistic proxy for atmospheric particles, Voges et al. developed a synthesis of tropospherically relevant terpenes bound to glass substrates.[14] In their study, the authors reported the oxidation of the surface at 1 atm with ozone at ppm levels. The authors monitored the reaction of the unsaturated terpene with vibrational broadband sum frequency generation spectroscopy. By monitoring the changes in structure of the system, the authors determined a reaction probability of 1×10^{-5}.

Although the aforementioned studies provide some of the answers to questions about the products, mechanism, and kinetics of the heterogeneous reactions of ozone with vinyl-terminated systems, many intriguing questions remain. How does the structure of the vinyl interface influence the reaction? What role do background gases play in this

reaction? In an effort to probe these questions, we have performed experiments monitoring the oxidation of vinyl terminated SAMs as proxies for atmospheric aerosols under ultrahigh vacuum conditions. As a control for these studies, we have also monitored the oxidation of fully saturated SAMs.

1.2.3 Reactions of Ozone with Fully Saturated Organics: Alkanethiol Monolayers

Alkanethiolate SAMs have been used as model systems to help develop a fundamental understanding at the molecular level of various surface related phenomena including friction, energy transfer, and adhesion.[42,43] SAMs on Au have been extensively studied for their various potential applications as molecular electronic devices, chemical sensors, corrosion inhibitors, and biomaterials.[42,43] A common belief among many researchers is that alkanethiol SAMs are extremely stable under ambient conditions.[42-44] However, few studies have explored the extent and rate of oxidation of alkanethiol SAMs.[45]

Huang and Hemminger were the first to report the UV photooxidation in air of SAMs of alkanethiols.[46] In their study, the authors exposed the SAMs in air to radiation from a mercury lamp and observed the formation of alkanesulfonates (RSO_3^-) with laser-induced desorption coupled with Fourier transform mass spectrometry (LID-FTMS). The researchers also monitored the thin films before and after exposure to radiation with X-ray photoelectron spectroscopy (XPS). They observed the formation of a new peak at 167.5 eV in the photoelectron spectrum of the monolayer and assigned this peak to a newly formed sulfonate species. The authors hypothesized that the photooxidation of the SAMs occurred via UV excitation of electrons in the metal substrate. They speculated that the transfer of "hot" electrons from the metal to either the RS species or coadsorbed O_2 caused the oxidation of the thiolate species. Although this paper identified some of

the oxidation products of SAMs, many questions still remained. What was the specific cause of this oxidation, and what was the mechanism of the photooxidation reaction? This paper stimulated several studies exploring these questions.[45,47-51]

Lewis et al. presented surface-enhanced Raman spectroscopy (SERS) results acquired from UV-irradiated SAMs on silver substrates.[50] In their study, the authors observed a decrease in all of the Raman peaks associated with the hydrocarbon backbone upon UV irradiation of the sample. They also observed the formation of Raman peaks at 958, 917, and 612 cm^{-1}. The researchers attributed the band at 958 cm^{-1} to the formation of a symmetric stretch of a coordinated sulfate ion (SO_4^{2-}). They also assigned the bands at 917 and 612 cm^{-1} to a sulfite ion (SO_3^{-}). The authors also reported that no oxidation peaks were detected until after a significant decrease in the intensity of the bands from the monolayer was observed. Lewis et al. also determined first-order rate constants for the photooxidation reaction using the decrease in signal of the bands from the C-S and C-C stretches. The reported rate constants were $(1.2 \pm 0.03) \times 10^{-2}$ s^{-1} and $(1.0 \pm 0.05) \times 10^{-2}$ s^{-1} for C6 and C10 CH_3 SAMs, respectively. The authors suggested that the rate of oxidation decreases with increasing chain length. They also hypothesized that the photooxidation of the monolayer proceeds by a two-step mechanism. First, UV exposure resulted in the cleavage of the C-S bond, followed by desorption of the hydrocarbon fragments from the surface; and second, the exposed sulfur was further oxidized to sulfite and sulfate species. Although this study explored the mechanism and kinetics of the oxidation of monolayers, it did not fully explain the specific cause of the oxidation process.

Zhang et al. were the first to prove that ozone was the primary cause of UV photooxidation of alkanethiolate monolayers.[52,53] In these experiments, the researchers monitored alkanethiolate SAMs under various reaction conditions using RAIRS. They observed no changes in the IR spectrum when the surface was exposed to UV for 30 min in a nitrogen environment. When the surface was exposed to UV for 30 min in air, they observed a peak that emerged at 1017 cm^{-1}. This same peak was also observed when the surface was exposed to ex situ generated ozone for 30 min in the dark. The researchers assigned the peak at 1017 cm^{-1} to a stretching mode of a sulfonate moiety. They also noted that this species could be easily removed by rinsing the surface in H_2O and 2-propanol. The authors also found that the oxidation of alkanethiols using UV radiation required both O_2 and UV irradiation at wavelengths competent for O_3 formation, i.e. $\lambda <$ 200 nm.

A few studies have reported the oxidation of alkanethiolate monolayers in an ambient atmosphere.[54-57] Schoenfisch and Pemberton monitored the air stability of alkanethiol SAMs using surface Raman spectroscopy and X-ray photoelectron spectroscopy.[45] When the monolayers were exposed to air, the authors observed the formation of peaks in the Raman spectrum at 615, 850, 917, 980, and 1010 cm^{-1}, which they attributed to sulfonate, sulfonite, sulfate, and sulfite species, respectively. The authors also noticed the appearance of bands at 1390 and 1590 cm^{-1}, which they assigned to graphitic carbon, and suggested that the formation of these bands might be due to considerable monolayer decomposition. Using XPS, the researchers observed rapid and complete loss of intensity of the thiolate sulfur 2p peak at 162 eV upon air exposure. They observed the formation of a new peak at 167 eV, which they assigned to oxidized sulfur. After long air exposure

times, shoulders on the band at 167 eV were observed at ~166.5 and 169 eV, which were attributed to multiple oxidation states of sulfur. The authors noted that the oxidation rate of the monolayer was a function of chain length with the short chain SAMs oxidizing more quickly than long chain SAMs. They suggested that the long chain monolayer oxidized more slowly because of an inability of the active oxidant species to penetrate the closely packed alkyl chain structure. The authors further hypothesized that the shorter chain monolayers contain a greater number of defects within the film and therefore oxidize quicker.

To our knowledge, only one study in the literature has been performed that exposes alkanethiol SAMs to relatively pure ozone. In this study, Poirier et al. characterized the reactions of decanethiol monolayers on Au (111) surfaces with ozone using XPS and scanning tunneling microscopy (STM) in ultrahigh vacuum.[58] The authors observed the formation of an O(1s) peak in the photoelectron spectrum of the oxidized monolayer and shifting of the S(2p) peak from ~162 eV to ~167 eV, consistent with the oxidation of sulfur. The researchers observed a loss of intensity in both the S(2p) and C(1s) regions, which suggests that a fraction of the molecules desorb during oxidation of the monolayer. The authors also exposed decanethiol monolayer to H_2O, CO_2, and O_2; and in each case, no oxidation of the monolayer was observed with XPS or STM. They concluded that ozone was the primary cause of the observed monolayer oxidation. In an effort to determine the initial reaction site of the ozone induced oxidation, the authors monitored decanethiol monolayers with STM during controlled exposure to ozone. They observed broadening of the domain boundaries and concomitant formation of linear features in the resulting regions. From this observation, the authors inferred that the domain boundaries

are the nucleation site of the reaction between ozone and decanethiol monolayers and that the reaction propagated from the initial reaction site into the domains.

The literature shows that alkanethiolate SAMs can be oxidized by the atmospheric pollutant, ozone. Products of sulfonate, sulfinate, sulfite, and sulfate have been observed, and a few details about the mechanisms of the reaction of ozone with SAMs have been addressed. Very few experiments can be found in the literature exploring the kinetics of this reaction. Thorough studies investigating the kinetics of the oxidation of SAMs should be performed. If rate constants of this reaction (along with products) are found, predicting the lifetime and final fate of the monolayer system can be accomplished and may lead to the development of more robust assemblies for commercial applications. In Chapter 3, we present a detailed kinetic analysis of the oxidation of a series of alkanethiolate monolayer performed in our laboratory. This study explores the products and mechanistic details of the reaction of these thin films with ozone in ultrahigh vacuum. The experiments that were performed with fully saturated monolayers also provided a control for the experiments that were performed with vinyl terminated SAMs. Understanding the reactions of ozone with fully saturated monolayers allowed us to develop a more complete knowledge of the reactions of ozone with unsaturated monolayers, the subject of Chapter 4.

1.3 Ultrahigh Vacuum Experiments

A common conclusion in the aforementioned experiments is that ozone reacts more rapidly with unsaturation sites at interfaces when compared to analogous gas-phase reactions, but ozone reacts slower with unsaturation sites at interfaces when compared to reactions in bulk liquids. When laboratory experiments are performed to determine

reaction probabilities, it is important that the conditions of the experiments be well defined.[9] If the conditions are well defined, the reaction probability can be used to predict the kinetics of a reaction at specific interfaces in atmospheric modeling. To this end, we have performed heterogeneous reactions of pure ozone with well-ordered, vinyl-terminated SAMs in ultrahigh vacuum conditions. The SAMs are good model systems for proxies of organic aerosols because surface parameters, such as chemical composition, can be controlled and the surface density of the monolayer is known.[9] The monolayers also allow us to monitor the changes to the surface before, after, and during the reaction in ultrahigh vacuum.

The reasons we perform the oxidation reaction in ultrahigh vacuum are twofold. First, we desire to precisely control the exposure of the surface to atmospheric gases. In an ultrahigh vacuum environment, we can control the flux of gas-phase molecules that react with the surface. This allows us to keep the surfaces "clean" until the reaction is started, accurately expose the surface to a known gas, and separate the competing reactions of background gases during the reaction. Ultrahigh vacuum conditions also allow us to eliminate reactions of background gases with reaction products during the experiment. We have therefore developed a method to study the reactions of vinyl-terminated organics with pure ozone with little influence of background gases like H_2O, O_2, and ·OH. Although these gases probably play a significant role in true atmospheric reactions, the studies presented here allow us to isolate the fundamental reactions for which only ozone is responsible. The second reason we study the oxidation reactions in ultrahigh vacuum is so that we can analyze the surface before and after the reaction with surface sensitive analytical techniques like X-ray photoelectron spectroscopy (XPS). In X-ray

photoelectron spectroscopy, electrons are ejected from the surface of a sample and the electron's kinetic energy is measured with an energy analyzer. The kinetic energy of the electrons is directly related to the chemical composition and oxidation state of the elements within the surface. It is essential that the ejected electrons not collide with other gas phase molecules before entering the detector. Ultrahigh vacuum conditions allow us to meet this requirement because the mean free path in this environment is $\sim 5 \times 10^5$ meters.

For the reasons mentioned above, an ultrahigh vacuum chamber was designed and constructed for the experiments presented in this thesis. The design and development of the first ever UHV system for studies of ozone interactions with surfaces represents one of the primary thrusts of the work described in this dissertation. The chamber was designed with a computer-aided design program (AutoCAD). Details of the chamber's design and construction are presented in Chapter 2. The chamber is capable of maintaining a base-pressure around 10^{-10} Torr. Reactions can be monitored within the chamber with reflection absorption infrared spectroscopy (RAIRS), X-ray photoelectron spectroscopy (XPS), and mass spectrometry (MS). A system was also developed to deliver concentrations of ozone >99% to surfaces within the chamber. Monitoring the surfaces in situ with RAIRS allows us to monitor the reaction kinetics as well as determine surface bound products. Products that form in the gas phase can be analyzed with the mass spectrometer. Elemental analysis and oxidation state determination can be performed before and after the reaction with XPS.

1.4 Summary

The reactions of ozone with atmospheric particles play an important role in determining the hygroscopic character, cloud condensation nuclei activity, and optical properties of molecules within the atmosphere. Therefore, detailed studies exploring the heterogeneous reactions of ozone with vinyl terminated surfaces should be performed to understand the products, mechanism, and kinetics of this reaction. Important questions about the structure of the interface and role of background gases should be addressed.

The encompassing focus of the research in this thesis is to better understand the fundamental reactions of ozone with vinyl functional groups oriented precisely at the gas/surface interface. In addition, the reactions occurring between ozone and methyl-terminated alkanethiolate monolayers are targeted. The chemical reactions are isolated from interfering reactions of background gases by performing the experiments in an ultrahigh vacuum environment. The ultrahigh vacuum environment also allows us to expose the surface to controlled amounts of pure ozone through a dosing device. In situ RAIRS will be used to identify surface-bound products, as well as provide insight into the kinetics of the reactions. The surfaces will be analyzed before and after the reaction with XPS to probe the chemical identity and oxidation state of the surface-bound molecules. These studies provide useful reaction probabilities and rate constants that can be used to predict the lifetime and fate of the system modeled.

Using RAIRS, we observed disordering of vinyl terminated monolayers concurrently with the disappearance of the vinyl functional group during oxidation with ozone. We also observed new bands within the RAIR spectra that we attribute to the formation of carbonyls or carboxylic acids bound to the surface. Using reflection absorption infrared

spectroscopy, we tracked the kinetics of the oxidation of vinyl groups that were positioned precisely at the gas/surface interface, and we monitored the changes in order/disorder of the system. We determined identical rate constants, 3.1×10^{-5} s^{-1}, for the disordering of the hydrocarbon chains and oxidation of the vinyl group by monitoring changes in the IR absorptions of the $\nu_a(CH_2)$ and $\nu(C=C)$ stretches. We suggest that the equality of the rate constants implies a mechanism that includes the disordering of the monolayer during the consumption of the double bond. Using the rate constant, we determine an initial reaction probability of $(1.1 \pm 0.5) \times 10^{-5}$.

The reaction probability that we measured agrees extremely well with others reported in the literature.[4,14,19] The reaction probabilities previously reported in the literature were determined with experiments performed between 10–760 Torr with ozone concentrations at ppm levels. Since each of these experiments would have contained significant amounts of background gases (H_2O, O_2, and CO_2), one may have predicted the reaction probabilities would be different under ultrahigh vacuum conditions, where the partial pressures of the background gases are negligible. The surprising result that the reaction probability at atmospheric conditions is the same under ultrahigh vacuum conditions suggests that the reactions of ozone with atmospheric background gases do not play a significant role in the oxidation of vinyl terminated organic thin films. Furthermore, the structure of the monolayer must not influence the kinetics of this reaction. During the oxidation of the unsaturated organic thin films, we observed the formation of carbonyls or carboxylic acids on the surface. Since these newly formed species are significantly more polar than the original vinyl functionalities, oxidation of atmospheric aerosols that

contain unsaturation sites will contribute to the particles cloud nucleation activity from the aerosol's enhanced water affinity.[6]

Chapter 2

Instrumental Design and Experimental Approach

2.1. Background

When studying the reactions that occur at a gas-surface interface it is very important to maintain a well characterized surface. Interfacial reactions also require a well characterized gas-phase reactant that can be precisely controlled when exposing a surface. To begin an experiment with a reasonably clean surface and ensure that the surface is not contaminated during the experiment with atmospheric molecules, the background pressure must be low enough whereby the time required for the surface to be contaminated is much greater then the time to conduct the experiment.[59] It is possible to obtain a minimum estimate of how long it would take for a clean surface to become covered with a complete monolayer, assuming a unit sticking probability (S=1). At atmospheric pressure, this time would be ~10^{-9} s; however, at a pressure of 10^{-10} Torr, this time would be ~10^{4} s. Therefore, ultrahigh vacuum (UHV) conditions, <10^{-10} Torr, are necessary for many surface characterization techniques, as well as determining the mechanisms that occur when gas-phase species react with surfaces. UHV conditions keep substrates clean, not contaminated by unwanted atmospheric gases, during the course of the experiment and allow one to expose the surfaces to controlled amounts of pure gases. Despite the numerous studies exploring the reactions of ozone at interfaces, no one has measured the reaction probability of ozone with vinyl terminated surfaces under highly controlled conditions. Many questions about the reaction of ozone at vinyl terminated interfaces remain. What is the initial reaction probability? What are the final products of the reaction and are these products bound to the surface or in the gas phase?

What is the mechanism of the reaction between ozone and unsaturated interfaces? What are the kinetics of this reaction? In an effort to help understand the interfacial reaction of ozone with vinyl terminated surfaces, I designed and built an ultrahigh vacuum chamber with the goal of providing the first detailed studies of ozone chemistry at an interface under well controlled ultrahigh vacuum conditions.

The instrument consists of three custom chambers (the main chamber, the load-lock chamber, and the detector chamber) attached to one another through ConFlat™ flanges. The instrument was also designed with the following analytical techniques: Reflection-Absorption Infrared Spectroscopy (RAIRS), X-ray Photoelectron Spectroscopy (XPS), and Mass Spectroscopy (MS). Surface structure was controlled by using SAMs. The monolayers were characterized before and after exposure to the gas-phase analytes by the analytical techniques available on the UHV chamber. A system was also designed to allow controlled dosing of pure ozone to the self-assembled monolayers. The remainder of this chapter describes the design of the surface analysis chamber including the synthesis, storage, and controlled dosing of pure gas-phase ozone. The synthesis of the SAMs is described in detail in subsequent chapters.

2.2. Instrumental Design

2.2.1 Surface Analysis Chamber

2.2.1.1 Main Chamber

The main chamber is a custom designed, dome-shaped, stainless steel chamber with nineteen strategically placed ConFlat™ flanged ports, see Figure 2.1. The port number, dimension, focal length, azimuthal angle, and polar angle for each port are listed in Table 2.1. The volume of the main chamber is approximately 23 L and is evacuated by a

magnetically suspended compound molecular pump from Osaka Vacuum, LTD (model: TG2003M). The magnetically suspended pump is attached to port 3, see Figure 2.1, and was chosen because of its high pumping speed, 2000 L/s, and minimum vibrations, which are necessary for the RAIRS analysis. Base pressures of 10^{-10} Torr are routinely reached with this compound molecular pump. The base pressures of the main chamber are monitored with a compact cold cathode gauge (Pfeiffer Vacuum, Inc., model: IKR 270) attached to port 15, see Figure 2.1. The magnetically suspended compound molecular pump is backed by a mechanical pump from BOC Edwards (model: E2M30, pumping speed 9.2 L/s). These two pumps are separated by a pneumatically actuated valve (A & N Corporation, model: AV150-QF-E-P) controlled by a custom-written software program described later in this chapter. On the low pressure side of the pneumatically actuated valve is an attached compact pirani gauge (Pfeiffer Vacuum, Inc., model: TPR 265), which allows one to monitor the backing pressure of the mechanical pump.

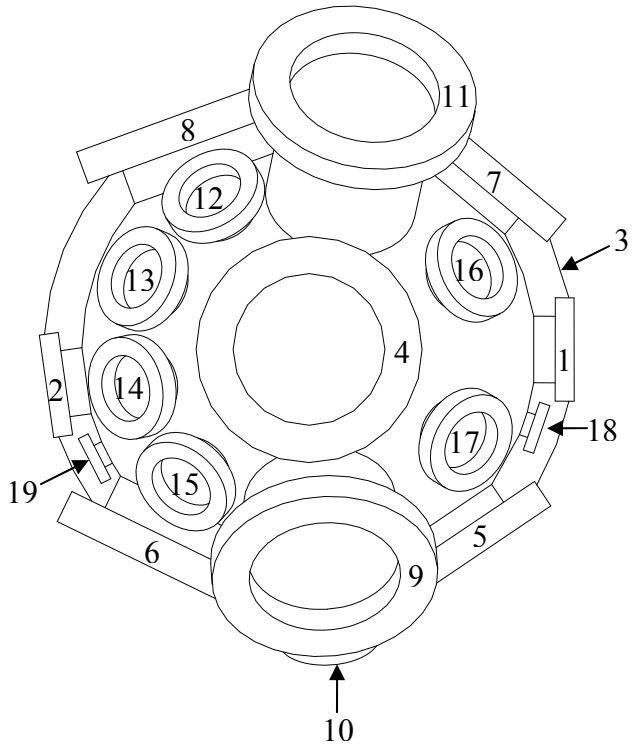

Figure 2.1. Top view of the main chamber with port numbers.

Table 2.1. Main Chamber Dimensions.

Port Number	Flange Size (Inches)	Focal Length (Inches)	Azimuthal Angle	Polar Angle
1	2 ¾	7.000	0°	90°
2	2 ¾	7.000	188°	90°
3	14	8.000	0°	180°
4	6	7.000	0°	0°
5	6	7.000	304°	90°
6	8	7.000	244°	90°
7	6	7.000	50°	90°
8	8	7.000	110°	90°
9	6	8.500	274°	45°
10	2 ¾	9.000	274°	122°
11	6	10.000	78°	45°
12	2 ¾	7.000	122°	45°
13	2 ¾	7.000	157°	45°
14	2 ¾	7.000	192°	45°
15	2 ¾	7.000	227°	45°
16	2 ¾	7.000	26°	45°
17	2 ¾	7.000	330°	45°
18	1⅓	6.500	341°	90°
19	1⅓	6.500	207°	90°

Attached to the port on the top of the main chamber, port 4, is a precision sample manipulator from McAllister Technical Services (model: MA1002). The manipulator allows one to precisely control the x, y, and z positions of a sample. The precision control is needed for accurate transfer and alignment of the sample for RAIRS and XPS analysis. Alignment and transfer of the sample can be monitored from one of the six viewports mounted on ports 9, 10, 13, 16, 18, and 19, see Figure 2.1. The sample manipulator is also equipped with a differentially-pumped rotary platform from McAllister Technical Services (model: DPRF275-SP), which allows 360° rotary-control around the z-axis of the sample. The low vacuum seal of the rotary platform is connected to a diaphragm pump (Ilmvac, model: MP601T) through a pneumatic valve (A & N Corporation, model: AV075-QF-E-P), while the high vacuum seal is connected to the load lock chamber also through a pneumatically controlled valve (A & N Corporation, model: AV150-CF-C-P). Attached to the top of the rotary platform is a custom-made (Applied Vacuum) top-hat, which consists of five, 1 $^1/_3$" mini-ConFlat™ flanged ports. These ports are used for the electrical and thermocouple feed-throughs that control and monitor the sample temperature. Located inside the main chamber is a precision-ground stainless steel rod threaded into a blank flange mounted on the upper port of the top-hat. Attached to the rod is a custom-made, variable-temperature sample holder, shown in Figure 2.2.[60] The sample holder consists of a removable stainless steel sample stub, which can be threaded onto the sample receiver. The sample receiver contains machined copper threads that allow optimal thermal contact between the sample stub and the sample receiver. Located inside the sample receiver is a heat shielded assembly containing a UHV button heater (HeatWave Labs, Inc., model: 101251-03). The button

heater allows elevation of the surface temperature up to ~500 °C. The sample can also be cooled to cryogenic temperatures by heat transfer through a braided-copper rope connecting the sample receiver to the second stage of a two-stage expander cryostat (SHI-APD Cryogenics, Inc., model: Displex DE-202), which is attached to port 11, see Figure 2.1. The expander is cooled by a helium compressor (APD Cryogenics, Inc., model: HC-2), which allows the sample to be cooled down to -184 °C. The cryostat is equipped with a 1", 25 psi rupture disk (BS&B Safety Systems, L.L.C.). The temperature of the sample is monitored with a K-type thermocouple, which is mounted to the sample receiver.

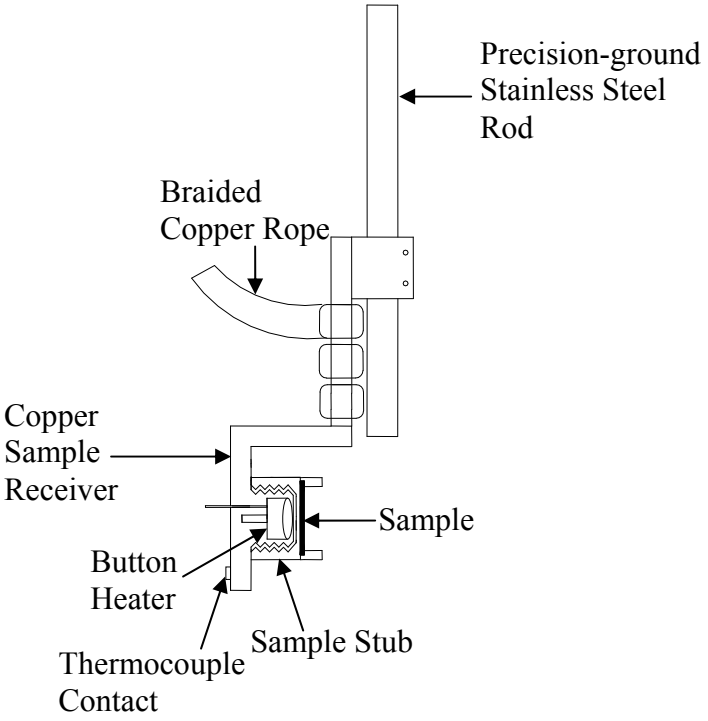

Figure 2.2. Sample receiver attached to the manipulator inside the UHV chamber equipped with heating and cryogenic cooling capabilities.

Attached to ports 1 and 2, see Figure 2.1, are 2 ¾" ConFlat™, differentially-pumped, KBr-window flanges from McAllister Technical Services (model: DPW275). RAIR

analysis is accomplished by passing infrared radiation from a FTIR spectrometer (Bruker Optics, Inc., model: IFS 66 v/S) through a custom-made wedge-shaped KBr window (Janos Technologies, Inc.) in the differentially-pumped flange attached to port 2, see Figure 2.1. The interferometer and optics of the FTIR spectrometer are maintained under low vacuum conditions by a Vacuubrand diaphragm pump (MD 4, pumping speed 1.1 L/s). The low vacuum conditions help remove unwanted background interferences from water and carbon dioxide vapors, as well as preserve the hygroscopic KBr window. After passing through the KBr window on port 2, see Figure 2.1, the infrared radiation is then reflected off the substrate at a grazing angle of approximately 86° to the surface normal and focused through the other KBr window on port 1, see Figure 2.1. Attached to the KBr window on port 1 is a custom-made box, which houses a mid-range, cryogenically-cooled, mercury-cadmium-telluride (MCT) detector (InfraRed Associates Inc., model: D313/6). The IR detector housing is also maintained under low vacuum conditions by a Vacuubrand diaphragm pump (MD 1, pumping speed 0.3 L/s).

X-ray photoelectron analysis is accomplished with ports 8 and 12, see Figure 2.1. Attached to port 12 is a twin anode (Mg/Al) X-ray source from SPECS Technologies Corporation (model: XR50). The X-ray source is water-cooled with a VWR re-circulator (model: 1177PD) and is also equipped with a linear translator (McAllister Technical Services, model: BLT27C-4), which allows the X-ray source to be position close to the sample for increased sensitivity. The kinetic energy of the ejected photoelectrons is detected with a 16.5” hemispherical energy analyzer (SPECS Technologies Corporation, model: PHOIBOS 100), which is attached to port 8. The energy analyzer is also equipped with a linear translator with 3” of travel from McAllister Technical Services

(model BLT63-3). The linear translator allows the focal point of the energy analyzer to be positioned precisely at the sample's interface. The translator also allows removal of the energy analyzer when the analyzer is not in use.

Exposure of samples within the main chamber to reactive gases is accomplished with two different effusive sources. Attached to port 5, see Figure 2.1, is a custom-made, all-glass, capillary array doser described in detail later in this chapter. The glass effusive doser has a direct line-of-sight path at 30° to the surface normal and is equipped with a linear translator (McAllister Technical Services, model: BLT27C-4) for optimal control of the flux of gas molecules striking the sample. A second effusive system, which affords a variable leak rate of 1×10^{-10} Torr L s^{-1}, is attached to port 14 (see Figure 2.1). The second effusive system is a sapphire-plate precision leak valve from MDC Vacuum Products, LLC (model: ULV-150). Partial pressures of the reactive gases or atmospheric contaminants can be monitored with a residual gas analyzer, which is attached to port 17, see Figure 2.1 (Stanford Research Systems, model: RGA 300). In addition to gas phase analyte detection, the residual gas analyzer is a valuable resource for determining the presence of a leak within the main chamber.

2.2.1.2 Load Lock Chamber

Ultrahigh vacuum conditions within the main chamber can be maintained during sample introduction if a load-lock system is used. Attached to port 7 on the main chamber, see Figure 2.1, is a stainless steel, Conflat™ flanged, manual gate valve (HVA, LLC, model: 11110-0600). The manual gate valve separates a custom-built sample introduction system (Applied Vacuum) from the main chamber allowing rapid introduction of samples without compromising the ultrahigh vacuum conditions of the

main chamber. The load lock chamber is equipped with a Conflat™ flanged hinged-door (Nor-Cal Products, model: AD-600), which allows easy transfer of the sample stub in and out of the load lock chamber. The load lock chamber can be vented to atmospheric pressure with ultrahigh pure nitrogen by opening an attached quarter turn Swaglok® valve (model: SS-4P4T). The sample stub can then be introduced through the hinged door and securely locked onto a transfer key, see Figure 2.3, which is attached to a linear/rotary precision magnetic manipulator (Transfer Engineering and Manufacturing, Inc., model: DBLRP) with a set screw. The load lock chamber can then be evacuated by an attached sorption pump. The pressure of the load lock chamber is monitored by a compact FullRange™ gauge from Pfeiffer Vacuum, Inc. (model: PKR 251). Once the sorption pump had lowered the pressure of the load lock chamber below 5×10^{-3} Torr, the sorption pump can be closed and a 6" UHV gate valve with pneumatic actuator (VAT, Inc., model: 10844-UE44), located at the bottom of the load lock chamber, can be opened. The gate valve separates the load lock chamber from a 60 L/s diode VacIon® pump (Varian Vacuum Products, model: 911-5038). The pressure of the ion pump is monitored by another compact FullRange™ gauge from Pfeiffer Vacuum, Inc. (model: PKR 251). The ion pump can quickly lower the pressure of the load lock chamber to $< 1 \times 10^{-7}$ Torr. Once this pressure is reached within the load lock chamber, the manual gate valve can be opened and the sample stub can be transferred into the main chamber with the linear/rotary magnetic manipulator. The transfer key contains a locking channel that attaches to the sample stub until the sample is securely fixed to the sample receiver. The magnetic manipulator is used to thread the sample stub onto the copper threads of the sample receiver. Once the sample is secured, the transfer key is disengaged and removed

from the main chamber and the manual gate valve is then closed. The complete procedure of transferring a sample from atmospheric pressure to ultrahigh vacuum conditions within the main chamber takes approximately 20 min. The load lock sample introduction system allows rapid transfers of numerous samples into the UHV surface analysis chamber daily.

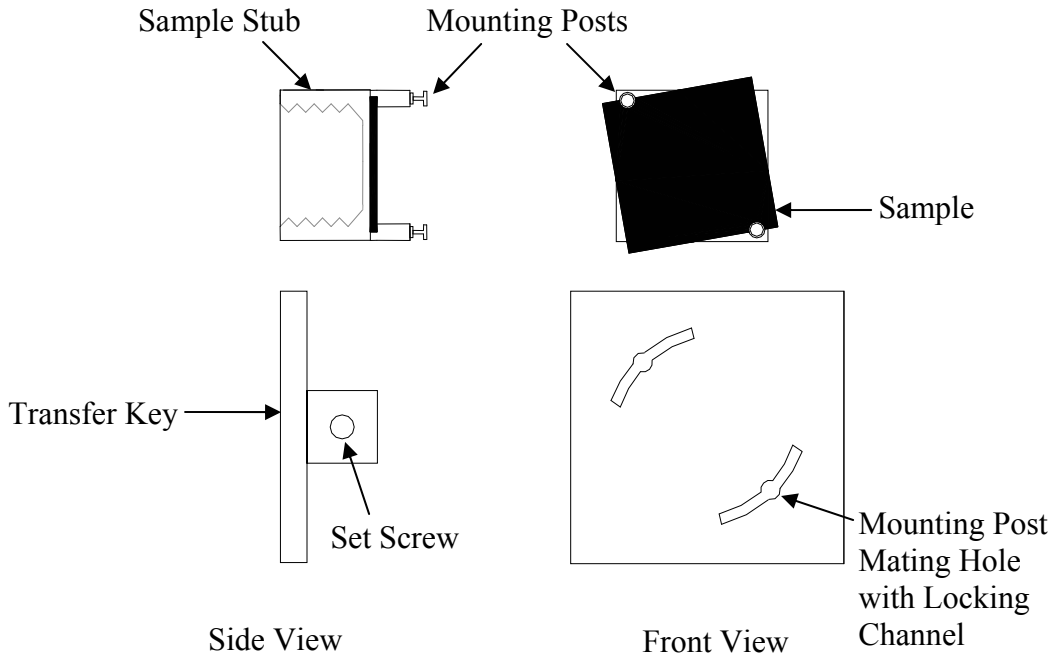

Figure 2.3. Devices for sample control: sample stub and transfer key.

2.2.1.3 Detector Chamber

Future work utilizing the UHV surface analysis chamber will include studies that monitor gas-phase products that desorb from the surfaces under analysis. The future work will also include temperature program desorbtion (TPD) analysis for further surface characterization. With these future studies in mind, a quadrupole mass-spectrometer detector chamber was designed and built, which is attached to port 6 (see Figure 2.1) of the main chamber. The doubly-differentially pumped detector chamber houses an ABB Extrel (model: MEXM 1000) quadrupole mass spectrometer completely within the

second differential stage. The mass spectrometer has a 2-1000 amu range with 1 amu resolution. The second differential stage is evacuated by a 220 L s^{-1} Triode VacIon® pump from Varian Vacuum Products (model: 912-7014). The second stage of the detector chamber is separated from the first differential stage by a 4.7 mm aperture, while the first differential stage is separated from the main chamber by a 4.3 mm aperture. The first differential stage is evacuated by a 250 L s^{-1} turbomolecular pump (Varian, Inc., model: 969-9908). The turbomolecular pump is backed by the same diaphragm pump backing the low pressure seal of the sample manipulator on the main chamber. The pressure of the mass spectrometer detector chamber is monitored with a compact cold cathode gauge (Pfeiffer Vacuum, Inc., model: IKR 270).

2.2.1.4 Ultrahigh Vacuum Chamber Assembly

Shown in Figure 2.4 is a schematic representing the complete assembly of the surface analysis chamber designed and built for the experiments presented in this work. One of the most important features of the surface analysis chamber is the ability to monitor a surface with reflection-absorption infrared spectroscopy while simultaneously exposing the surface to a controlled amount of a reactive gas of interest. Figure 2.5 shows a cut-away schematic demonstrating the alignment of the sample during RAIRS analysis and simultaneous dosing of the substrate by the capillary array doser. The surface analysis instrument allows one to monitor the products and intermediates that form during exposure of the surface to the reactive gases. Another important feature is the ability to characterize the surface before and after exposure with X-ray photoelectron spectroscopy. XPS is a valuable surface characterization technique that can be performed on a surface after exposure without removal of the surface from the chamber and therefore without

exposure of the surface to an atmospheric environment. One is therefore able to determine an elemental composition and oxidation state of the products that form during the reaction without removal of the surface from UHV conditions. Any new elements on the surface are the result of reactions as opposed to contamination.

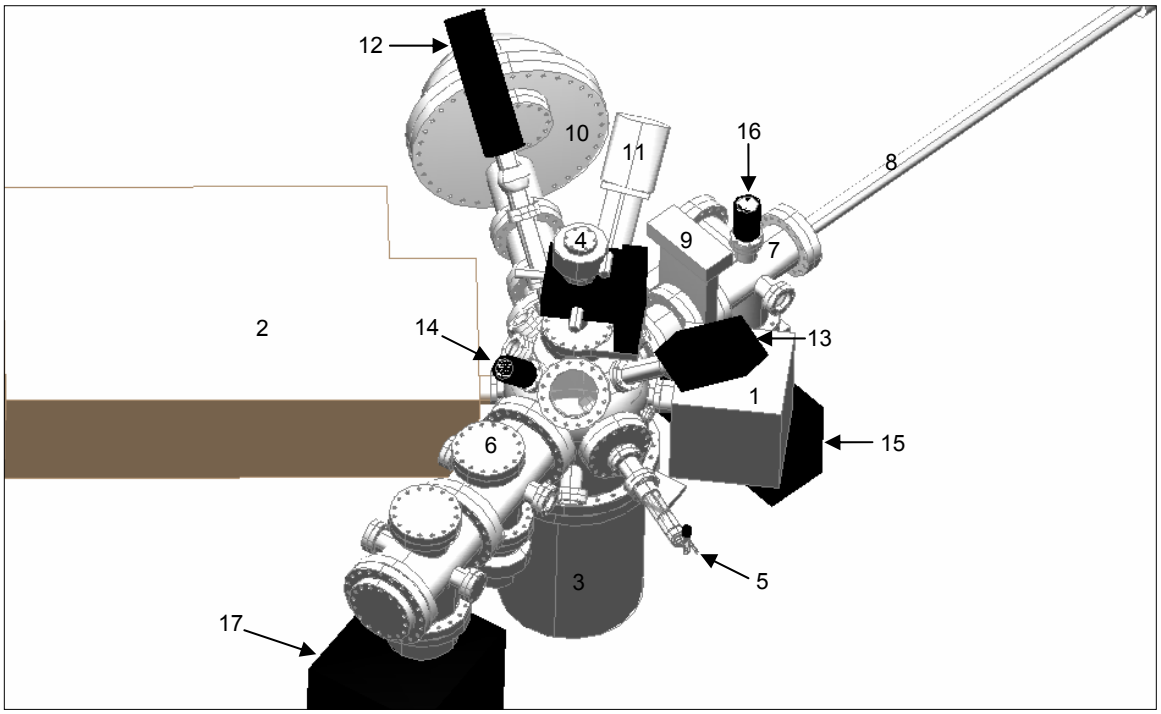

Figure 2.4. Overview of the surface analysis chamber. The labeled components are: (1) IR detector box, (2) FTIR spectrometer, (3) magnetically levitated compound molecular pump, (4) manipulator, (5) glass-capillary array doser, (6) differentially pumped detector chamber (Extrel MS), (7) load-lock chamber, (8) linear/rotary magnetic manipulator, (9) manual gate valve, (10) hemispherical energy analyzer, (11) cryostat, (12) X-ray source, (13) residue gas analyzer, (14) cold-cathode gauge, (15) load-lock ion pump, (16) FullRange™ gauge, (17) detector ion pump.

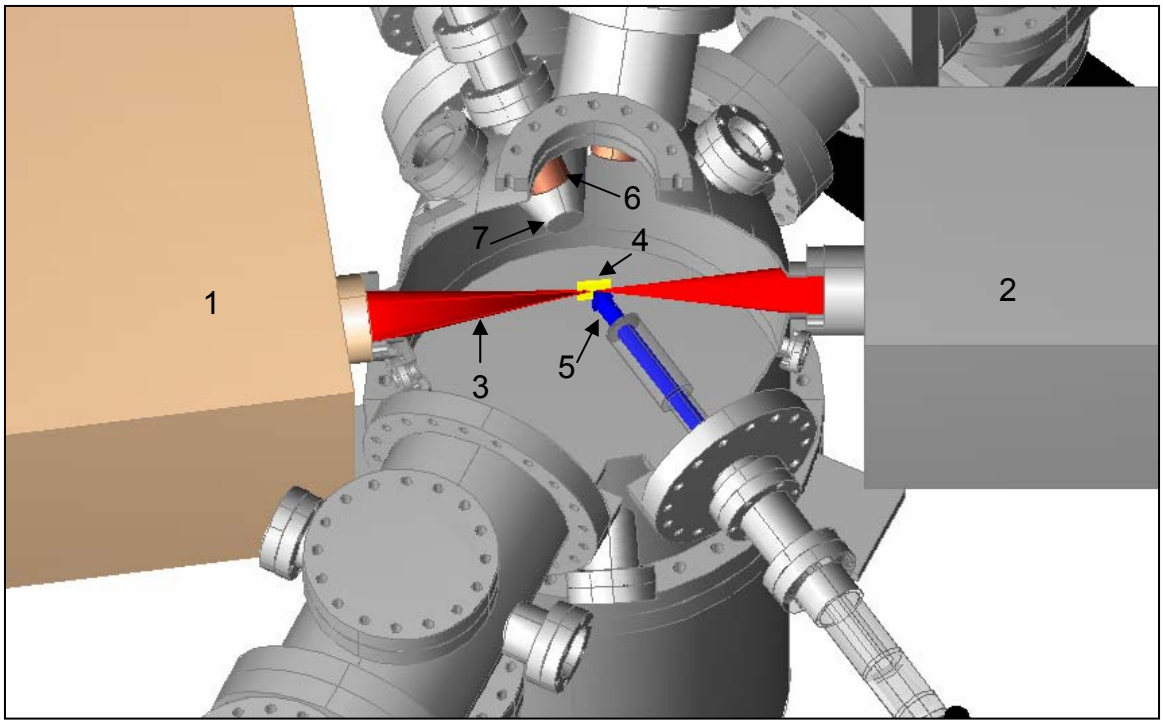

Figure 2.5. Cut-away view of the surface analysis chamber demonstrating the sample alignment during RAIRS analysis and simultaneous dosing with the capillary array doser. The sample mount and manipulator have been omitted for clarity. The labeled components are: (1) FTIR spectrometer, (2) MCT detector box, (3) IR beam, (4) sample, (5) effusive ozone beam, (6) X-ray source, (7) entrance to hemispherical analyzer.

2.2.2 Ultrahigh Vacuum Surface Analysis Chamber Interlock

2.2.2.1 LabView® Program

When using ultrahigh vacuum equipment, it is extremely important to have the equipment well protected with an interlock program. In the event of pressure bursts, power failures, or other unforeseen misfortunes, an interlock program can protect the very expensive pumps and instrumental equipment from total destruction. An interlock program was developed for the UHV surface analysis chamber discussed above with the National Instruments LabView® graphical programming language. For reference by Morris group members and others interested in reproducing this instrument, the complete source code is displayed in the appendix of this thesis (see section 6.2, Figures A.1–

A.15). The software program interfaces with a series of pressure gauges, switches, and FieldPoint™ relays to control the equipment in the event of a pressure burst or power failure. The interlock program continually checks the pressures of the chambers and verifies that these pressures are lower than user defined set points. In the event of a pressure burst, the affected chamber is isolated and the attached equipment is turned off for protection. The software also contains a front panel, see Figure A.1, which allows the user to manually control the pumps, set points, gate valves, and instrumentation.

The interlock program is named Interlock Program.vi; and requires the following files to run: FieldPoint_Relay.vi, Alarm.vi, and InterLock.iak. When the program is initially started, the imbedded subvi, FP Open.vi, opens a communication session with the FieldPoint™ server, which uses the configuration file, InterLock.iak. When the program is stopped, an imbedded subvi, FP Closed.vi, closes the communication session. The interlock program consists of one while loop that contains 14 different sequence structures. The sequence structures are performed in numerical order and each sequence structure contains internal sequence structures or case structures. The following section provides details about the flow of this graphical program.

2.2.2.1.1 Pressure Readings

In the first sequence structure, see Figures A.2a-2c, eight separate subvi's record the voltage signal from specific channels in a data acquisition board (DAQ) within the computer. The DAQ board obtains the voltages from the individual gauges, which are attached to the pressure gauge module described later in this chapter. The first sequence structure converts the voltages into pressure values, with units of Torr, with the appropriate formulas for the specific type of gauge attached to each channel. The

pressure values are then displayed on the front panel. The first sequence structure also plots on the front panel the pressure value of the main chamber every 24,000 times through the while loop, about 15 minutes. One can therefore inspect the front panel at any time to obtain a 30 hour history of the pressure in the main chamber.

2.2.2.1.2 Pressure Set Points

In the second and third sequence structures, see Figures A.3a, A.3b, A.4a, and A4b, separate internal set point are set for the Extrel mass spectrometer electronics, RGA mass spectrometer, and X-ray photoelectron spectrometer. The internal set points ensure that these pieces of equipment are not turned on when the front panel set points for the main and detector chambers have been set too high, for example, when started the pumps from atmosphere. The internal set points are fixed within the program and cannot be changed from the front panel.

The fourth sequence structure, see Figures A.5a-d, checks to ensure that the pressure of the main chamber foreline or detector chamber foreline is below the set point for each individual chamber. If the pressure is higher than the set point, all equipment is turned off and all valves are closed. The chamber vent timers, described in section 2.2.2.1.6, are also started. The fifth sequence structure, see Figures A.6a-d, checks to ensure that the pressures of the main chamber and detector chamber are below their individual set points. If the main chamber or detector chamber pressure is above its set point, all equipment is turned off and all valves are closed. Sequence structure five also activates the chamber vent timers.

The sixth sequence structure, see Figures A.7a and A.7b, checks the pressure of the load lock chamber and ensures that the pressure is lower then the load lock chamber set

point. If the pressure in the load lock is higher than the set point, the UHV gate valve separating the load lock chamber from the load lock cross is closed. The seventh sequence structure, see Figures A.8a and A.8b, checks the pressure of the load lock cross, which contains the ion pump and pneumatic actuator controlling the high vacuum seals of the sample manipulator. If the pressure in the load lock cross is higher than its set point, the UHV gate valve and high-vacuum seal valve are closed and the ion pump is turned off. All of the set points mention above, except for the internal set points, can be changed by the user within the front panel, see Figure A.1.

2.2.2.1.3 Load Lock Chamber Alarm

Catastrophic damage could be caused if the manual gate valve separating the main chamber from the load lock chamber is opened when the load lock chamber is at atmospheric pressure. To help prevent this type of error, an alarm system is installed on the manual gate valve. When opening the manual gate valve, a magnetic relay contact switch is opened. The eighth sequence structure, see Figures A.9a and A.9b, in the interlock program monitors the pressure of the load lock chamber. If the pressure is greater than 1.0×10^{-5} Torr, the eighth sequence structure, along with a mechanical relay located next to the FieldPoint™ relays, activates an alarm when the magnetic relay contact is opened. If the pressure is lower than 1.0×10^{-5} Torr, the eighth sequence structure does nothing and one can open the manual gate valve safely.

2.2.2.1.4 FieldPoint™ Relays Update

Power to all equipment and valves is supplied through FieldPoint™ relays located inside the FieldPoint™ relay electronics described in section 2.2.2.3. The interlock program is actually controlling the state of the FieldPoint™ relays. The ninth sequence

structure, see Figures A.10a-c, sends the updated Boolean values to the FieldPoint™ relays if specific conditions for each controller are met. If the appropriate conditions are not met, a false signal is sent to the Fieldpoint™ relays. The ninth sequence structure therefore prevents a user from opening a controller before the program has time to update. The Boolean values from the front panel are fed into an array before they are sent to the subvi, FP-RLY 420.vi. The positions in the array correspond to specific channels in the FP-RLY-420 modules. The string "FP-RYL-420@#" within the ninth sequence structure corresponds to the position of the FP-RLY-420 module on the FieldPoint™ network module. The subvi, FP-RLY 420.vi, communicates with the FieldPoint_Relay.vi and Alarm.vi programs to open or close the individual relays on the FP-RLY-420 modules.

2.2.2.1.5 Chamber Venting

If the pressure in the main chamber, detector chamber or either of the foreline pumps rises above its corresponding set point, sequence structure ten, see Figure A.11, starts two chamber vent timers. In sequence structure eleven (Figures A.12a and A.12b), the first timer will open the chamber vent valve after five minutes. Sequence structure twelve (Figures A.13a and A.13b) will close the chamber vent valve after one hour and reset both vent timers. The time elapsed, from when the timers were first activated, is displayed on the front panel under the "Elapsed Time" display. The front panel also contains an indicator light, which is red when the vent valve is closed and is green when the vent valve is opened. The vent valve cannot be turned on from the front panel, but at any time during a chamber vent, the large button labeled "Press to STOP A Chamber Vent" can be pressed. This button is a momentary switch and must be held down for

approximately 1 second in order to work. If the button is pressed, the chamber vent timers will be stopped and reset, and the vent valve will be closed. The "Press to STOP A Chamber Vent" button is controlled by the thirteenth sequence structure, see Figures A.14a and A.14b.

2.2.2.1.6 Front Panel Update

The last sequence structure, Figures A.15a and A.15b, was placed into the code to ensure that the color of the Boolean switches on the front panel matched the actual conditions of the FieldPoint™ relays. A few scenarios exist in which the code could actually cause the front panel Boolean switches to be inconsistent with the state of the FieldPoint™ relays. The fourteenth sequence structure was added to correct this error.

2.2.2.2 Pressure Gauge Electronics

The interlock program interfaces with two different custom built electronic modules. All input to the program comes from the pressure gauge interface, and all output from the program is sent to the Fieldpoint™ relay modules. The input to the pressure gauge electronics comes from the gauges on the instrument. A representative electrical schematic of one of the circuits in the pressure gauge electronics is shown in Figure 2.6. Power to the pressure gauge electronics is provided through a 110V AC fused-protected power cord. The pressure gauge module contains eight identical circuits and can be used to monitor eight individual gauges simultaneously. A 24V DC power supply (OMRON, Corp., model: S8K2-09024) inside the module, provides power to all the gauges attached to the UHV surface analysis chamber. Each individual gauge can be turned on or off from a single-pole single-throw switch on the front of the gauge module. When the gauge is on, a green LED is lit on the front panel, and 24V DC power is supplied to the

individual gauge through pins 1 and 4 of the plug on the gauge module. When the gauge is powered, a voltage signal from the gauge is sent to pin 6 of the plug on the gauge module. Pin 6 is internally wired to one of the eight differential analog input channels on a 68-pin digital and trigger input/output terminal block (National Instruments, model: CB-68LP) located inside the pressure gauge module. The reference signal from the gauge is connected to pin 3 of the plug, and is internally wired to the corresponding analog input channel of the terminal block. Pin 2 of the plug is connected to an earth ground and pin 5 (gauge identification pin) is left open intentionally. The terminal block is connected to a 16 analog input, data acquisition (DAQ) board (National Instruments, model: PCI-6014) through a noise rejecting shielded cable (National Instruments, model: SH68-68-EP). The DAQ board is located inside a PC and converts the analog voltage signal to the digital signal used in the interlock program, see section 2.2.2.1.2.

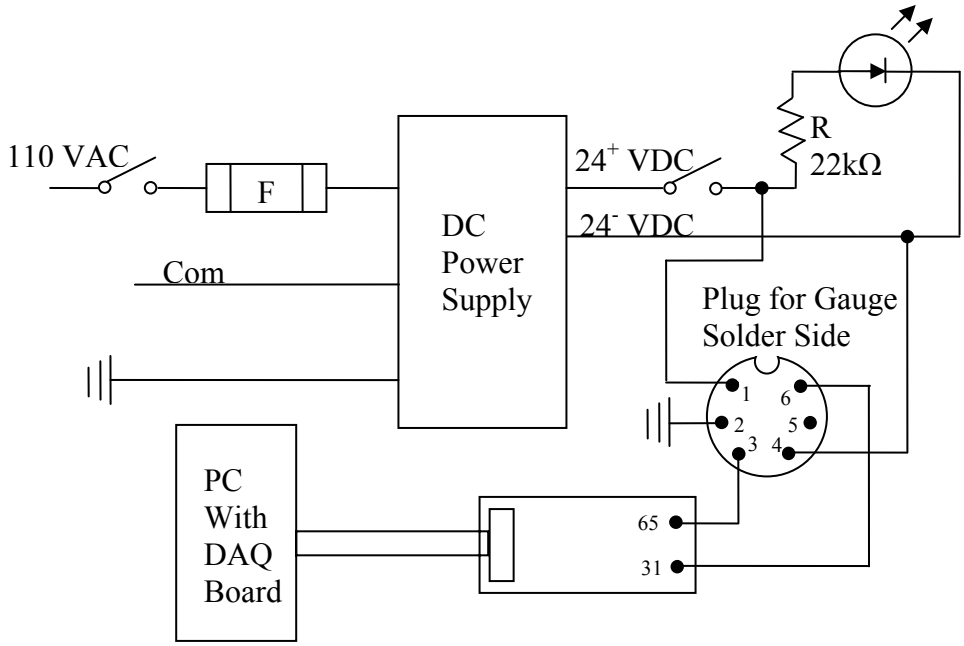

Figure 2.6. An electrical schematic of the circuits in the gauge box used to monitor the pressures of the surface analysis chamber.

2.2.2.3 Fieldpoint ^{TM} Relay Module

A custom designed Fieldpoint^{TM} relay module was made to control 20 individual receptacles. The vacuum pumps, gate valves, and pneumatic actuators described in this chapter are connected to the receptacles and therefore controlled by the relay electronics. An electrical schematic showing one of the individual circuits for the load plugs is shown in Figure 2.7. A three-way switch on the front panel of the relay electronics provides three different modes in which the relay electronics can be operated. When the switch is in the up position, the load plug is provided with 110V AC fuse-protected power. When the switch is in the down position, no power will be provided to the load plug. When the switch is in the middle position, the load plug's circuit is through the FieldPoint^{TM} relays and therefore controlled by the interlock program described previously in this chapter. When in the computer controlled mode, the interlock program controls pins 1 and 2 in an eight channel relay module (National Instruments, model: FP-RLY-420). When the Boolean switch on the front panel (see Figure A.1) is green, the computer closes the switch between pins 1 and 2 providing fuse-protected 110V AC power to the load plug. When the Boolean switch is red, the relay switch between pins 1 and 2 is opened, and no power is sent to the load plug. The FP-RLY-420 relay modules are plugged into terminal bases (National Instruments, model: FP-TB-1) that are connected to a network module (National Instruments, model: FP-1000). The custom relay electronics contain three of the FP-RLY-420 relay modules attached to one FP-1000 network module. The network module communicates with a PC through an RS-232 connection and is powered from a DC power supply (OMRON, Corp., model: S8K2-09024) located within the relay electronics. The circuit, see Figure 2.7, within the relay electronics is completed with a

mechanical relay (IDEC, Corp., model: RR2P-UAC120V) and LED. An LED on the front panel of the relay electronics can be lit either green or red. When the three-way switch is in the on position, the mechanical relay will provide power (+5V) to the LED, turning it green. When the three-way switch is in the off position, the mechanical relay will provide power (+5V) to the LED, turning it red. When the relay electronics are in the computer controlled mode, the mechanical relay will provide power to the LED. The LED will turn green when the FieldPoint™ relay is closed and red when the FieldPoint™ relay is opened.

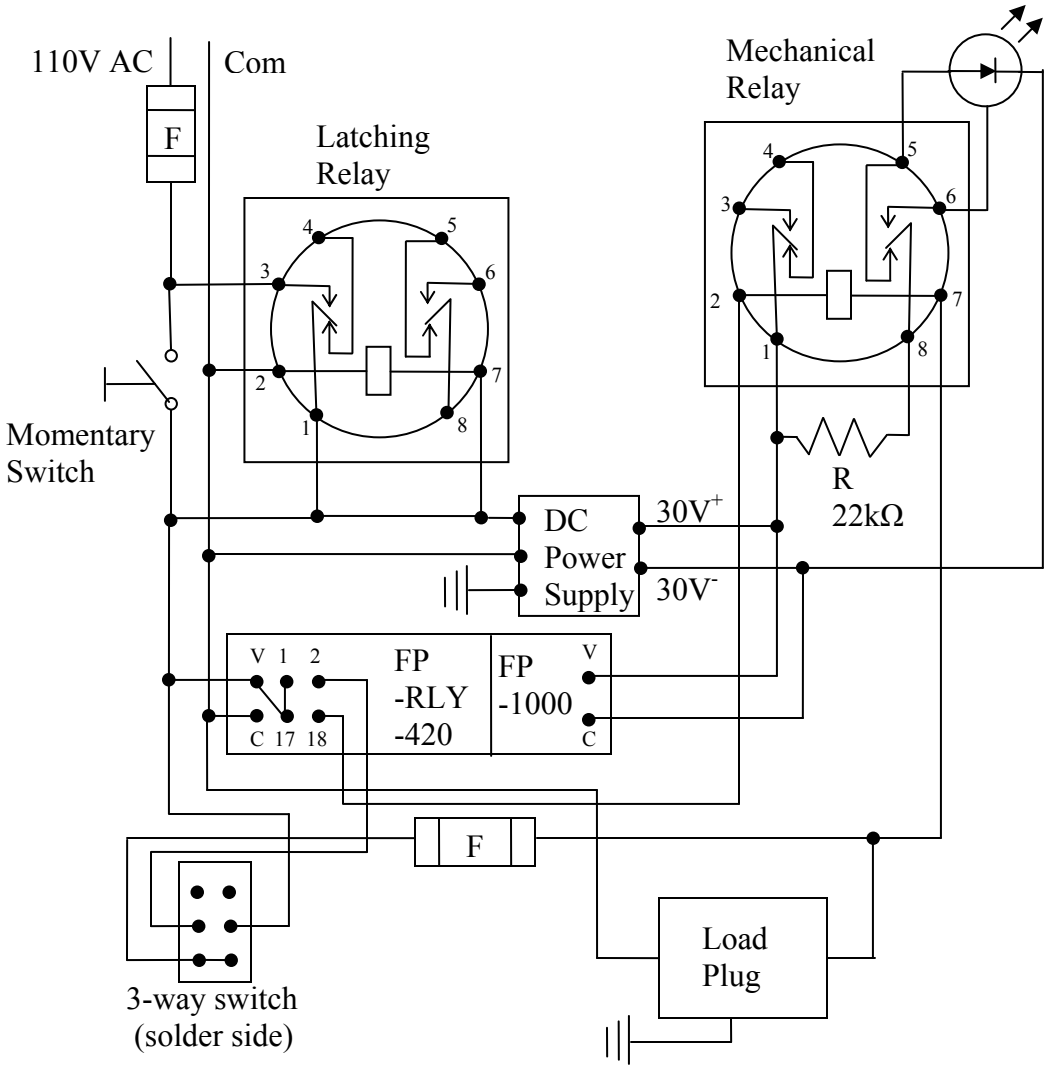

Figure 2.7. An electrical schematic of the circuits in the Fieldpoint™ relay box providing power to the individual load plugs.

The FieldPoint™ relay electronics are provided 110V AC power through a latching relay located inside the FieldPoint™ relay electronics. When the reset button on the back of the relay electronics is pushed in, a momentary switch provides power to the latching relay. The latching relay will continually provide power to the relay electronics until there is a power interruption. In the event of a power interruption, the latching relay will open and power will not be provided to the relay electronics until the reset button on the

back of the relay electronics is pushed in again. The latching relay was installed in the relay electronics to prevent a return in power to the relay electronics after a power failure. Therefore, the latching relay allows a user to ensure all necessary conditions are met before power is restored to any instrumentation.

The ultrahigh vacuum surface-analysis interlock system described above allows the chamber to be operated 24 hrs per day, 7 days per week because the interlock system monitors the pressure of the chambers and controls the electronics and vacuum pumps continuously. This continuous operation permits the chamber to achieve and maintain ultrahigh vacuum conditions.

2. 3 Ozone Generation, Storage, and Exposure Monitoring

2. 3.1 Background

Ozone is one of the most efficient oxidizing agents and has gained wide application in the growth of superconducting oxide films by the *in vacuo* molecular beam epitaxy (MBE) method.[37,61-63] Ozone's chemical reactivity is most likely due to ozone's ability to decompose to atomic oxygen (a highly reactive species) and O_2, and ozone's high electron affinity.[34,37] Ozone is also highly toxic and extremely explosive in high concentrations.[30,35] Because of ozone's toxicity and explosive nature, pure ozone is extremely difficult to generate, store, and handle. Previous researchers have designed systems that deliver high concentrations of ozone from liquid,[34,63] solid,[62] or adsorbed phases.[37,64] The following section of this chapter describes the methods in which we generate, store, and handle pure ozone. Due to the highly explosive conditions when handling liquid ozone, we have adapted and modified the methods of Zhukov et al. and Stevens et al. that store adsorbed ozone on silica gel.[37,64]

2.3.2 Ozone Generators

Caution: Ozone is toxic, unpredictable, and explosive! [35,36]

Care should be used at all time when synthesizing or handling!

All work with ozone was performed behind blast shields made from plexi-glass to protect personal in the event of an explosion. Two different instruments have been used when generating ozone for the research described in this thesis. The first instrument is a custom-built corona discharge ozone generator, and the second instrument is a commercial ozone generator (Ozone Solutions, model: SR-32). The custom-made ozone generator is roughly based on the work of Yagi and Tanaka,[65] and Sponholtz et al.[66] Figure 2.8 shows an instrumental schematic representing the components of the custom-made ozone generator. A 12" precision-ground 303 stainless steel rod (Small Parts, Inc.) is incased in a custom glass-blown quartz vessel. Originally, Pyrex was used for the vessel, but proved to become very brittle after continuous use of the ozone generator. The stainless steel rod is the primary electrode and is centered in the quartz vessel with a 3 mm gap between the rod and the walls of the vessel. The rod is connected to a tungsten wire by a set screw. The tungsten wire passes through the quartz vessel in a grade-glass seal and is connected to one of the outputs of a neon sign transformer (Everbrite Electrontics, Inc., model: Evertron 2610D). The entire quartz vessel is immersed in a 0.3 M solution of $CaCl_2$ in a custom-jacked glass Dewar. Pure ethanol, cooled by a re-circulator (VWR Scientific Products, model: 1160A) to 2.9 °C, is passed through the jacked-vessel to provide cooling to the ozone generator. The other output of the transformer is placed into the $CaCl_2$ solution causing the $CaCl_2$ to become the secondary electrode. The neon sign transformer is powered by 110V AC and outputs 5.5 kV at

20 kHz. Research grade oxygen (Airgas Specialty Gases) is fed into the top of the ozone generator. A silent electrical discharge within the generator, consisting of thousands of micro discharges, creates electrons with sufficient energy to split the O=O bonds of the molecular oxygen.[65,66] The oxygen atoms that are created recombine with unreacted molecular oxygen to form ozone. The output of the custom ozone generator, with a flow of oxygen at 10 L/min, is 0.4% ozone, which is 3.8 g of ozone per hour. The output of the commercial generator at the same flow rate is 2.0% ozone, which is 31 g of ozone per hour. The commercial generator proved to be more reliable and durable, and the commercial generator has a higher throughput.

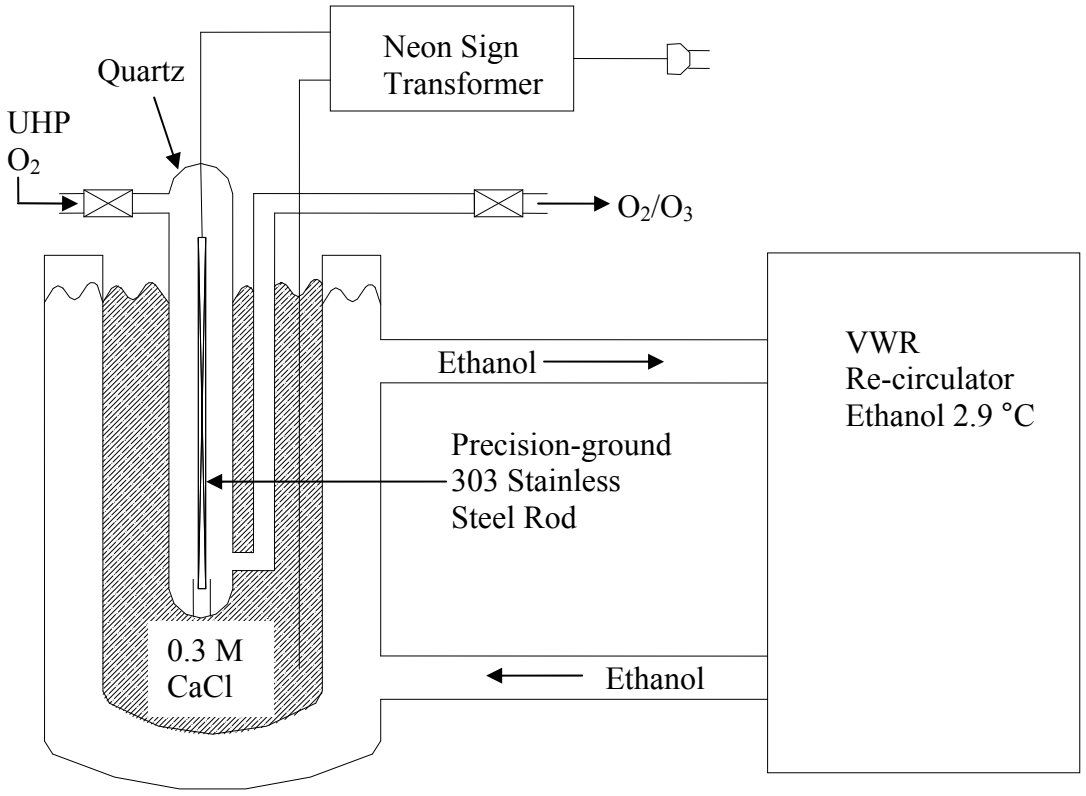

Figure 2.8. Custom-made corona discharge ozone generator with cooling jacket.

2.3.3 Ozone Purification and Storage System

Due to highly explosive conditions when handling liquid ozone, we chose a method that allows us to purify and store ozone by trapping it in the pores of high area silica gel at cryogenic temperatures.[30,37] The ozone storage system allows the delivery of ~50 Torr of pure ozone to samples within the ultrahigh vacuum surface analysis chamber described previously in this chapter. Extreme caution should be used when handling pure ozone. One should not allow the ozone system to obtain pressures above 50 Torr of pure ozone. Ozone concentrations above 12% by volume at 1 atm have been shown to cause an explosive chain decomposition and convert into oxygen completely.[35] In our laboratory, pressures above 50 Torr of pure ozone have proven to spontaneously detonate causing an over pressurization of all glassware connected to the ozone storage system. Figure 2.9 shows a schematic representing the various components of the ozone purification and storage system. Ozone catalytically decomposes on metal surfaces; therefore, the ozone system is designed with minimal amounts of metal.[37] The ozone storage system consists mostly of Pyrex glass containing Teflon-sealed glass valves. The ozone trap contains grade 03, >8 mesh, silica gel (Sigma-Aldrich) placed between two coarse sintered-glass frits.[67]

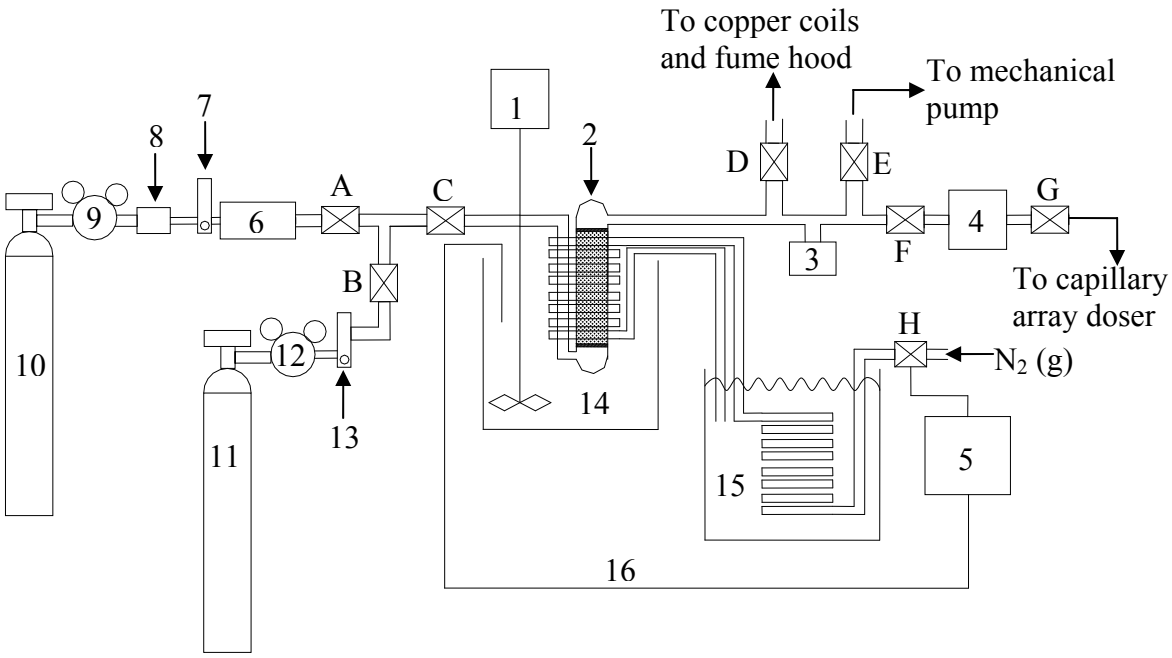

Figure 2.9. Ozone purification and storage system. The labeled components are: (1) mechanical stirrer, (2) silica gel trap, (3) capacitance monometer, (4) UV/Vis spectrometer, (5) profile controller, (6) ozone generator, (7) oxygen flow meter, (8) flame arrestor, (9) oxygen regulator, (10) research grade oxygen cylinder, (11) ultrahigh pure nitrogen cylinder, (12) nitrogen regulator, (13) nitrogen flow meter, (14) dry ice/acetone bath containing copper coils, (15) liquid nitrogen bath containing copper coils, (16) thermocouple feedback, (A-H) Teflon®-sealed glass valves described in the text.

To trap ozone, the silica gel was dried at 200 °C by heating under vacuum with heat tape. The system was then evacuated by a mechanical pump. The mechanical pump was lubricated with Fomblin® oil, which is stable in the presence of ozone.[37] Once the system was evacuated, valves A, B, D, E, and F (see Figure 2.9) were closed, and the system was brought to atmospheric pressure by opening valves B and C and adjusting the nitrogen flow meter. The pressure of the system was monitored with a compact capacitance manometer (Pfeiffer Vacuum, Inc., model: CMR 261). Once the system was slightly above atmospheric pressure, the exhaust valve (D) was opened. Copper coils were then placed around the silica gel trap. The copper coils were attached to a cryogenic solenoid

valve (ASCO Valve, Inc., model: 8210LT) that was controlled by a microprocessor-based profile controller (Omega Engineering, model: CN-2041). The copper coils and solenoid valve were used to control the temperature of the silica gel during the purification process described below. The entire ozone trap with copper coils was placed into a vacuum Dewar containing acetone. A K-type thermocouple, which was placed in the solvent within the vacuum Dewar, was attached to the profile controller, providing the controller with feedback. Initially, the acetone was cooled to -80 °C with dry ice. When trapping ozone, the acetone was maintained at -80 °C by constantly adding dry ice. Once the silica gel trap was cooled to -80 °C, valve A was opened and the flow of oxygen through the ozone generator was adjusted to ~85 mL/min with the oxygen flow meter (Matheson Gas Equipment Technology Group, model: ME16D491E910). Once the oxygen flow was achieved, valve B was closed and the ozone generator was turned on. At -80 °C, ozone adsorbed to the silica gel, and the mixture of ozone and oxygen that was not fully trapped was vented through copper coils to a fume hood. The copper coils catalytically decomposed the excess ozone to molecular oxygen.[30] When sufficient ozone was trapped, the silica gel turned dark blue and valves A, C, and D were closed. The absorbed ozone was stable on the silica gel as long as the acetone temperature was maintained at -80 °C.

When one is ready to dose a sample within the ultrahigh vacuum chamber with ozone, the absorbed ozone must first be purified. To purify the ozone, valves C, D, and G were closed and valves E and F were opened. The vacuum Dewar was lowered and all dry ice was quickly removed from the acetone. The vacuum Dewar was then placed back around the coils and more acetone was added. The mechanical stirrer (see Figure 2.9) was then

turned on, and the set point of the profile controller was set to -55 °C. The profile controller opened and closed the solenoid valve (H) allowing $N_{2(g)}$ to flow through copper coils submerged in liquid nitrogen. After passing through the liquid nitrogen submerged coils, the $N_{2(g)}$ passed through the coils surrounding the ozone trap. This system slowly raised the temperature of the acetone in the vacuum Dewar to -55 °C. Once the system was evacuated to ~4 Torr and was at -55 °C, valve E was closed. The evacuation and thermal increase removed all excess oxygen from the absorbed silica gel. The concentration of the gas-phase ozone desorbing from the silica gel was monitored by the custom flow cell (0.5 cm path length) and the UV/Vis spectrometer (StellerNet, Inc., model: EPP200C with deuterium light source). The purification process provided 100% pure ozone at ~50 Torr. The pressure of the pure ozone can be decreased by lowering the temperature of the acetone bath, which can be accomplished by decreasing the set point of the profile controller. Dosing of a sample within the ultrahigh vacuum chamber was accomplished by opening valve G, which is attached to an all-glass capillary array doser described below. During dosing, the gas-phase ozone can slowly decompose to oxygen and lower the concentration of the ozone. The concentration was quickly brought back to 100% by opening valve E for ~30 s. The evacuation caused by opening valve E removed the unwanted oxygen and re-purified the ozone. The ozone system provided a stable source of pure ozone at a pressure of ~50 Torr for the capillary array doser for over 8 hours. The profile controller maintained a set point to within ± 1.0 °C. Oscillations in temperature of the acetone bath were observed in the absorbance values from the UV/Vis spectrometer, see Figure 2.10. The overall decrease in absorbance over time was due to the slow decomposition of the ozone to molecular oxygen.

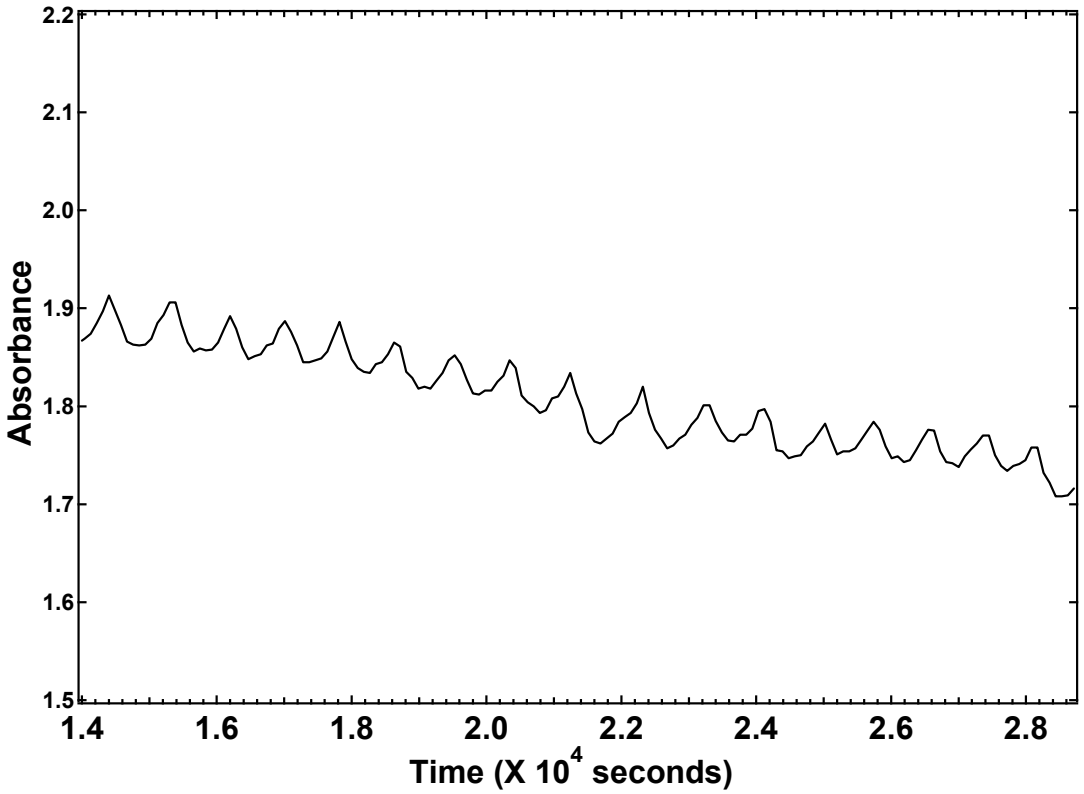

Figure 2.10. A graph of the absorbance vs. time of the ozone in the UV/Vis spectrometer demonstrating the stability of the ozone storage system.

2.3.4 Ozone Doser Design

An all-glass capillary array doser was designed based on the previous work of Zhukov et al.[37] and Yates.[30] The capillary array doser allowed controlled dosing of pure ozone to surfaces within the previously described UHV surface analysis chamber at a calculated conductance of 1.6×10^{-2} cm^3 s^{-1}. The effusive molecular beam doser, Figure 2.11, contains a Pyrex capillary with an internal diameter of 0.08 mm and a total length of 20 mm. When exposing a sample, the high pressure side of the capillary was raised to ~50 Torr of ozone by opening the Teflon-sealed glass valve attached to the doser. The ozone beam leaving the capillary entered the UHV chamber through a glass-to-stainless steel Conflat® flange and collided with a glass baffle plate at the head of the doser. The baffle plate randomized the motions of the ozone molecules before they escaped through

a glass array containing 120 holes each 0.5 mm in diameter. The baffle plate therefore allows a uniform flux of ozone molecules to leave the head of the doser, which extends into the ultrahigh vacuum chamber ~3.5 cm away from the sample. While dosing with the capillary array doser, typical pressures within the UHV chamber reached 2×10^{-7} Torr. Under these conditions, a calculated flux of ozone molecules at the sample was $\sim 1.7 \times 10^{15}$ molecules s^{-1} cm^{-2}.

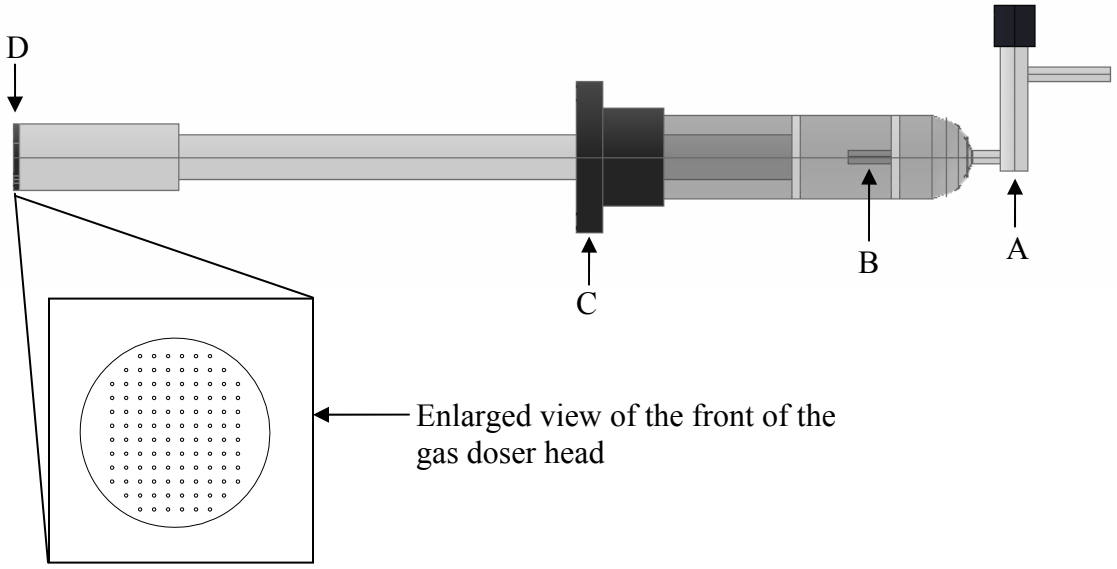

Figure 2.11. Schematic drawing of the all-glass capillary array doser designed to deliver controlled fluxes of pure ozone. The following components are labeled: (A) Teflon®-sealed glass valve, (B) 0.08 mm glass capillary, (C) 2 ¾" Conflat® flange, (D) gas doser head.

2.4 Surface Analysis Instrumentation

2.4.1 Reflection-Absorption Infrared Spectroscopy

The initial studies demonstrating the use of reflection-absorption infrared spectroscopy (RAIRS) to analyze thin layers on metal surfaces were performed by Greenler.[68,69] We chose to use RAIRS to study the reactions of ozone at interfaces

because RAIRS provided us with a non-destructive, real time analysis that was sensitive to C=C, C=O, and C-H moieties. RAIRS also provided us with information about the orientation and chemical environment of absorbed molecules on the surface.[68,70] In this thesis, RAIRS was the primary tool used to characterize SAMs before and after exposure to ozone. The SAMs were assembled on gold-coated substrates that provide the reflective surface necessary for RAIR measurements.

The basic principles of reflection-absorption infrared spectroscopy are very similar to traditional FTIR transmission spectroscopy experiments. Infrared radiation is directed toward a sample and photons from the radiation excite vibrations within the molecules of the sample. Like traditional FTIR, a Michelson interferometer is used in RAIRS to simultaneously measure all infrared frequencies of interest, generating an interferogram. The interferogram is converted into a spectrum by a Fourier transform within the spectrometer's electronics. The resulting spectrum is a plot of intensity versus wavenumber (cm^{-1}). The main difference between RAIRS and transmission spectroscopy is that RAIR measurements obey a set of surface selections rules, first described by Greenler.[68,69]

Figure 2.12 is a schematic demonstrating the findings of Greenler. A beam of infrared radiation that is reflective off a planar substrate can be resolved into two components: perpendicular (s-polarized) and parallel (p-polarized) to the plane of incidence. When light that is polarized perpendicular to the incident plane (E_s) is reflected off a planar substrate, the reflected light undergoes a phase shift close to 180º at all angles of incidence (φ). The phase shift causes destructive interference, which almost completely cancels out the component that is perpendicular to the plane of incidence directly at the

surface. Therefore, s-polarized light has very little interaction with dipole moments of molecules absorbed on the reflective interface. In contrast, light that is polarized parallel to the plane of incidence (E_p) undergoes a phase shift at the interface that increases rapidly as the incident angle approaches grazing angles. Greenler determined that p-polarized light reflected from a substrate at an incident angle near 86º would have a ~90º phase shift.[68,69] A phase shift near 90º results in a net doubling of the p-polarized light's amplitude at the reflective surface, and therefore, p-polarized light will interact significantly with dipoles of molecules absorbed at the interface. Greenler's findings can be summarized by a surface selection rule that states: only surface bound molecules with active IR modes that have a component of their transition dipole moment perpendicular to the surface will be observable in RAIR measurements.

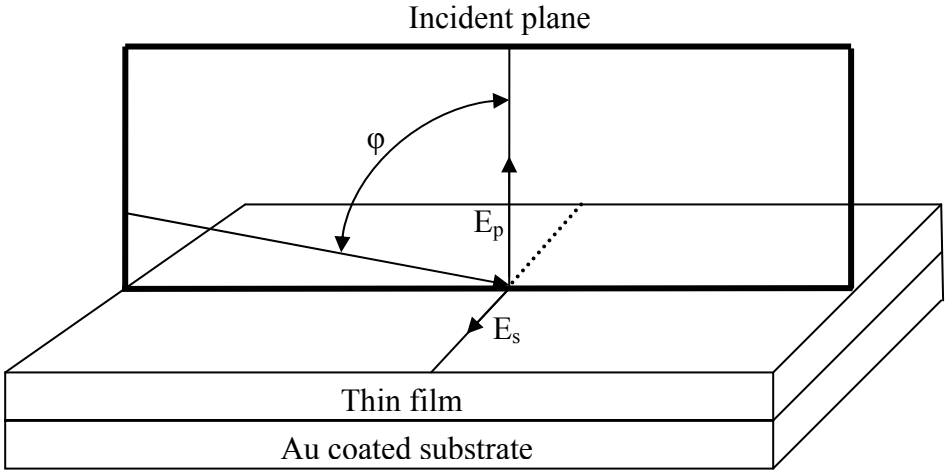

Figure 2.12. Infrared radiation reflecting from a substrate at incident angles (φ) near grazing can be resolved into two components: perpendicular to the plane of incidence (E_s) and parallel to the plane of incidence (E_p).

In this work, in situ RAIR measurements were performed with a Bruker IFS 66v/S spectrometer attached to the UHV chamber previously described, see Figure 2.13. Infrared radiation from a SiC globar source was reflected off a gold coated parabolic

mirror (focal length 180 mm) and focused through a slit (0.9 mm × 4 mm) on a variable aperture wheel. The IR beam was then sent through an interferometer and focused onto a movable mirror. The moveable mirror allowed the IR radiation to be sent to either an internal sample compartment or an external sample compartment. In the external sample compartment, the IR light was focused by a parabolic mirror (focal length 250 nm) through a KBr window attached to the UHV chamber previously described. The IR radiation was reflected off the gold substrate in the UHV chamber at ~ 86º relative to the surface normal. After reflecting off the surface, the IR radiation exited the UHV chamber through a KBr window and was focused by a parabolic mirror (focal length 250 mm), reflected from a flat mirror, and finally focused by a second parabolic mirror (focal length 43 mm) into a mid-range (750–4000 cm^{-1}) mercury cadmium telluride (MCT) detector, which was cooled with liquid nitrogen. The spectrometer also has the option to collect spectra from samples within the internal sample compartment. Using this option, one can chose to use either an MCT detector or deuterated triglycine sulphate (DTGS) detector. The internal sample compartment was not used in the experiments presented in this work. All spectra presented in this thesis are the result of the co-addition of 100 scans taken over 90 seconds obtained with a 2 cm^{-1} resolution and a scanner velocity of 20.0 kHz. All spectra are presented with the unit of intensity defined as $-\log(R/R_0)$, where R was the reflectivity of the monolayer and R_0 was the reflectivity of a reference spectrum. Two different types of reference spectra were used throughout this thesis and will be specified accordingly.

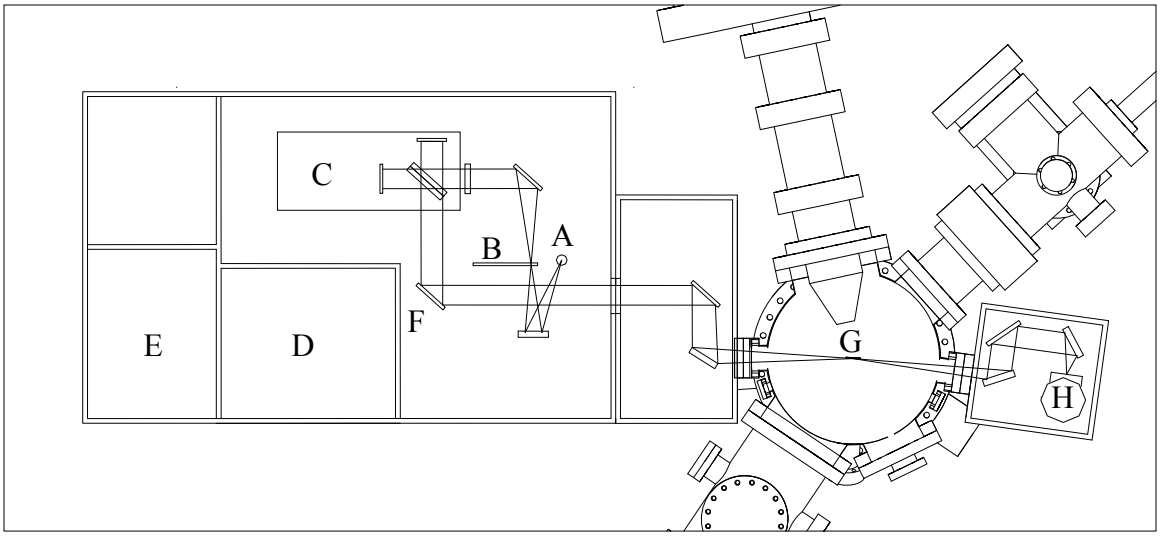

Figure 2.13. A schematic representing the path of the IR radiation from the Bruker IFS 66v/S spectrometer. The labeled components are: (A) SiC globar source, (B) variable aperture wheel, (C) interferometer, (D) internal sample compartment, (E) internal detector housing (MCT and DTGS), (F) movable mirror, (G) sample within the external UHV chamber, (H) MCT detector.

2.4.2 X-ray Photoelectron Spectroscopy

X-ray photoelectron spectroscopy (XPS) is a well established analytical technique that is used to determine the chemical identity and local chemical environment of elements on substrates. XPS relies on the photoelectric effect described by Einstein in 1905.[71] The photoelectric effect describes the phenomenon of core level electrons being ejected from a surface when exposed to photons of sufficient energy. Surfaces that are examined by X-ray photoelectron spectroscopy must be placed in high vacuum conditions where the mean free path is large. The samples are then irradiated with photons with energies in the range of 200–2000 eV, which have sufficient energy to eject core level electrons from the interfacial region of a sample. An energy analyzer is used to determine the kinetic energy of the ejected electrons, see Figure 2.14. The kinetic energy of the ejected electrons is related to the energy of the exciting photon (***hv***), the binding

energy of the core electron ($\mathbf{E_b}$), and the work function of the sample within the spectrometer ($\mathbf{\Phi}$) by the relation shown in Equation 2.1 and demonstrated in Figure 2.15:

$$\mathbf{E_k} = \boldsymbol{h\nu} - \mathbf{E_b} - \mathbf{\Phi} \qquad \text{Equation 2.1}$$

The chemical identity and local environment can be determined by the binding energy of the ejected electron; therefore, XPS is a valuable technique that can be used to determine the oxidation states of the surface atoms.

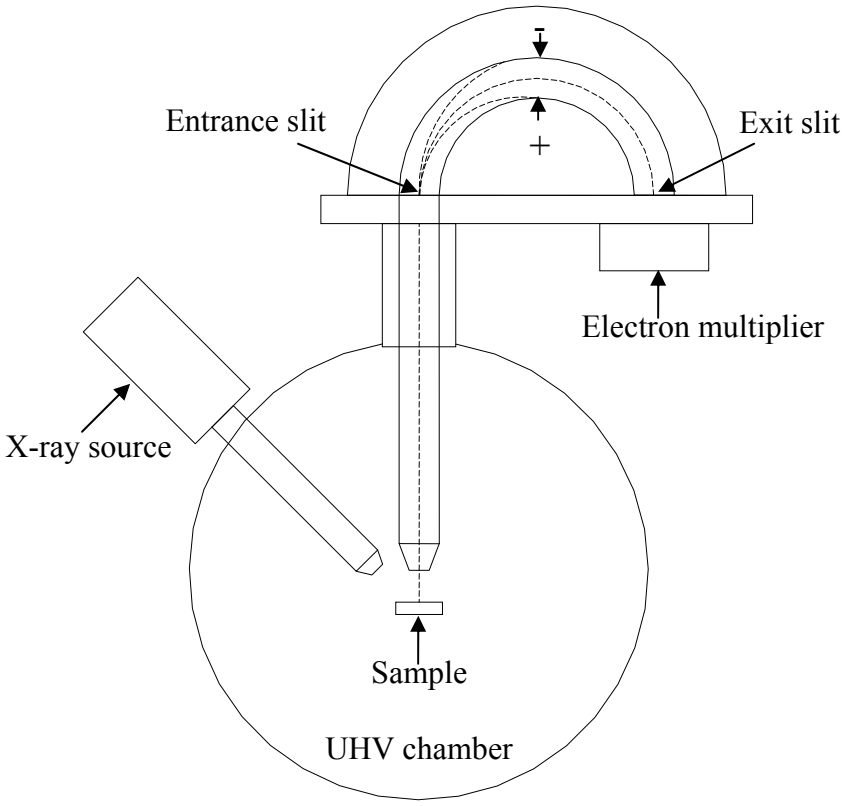

Figure 2.14. A schematic demonstrating the experimental setup of an X-ray photoelectron spectrometer containing an X-ray source, hemispherical energy analyzer, and single channel electron multiplier. The dashed lines represent the path of a photoelectron through the hemispherical analyzer. Only electrons with certain energy with pass through the field created by the charged hemispheres and be detected by the electron multiplier.

In the research presented in this thesis, achromatic Al Kα (1486.6 eV) or Mg Kα (1253.6 eV) radiation was generated from a SPECS XR50 X-ray source operating at

250 W (12.5 kV and 20 mA). Ejected photoelectrons were detected by a 16.5" hemispherical energy analyzer (SPECS, Phoibos 100) operating with pass energies between 20–50 eV. The energy analyzer was equipped with an entrance slit of 7 × 20 mm, exit slit of 20 × 39 mm, and a single channel electron multiplier. Survey spectra were collected with a step size of 1 eV, and high resolution spectra were collected with a step size of 0.1 eV. All spectra were collected with a take-off angle of 90º with respect to the surface normal. The binding energies for all spectra are referenced to the Au($4f_{7/2}$) peak at 83.8 eV.

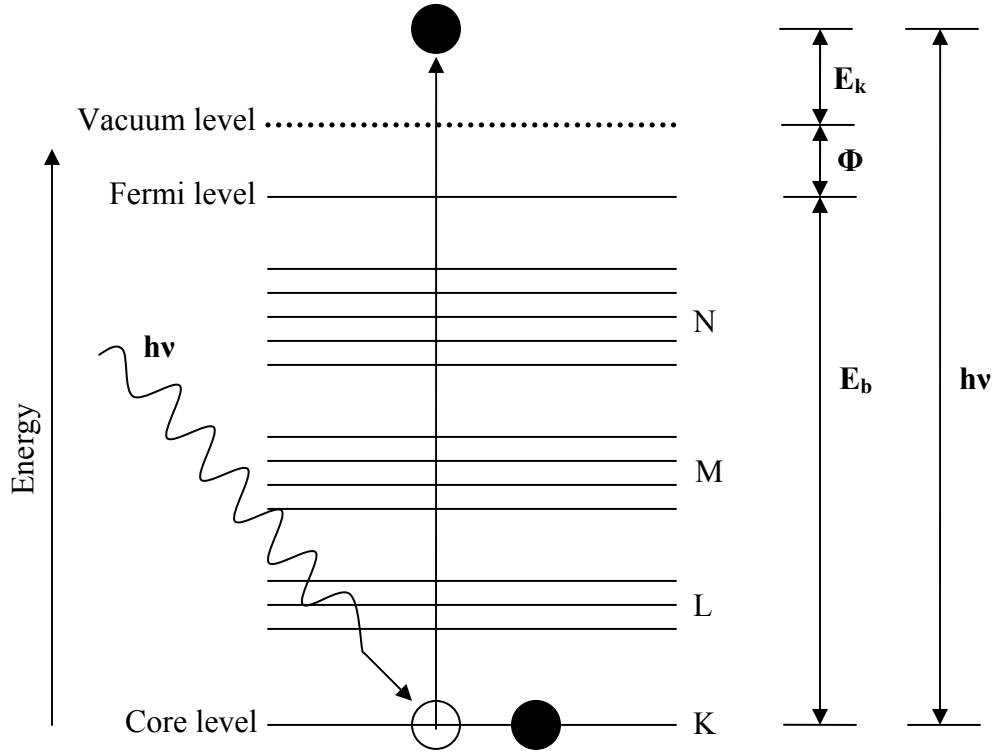

Figure 2.15. Energy level diagram of an ejected photoelectron. E_k is the kinetic energy of the ejected photoelectron, Eb is the binding energy of the electron, and Φ is the work function of the instrument.

2.5 Summary

When studying the reactions that occur at a gas-surface interface, precise characterization of the surface and control of the gas-phase reaction is extremely

important. Various techniques that allow surface-sensitive characterization require ultrahigh vacuum conditions. The ultrahigh vacuum conditions also permit accurate control over gas-phase analyte exposure. In order to perform the experiments described in this thesis, an ultrahigh vacuum chamber was designed and built that allows simultaneous dosing of pure ozone and in situ characterization of the surface with RAIRS. The surface analysis chamber is also capable of pre- and post-characterization of the surface by XPS, as well as detection of gas-phase products by mass spectroscopy. A system was also developed and described in this chapter that allows precise control over the synthesis, storage, and gas-phase exposure of surfaces to pure ozone.

Chapter 3

The Reactions of Ozone with Alkanethiol Self-Assembled Monolayers: Mechanism and Kinetics

3.1. Introduction

3.1.1 Self-Assembled Monolayers

Self-assembled monolayers (SAMs) have been extensively studied over the past 24 years for their various potential applications as chemical sensors, molecular electronic devices, corrosion inhibitors, and biomaterials.[42,43] SAMs have also been used as model systems to help develop a fundamental understanding at the molecular level of various surface related phenomena. These phenomena include wetting, adhesion, friction, and energy transfer.[43,72-75] Various types of self-assembled monolayers exist, each differing from the others by the interactions of the head group with the substrates. Figure 3.1 shows a representation of how the two-dimensional systems attach to a substrate. Self-assembly relies on the chemical affinity of the head group to the substrate, which allows spontaneous adsorption of appropriate amphiphiles with numerous surfaces.[54] A few examples of these systems are the following: fatty acid interactions with metal oxides, organosilicon derivatives bound to hydroxylated surfaces, and organosulfur adsorbates attached to coinage metal substrates.[43]

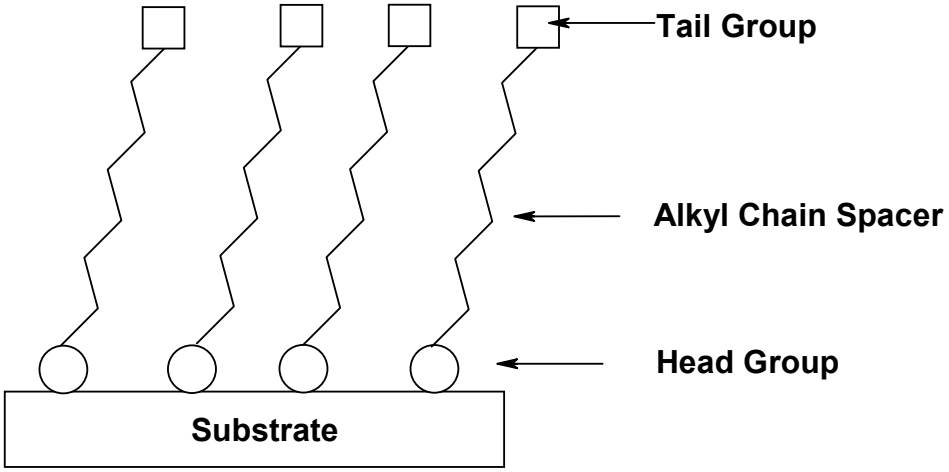

Figure 3.1. Schematic representation demonstrating the three components of self-assembled monolayers and how they bind to substrates.

The most extensively studied form of self-assembled monolayers is that of the alkanethiols on Au (111) surfaces due to their relative ease of preparation and perceived stability. Alkanethiolate SAMs spontaneously form well-ordered, robust thin films. Alkanethiolate monolayers assemble when the sulfur atom of a thiol forms a strong covalent bond (44 kcal/mol) with three-fold hollow sites of the gold substrate.[43] The resultant ordered domain forms a $\sqrt{3} \times \sqrt{3}$, R30° overlayer with chain-chain separation of ~5 Å, shown in Figure 3.2.[76-79] The van der Waals interactions of the hydrocarbon chains within the alkanethiol monolayers help align the structures with all-trans, zigzag chains tilted ~32° away from the surface normal.[77]

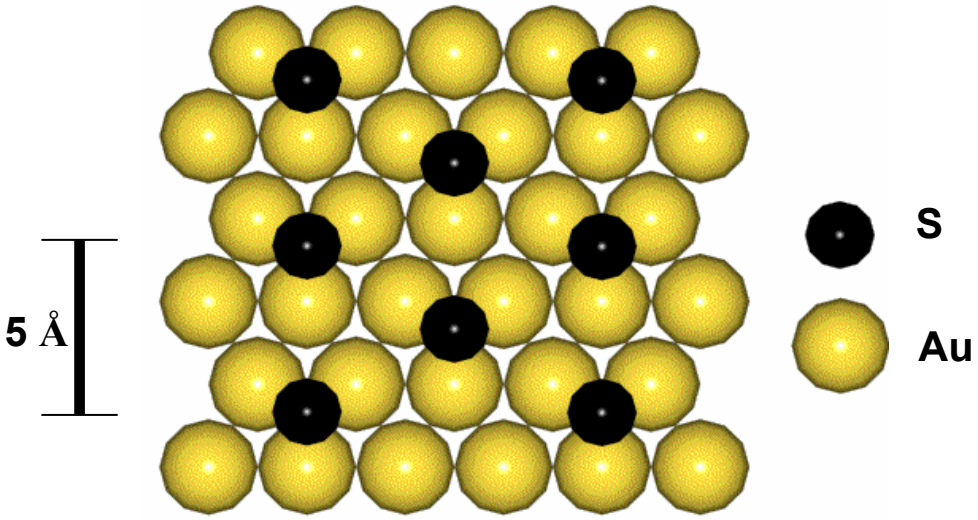

Figure 3.2. Schematic representation of the three-fold hollow absorption sites of the sulfur atoms in an alkanethiol SAM on a Au(111) substrate with inter-chain spacing of ~5 Å.

3.1.2 Monolayer Stability

Despite their importance, very few studies have explored the extent and rate of oxidation of alkanethiol SAMs with ozone.[45] Although the alkanethiol monolayers are particularly useful as model systems for fundamental studies at the molecular level, questions about the stability of SAMs, as model systems, must be addressed before their commercial applications can be realized. A common belief among many researchers who use alkanethiol self-assembled monolayers is that SAMs are extremely robust under ambient conditions.[42-44] A few studies have shown that alkanethiol monolayers react with ambient atmosphere, degrading the monolayer and forming alkanesulfinates (RSO_2^-) and alkanesulfonates (RSO_3^-).[45,49,54-57,80,81] UV photo-oxidation, in oxygen containing environments, has also been shown to damage alkanethiol monolayers forming oxidized

sulfur species.[46-48,50-52,82] The oxidized sulfur species are easily removed or displaced by rinsing in deionized water[83] or emersion in fresh thiol solutions.[57] Zhang et al. were the first to show that ozone is the primary cause of sulfur oxidation when alkanethiols are exposed to UV radiation.[53] Several recent studies have indicated that ozone is the primary reactant in alkanethiol self-assembled monolayer oxidation in ambient environments; however, very little is known about the mechanistic details of this reaction.[58,84-86] Poirier et al. were the first to provide insight into the origin of the reaction site of the oxidation of decanethiol monolayers with ozone, suggesting that the reaction initiates at the domain boundaries and progresses into the domains of the monolayer.[58]

Kinetic studies, involving the photo-oxidation of alkanethiol monolayers[87] and ambient air oxidation of alkanethiol monolayers,[45,54,81] have shown that the rate of the reactions is dependent on the chain length of the monolayers. Experimentally, the rate of the oxidation of alkanethiols in air varies significantly from minutes,[56] to days,[45] to months.[54] The deviations in the kinetic rates are presumably due to local variation in ozone concentration in the ambient atmosphere. The ambient atmosphere also contains numerous other oxidizing species (O_2, O_2^*, ·O, and ·OH), as well as various background gases (CO_2, NO_2, and H_2O).[3,5,9] Separating the chemistry of this assortment of gases is particularly challenging. Experiments need to be performed with pure ozone to isolate the chemistry for which ozone is responsible. To date, few studies involving the oxidation of alkanethiol monolayers with pure ozone have been performed.[58] Understanding the products that form when pure ozone reacts with alkanethiol SAMs,

and the mechanistic pathways for product formation, will help in the design and fabrication of more robust assemblies for commercial applications.

The goals of the research presented in this chapter are to develop a more complete understanding of the products that form and the route to their formation when pure ozone oxidizes alkanethiol self-assembled monolayers. We also explore how the chain length of the monolayers affects the rate and extent of oxidation of the monolayers. Furthermore, we relate the oxidation rates with the initial site of reaction. From a fundamental perspective, we explore the diffusion and reaction of ozone in a confined environment of an organized monolayer system. We accomplish these goals by monitoring the changes of a series of alkanethiol SAMs on polycrystalline gold substrates during exposure to pure ozone. The series of SAMs used in this study was formed from solution deposition of $HS\text{-}(CH_2)_n\text{-}CH_3$ (n = 4,5,6,7,9,10,11,14,15, and 17) alkanethiols onto polycrystalline gold substrates. For the rest of this chapter the monolayers will be abbreviated as (C# CH_3 SAMs), where # represents the total number of carbons in the chain. The monolayers are characterized by Reflection-Absorption Infrared Spectroscopy (RAIRS) and X-ray Photoelectron Spectroscopy (XPS). The order-disorder of the systems during exposure to ozone is monitored with in situ RAIRS. Post-exposure elemental analysis and oxidation state determination is performed with XPS.

We find that the CH_3 SAMs assemble into systems that transition from disordered (liquid-like) systems to ordered (crystalline-like) system as the length of the alkyl chain increases. During oxidation, we observe the initial formation of sulfonate moieties. The sulfonate species are further oxidized to sulfate species with concomitant loss of the alkyl chains. We propose a mechanism for this transformation. During the oxidation of the

sulfur head group, the monolayers are disordered. We show that the disordering event is dependent upon the length of the alkyl chain in the monolayer. From our data, we demonstrate that the initial site of attack of ozone with the monolayer is at domain boundaries or defects within the film.

3.2. Experimental Details

3.2.1 Materials

All chemicals were used as received without further purification unless otherwise noted. HPLC grade hexanes were purchased from Fisher Scientific Inc. 1-Pentanethiol (98%), 1-hexanethiol (95%), 1-heptanethiol (95%), 1-octanethiol (98.5+%), 1-decanethiol (96%), 1-undecanethiol (98%), 1-dodecanethiol (98.5+%), 1-pentadecanethiol (98%), 1-hexadecanethiol (92%), 1-octadecanethiol (98%), and silica gel (grade 03) were obtained from Sigma-Aldrich, Inc. Research grade oxygen, ultrahigh purity nitrogen, ultrahigh purity carbon dioxide, and dry ice were purchased from Airgas Specialty Gases. Isotopically labeled oxygen ($^{18}O_2$, 97%) was obtained from Cambridge Isotope Laboratories. Polycrystalline gold substrates were received from Evaporated Metal Films. Reagent grade acetone was obtained from Pharmco-Aaper and Commercial Alcohols.

3.2.2 Ozone Synthesis and Storage

Caution: Ozone is toxic, unpredictable, and explosive!

Care should be used at all time when synthesizing or handling!

A detailed description of how ozone is synthesized and stored was previously described in Chapter 2. A brief description of the ozone synthesis and storage is presented here. Research grade oxygen is admitted through a commercial ozone

generator (SR-32 Ozone Solutions). A mixture of O_2/O_3 (2% O_3) from the output of the ozone generator is passed through previously dried silica gel held at -78 °C in a glass trap submerged in a dry ice/acetone bath. At -78 °C, the ozone preferentially absorbs into the silica gel. When sufficient ozone is trapped on the silica gel, the silica gel turns dark blue. This procedure takes approximately 8 hours. The silica gel trap is then isolated and the dry ice is removed. The ozone is purified by pumping on the trap with a mechanical pump while slowly raising the temperature of the acetone to -55 °C. The purification procedure removes all of the O_2 impurity. Once -55 °C is reached, the system is isolated from the mechanical pump and opened to a custom-made UV/Vis flow cell with a path length of 0.5 cm. The UV/Vis flow cell is attached through a valve to the UHV chamber described in Chapter 2. The temperature of the acetone is continually maintained at -55 °C. Typical pressures of the isolated system reach ~50 Torr of pure ozone. Extreme caution should be used when handling pressures above 100 Torr of pure ozone since ozone can rapidly decompose to oxygen causing over pressurization of the glass vessel. The concentration of the ozone is calculated by monitoring the absorbance at 254 nm with a UV/Vis spectrometer (EPP2000, StellarNet, Inc.) and applying Beer's law. The absorption cross section of pure ozone at this wavelength is 1159×10^{-20} cm^2 $molecules^{-1}$ at 298 K.[88] If the concentration of ozone drops below 90%, the headspace of the silica gel/ozone trap is evacuated with the mechanical pump for approximately 30 seconds. This process brings the concentration back to 100% pure ozone. When the SAMs are exposed to ozone, the ozone/silica gel trap is maintained at -55 °C by passing gas-phase nitrogen through copper coils in a mechanically stirred acetone bath. Prior to flowing through the copper coils, the $N_{2\,(g)}$ is passed through separate copper coils, which

are immersed in liquid nitrogen. A J-type thermocouple and PID controller are used to control the flow of the gas-phase nitrogen to constantly maintain the acetone bath temperature at -55 °C ± 1 °C.

3.2.3 Synthesis of Self-Assembled Monolayers

Polycrystalline gold substrates are prepared by evaporation of 50 Å of chromium onto a glass substrate, 1" × 1" × 0.062". The chromium layer is followed by evaporation of 1000 Å of Au (Evaporated Metal Films). The Au surfaces are then immersed in a piranha solution (7:3 ratio, sulfuric acid/30% hydrogen peroxide) for at least 1 hour to remove most surface contaminates. *Caution: piranha solution is an oxidizing agent that can cause explosions when in contact with organic materials!* The Au substrates are then removed from the piranha solution and rinsed thoroughly with deionized water (Millipore Purification Systems, 18.2 MΩ). Each substrate is then dried in a stream of ultrahigh purity nitrogen and immediately placed in a ~2 mM solution of the appropriate thiol in hexanes for at least 48 hours. Incubation times less than 48 hours produced irreproducible results.

3.2.4 Monolayer Exposure

For exposure of the SAMs to pure ozone, the surfaces are removed from the thiol solutions and rinsed with copious amount of hexanes. The monolayers are then dried with a stream of ultrahigh purity nitrogen, attached to a sample mount, and transferred into the ultrahigh vacuum chamber by the load-lock system described in Chapter 2. The total time from thiol solution to ultrahigh vacuum is approximately 20 minutes. The sample mount is transferred to a precision manipulator, which allows the alignment of the sample for monitoring with RAIRS. Pure ozone is passed through a capillary of known

conductance, 1.6×10^{-2} cm^3 s^{-1}. The capillary is attached to a custom-made all-glass effusive molecular beam doser. The head of the doser consists of a glass plate, which contains 120 holes (each 0.5 mm in diameter). The effusive doser extends into the UHV chamber and is positioned approximately 3.5 cm away from the self-assembled monolayer during exposure.[37] Ozone exposure time is controlled by a Teflon® value on the high pressure side of the capillary.

3.2.5 Reflection-Absorption Infrared Spectroscopic Measurements

The reactions of ozone with the SAMs are monitored in situ with a Bruker IFS 66v/S spectrometer. Infrared radiation from a SiC globar source is reflected off of the gold substrates in the UHV chamber at ~86 degrees relative to the surface normal. The reflected light is detected with a mid-range (750–4000 cm^{-1}) mercury cadmium telluride (MCT) detector, which is cooled with liquid nitrogen. All spectra presented in this thesis are the result of the co-addition of 100 scans taken over 90 seconds with a 2 cm^{-1} resolution (zero-filled = 2) with Blackman-Harris, three-term appodization and a scanner velocity of 20.0 kHz. All spectra are presented with the unit of intensity defined as $-\log(R/R_0)$, where R is the reflectivity of the monolayer and R_0 is the reflectivity of a reference spectrum. Two different types of reference spectra are used throughout this thesis and will be specified accordingly. Some spectra are recorded with a clean Au substrate as a reference. These Au surfaces are cleaned by immersion in piranha solution for at least 1 hour to remove most surface contaminants. The Au substrates are then removed from the piranha solution and rinsed thoroughly with deionized water. Each substrate is then dried in a stream of ultrahigh purity nitrogen and immediately transferred into the UHV chamber through the load-lock system. The Au backgrounds

are further cleaned by exposing the surface to pure ozone for 30 minutes within the ultrahigh vacuum chamber before recording the spectrum. The other type of reference spectrum used is that of the monolayer before any exposure to ozone. These spectra will be labeled as difference spectra. The kinetics of the ozone reactions are monitored with OPUS® software, which is set to continuously record spectra every 90 seconds during the ozone exposure.

3.2.6 Infrared Spectrum Analysis

The ability of reflection absorption infrared spectroscopy to characterize the order-disorder transitions occurring in organic thin films has been previously demonstrated.[89] Numerous spectral features are sensitive parameters to structural changes in the films. The full width at half the maximum (FWHM), peak frequency, and area of the peaks due to the C-H stretches of hydrocarbon films are the most sensitive parameters to initial changes within these monolayers. The C-H stretching region of the self-assembled monolayer spectrum (~2800–3000 cm^{-1}) is complicated and is composed of the sum of numerous modes. Laibinis et al. showed that the hydrocarbon region of an alkanethiol monolayer contains nine separated stretches.[90] To analyze the FWHM or area of one particular peak, without influences occurring from the other peaks, a custom spectral fitting program was written in Fortran 77, see Appendix 6.2. The software implements the Minpack subroutines,[91] which use a variant of the Levenberg-Marquardt algorithm, to solve nonlinear least-squares fitting of Lorentzian functions to the RAIRS data. Specifically, the sum of five Lorentzian functions is fit to the data. The five Lorentzian functions are chosen to represent the stretches from the symmetric and asymmetric modes of both the methyl and methylene units of the hydrocarbon chains, as well as the Fermi

resonance from the methyl groups. Inclusion of more than five Lorentzian functions to the least-squares analysis yield unrealistic and poor fits of the data. During the fitting analysis, the FWHM, peak position, and peak area of four of the Lorentzian functions are allowed to vary to optimize the fit. The peak position and FWHM of the Fermi resonance is not allowed to vary during the optimization, but the area of the Fermi resonance is allowed to vary. The program allows one to determine the changes, upon exposure to ozone, of the peak frequency, FWHM, and area of any of the C-H stretches within the monolayer. A slight modification of the program was also used to fit single Lorentzian functions to individual peaks in other regions of the spectrum. This modification allows analysis of peaks, due to products forming on the substrate, to be easily performed for a very large set of time resolved spectra.

3.2.7 X-ray Photoelectron Spectroscopic Measurements

The monolayers are characterized before and after exposure to ozone with X-ray photoelectron spectroscopy (XPS). The characterization is performed within the same ultrahigh vacuum chamber used for exposure. After exposure, the surface is simply rotated by the precision manipulator to align the surface so that a hemispherical analyzer (Phoibos 100, SPECS) is normal to the surface. Achromatic Al Kα (1486.6 eV) X-ray radiation is generated from a SPECS XR50 X-ray source operating at 250 W (12.5 kV and 20 mA). Ejected photoelectrons are detected by the hemispherical analyzer operating with a pass energy of 50 eV. Upon alignment, an initial survey scan of each surface is performed with a step size of 1 eV, to verify alignment. Low energy electrons have been shown to cause X-ray induced damage to self-assembled monolayers.[92] Therefore, high resolution spectra of the following elements are recorded in the following order: S(2p),

C(1s), Au(4f). All high resolution spectra are recorded with a step size of 0.1 eV. The pass energy is then lowered to 20 eV, which minimizes the signal from the Au($4p^3$) electrons. This minimization allows one to analyze the signal coming from the O(1s) electrons with better efficiency. Finally, high resolution spectra are then recorded for the O(1s) and Au(4f) electrons, respectively. The binding energies for all spectra are referenced to the Au($4f_{7/2}$) peak at 83.8 eV.[93]

3.3 Results and Discussion

3.3.1 Monolayer Characterization

3.3.1.1 Reflection-Absorption Infrared Spectroscopic Data

Figure 3.3 shows the reflection-absorption infrared data, in the C-H stretching region, for a series of alkanethiol SAMs on polycrystalline gold substrates. In this data set, the intensity is defined as $-\log(R/R_o)$ where R is the reflectance of the monolayer and R_o is the reflectance of a clean Au substrate. The data shown is for a series of methyl terminated monolayers of increasing chain length (C# CH_3 SAMs, where # = 5,6,7,8,10,11,12,15,16, and 18). Several key features of the spectra are discussed below.

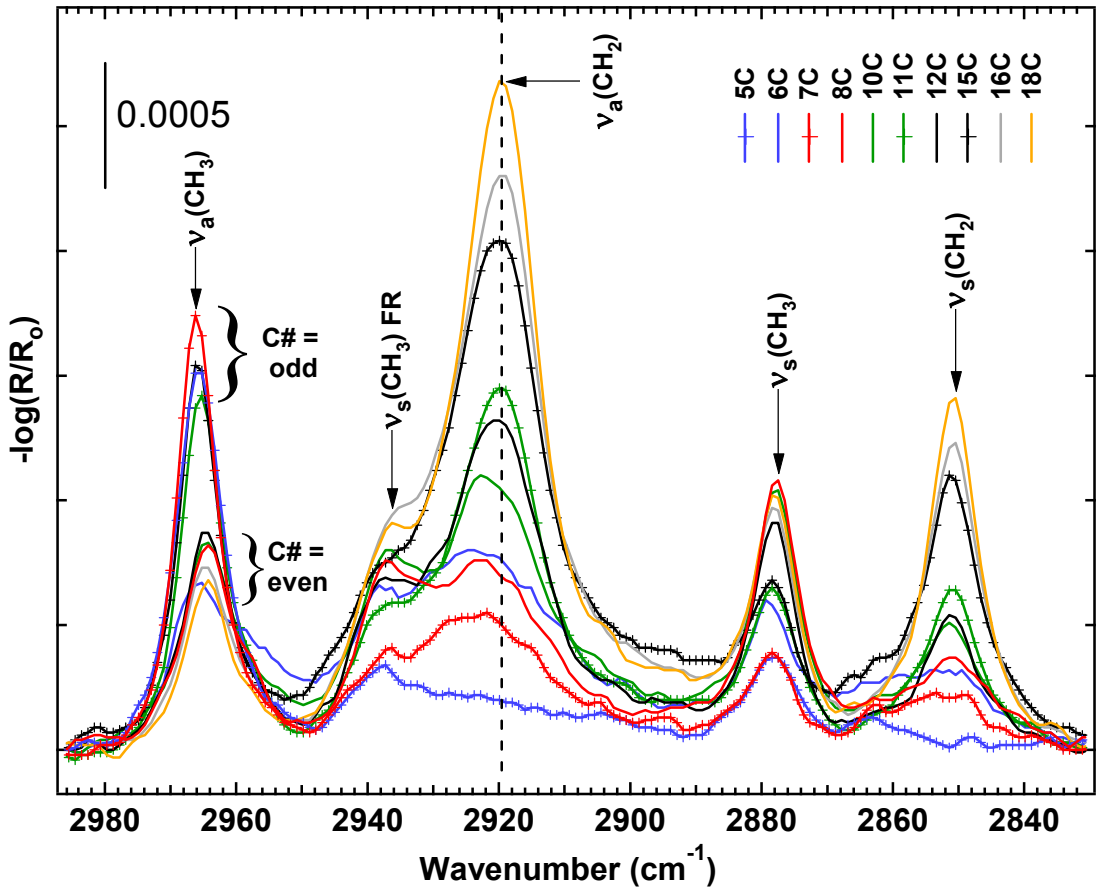

Figure 3.3. Reflection Absorption Infrared characterization of a series of n-alkanethiol SAMs, HS-$(CH_2)_nCH_3$(n=4,5,6,7,9,10,11,14,15,17), on polycrystalline Au substrates

First, five important peak positions are noted in Figure 3.3. The positions and vibrational mode assignments are shown in Table 3.1, and are based on literature precedence from experimental and theoretical analysis.[90] The Lorentzian functions discussed in section 3.2.6 represent the five peaks displayed in Figure 3.3. Second, it is interesting to note in the spectra that as the number of carbons increases, two specific changes for the bands assigned to the symmetric (ν_s) and asymmetric (ν_a) stretches of the methylene units of the chains are observed. Both bands increase in intensity and red-shift with increasing number of carbons. The increase in intensity is directly related to the increase of methylene units in the monolayers. The shifting of the peak positions of the

bands is clearly evident if one studies the position of the peak from the $\nu_a(CH_2)$ stretch versus the dashed line shown in Figure 3.3. The dashed line is positioned at 2919 cm^{-1}. As the number of carbons increase, the position of the band from the $\nu_a(CH_2)$ stretch approaches the dashed line from higher wavenumbers. The observed trend is indicative of an increase in order of the monolayer from a disordered (liquid-like) system to an ordered (crystalline-like) system. The position of the peaks from the $\nu_a(CH_2)$ and $\nu_s(CH_2)$ stretches has been shown to be a sensitive indicator of the ordering of the alkyl chain.[79,94-98] In a crystalline polyethylene chain,[99,100] the position of the peaks from the $\nu_a(CH_2)$ and $\nu_s(CH_2)$ stretches are found at 2920 and 2850 cm^{-1}, respectively; whereas, in a liquid phase, the values blue-shift to 2928 and 2856 cm^{-1}. The increase in order is due to the increasing van der Waals interactions amongst the chains as the chains increase in size. The spectra of the short chain monolayers show a liquid-like disordered system, while the spectra of the long chain monolayers show an ordered system indicative of an all-trans, densely packed, crystalline-like environment.

Table 3.1. Selected spectral positions and vibrational mode assignments for methyl terminated SAMs on Au.

Wavenumber (cm^{-1})	**Vibrational Modes**
2964	ν_a (CH_3), r_a^-
2954	ν_a (CH_3), r_b^-
2936	ν_a (CH_3), Fermi resonance
2925	ν_a (CH_2), d^- (α)
2918	ν_a (CH_2), d^-
2895-2907	ν_s (CH_2), Fermi resonance
2878	ν_s (CH_3), r^+
2853	ν_s (CH_2), d^+ (α)
2850	ν_s (CH_2), d^+

α = CH_2 groups located at either end of the chain

A third key feature of Figure 3.3 is the relative intensities of the bands from the symmetric, $\nu_s(CH_3)$, and asymmetric, $\nu_a(CH_3)$, stretches of the methyl units of the monolayers. When the total number of carbons in the monolayer is an even number, the intensities of these two peaks are approximately equal. This is in sharp contrast to the case when an odd number of carbons are in the chain. In the case where the total number of carbons is odd, the intensity of the band from the asymmetric stretch of the methyl unit is approximately three times stronger than the intensity of the band from the symmetric stretch. The greater intensity for the peak assigned to the asymmetric stretching mode of the odd chain length monolayers, relative to the even chain length SAMs, is clearly evident in Figure 3.3 (odd chain spectra are shown with dashed lines).

Previously shown by Nuzzo and co-workers,[97] the change in relative intensities of the modes assigned to the symmetric and asymmetric stretches of the methyl units of the monolayers can be explained if one considers the direction of the transition dipole moments of these stretches and the surface selection rule. The surface selection rule states that only those motions that produce a transition dipole moment in a direction that is perpendicular to the plane of the surface can be detected with RAIRS. The transition dipole moment directions of the methyl stretches for odd verses even chains are shown in Figure 3.4. This figure illustrates that the symmetric methyl stretch for the even chains has a transition dipole moment direction that is more normal to the surface than for the odd chains. Conversely, the asymmetric stretch of the methyl units for the odd chains has a transition dipole moment direction that is more normal to the surface than for the even chains.

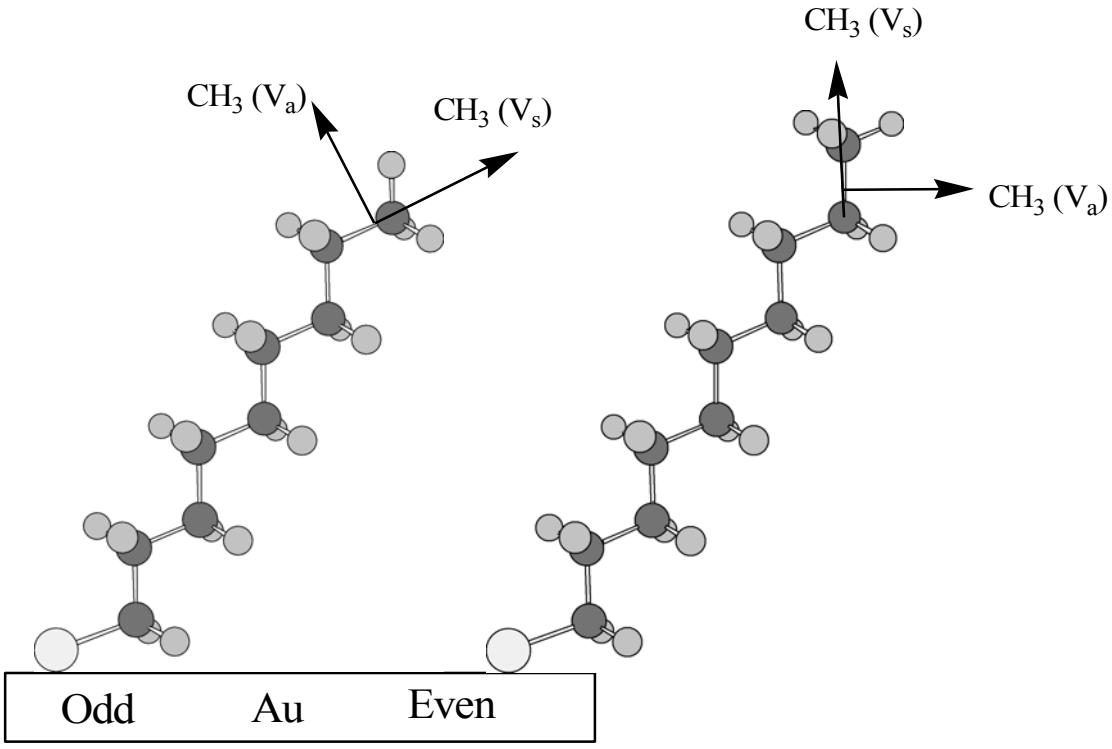

Figure 3.4. A schematic demonstrating the alignment of the transition dipole moments of the asymmetric and symmetric stretches for the methyl functional groups within self-assembled monolayers with an odd and even total number of carbons in the chains.

3.3.1.2 X-ray Photoelectron Spectroscopic Data

Further characterization of the monolayers was performed with X-ray photoelectron spectroscopy (XPS). XPS provides qualitative analysis of the monolayer with sensitivity to elemental composition and the binding environment. A typical survey spectrum of a methyl terminated SAM is shown in Figure 3.5. This spectrum is representative of all monolayers used in this chapter prior to ozone exposure (data not shown). The primary feature of the survey spectrum is the presence of signal from the C(1s) photoelectron at 284 eV. Gold photoelectrons (4s, 4p, 4d, 4f, and 5p) from the substrate are also present in the spectrum. Barely distinguishable at this resolution, is signal from the S(2p) photoelectrons at 162 eV. No other signals due to contamination of the samples are noted.

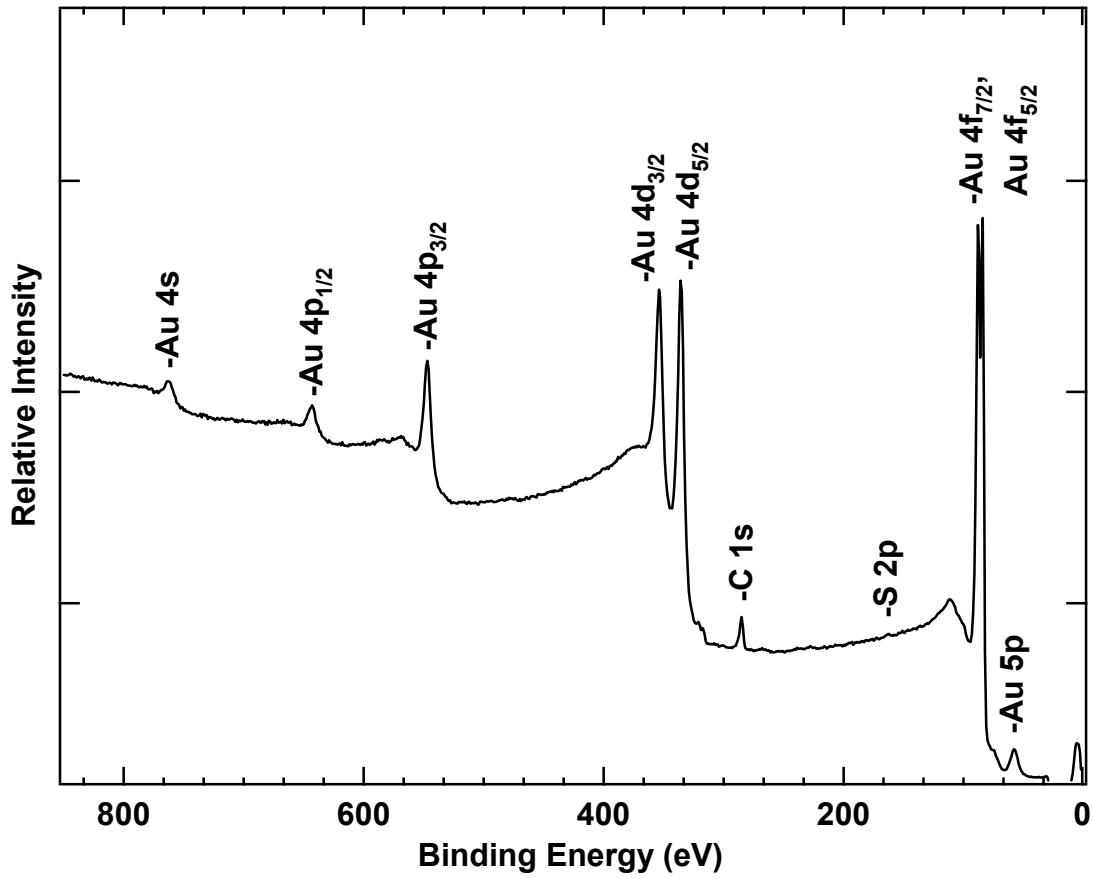

Figure 3.5. A representative X-ray photoelectron survey spectrum of methyl-terminated self-assembled monolayers.

Further inspection at higher resolution yields information about the binding environments of the elements. Representative high resolution spectra of the S(2p), C(1s), O(1s), and Au(4f) regions of a methyl-terminated SAM are shown in Figure 3.6. All spectra are shown with a take-off angle of 90°. The S(2p) region of the SAM displays a broad peak centered at 162.8 eV. Binding energies of native thiolate species on Au are typically characterized by a S ($2p_{3/2,\ 1/2}$) doublet with the S ($2p_{3/2}$) peak centered at 161.9 eV and splitting of the doublet by 1.2 eV.[101] Resolution of the achromatic source and detector used in this study does not provide separation of this doublet. The multiplex spectrum of the S(2p) region is consistent with the sulfur atoms being bound to the gold

substrate as thiolate species. The high resolution spectrum for the C(1s) electrons shows a sharp, symmetric peak centered at 284.9 eV. This binding energy is in excellent agreement with literature values for CH_3 SAMs and is characteristic of aliphatic hydrocarbons.[102] The photoelectron spectrum of the O(1s) binding energy region shows no detectable oxygen for methyl terminated monolayers. A well-resolved doublet is shown in the Au(4f) region with peak positions at 87.3 and 83.8 eV due to the Au($4f_{7/2, 5/2}$) photoelectrons.[103]

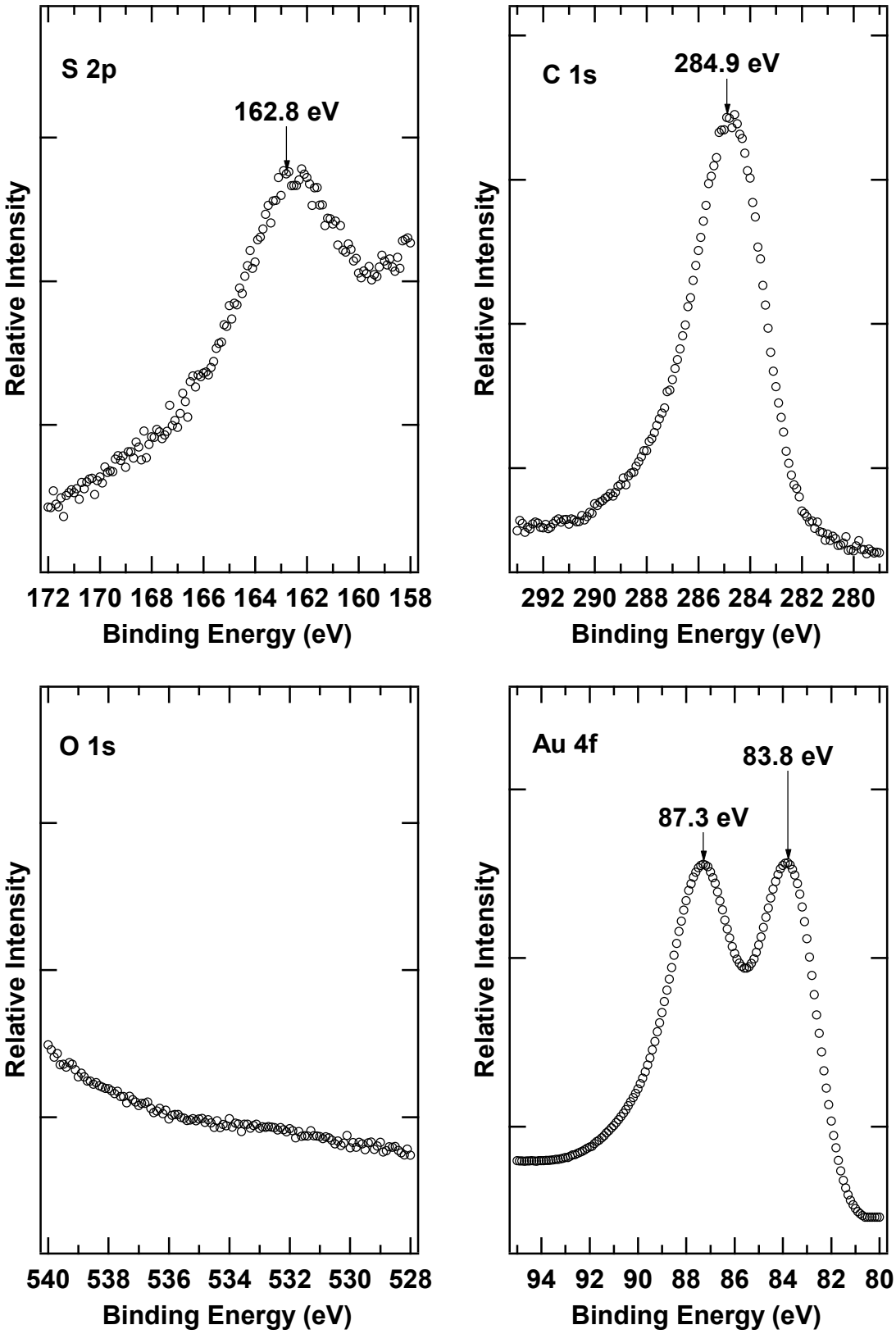

Figure 3.6. High resolution X-ray photoelectron spectra of the S(2p), C(1s), O(1s), and Au(4f) regions of a methyl terminated self-assembled monolayers.

3.3.2 Ozone Exposure

3.3.2.1 Reflection-Absorption Infrared Spectroscopic Data

The effects of ozone exposure on the RAIR spectra of a 16C CH_3 SAM are shown in Figure 3.7. In this figure, the reference spectrum (R_0) is that of a clean gold substrate. The top spectrum is that of a 16C CH_3 SAM before exposure to ozone. The prominent features of this spectrum are bands assigned to the asymmetric and symmetric stretches of the methylene and methyl moieties within the monolayer. The positions of the band assigned to the $\nu_a(CH_2)$ and $\nu_s(CH_2)$ stretches, 2919 and 2850 cm^{-1}, are indicative of a well-ordered, crystalline-like environment. Two other absorptions are also noted in the spectrum at 1470 and 1383 cm^{-1}. The peak at 1470 cm^{-1} is attributed to the CH_2 scissor deformations, and its narrow line width is also consistent with a crystalline-like environment.[97] Also noted in the spectrum, is a peak at 1383 cm^{-1}, which is assigned to CH_3 symmetric deformations.

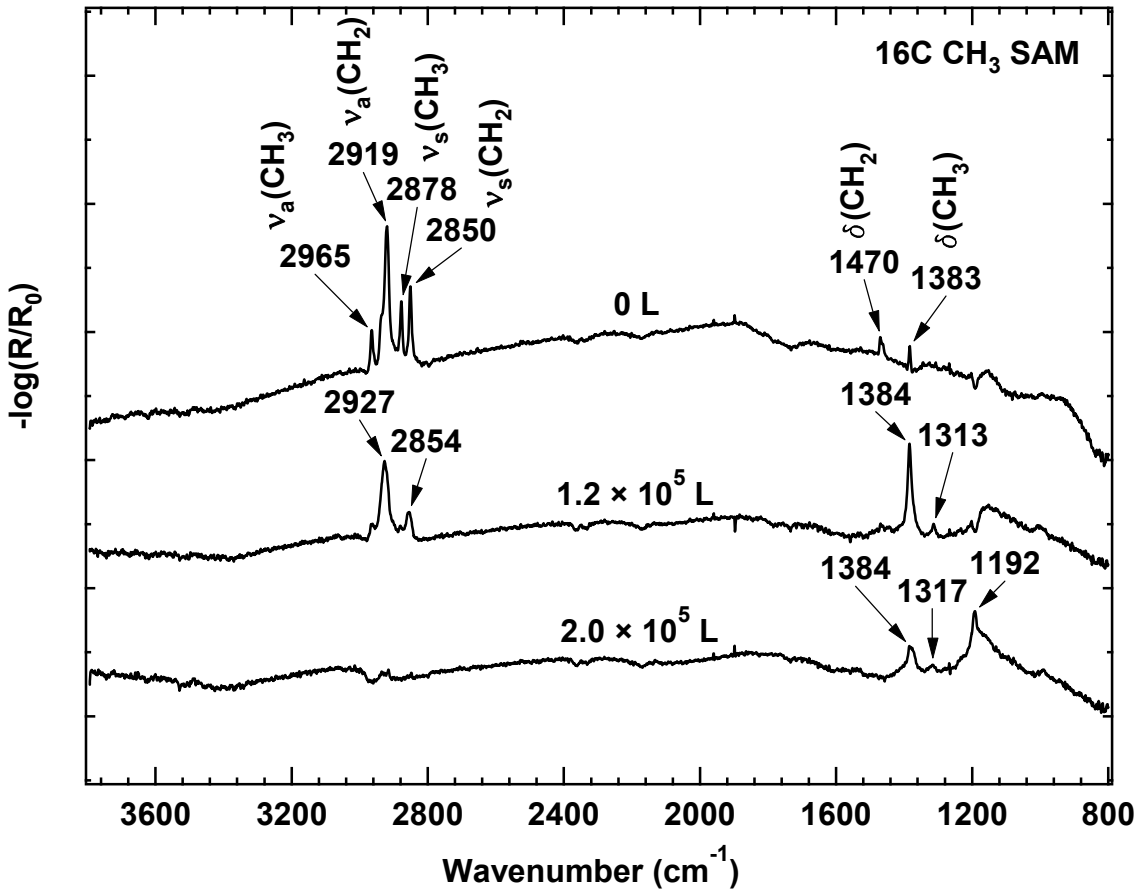

Figure 3.7. Reflection Absorption Infrared spectra showing the changes in reflectivity of a 16C CH_3 SAM after 0, 1.2×10^5, and 2.0×10^5 L of exposure to ozone.

The middle spectrum in Figure 3.7 is that of a 16C CH_3 SAM after exposure to ~1.2×10^5 Langmuirs (L) of ozone, where 1 L is equal to 1×10^{-6} Torr s. Significant differences in this spectrum, relative to the unexposed spectrum, are highlighted. First, the intensities of all the C-H stretching modes significantly decrease upon ozone exposure. In RAIRS, the intensity of the signal is controlled by the number density of the moieties, as well as the surface selection rule. The surface selection rule states that only those molecules that have a transition dipole moment perpendicular to the substrate will be observable in RAIRS. Therefore, this observed decrease in intensity of the bands associated with the C-H stretching may be due to a combination of both a decrease in the number density and

a change in orientation of the molecules on the surface. In addition to intensity changes, the peak frequencies of the CH_2 stretching modes also change significantly. Both positions of the bands assigned to the $\nu_a(CH_2)$ and $\nu_s(CH_2)$ stretches blue-shift upon exposure to ozone. As noted above, previous researchers have shown that the peak positions of the asymmetric and symmetric methylene stretches are sensitive indicators of the extent of van der Waals interactions between long alkyl chains.[98-100] The band from the $\nu_a(CH_2)$ stretch for bulk crystalline n-alkyl thiols is reported at 2918 cm^{-1}, whereas, the band from the $\nu_a(CH_2)$ stretch for bulk liquid n-alkyl thiols is shown to be at 2924 cm^{-1}.[98] A similar trend is noted for the peak position of the band assigned to the $\nu_s(CH_2)$ stretches, a change from 2851 cm^{-1} for bulk crystalline environments to 2855 cm^{-1} in liquid states.[98] Blue-shifting of the bands from the CH_2 modes was also noted in thermal studies of methyl terminated SAMs, and was described as a gradual transformation of the monolayers from a polycrystalline state to a liquid-like state.[89] Therefore, it is reasonable to hypothesize that the shifting of the peak position of the band from the $\nu_a(CH_2)$ stretch from 2919 to 2927 cm^{-1} in Figure 3.7, upon exposure to ozone, is consistent with a transition from an ordered crystalline environment to a disordered liquid-like system. This same transition is observed in the band associated with the $\nu_s(CH_2)$ stretch when comparing the upper unexposed spectrum to the middle spectrum in Figure 3.7, a shifting from 2850 to 2854 cm^{-1}.

An intense narrow peak is also observed in the middle spectrum of Figure 3.7 at 1384 cm^{-1}. This peak is the most intense peak in the spectrum after ~1.2×10^5 L of exposure. We attribute this strong band at 1384 cm^{-1} to the asymmetric stretch of a sulfonate moiety. This assignment is based on numerous XPS and IR measurements

showing a direct correlation between sulfur oxidation and the intensity of the peak at 1384 cm^{-1}. The S=O symmetric stretch is not observed in the middle spectrum, and its absence will be discussed below. Reports by Detoni[104] and Paulson[105], who studied the IR spectrum of dialkyl and diaryl sulfates, show the absorption bands for symmetrical O=S=O stretches at 1195-1225 cm^{-1} and the asymmetrical O=S=O stretches at 1360–1420 cm^{-1}. Frequency ranges for the absorption bands associated with the ν_a and ν_s SO_2 stretches for sulfonates, sulfones, sulfoamides, and sulfochlorides are generally in the ranges of 1415–1336 and 1200–1152 cm^{-1}, respectively.[106,107] Substituents on an SO_2 moiety have been shown to shift the position of the bands from the asymmetric and symmetric stretches.[106,108,109] The more electronegative the substituent is, the further the shift will be. Furthermore, a relationship between the asymmetric and symmetric SO_2 stretches has been shown to occur[106,109,110] and is expressed by Equation 3.1.

$$\nu_a\,(SO_2) \approx 200\ cm^{-1} + \nu_s\,(SO_2) \qquad (3.1)$$

Therefore, we conclude that the band at 1384 cm^{-1} is due to the SO_2 asymmetric stretch of a sulfonate species, but the spectrum should also show a band associated with the symmetric stretch around 1184 cm^{-1}. We attribute the absence of signal from the symmetric SO_2 stretch in the middle spectrum of Figure 3.7 to the surface selection rule. We speculate that the transition dipole moment of the symmetric SO_2 stretch lies parallel to the gold substrate and is therefore not observable with RAIRS.

Precedence for the absence of peaks from the symmetric SO_2 stretch caused by the surface selection rule has been set in the literature by Ulman et al.[43,111] These researchers synthesized sulfone-containing SAMs on gold substrates and characterized the monolayers with RAIRS. Ulman et al. showed the absorption for the asymmetric SO_2

stretch near 1326 cm^{-1}, but no signal for the symmetric SO_2 stretch was observable in the monolayers. When the researchers analyzed the neat thiols in a KBr matrix, a large peak from the symmetric SO_2 stretch appeared near 1127 cm^{-1}. They attributed the absence of a band due to the symmetric SO_2 stretch in the monolayers to the dipoles of the SO_2 moieties aligning the transition dipole moments of the symmetric SO_2 stretch parallel to the substrate, thus causing the stretches to not be observed with RAIRS. Because the peak at 1384 cm^{-1} in the middle spectrum of Figure 3.7 is intense and has a very narrow line width, the species causing this absorption is highly ordered. Therefore, it is plausible that the 1384 cm^{-1} signal is due to the asymmetric stretch of a sulfonate moiety and the symmetric stretch is not observable due to the ordered orientation of the product on the surface.

Upon further exposure to ozone, the changes in the monolayer are even more dramatic. The bottom spectrum in Figure 3.7 is that of a 16C CH_3 SAM after a total of ~2.0×10^5 L of exposure. In the C-H stretching region of the spectrum, signal from the symmetric and asymmetric methylene stretches are barely observable above the noise, and signal from the CH_3 stretches has completely disappeared. These changes are attributed to near complete removal of the hydrocarbon chains from the surface. The peak at 1384 cm^{-1} has also decreased in intensity and broadened. Furthermore, an intense broad peak at 1192 cm^{-1} is observed in the final spectrum. We attribute the decrease in intensity of the sulfonate peak and the formation of the peak at 1192 cm^{-1}, to a change of the sulfonate moiety to a sulfate species. The sulfonate moiety is further oxidized by ozone removing the hydrocarbon chains and forms a sulfate species that remains bound to the surface even after prolonged ozone exposure. This sulfate species is oriented on

the surface such that both the symmetric and asymmetric SO_2 stretches are now observable with RAIRS. We therefore assign the band at 1192 cm^{-1} to the symmetric SO_2 stretch and the band at 1384 cm^{-1} to the asymmetric SO_2 stretch of a sulfate moiety.

We performed experiments with isotopically labeled oxygen to further verify the IR assignments of the bands at 1383 and 1192 cm^{-1}. Isotopically labeled ozone was synthesized and stored with the same procedures described previously in Chapter 2 and Chapter 3. The only difference made to the procedures was the use of isotopically labeled oxygen ($^{18}O_2$, 97%) as the feedstock to the ozone generator instead of research grade oxygen. The SRS RGA attached to the UHV chamber, see Chapter 2, was used to verify the presence of isotopically labeled ozone during the reaction by monitoring mass m/z = 54. A 16C CH_3 SAM was exposed to isotopically labeled ozone and the reaction was monitored in situ with RAIRS. If the oxidized products (which cause the bands at 1383 and 1192 cm^{-1}) contain oxygen, then the oxidation performed with isotopically labeled ozone will cause both bands to shift toward lower wavenumbers. This is indeed what happened (data not shown). The band at 1383 cm^{-1} red-shifted to a broad band between 1363 and 1371 cm^{-1}. The band at 1192 cm^{-1} also red-shifted to a peak at 1186 cm^{-1}. The broadness of the band between 1363 and 1371 cm^{-1} is most likely due to the formation of products containing mixtures of oxygen isotopes. The isotopically labeled ozone was not pure $^{18}O_3$, but rather a mixture of $^{18}O^{18}O^{18}O$, $^{16}O^{18}O^{18}O$, and $^{16}O^{16}O^{18}O$. The isotopically labeled experiments prove that the bands at 1383 and 1192 cm^{-1} can be assigned to vibrations of a molecule containing oxygen atoms. XPS studies described later in this chapter suggest that the products causing the bands at 1383 and 1192 cm^{-1} also contain oxidized forms of sulfur.

To elucidate mechanistic details about the reactions of ozone with SAMs, we performed in situ time-resolved RAIRS studies on the exposure of a 16C CH_3 SAM to ozone. Figure 3.8 shows a subset of the RAIR spectra from the time-resolved studies. The reference spectrum (R_o) for theses spectra is that of the monolayer before any exposure to ozone. The difference spectra, shown in Figure 3.8, are offset along the ordinate axis for clarity and are arranged from bottom to top in increasing order of exposure to ozone. The bottom spectrum is that of the monolayer before exposure to ozone. The exposure of ozone between each spectrum is ~7.7×10^3 L. The uppermost spectrum in Figure 3.8 is that of the monolayer before exposure to ozone with a clean Au reference spectrum.

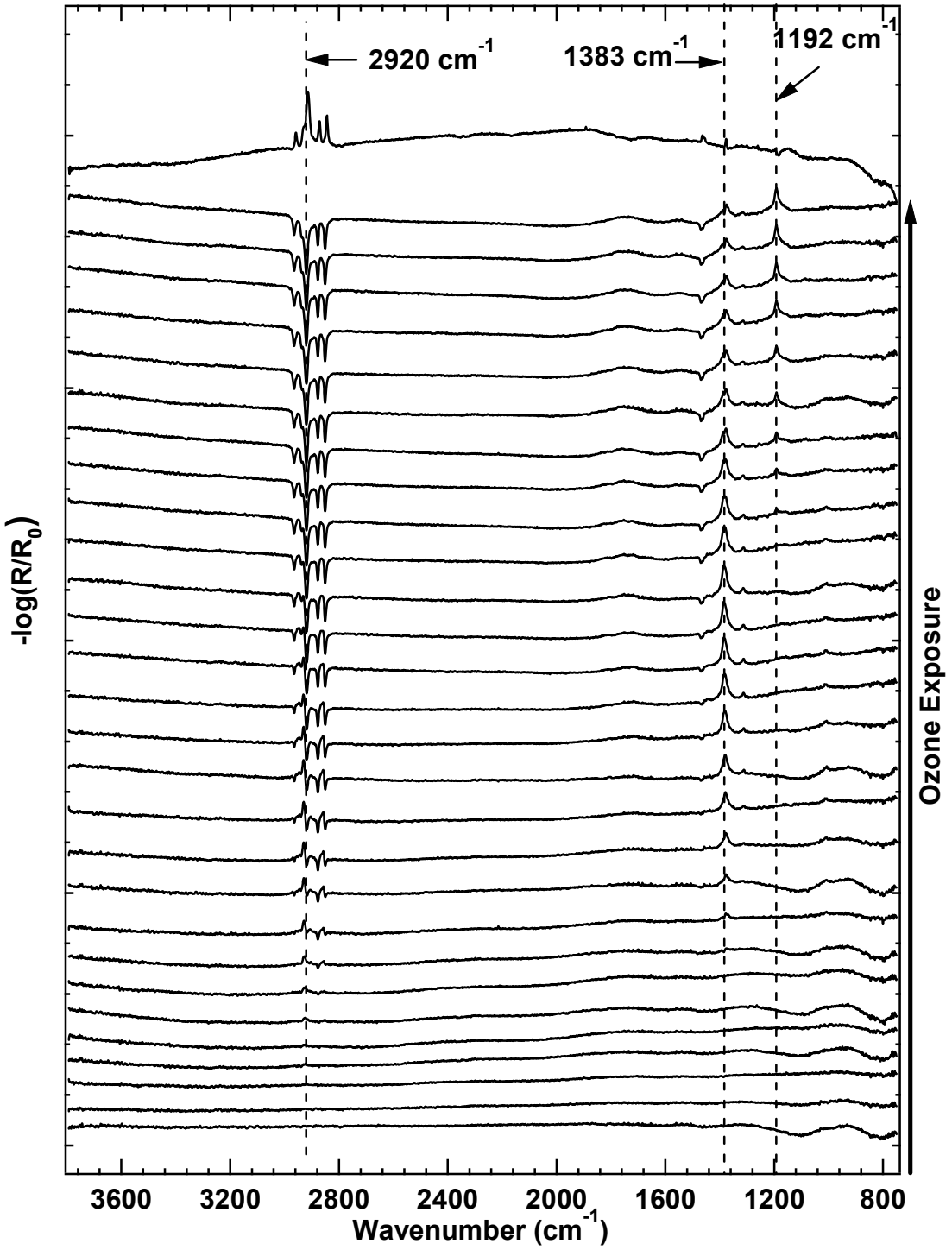

Figure 3.8. Difference RAIR spectra of a 16C CH_3 SAM demonstrating the changes in reflectivity of the monolayer during exposure to ozone. Exposure increases from bottom to top ~7.7×10^3 L per scan. The uppermost spectrum is that of the monolayer before exposure to ozone with a clean Au reference spectrum.

The first changes in the spectra at early times are attributed to shifting of the peak frequencies for the asymmetric and symmetric methylene stretches. Both of these modes blue-shift upon initial exposure to ozone, causing a combination of negative and positive features within the difference spectra. This is clearly evident if one focuses on the changes of the band from the asymmetric methylene stretch by studying the signal around 2920 cm^{-1}. Negative features are formed at 2920 cm^{-1} while positive features are formed at slightly higher wavenumbers. This shifting is consistent with the transformation of an ordered system to a disordered system. At slightly longer exposure times, negative features start to form at 2965 and 2878 cm^{-1}. Initial negative features at these positions are most likely due to disordering in the monolayer causing a change in the direction of the transition dipole moments of the methyl stretches.

At the same time that the methylene stretches are blue-shifting, a peak begins to grow in at 1383 cm^{-1}, and upon further exposure to ozone this peak increases in intensity. After 1.4×10^5 L of exposure another peak emerges around 1192 cm^{-1}. During further exposure, the peak at 1192 cm^{-1} increases in intensity while the peak at 1383 cm^{-1} starts to decrease in intensity and broaden. Furthermore, during the changes of the bands at 1383 and 1192 cm^{-1}, negative features form in the spectrum in the C-H stretching region. The negative features eventually result in a complete mirror image of the spectrum for the original monolayer recorded with a clean Au reference spectrum (R_0), (see the upper spectrum in Figure 3.8). During the formation of the negative features in the hydrocarbon region of the spectra, a negative feature begins to appear at 1470 cm^{-1}. This negative feature continues to decrease in intensity, during further exposure, until it is also

a complete mirror image of the same absorbance of the original monolayer at 1470 cm^{-1} with a clean Au reference spectrum.

The changes in the spectra in the hydrocarbon region, 2800-3000 cm^{-1}, in Figure 3.8 suggest that upon exposure the monolayer goes through a transition from an ordered system to a disordered system. After this transition, the data show that the hydrocarbon chains are almost completely removed from the substrate upon further exposure. All of the vibrational modes caused by the hydrocarbon chain, see Table 3.1, have formed negative features in the full exposure spectrum of Figure 3.8. The changes in the spectra in Figure 3.8 at both 1383 and 1192 cm^{-1}, along with the analysis of the XPS data presented below, are consistent with the formation of a sulfonate species that is further oxidized to a sulfate moiety.

To glean further mechanistic details from the time-resolved studies, we analyzed the position, FWHM, and integrated area of the band assigned to the asymmetric methylene stretch. We chose the asymmetric methylene stretch because this stretch is the most sensitive stretch to changes in the monolayer during exposure (see early exposure times in Figure 3.8). We performed the spectral analysis using a clean Au substrate as the reference spectrum and the Lorentzian fitting procedures described in section 3.2.6. Figure 3.9 shows the position of the band from the asymmetric methylene stretch for a 16C CH_3 SAM during exposure to ozone. The data in Figure 3.9 show that the position of the peak from the asymmetric stretch begins around 2920 cm^{-1}, which is indicative of a well-ordered crystalline environment. The position of this band changes very little from 0–5.0 $\times$ 10^4 L of exposure. From 5.0 $\times$ 10^4 –1.5 $\times$ 10^5 L, the peak position of the asymmetric stretch increases and approaches 2928 cm^{-1}. This increase is consistent with

a change from an ordered system to a disordered system. After ~1.5 × 10^5 L, the data show significant scatter in Figure 3.9. The significant scatter at long exposure time occurs because of difficulties of the fitting procedures used in section 3.2.6 when fitting peaks with very low intensities.

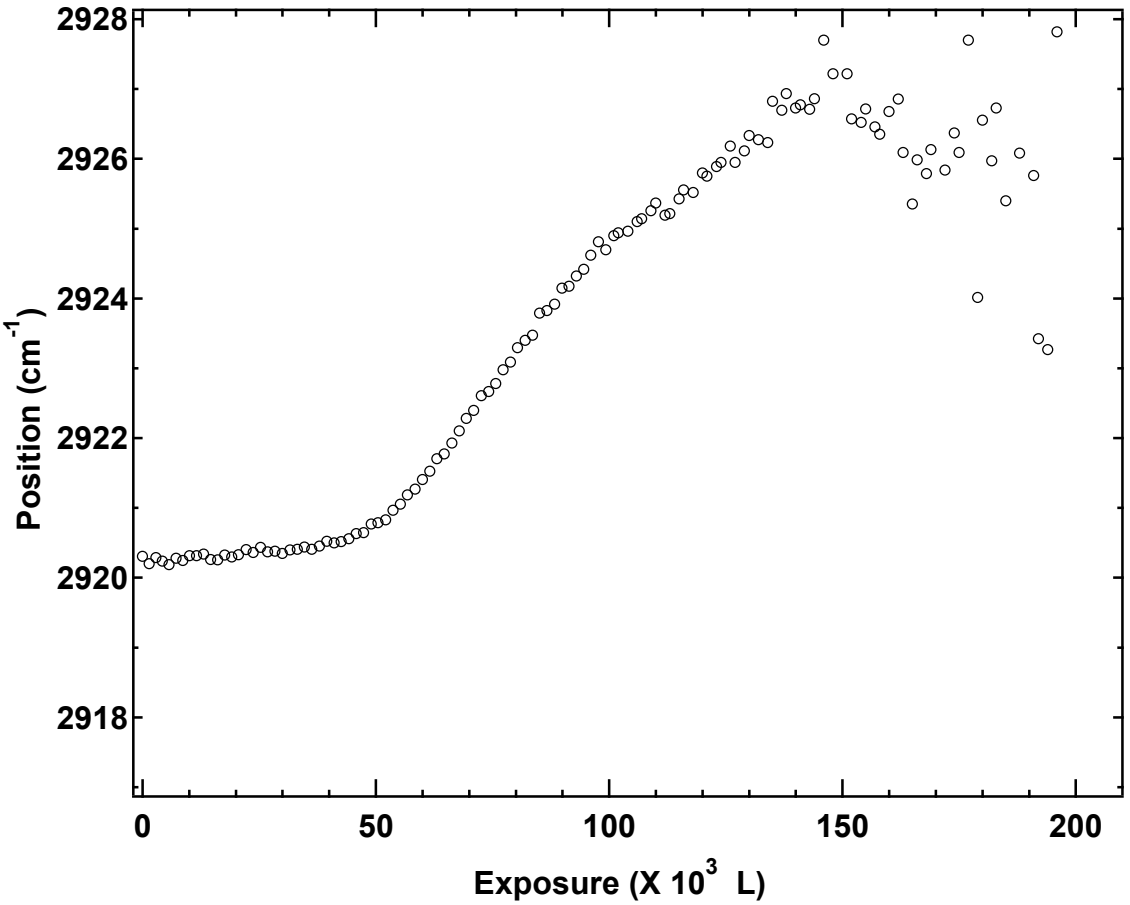

Figure 3.9. A plot showing how the position of the band from the asymmetric methylene stretch for a 16C CH_3 SAM changes during exposure to ozone. This graph demonstrates that the monolayer transitions from an ordered system to a disorder system upon oxidation. The data becomes particularly noisy after ~1.5 × 10^5 L of exposure due to difficulties of the fitting procedure used in section 3.2.6 when fitting bands with very low intensities.

Another metric we used to monitor the order-disorder transition of the monolayer was the FWHM of the absorption band assigned to the asymmetric methylene stretch. Figure 3.10 demonstrates the changes of the FWHM of this peak in a 16C CH_3 SAM during

exposure to ozone. The trend of the FWHM of the band is slightly different from that of the peak position. At early exposure times, the FWHM is around 15 cm^{-1} and remains steady up to around 5.0×10^4 L, but from 5.0×10^4–1.0×10^5 L the FWHM rises dramatically and plateaus around 25 cm^{-1}. Significant scatter develops in the data after approximately 1.2×10^5 L, and this scatter is also attributed to inefficiencies of the fitting routes used. An ordered system should exhibit very narrow line widths, while a disordered system would display very broad line widths. Therefore, the changes observed in Figure 3.10 remain consistent with a change of the monolayer from an ordered to disordered state.

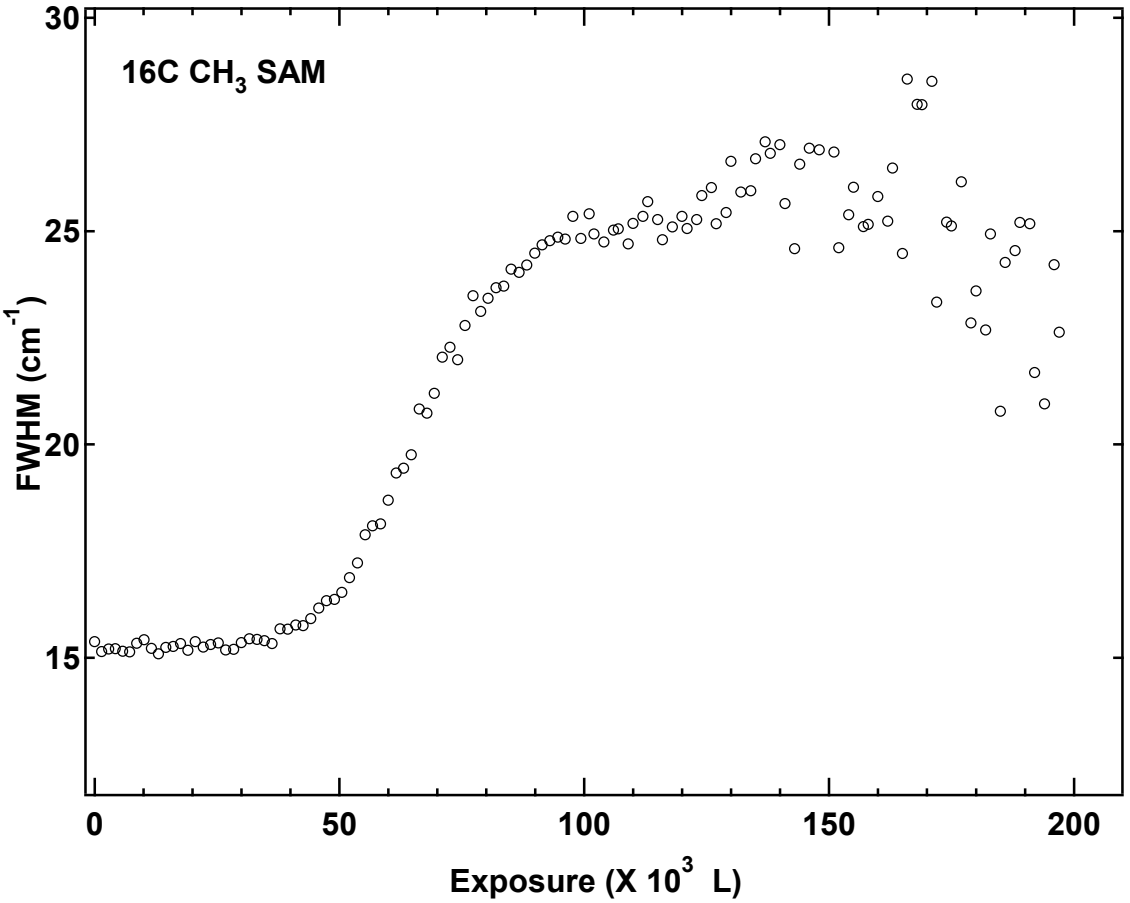

Figure 3.10. A plot demonstrating the changes in the FWHM of the band from the asymmetric methylene stretch for a 16C CH_3 SAM during exposure to ozone. The increase of the FWHM is caused by disordering of the monolayer. The data becomes particularly noisy after ~1.5×10^5 L of exposure due to difficulties of the fitting procedure used in section 3.2.6 when fitting bands with very low intensities.

For complete analysis of the asymmetric methylene stretch for a 16C CH_3 SAM, we monitored the behavior of the integrated area of the band assigned to this stretch during ozone exposure, see Figure 3.11. The area of this band begins to change immediately at the onset of ozone exposure, and exponentially increases until the area reaches a maximum after approximately 9.0×10^4 L. Between 9.0×10^4–2.0×10^5 L, the integrated area quickly decreases and approaches zero.

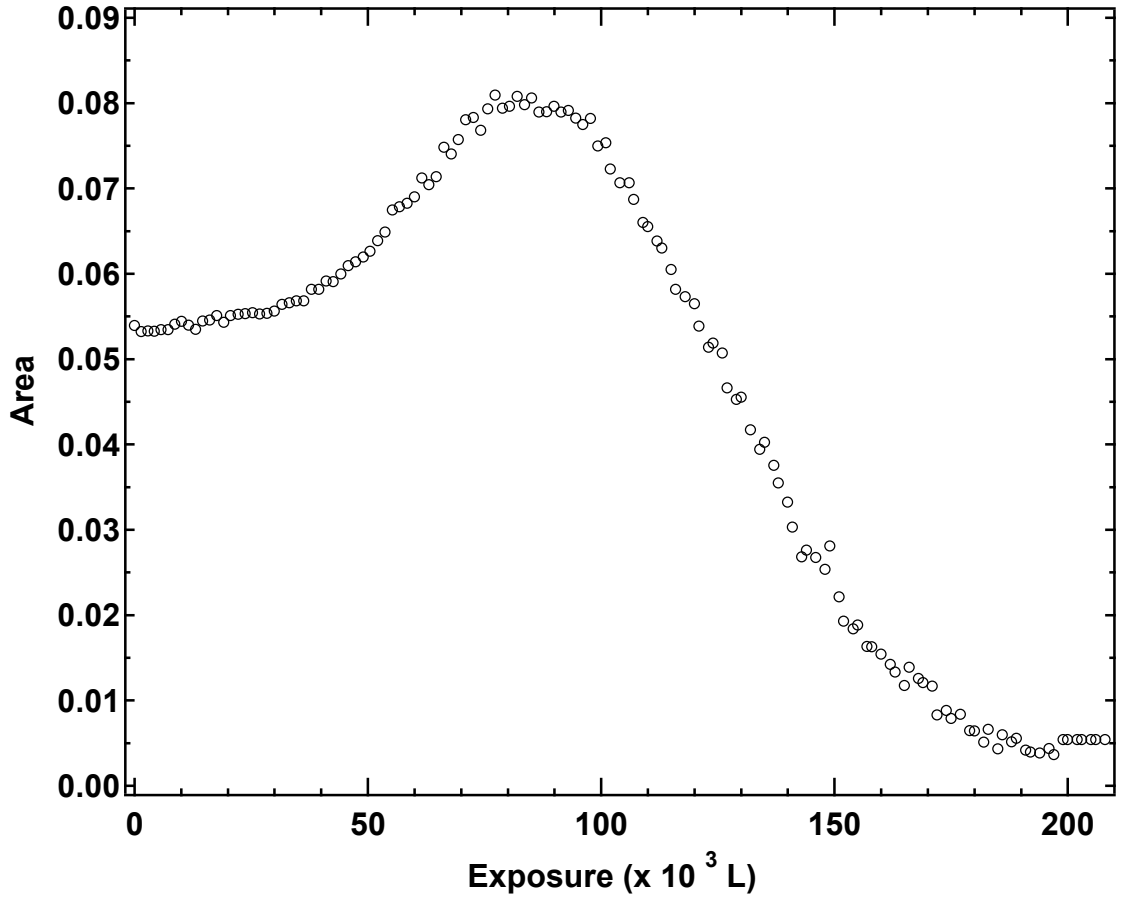

Figure 3.11. A graph indicating how the integrated area of the band from the asymmetric methylene stretch for alkanethiol SAMs changes upon exposure to ozone. The area initially rises due to a disordering of the monolayer followed by a significant decrease in area caused by the direct removal of the aliphatic hydrocarbons during the oxidation.

When considering the original orientation of the monolayer, any disruption or disordering of the chains (i.e., oxidation of the sulfur head group or gas-phase molecule diffusing into the monolayer) will cause the chains to reorient. If the chains stand less upright, the area of the band assigned to the methylene asymmetric stretch will increase since the reorientation will cause the transition dipole moment of the methylene asymmetric stretch to lie more normal to the plane of the surface.[112] Therefore, the initial increase in area of the asymmetric methylene stretch is most likely due to a disordering event within the hydrocarbon chains. This event could be caused by ozone diffusing into

the chains and causing disorder. However, exposure of the monolayers to pure $CO_{2(g)}$, with the same capillary array doser, showed no disordering of the chain as measured by RAIRS (data not shown). Another possible disordering event could be the diffusion of ozone at defects within the monolayers causing oxidation of the sulfur head groups. The bulky ozone molecule or oxidized sulfur species would disrupt the monolayer and cause disorder. The decrease in area of the band assigned to the asymmetric methylene stretch from 9.0×10^4–2.0×10^5 L is caused by the slow removal of the hydrocarbon chains. It is evident that most of the hydrocarbon chains are removed from the surface during the reaction since the area of the band associated with the methylene stretch approaches zero. We also observe a concomitant decrease in C(1s) XPS signal.

If we plot the integrated area of the band assigned to the asymmetric methylene stretch (2919 cm^{-1}), the asymmetric SO_2 stretch (1383 cm^{-1}), and the symmetric SO_2 stretch (1192 cm^{-1}) on the same graph, we can begin to further develop a mechanistic picture of the reaction of ozone with SAMs. Figure 3.12 demonstrates how these bands in a 16C CH_3 SAM change during exposure to pure ozone. The integrated area of the peak from the asymmetric methylene stretch begins to change immediately upon exposure to ozone and rises exponentially to reach a maximum. During this rise, we begin to see a band emerge at 1384 cm^{-1}, which we assign to the asymmetric stretch of an SO_2 moiety. This happens after approximately 5.0×10^4 L of ozone exposure. The area of the adsorption band from the asymmetric SO_2 stretch increases from 5.0×10^4–1.4×10^5 L. During the initial increase in area of the band from the asymmetric SO_2 stretch, significant disordering is noticed in the monolayer, which is evident by the increase in area of the peak assigned to the asymmetric methylene stretch. From these changes, we hypothesize

that it is the oxidation of the thiolate head groups that cause the disordering of the monolayer. The area of the adsorption band from the asymmetric SO_2 stretch continues to increase until it reaches a maximum at approximately 1.4×10^4 L. At this exposure, a signal starts to emerge that we assign to the symmetric SO_2 stretch (1192 cm^{-1}). As the area of the band from the symmetric SO_2 stretch increase, there is a gradual decrease of the area from the asymmetric SO_2 stretch until both peaks approach the same integrated area. We notice that during the changes occurring to the peaks at 1383 and 1192 cm^{-1}, there is a monotonic decrease in the area associated with the asymmetric methylene stretch. Because we do not observe signal from the symmetric SO_2 stretch until the integrated area from the asymmetric SO_2 stretch has reached its maximum, we conclude that the species responsible for the signal assigned to the asymmetric SO_2 stretch is further oxidized to form a structure that produces the signal associated with the symmetric SO_2 stretch. During this further oxidation of the SO_2 moiety, we observe significant loss of the hydrocarbon chains as evident by the decrease in the integrated area of the band assigned to the asymmetric methylene moiety.

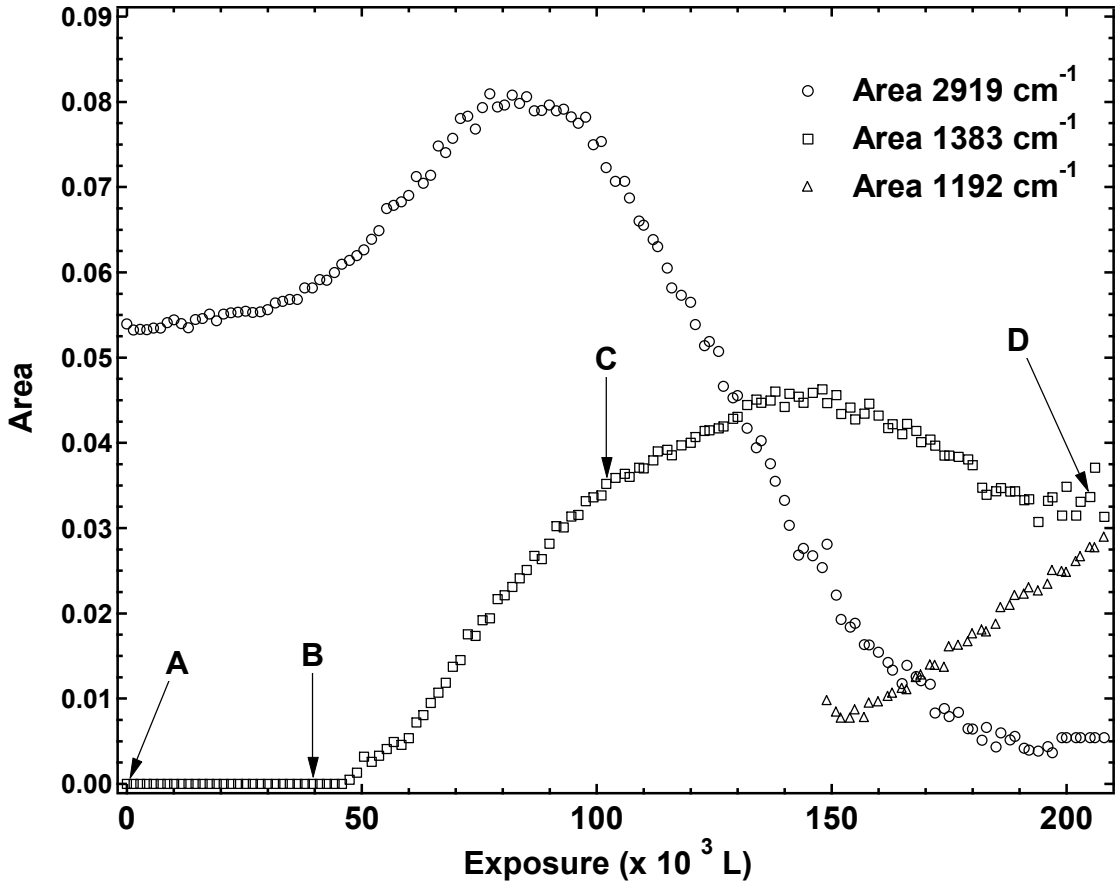

Figure 3.12. Plots of the changes in integrated area of the bands from the asymmetric CH_2 stretch (2919 cm^{-1}), asymmetric SO_2 stretch (1383 cm^{-1}), and symmetric SO_2 stretch (1192 cm^{-1}) of a 16C CH_3 SAM during exposure to pure ozone. No peak intensity above the noise was observed in the RAIR spectra at 1383 cm^{-1} between 0–5.0 × 10^4 L. The positions A, B, C, and D represent exposure times in which the monolayer was analyzed by XPS, see Figure 3.14 and text for details.

The reaction dynamics observed for the 16C CH_3 SAM presented in this chapter, were also observed for a series of methyl terminated monolayers of varying chain lengths (C# CH_3 SAMs, where # = 6,10,12,15,16, and 18). The data for the 16C CH_3 SAM has been shown as representative of all monolayers studied. Only one major difference is noticed in the exposure of the various chain length SAMs. Specifically, the rate of oxidation of each chain length is significantly different and this difference will be discussed later in this chapter.

3.3.2.2 X-ray Photoelectron Spectroscopic Data

To further characterize the reactions occurring at the substrate from the exposure of the SAMs to ozone, we analyzed the surfaces using X-ray photoelectron spectroscopy. Figure 3.13 shows representative high resolution X-ray photoelectron spectra for the S(2p), O(1s), and C(1s) binding energy regions of self-assembled monolayers before and after exposure to ozone. In each region, the upper trace (a) is that of the monolayer before any exposure to ozone and the bottom trace (b) is that of the monolayers after exposure to ozone. All post-exposure X-ray photoelectron spectra in Figure 3.13 were obtained after no further changes were noticed in the monolayer by RAIRS. The ozone exposure was then stopped and the samples were aligned with a take-off angle of 90° for analysis. All binding energies and intensities of the post-exposure spectra, shown in Figure 3.13, were normalized to the Au(4f) peak position and intensity before exposure to ozone.

The S(2p) binding energy region before exposure to ozone (a) shows a single peak at 162.8 eV, consistent with an unoxidized form of sulfur.[101,103] After exposure to ozone (b), there is no observable signal above the noise that can be attributed to unoxidized sulfur (< 164 eV). Instead, we observe a weak broad peak at ~167 eV. This shift to high binding energy and significant decrease in the S(2p) intensity is consistent with the finding of Poirier et al., who also exposed methyl-terminated SAM to pure ozone.[58] We attribute these changes in the S(2p) region to the oxidation of the sulfur moieties within the monolayer.[45,58]

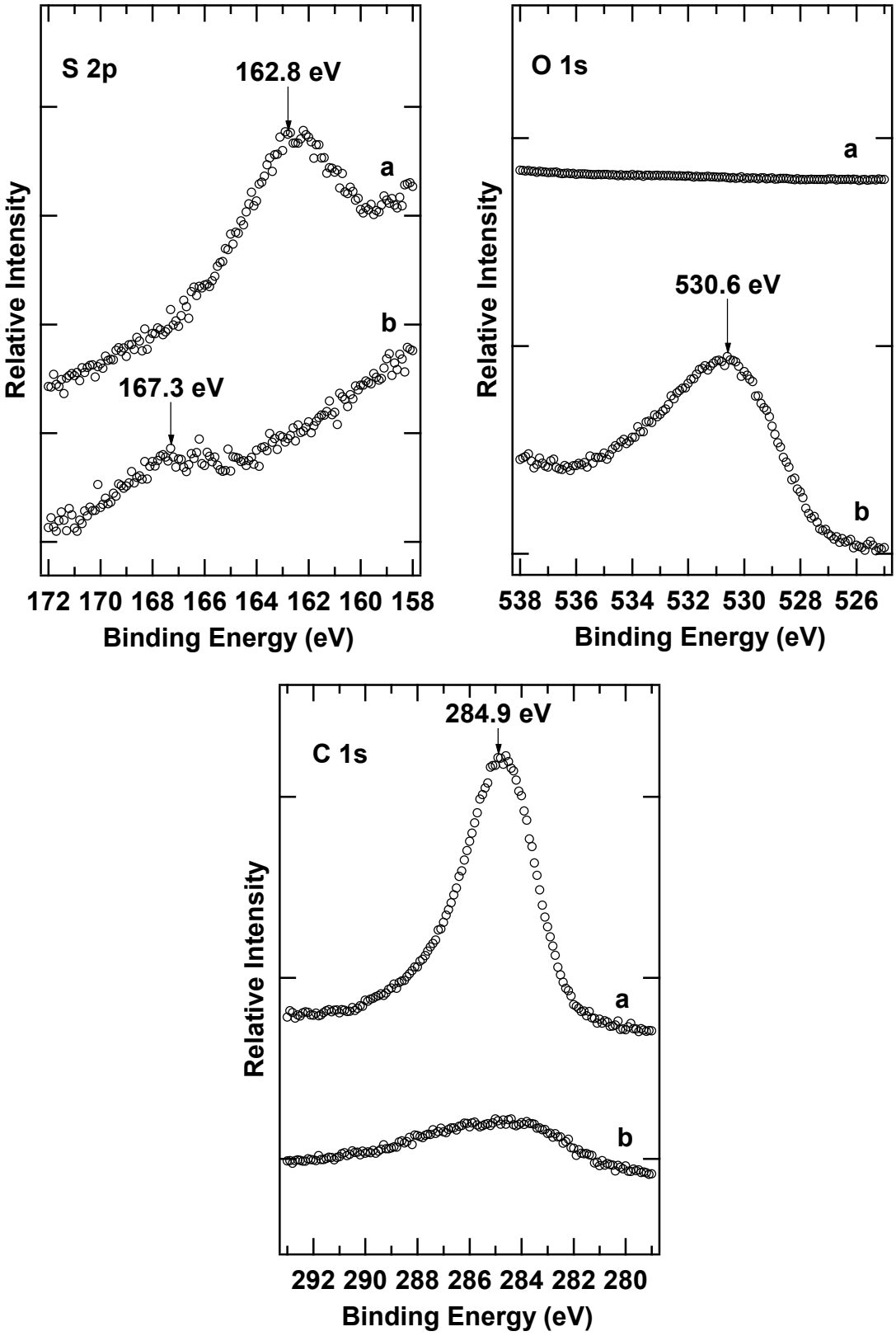

Figure 3.13. High resolution X-ray photoelectron spectra of the S(2p), O(1s), and C(1s) regions of self-assembled monolayers a) before and b) after exposure to ozone.

Photoemission spectra acquired for the O(1s) binding energy region of the monolayer before exposure to ozone (a) show no detectable signal for oxygen. However, after exposure to ozone, the photoemission spectra (b) shows a significant broad peak centered around 530.6 eV. This spectrum suggests that a significant amount of oxygen is added to the monolayer upon exposure to ozone. Furthermore, binding energy of O(1s) electrons for SO_x species have been previously reported to be around 530 eV; therefore, the added oxygen is consistent with oxygen bound to sulfur atoms.[113] We attribute the addition of oxygen to the monolayer to the direct oxidation of the sulfur species within the monolayer.

The effect of ozone exposure on the C(1s) photoelectron spectra of methyl-terminated monolayers is shown in Figure 3.13. The un-exposed spectrum (a) contains a sharp peak centered around 284.9 eV, which is characteristic of aliphatic hydrocarbons.[102] Upon exposure to ozone, this peak shows significant decrease in intensity. We attribute this decrease in signal from the C(1s) photoelectrons to direct desorption of the aliphatic chains upon oxidation of the sulfur moiety.

We conclude from the XPS data shown in Figure 3.13 that exposure of a methyl-terminated monolayer to ozone causes oxidation of the sulfur moieties within the monolayer. This oxidation process allows significant desorption of the molecules in the monolayer as evident by the considerable loss in intensity of the S(2p) and C(1s) photoelectron signals. Substantial addition of signal from O(1s) photoelectrons is also noted, which we attribute to the oxidized sulfur species.

To confirm our assignments of the 1383 and 1192 cm^{-1} RAIR peaks to the asymmetric and symmetric SO_2 stretches, respectively, we performed XPS measurements of the

S(2p) regions of the monolayers at various amounts of ozone exposure. Figure 3.14 shows a series of photoelectron spectra of the S(2p) binding energy region of methyl-terminated monolayer exposed to varying amounts of ozone. The uppermost spectrum, Figure 3.14 (A), is the spectrum of a methyl-terminated monolayer before exposure to ozone. A broad peak at 162–163 eV is displayed that is consistent with un-oxidized sulfur bound to the Au substrate. The second spectrum, Figure 3.14 (B), is that of a methyl-terminated monolayer exposed to ozone, but the exposure was stopped just before any detectable formation of the RAIR peak at 1383 cm^{-1} (see position B in Figure 3.12). This surface was exposed to ~4×10^5 L of ozone. The surface was then rotated and analyzed with XPS. The photoelectron spectrum, Figure 3.14 (B), is nearly indistinguishable from the photoelectron spectrum of a methyl-terminated monolayer before exposure to ozone, Figure 3.14 (A). The third spectrum, Figure 3.14 (C), is that of a methyl-terminated monolayer exposed to ozone with the exposure stopped after the RAIR data show a large peak at 1383 cm^{-1} but no detectable peak at 1192 cm^{-1} (see position C in Figure 3.12). This surface was exposed to ~9×10^5 L of ozone. The photoelectron spectrum, Figure 3.14 (C), displays a significant reduction is the signal of the un-oxidized sulfur moieties, 162–163 eV. In fact, the signal is barely distinguishable above the noise in the spectrum. The spectrum does exhibit a new small broad peak at 167 eV. This peak has been previously observed by Tarlov et al.,[51,58] Hutt and Leggett,[48] and Huang and Hemminger,[46] who assigned this feature to sulfur bound to three oxygen atoms. The last spectrum, Figure 3.14 (D), is of a methyl-terminated monolayer exposed to >2.0×10^6 L of ozone. This surface displayed IR absorption at both 1383 and 1192 cm^{-1} (see position D in Figure 3.12). The X-ray photoelectron spectrum shows

complete disappearance of the reduced form of sulfur (162–163 eV), and a small peak is left at 167 eV.

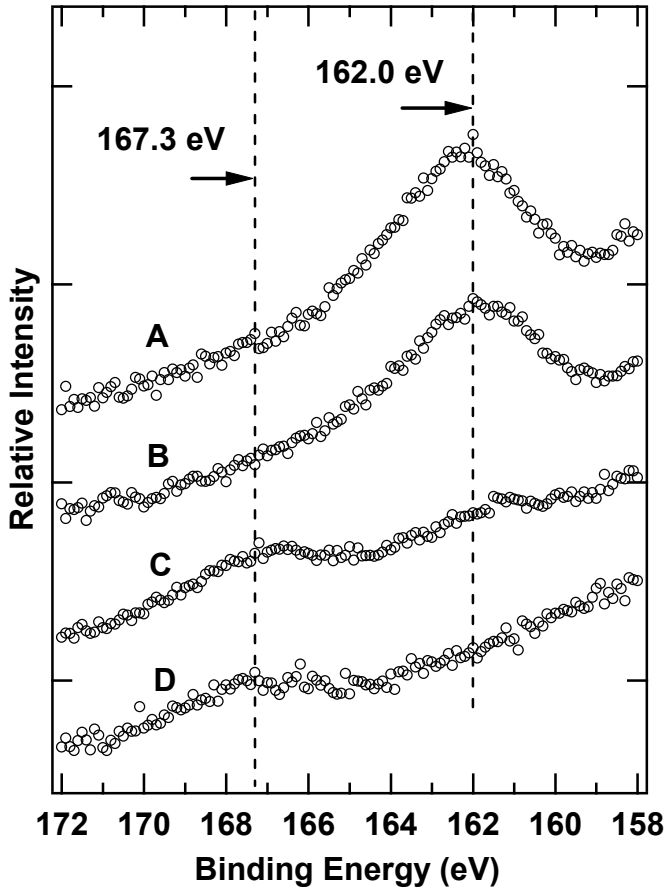

Figure 3.14. High resolution X-ray photoelectron spectra of the S(2p) binding energy region of methyl terminated monolayers: before exposure to ozone (A), after exposure to ozone but before any formation of a RAIR peak at 1383 cm^{-1} (~4.0×10^5 L of exposure) (B), after exposure to ozone but before any formation of a RAIR peak at 1192 cm^{-1} (~9.0×10^5 L of exposure) (C), after oxidation by ozone and formation of RAIR peaks at both 1383 and 1192 cm^{-1} (>2.0×10^6 L of exposure) (D).

From the data shown in Figure 3.14, we conclude that there is no detectable oxidation using XPS of the original sulfur moieties of the monolayers before the formation of the RAIR peak at 1383 cm^{-1}. It is during the formation of the RAIR peak at 1383 cm^{-1} that oxidation of the sulfur is observed with XPS. No intermediate binding energies were observed in XPS during oxidation. In fact, we observed no evidence, in both the RAIR

data and the XPS data, that indicate the sulfur moieties of the original monolayer were partially oxidized to SO or SO_2 intermediates. The simultaneous rise in the XPS intensity of an oxidized sulfur moiety and the IR intensity of the bands at 1383 cm^{-1} and 1192 cm^{-1}, strongly suggests that both the 1383 and 1192 cm^{-1} RAIR peaks are caused by absorptions from oxidized forms of sulfur.

3.3.2.3 Mechanistic Details

Based on the data displayed in Figures 3.7-3.14, we propose the mechanism outlined in Figure 3.15. The mechanism illustrates direct oxidation of the thiolate monolayers forming sulfonate moieties within the monolayer. We hypothesize that these bulky sulfonate groups are causing the disordering of the monolayer, which leads to the increase in area of the band assigned to the asymmetric methylene stretch in the RAIR data. We speculate that the sulfonate moieties are aligned by van der Waals forces between the alkyl chains, such that only the SO_2 asymmetric stretches are observed. We hypothesize that the SO_2 symmetric stretches are not observed because their transition dipole moments are aligned parallel to the surface.[43,111] Upon further oxidation of the sulfonate species with ozone, the alkyl chains are removed from the surface to form sulfate functionalities. Chain desorption can also cause disordering within the monolayers. The sulfate groups display both asymmetric and symmetric SO_2 stretches in the RAIR data. A mechanism that includes the intermediate species of sulfoxide, sulfone, and sulfinate species is possible,[49,56] but the RAIR and XPS data that we have observed shows no indication of these intermediates. We only observe the oxidation of the thiolate directly to a sulfonate with further oxidation to a sulfate.

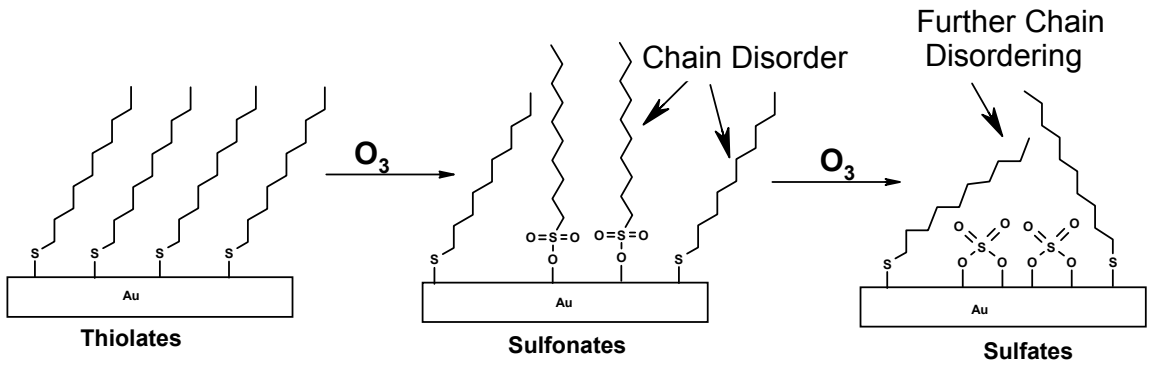

Figure 3.15. Proposed mechanism demonstrating the changes that occur during the ozone oxidation of methyl-terminated self-assembled monolayers.

What is the initial site of attack of the monolayer for the ozone molecule? One possible mechanism involves the diffusion of ozone through the alkyl chains down to the sulfur atoms that are bound to the Au substrate. This type of mechanism would show a diffusion limited reaction rate, which would decrease with increasing chain length due to the difficulty of ozone penetrating the closely packed monolayers. Another mechanism for the initial site of attack of ozone could include defects within the monolayers. There are numerous defects that are observed in SAMs on Au substrates including: domain boundaries, step edges, and point defects. A mechanism that has its origin at one of the defects might also show dependence upon chain length since the distribution and number of defects within monolayers have been shown to depend on the length of the alkyl chains.[44] This phenomenon is a direct result of the increasing van der Waals interactions as the alkyl chains lengthen. It is hypothesized that these increased van der Waals interactions help heal the defects within the monolayers; therefore, longer chain monolayers have fewer defects then shorter chain monolayers.

3.3.2.4 Kinetic Measurements

We performed a detailed analysis of the changes to the RAIR spectra of the CH_3 SAMs during ozone exposure with hopes of developing a kinetic model of the entire

oxidation process. We were unable to develop a kinetic model of the total reaction using RAIRS data. The intensity of absorption bands in RAIRS depends not only on the number of molecules (concentration) but also on the orientation of the molecules on the surface (surface selection rule). Kinetic modeling requires knowledge about the concentration of products or reactants during the reaction. Further studies need to be performed, perhaps molecular dynamic simulations, to predict how the orientation of a monolayer changes as the alkyl chain desorbs. This type of study might allow one to separate the changes in the RAIR data that depend on concentration and the changes that depend upon orientation.

Because of the difficulties with full kinetic modeling mentioned above, we performed the kinetic analysis presented below to model the data for the changes in the RAIR spectra during the initial stages of the reaction. This analysis was performed to help explore the mechanism of the site of attack of ozone. To accomplish this goal, we performed oxidation experiments of monolayers with increasing chain length. Methyl-terminated monolayers with the total number of carbons in the chain of 6,10,12,15,16, and 18 were exposed to pure ozone and in situ kinetic measurements were performed with RAIRS. Figure 13.16 reveals how the rate of oxidation of the monolayers depends upon chain length. Figure 13.16 shows the changes in the integrated area of the adsorption band assigned to the asymmetric methylene stretch upon exposure to ozone for methyl-terminated monolayers with 10,12,15,16, and 18 total carbons. The oxidation rate of the methyl-terminated monolayer with 6 total carbons was too fast to measure with our current time resolution. We chose the change in integrated area of the methylene asymmetric stretch for kinetic analysis because this metric is the most

sensitive to changes within the monolayer. Single exponential functions of the form shown in Equation 3.2 were fit to the data and are shown as solid lines in Figure 3.16.

$$\Delta A(t) = Be^{k_{obs}t} \tag{3.2}$$

In this equation, B is a fitted scaling factor and k_{obs} is a fitted first-order observed rate constant. The exponential functions were fit only to the initial oxidation times. At later oxidation times, the kinetics of the reaction change because most of the monolayer is significantly disordered. Thus, the fitted rate constant is an observed rate constant for the initial disordering occurring within the monolayer due to oxidation of the thiolates. From Figure 3.16, it is evident that, as the number of carbons within the chains of the monolayer increase, the rate of change in the area of the band assigned to the methylene asymmetric stretch decrease significantly.

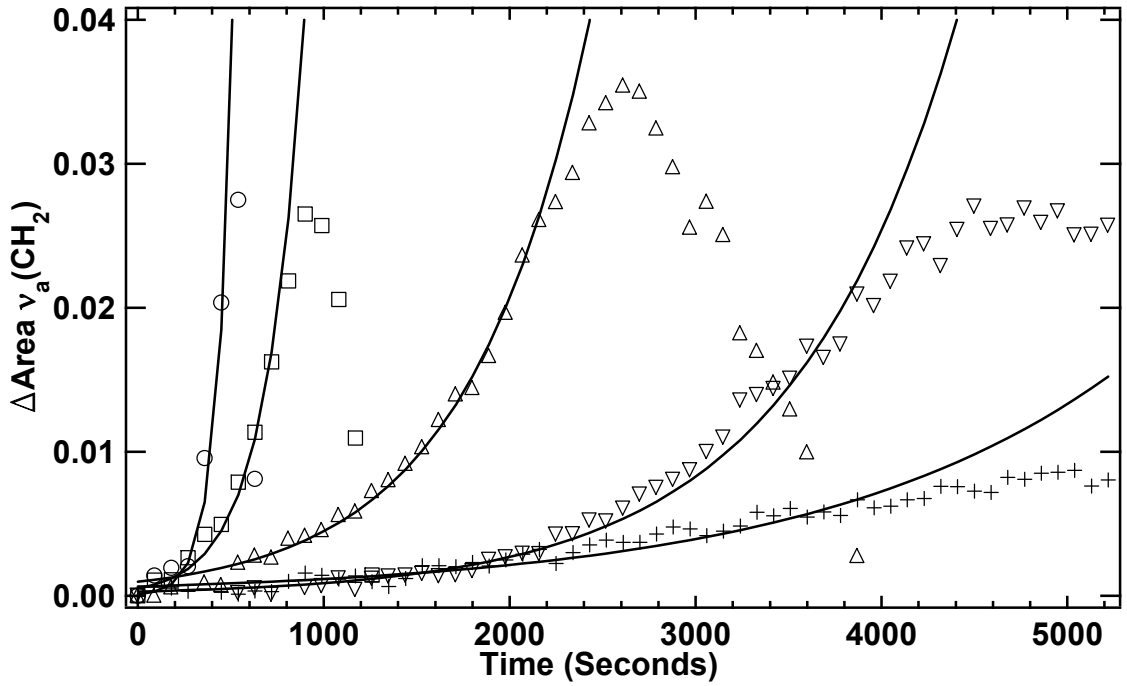

Figure 3.16. Changes in the integrated peak area of the asymmetric methylene stretch during ozone exposure of methyl-terminated SAMs with differing numbers of methylene groups. The solid lines represent single exponential fits to the early exposure times of the individual monolayers, which demonstrate that the initial rate of disorder from ozone oxidation is dependent on chain length. The fitted parameters are as follows: 10C (B = 0.0001, k_{obs} = 0.0116); 12C (B = 0.0005, k_{obs} = 0.00489); 15C (B = 0.00097, k_{obs} = 0.00153); 16C (B = 0.00026, k_{obs} = 0.00112); 18C (B = 0.0006, k_{obs} = 0.000609).

Figure 3.17 summarizes how the observed rate constants depend on alkyl chain length. Previous researchers have suggested that the transport of small molecules across lipid layers or monolayers occurs at gauche defects in the layer.[42,114] Specifically, Laibinis and Whitesides studied the oxidation of SAMs on copper by O_2 molecules, and they suggested that the observed exponential dependence of oxidation on chain length could be explained by the chain-length dependence of the average probability of finding a methylene in a gauche conformation.[42] If gauche defects within monolayers are responsible for the initial sites of attack of ozone, one might therefore hypothesize that the rate of oxidation would be exponentially dependent on chain length. An exponential

dependence of the observed rate constant on chain length is indeed displayed in Figure 3.17 (see solid line). Furthermore, other types of defects including: missing rows, missing chains, or phase boundaries may also depend on chain length. Attack of ozone at such sites may also lead to a strong chain length dependence of the initial reaction rated.

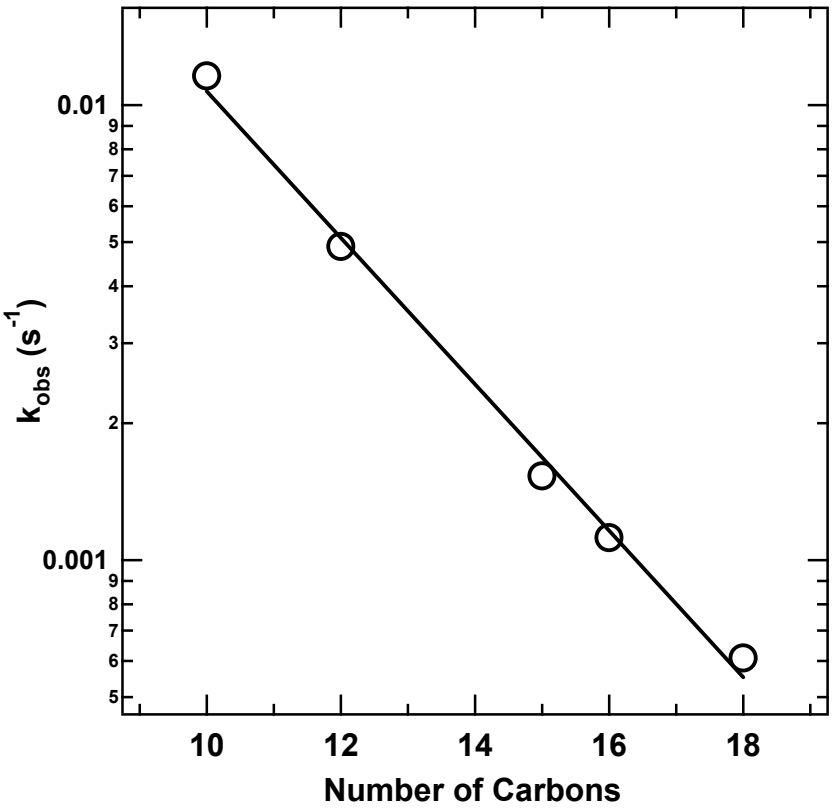

Figure 3.17. The observed rate constant of the initial disordering from ozone oxidation vs. the total number of carbons in the exposed monolayers. The solid line is an exponential fit to the data (Y= 0.437 × EXP(-0.3707 × X)).

An alternative mechanism is one in which the ozone molecules diffuse through the ordered alkyl chains to the substrate where oxidation occurs. This type of mechanism would be diffusion limited due to the difficulty of the ozone molecule penetrating the closely packed monolayers. The rate of oxidation would be expected to follow diffusion kinetics as expressed in Equation 3.3: [9]

$$L^2 = D / k \qquad (3.3)$$

In this equation, L is the reactodiffusion length. D is the diffusion constant of ozone in the SAM, and k is the first-order rate constant. This equation predicts that the inverse of the rate constant should be linearly dependent on the square of the diffusion length. Figure 3.18 displays how the inverse of the observed rate constant depends on the square of the diffusion distance for the SAMs studied. From this figure, we see that this dependence is not linear, which indicates that the mechanism of oxidation of the monolayers cannot simply be described by ozone diffusion through the monolayers.

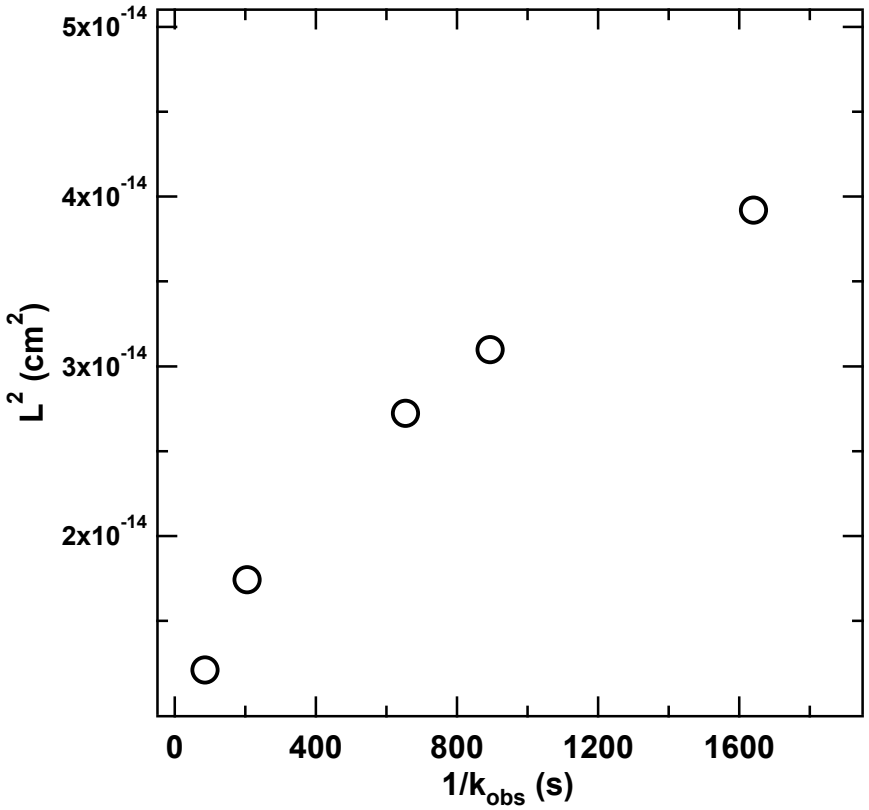

Figure 3.18. A plot of the square of the reactodiffusion lengths vs the inverse of the observed rate constants for a series of n-alkanethiol SAMs.

Our data suggest that the initial site of attack of ozone in methyl-terminated monolayers is at defects within the film. Because defects within monolayers are dependent on chain length,[44,95] the oxidation dependence on chain length could be a

direct result. Our results are consistent with the findings of Poirier et al., who monitored the oxidation of decanethiol monolayers with ozone with XPS and scanning tunneling microscopy in UHV.[58] Poirier et al. found that the reaction initiates at domain boundary networks of the alkanethiol monolayers and propagates into the domains. They also observed a transformation of the monolayer from a highly-ordered structure to a disorder liquid-like phase. During the transformation, they also observed desorption of the alkanethiol molecules during oxidation. In the reflection absorption infrared spectroscopy experiments presented in this chapter, the area of the peak assigned to the methylene asymmetric stretch initially increases due to a disordering event within the monolayer; however, the area of this peak also depends on the number of methylene molecules on the surface, which is decreasing during the reaction. Because the oxidized chains are desorbing from the surface, further studies need to be performed to better understand how the orientation of the monolayer (which determines the RAIRS surface selection rule) depends on oxidation.

3.4 Summary

In summary, we have characterized a series of SAMs with increasing chain length. The monolayers assemble into structures that transition from disordered (liquid-like) systems to ordered (crystalline-like) systems as the length of the alkyl chain increases. We performed in situ monitoring of CH_3 SAMs during oxidation with pure ozone using RAIRS. The RAIR data show that oxidation of the monolayer initially forms a sulfonate species. The sulfonate species is further oxidized forming a sulfate moiety with concomitant loss of the hydrocarbon chains. The sulfate product remains on the surface even after prolong exposure to ozone. X-ray photoelectron spectroscopy data show that

the monolayers are oxidized from the thiolate directly to a sulfonate species. Intermediate oxidation of the monolayer is not observed with either RAIRS or XPS. Significant losses of carbon and sulfur are also observed by XPS during oxidation. A mechanism is suggested that demonstrates the transformation of the monolayer from the thiolate to the sulfonate with further oxidation of the sulfonate to a sulfate species.

We also performed a kinetic analysis of the oxidation of a series of n-alkanethiols with pure ozone. We noticed an exponential decrease in the observed rate constant, for the initial disordering of the monolayers, with increasing chain length. The kinetic analysis suggests that the initial site of attack of ozone with SAMs is at defects within the films and not direct diffusion through the hydrocarbon chains. The knowledge gained from the study presented in this chapter should help predict rates of oxidation of alkanethiols as well as guide in designing more robust monolayers.

Chapter 4

Synthesis, Characterization, and In situ Monitoring of the Reactive Uptake of Gas-phase Ozone with Vinyl-terminated Self-assembled Monolayers

4.1 Introduction

Aerosols play an important role in atmospheric chemistry, affecting both air quality and global climate.[13,21] Atmospheric aerosols absorb and scatter solar radiation as well as act as cloud condensation nuclei (CCN).[4,11,13,115] Field measurements have shown that atmospheric aerosols can contain significant amounts of organic matter.[10-12] Ellison et al. suggested a chemical model for organic aerosols in the form of an inverted micelle.[5] The inverted micelle consists of an aqueous core that is encapsulated by a hydrophobic organic monolayer, which consists of surfactants of biological origin. Other atmospheric aerosols consist of dust particles coated with nitrates, sulfates, or organic materials.[7] The reactions of these organic aerosols with trace gases in the atmosphere can affect the aerosols chemical properties. For example, the reactive uptake of trace gases by organic aerosols can influence the hygroscopic character, optical property, or CCN activity of the organic aerosol.[4-6] Ellison et al. suggested that unsaturated organic aerosols could be oxidized by gas-phase hydroxyl radicals or ozone, forming polar functional groups.[5] This chemical transformation of the atmospheric particle can greatly change the hygroscopic character or CCN activity of the aerosol. Therefore, understanding the products that form in the heterogeneous reaction of gas-phase oxidants with surface bound organic molecules is important in predicting the fate of the particle. Furthermore, quantifying the reactive uptake of atmospheric oxidants by organic particles is an important step in determining the lifetime of the oxidant and the organic aerosol.

Because unsaturated hydrocarbons are prevalent in the troposphere, the reactions of ozone with unsaturated hydrocarbons have been proposed to play a significant role in atmospheric chemistry.[13,14] Numerous studies have explored the reactions of ozone with unsaturated hydrocarbons both in the gas-phase and in solution.[13,15-17] Recently, the kinetics and mechanisms of the surface oxidation of unsaturated hydrocarbons in thin films or absorbed on solid supports, as models for organic aerosols, have received significant attention.[4,6,9,14,18-22] One of the underlying goals of these studies is determining the reaction probability of ozone with the unsaturated hydrocarbons.[2] A reaction probability is a unitless parameter that is defined as the fraction of collisions of gas with a surface that leads to a reaction. In general, atmospheric models use reaction probabilities derived from gas-phase reaction data.[2] The reaction probability of gas-phase 1-hexene, a vinyl-terminated hydrocarbon, with ozone is $\sim 3 \times 10^{-8}$, based on a rate constant of 1×10^{-17} cm^3 $molecules^{-1}$ s^{-1} and a diffusion-controlled rate constant of $\sim 3 \times 10^{-10}$ cm^3 $molecules^{-1}$ s^{-1}.[4,13] Previous studies exploring the oxidation by ozone of alkenes adsorbed on surfaces have reported reaction probabilities of 10^{-4}–10^{-5}.[4,9,14,19]

Dubowski et al. studied the reactions of ozone with vinyl-terminated SAMs on silica surfaces.[4] The authors reported that the initial reaction probability is inversely and non-linearly dependent upon the ozone concentration, suggesting that the reaction follows a Langmuir–Hinshelwood mechanism. In a Langmuir–Hinshelwood mechanism, ozone first physisorbs onto a surface and then reacts. Reactions of ozone with the surface would compete with ozone's desorption from the surface. By monitoring the time-dependant change of the formation of carbonyl products by FTIR with an attenuated total reflection crystal, the authors reported an initial reaction probability of $\sim 10^{-5}$ with ozone

concentrations of 1×10^{11} molecules cm^{-3}. Moise and Rudich, investigating the same vinyl-terminated SAMs on silica surfaces at 298 K, determined an uptake coefficient from the first-order loss of gas-phase ozone within a flow-tube reactor.[9] Moise and Rudich reported a reactive uptake coefficient of $(1.7 \pm 0.3) \times 10^{-4}$ for SAMs containing 8 total carbons and $(2.7 \pm 0.4) \times 10^{-4}$ for SAMs containing 3 total carbons.

In a separate experiment, Moise and Rudich explored the reaction of unsaturated organic fatty acids, in liquid and frozen states, with ozone using a cylindrical rotating-wall flow-tube reactor coupled to a mass spectrometer.[19] Oleic acid was determined to have a reactive uptake coefficient of $(8.3 \pm 0.2) \times 10^{-4}$ in a liquid state and $(5.2 \pm 0.1) \times 10^{-5}$ in a frozen state. The authors suggested that the order of magnitude decrease in the uptake coefficient upon freezing of the organic acid indicated that diffusion, solubility, and reactions within the bulk liquid contributed substantially to ozone uptake. The authors hypothesized that the reactions of the frozen oleic acid are limited to the surface.

The studies mentioned above all used commercially available chemicals to create models of atmospheric aerosols. In an effort to provide a more realistic proxy for atmospheric particles, Voges et al. developed a synthesis of tropospherically relevant terpenes bound to glass substrates.[14] The authors' aim in the experiments was to closely mimic tropospheric molecules and track the reaction of the surface-bound species with ozone in real-time with vibrational sum frequency generation spectroscopy. The authors report an initial reaction probability of $< 1 \times 10^{-5}$ for the cyclic terpene attached to the surface.

One common conclusion in the above mentioned experiments is that ozone reacts more rapidly with surface bound alkenes when compared to analogous gas-phase

reactions. The increased reaction probability can be explained by considering the percentage of collisions between ozone and the unsaturation sites in each system. When ozone collides with the surface bound alkene, the initial collision must be with an unsaturation site because these sites are at the gas/surface interface. This collision is a potential reaction; however, when ozone collides with the gas-phase terminal alkene, the initial collision does not necessarily involve the carbon–carbon double bond. Collisions with the saturated hydrocarbons do not lead to reactions. Because the reaction probability for surface bound alkenes is higher than the probability for gas-phase alkenes, using reaction probabilities from gas-phase reactions when modeling atmospheric processes may not be appropriate and detailed studies should be performed to accurately determine the reactive uptake coefficients for surface bound alkenes.

Presented in this chapter, vinyl-terminated alkanethiol SAMs were used as proxies for unsaturated organic molecules adsorbed on solid supports. Details of the synthetic strategies used to prepare these model systems are presented. SAMs provide a model system that is highly organized and extremely reproducible. SAMs make good proxies for organic aerosols because important chemical properties, like the chemical identity of the gas/surface interface, can be controlled. The surface density of SAMs is also well known. With SAMs, the surface orientation can even be determined. The benefits of SAMs as model systems provide us with an important opportunity to study the structure/reactivity relationship of the heterogeneous reactions of ozone with vinyl terminated organic thin films.

In the studies presented in this chapter, we investigate the heterogeneous reaction of ozone with vinyl terminated organic thin films as proxies for atmospheric aerosols. The

objective of this research is to develop a fundamental understanding of the reactions of ozone with vinyl terminated interfaces, both from a mechanistic and kinetic perspective. We seek to understand how the unsaturated organic surface reacts with pure ozone when it is isolated in ultrahigh vacuum from interfering reactions of background gases.

We characterized the SAM proxies using reflection absorption infrared spectroscopy (RAIRS) and X-ray photoelectron spectroscopy (XPS). In situ kinetic measurements of the condensed phase oxidation by an effusive beam of pure ozone were performed in real-time with RAIRS. During the oxidation of the vinyl terminated monolayers, we observed disordering of the monolayer concurrently with the disappearance of the vinyl functional groups. We also observed the formation of bands within the RAIR spectra, which we attribute to newly formed carbonyls or carboxylic acids on the surface. Using XPS, we observed little oxidation of the sulfur head group and no significant loss of carbon upon exposure of the SAMs. We propose a mechanism that includes the cross linking of the hydrocarbon chains that impedes further oxidation of the head group and stops desorption of the chains. We tracked the kinetics of the oxidation of the vinyl groups by monitoring the changes in IR absorbance of the ν(C=C) stretch. We report an observed rate constant for this reaction of $(2.5 \pm 0.5) \times 10^{-5}$ s^{-1}. Using the observed rate constant, we determined an initial reaction probability of $(1.1 \pm 0.5) \times 10^{-5}$.

4.2 Experimental Details

4.2.1 Materials

All chemicals were used as received without further purification unless otherwise noted. HPLC grade hexanes and tetrahydrofuran (THF) were purchased from Fisher Scientific Inc. 11-bromo-1-undecene (95%), 10-bromo-1-decene (97%), thiourea

(≥ 99.0%), tetrabutylammonium fluoride (1.0 M solution in THF with 5% water), silica gel (grade 03), and hexamethyldisilathiane (99.9%) were obtained from Sigma-Aldrich, Inc. Sodium hydroxide, anhydrous magnesium sulfate, and diethyl ether were purchased from EMD Chemicals, Inc. Silica gel (for flash chromatography, 60 Å) was purchased from SiliCycle, Inc. 18-bromo-1-octadecene was obtained from TCI America, Inc. Research grade oxygen, ultrahigh purity nitrogen, ultrahigh purity argon, and dry ice were purchased from Airgas Specialty Gases. Polycrystalline gold substrates were received from Evaporated Metal Films. Reagent grade acetone and ethanol were obtained from Pharmco-Aaper and Commercial Alcohols. 14-Pentadecene-1-thiol was obtained as a gift from T. Randle Lee and used as received.

4.2.2 Synthesis of Thiols

Two different synthetic routes were developed for the synthesis of the vinyl-terminated thiols. 10-undecene-1-thiol was synthesized from 11-bromo-1-undecene with the well-known thiourea route.[112] The thiourea route is performed under extremely basic conditions and consequently the direct mercapto-dehalogenation of the alkyl bromides suffers from side reactions forming dialkyl sulfide byproducts.[116] An alternative more efficient and rapid synthetic route was developed to synthesize 9-decene-1-thiol, 10-undecene-1-thiol, and 17-octadecene-1-thiol. The alternative route employed a trimethylsilylthioxy-dehalogenation reaction to form the neat thiols in excellent yields.[116] Both synthetic strategies are briefly outlined below.

4.2.2.1 Thiourea Reaction

When synthesizing the 10-undecene-1-thiol with the thiourea route, the procedures of Peanasky and McCarley were followed.[112] Purged with argon, 100 mL of absolute

ethanol were added to a three-neck round-bottom flask equipped with a reflux condenser and bubbler. To the flask, 25 mmol of thiourea were added and stirred by a magnetic stirrer on a hot plate. Once the thiourea was dissolved, the system was purged with argon and 8 mmol of 11-bromo-1-undecene was slowly added to the solution with a syringe. The system was heated to reflux and held for 19 hrs. Conversion of the bromide into the thiouronium salt was monitored during the reflux with thin-layer chromatography (TLC). The reaction was then allowed to cool to room temperature with a continuous purge of argon. To the reaction, 10 mL of a 10% (w/w) solution of NaOH was added by a syringe, and the reaction was then heated to reflux and held for 4 hrs. After cooling to room temperature, the reaction was titrated with dilute HCl until a pH of 7 was reached. The reaction mixture was then transferred to a 500 mL separatory funnel and diluted with 200 mL of hexanes. The aqueous layer was drained and the organic layer was washed three times with 20 mL of 18.2 MΩ H_2O. The organic fraction was dried with anhydrous magnesium sulfate and then the magnesium sulfate was filtered off. The crude thiol was obtained by evaporation of the solvent under low vacuum. Flash column chromatography with hexanes as the eluent was performed on the crude product to obtain the neat thiol; ^{1}H NMR ($CDCl_3$) δ 5.8 (m, 1H), 4.9 (m, 2H), 2.7 (t,0.4H), 2.5 (q, 2H), 2.0 (q, 2H), 1.6 (m, 2H), 1.2–1.5 (m, 14H).

4.2.2.2 Trimethylsilylthioxy-Dehalogenation Reaction

The procedures of Hu and Fox were followed when synthesizing 9-decene-1-thiol, 10-undecene-1-thiol, and 17-octadecene-1-thiol with the trimethylsilylthioxy-dehalogenation reaction.[116] A 0.5 M solution of the appropriate bromide in freshly distilled THF was placed into a 50 mL round bottom flask with a magnetic stirrer bar and sealed with a

rubber septum. The flask was purged with argon and then cooled to -10 °C while stirring in a $CaCl_2$ ice bath. Hexamethyldisilathiane (1.2 equiv) was then injected with a syringe into the reaction mixture. A 1.0 M solution of tetrabutylammonium fluoride in THF with 5% water (1.1 equiv) was then injected into the reaction mixture with a syringe. The reaction was allowed to stir in the ice bath for ~15 min., and then removed and immediately shielded from light with aluminum foil. The reaction was allowed to warm to room temperature while stirring for 1 hr and then 25 mL of diethyl ether was added to the reaction with a syringe. The crude solution was filtered through ~6 inches of silica gel in a vacuum funnel. A green color formed on the silica gel when the reaction mixture was filtered through. The silica gel was rinsed three times with 25 mL of diethyl ether and all organic fractions were combined and the solvent was removed under low vacuum. The product was then purified by flash chromatography with hexanes as an eluent. The 9-decene-1-thiol, 10-undecene-1-thiol, and 17-octadecene-1-thiol reactions produced a 47, 84, and 59% yield, respectively. Figure 4.1 is a nuclear magnetic resonance (NMR) spectrum of the neat 17-octadecene-1-thiol and is representative of all three thiols that were synthesized. The small triplet at 2.7 is believed to be an impurity (~5%) due to the formation of a dialkyl sulfide.

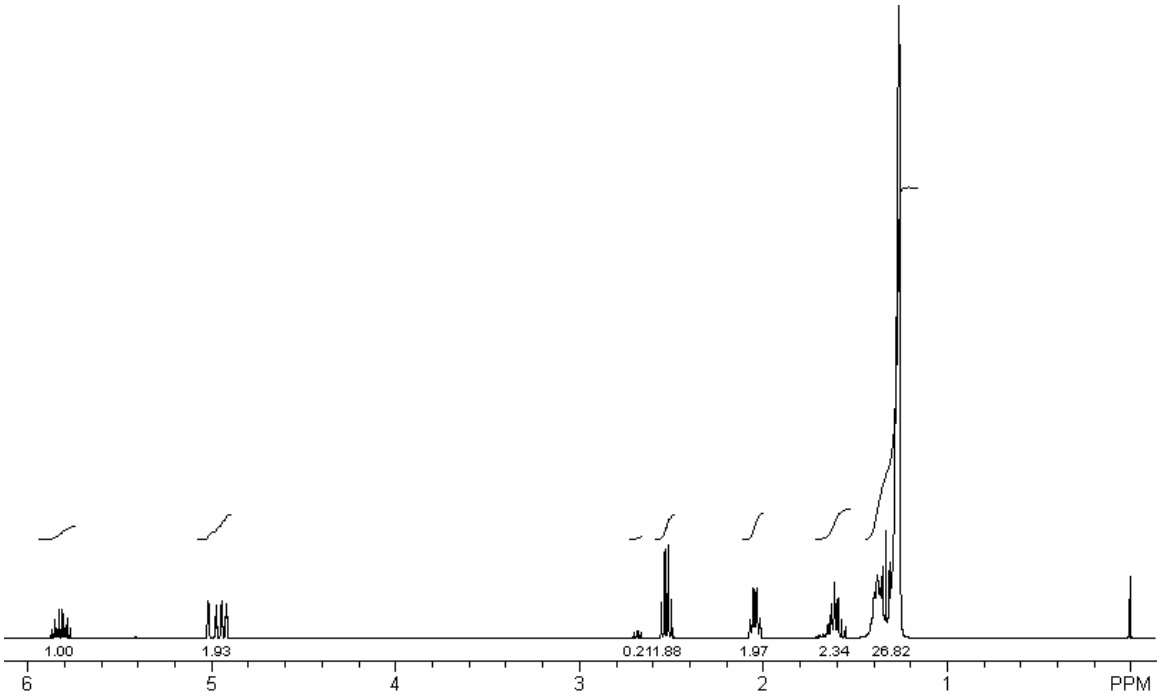

Figure 4.1. Nuclear magnetic resonance spectrum of the neat 17-octadecene-1-thiol.

4.2.3 Synthesis of Monolayer

Polycrystalline gold substrates were prepared by evaporation of 50 Å of chromium onto a glass substrate, 1" × 1" × 0.062". The chromium adhesion layer was followed by evaporation of 1000 Å of Au (Evaporated Metal Films). The Au surfaces were then immersed in piranha solution (7:3 ratio, sulfuric acid/30% hydrogen peroxide) for at least 1 hour to remove surface contaminates. *Caution: piranha solution is an oxidizing agent that can cause explosions when in contact with organic materials!* The Au substrates were then removed from the piranha solution and rinsed thoroughly with deionized water (Millipore Purification Systems, 18.2 MΩ). Each substrate was then dried in a stream of ultrahigh purity nitrogen and immediately placed in a ~1 mM solution of the appropriate thiol in hexanes for at least 48 hours.

4.2.4 Monolayer Exposure

After the 48 hrs incubation time, the vinyl-terminated self-assembled monolayers were removed from the solution and rinsed by dipping numerous times in a solution of hexanes then dried under a stream of ultrahigh purity nitrogen. The surface was then immediately placed onto the sample mount in the load-lock chamber (previously described in Chapter 2). The monolayer surface sample was then transferred into the UHV chamber and aligned for RAIR measurements with the sample positioning manipulator. The total time between removing the monolayer from solution and transferring into UHV was ~20 min. Ozone was prepared as previously described in Chapters 2 and 3, and the ozone concentration was monitored by the attached UV/Vis flow cell. The all-glass effusive ozone doser was positioned ~3.5 cm away from the sample, and the monolayer was exposed to pure ozone at a measured flux of $\sim 1.7 \times 10^{15}$ molecules s^{-1} cm^{-2}. The ozone exposure time was controlled by a Teflon value on the high pressure side of the capillary in the ozone doser.

4.2.5 RAIRS Data Acquisition

The reactive uptake of ozone by the vinyl-terminated SAMs was monitored in situ with a Bruker IFS 66v/S spectrometer. Details of the RAIRS measurements have been previously described in Chapters 2 and 3 but will be briefly discussed here. Infrared radiation was reflected off of the gold substrates in the UHV chamber at ~86 degrees relative to the surface normal. The reflected light was detected by a cryogenically-cooled mid-range (750–4000 cm^{-1}) mercury cadmium telluride (MCT) detector. The RAIR spectra are the result of the co-addition of 100 scans taken over 90 seconds with a 2 cm^{-1} resolution. All spectra are presented with the unit of intensity defined as $-\log(R/R_0)$,

where R is the reflectivity of the monolayer and R_0 is the reflectivity of a reference spectrum. Two different types of reference spectra were used throughout this thesis and will be specified accordingly. The kinetics of the ozone reactions are monitored by the OPUS software program, which was set to continuously record spectra every 90 seconds during the ozone exposure.

4.2.6 XPS Measurements

The monolayers were characterized with X-ray photoelectron spectroscopy before and after exposure to ozone. For XPS measurements, the sample was aligned normal to the hemispherical energy analyzer described in Chapter 2. An X-ray source operating at 250 W (12.5 kV and 20 mA) was used to generated achromatic Al Kα (1486.6 eV) X-ray radiation. Ejected photoelectrons were detected by the hemispherical analyzer operating with a pass energy of 50 eV. A survey scan of each surface was performed with a step size of 1 eV, in order to verify alignment and surface contamination. High resolution spectra of the following elements were recorded: S(2p), C(1s), Au(4f). All high resolution spectra were recorded with a step size of 0.1 eV. The pass energy was then lowered to 20 eV, which minimizes the signal from the Au($4p^3$) electrons. The minimization allows one to analyze the signal coming from the O(1s) electrons with better efficiency. High resolution spectra were then recorded for the O(1s) and Au(4f) electrons in that order. The binding energies for all spectra are referenced to the Au($4f_{7/2}$) peak at 83.8 eV.[93] XPS analysis was performed with commercially available software. All high resolution spectra were fit with 100% Gaussian peaks and a linear baseline.

4.3 Results

4.3.1 Monolayer Characterization

4.3.1.1 RAIRS

Figure 4.2 is a reflection absorption infrared spectrum of a monolayer made from a 1 mM solution of 17-octadecene-1-thiol in hexanes. Figure 4.2 shows each individual peak frequency. Mode assignments for each band are taken from the literature and are shown in Table 4.1.[95,112,117-120] The two most prominent peaks in the spectrum are due to the $\nu_a(CH_2)$ and $\nu_s(CH_2)$ stretches at 2920 and 2851 cm^{-1}, respectively. The position of the peaks from the $\nu_a(CH_2)$ and $\nu_s(CH_2)$ stretches has been shown to be a sensitive indicator of the ordering of the alkyl chain.[79,94-98] In a polyethylene crystal,[99,100] the $\nu_a(CH_2)$ and $\nu_s(CH_2)$ stretches are found at 2920 and 2850 cm^{-1}, respectively; whereas, in a solution, the values blue-shift to 2928 and 2856 cm^{-1}. The observed position of the peaks from the $\nu_a(CH_2)$ and $\nu_s(CH_2)$ stretches (2920 and 2851 cm^{-1}) and narrow line width (15 and 9 cm^{-1}, FWHM) indicate that the 18C C=C SAMs have a well-ordered chain environment, similar to that of a crystalline structure.

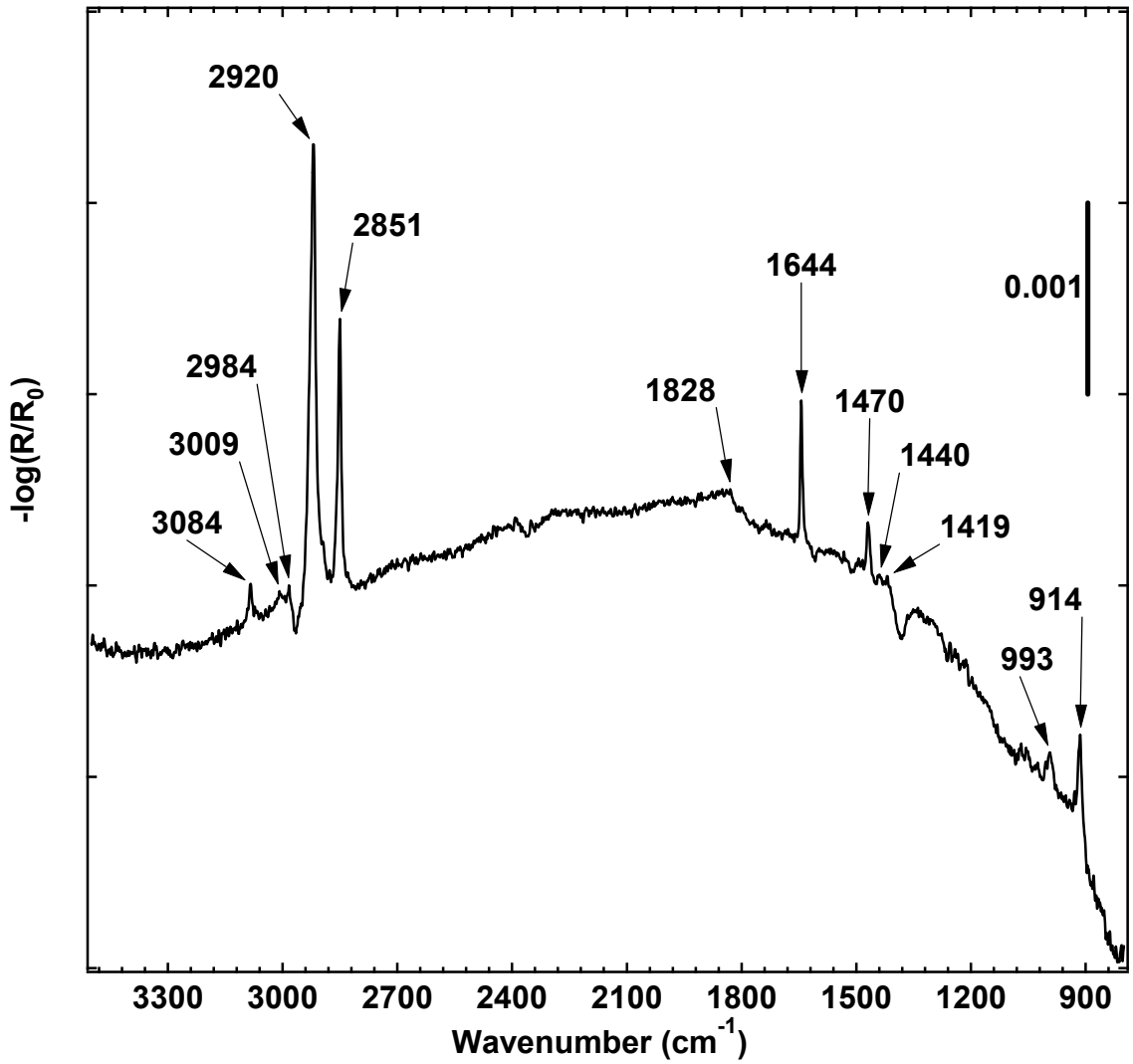

Figure 4.2. Reflection-absorption infrared spectrum with band positions of an 18C C=C SAM.

Modes associated with methylene C-H scissoring are observed at 1470, 1440, and 1419 cm^{-1}.[112] The peak at 1470 cm^{-1} can be assigned to the scissoring of an all-trans methylene chain (δ). The band at 1440 cm^{-1} has been previously assigned as a mode due to the scissoring of a methylene group next a chain end-gauche defect (δ_D),[95] and we assign this mode as such. The band at 1419 cm^{-1} has been previously assigned to methylene scissoring next to a S-Au bond (δ_S).[95] Peanasky et al. observed a peak at 1416 cm^{-1} in a RAIR spectrum of a 10-undecene-1-thiol SAM, and the authors suggested

that this band results from the overlap of the methylene scissoring mode of the terminal $=CH_2$, $\delta(=CH_2)$, with the δ_s mode.[112] Because peaks at 1419 cm^{-1} have been previously observed in fully saturated alkanethiolates on gold surfaces,[95] we assign the peak at 1419 cm^{-1} to a mode associated with methylene scissoring next to a S-Au bond (δ_S).

Table 4.1 RAIR band positions and assignments for SAMs made from 9-decene-1-thiol, 10-undecene-1-thiol, 14-pentadecene-1-thiol, and 17-octadecene-1-thiol

Wavenumber (cm^{-1})				
10C C=C	11C C=C	15C C=C	18C C=C	Mode
3084	3085	3085	3084	$\nu_a(=CH_2)$
3005	3003	3005	3009	$\nu(H_2C=C-H)$
2985	2983	2984	2984	$\nu_s(=CH_2)$
2924	2921	2920	2920	$\nu_a(CH_2)$
2851	2851	2851	2851	$\nu_s(CH_2)$
~1828	~1832	~1825	~1828	$\omega(=CH_2)$ overtone
1643	1644	1644	1644	$\nu(C=C)$
A	a	1470	1470	$\delta(CH_2)$
A	a	1437	1440	$\delta_D(CH_2)$
A	a	1419	1419	$\delta_S(CH_2)$
995	995	993	993	C=C oop def
916	913	915	914	$\omega(=CH_2)$

[a] No signal observed above the noise

Seven of the bands in Figure 4.2 arise from the terminal vinyl group.[117,120] The peaks at 3084 and 2984 cm^{-1} can be assigned to the asymmetric , $\nu_a(=CH_2)$, and symmetric, $\nu_s(=CH_2)$, stretches of the $=CH_2$ group, respectively. The mode at 3009 cm^{-1} we assign to the β C-H stretch, $\nu(H_2C=C-H)$. A large band associated with the C=C stretch, $\nu(C=C)$, is found at 1644 cm^{-1}. We attribute the small band at 993 cm^{-1} to the out-of-plane (oop) deformation of the C=C group, and the larger band at 914 cm^{-1} to the out-of-plane

deformation of the $=CH_2$ group. An overtone of the out-of-plane deformation of the $=CH_2$ group is also observed at ~1828 cm^{-1}.[112]

Two negative features also appear in the RAIR spectrum of the 18C vinyl terminated monolayer. The negative features at ~2965 and ~1381 cm^{-1} appear in the IR spectra of each vinyl SAM studied in this work. The negative features are most likely optical effects, defined as those features in the RAIR spectrum that are absent in the dielectric function.[121] Numerous optical phenomena are observed in RAIRS such as baseline shifts, band shifts, band distortions, waveguide effects, and surface polaritons.[121] The optical effects depend on the angle of incidence, the film thickness, and refractive indices.[121,122] The observed negative feature at 1381 cm^{-1} is possibly an optical effect from an overlayer on the gold background. Many metal surfaces contain an oxide overlayer that show Reststrahlen bands in the mid-IR region.[121] The Reststrahlen band introduces optical effects, such as the Berreman effect.[121,123] Negative features have been previously observed in thin layers of metal oxides in RAIRS due to this effect.[122-126] Sharp negative features in the RAIR spectrum of vinyl terminated SAMs have also been previously reported and were attributed to polarizer artifacts.[112,127]

The reflection absorption infrared spectra of the 10, 11, 15, and 18C vinyl-terminated SAMs are shown in Figure 4.3, and have been offset along the ordinate axis for clarity. The positions of all the bands for all the vinyl terminated monolayers investigated are shown in Table 4.1. All seven of the bands arising from the terminal vinyl group that were observed in the 18C C=C SAM (Figure 4.2) are also observable in the 10, 11, and 15C C=C SAMs, see Figure 4.3. The relative intensities of the $\nu_s(=CH_2)$, $\nu(H_2C=C-H)$, $\nu(C=C)$, C=C oop def, and $\omega(=CH_2)$ are all vary similar for all of the vinyl terminated

monolayers, but the intensity of the $\nu_a(=CH_2)$ is dependent upon the odd or even number of carbons within the hydrocarbon chain and will be discussed later. All three of the modes associated with methylene C-H scissoring are not observed above the noise in the two shortest chains, 10 and 11C C=C SAMs; however, all three modes are observed in the two longest chains, 15 and 18C C=C SAMs. This observation is most likely a consequence of the decreased number of methylene units in the shorter chain SAMs, as well as, the increased "noise" from atmospheric gases (water) in the 10 and 11C C=C SAM spectra. The atmospheric water does not enter the ultrahigh vacuum system, but is most likely entering the IR detector box. The negative features in the 18C C=C SAM spectrum are also observed in all four vinyl terminated SAMs spectra, see Figure 4.3. We note that the negative feature at ~1381 cm^{-1} is significantly larger in the two shorter chain SAMs, and might be dependent upon the film's thickness affecting the index of refraction of the substrate.[126]

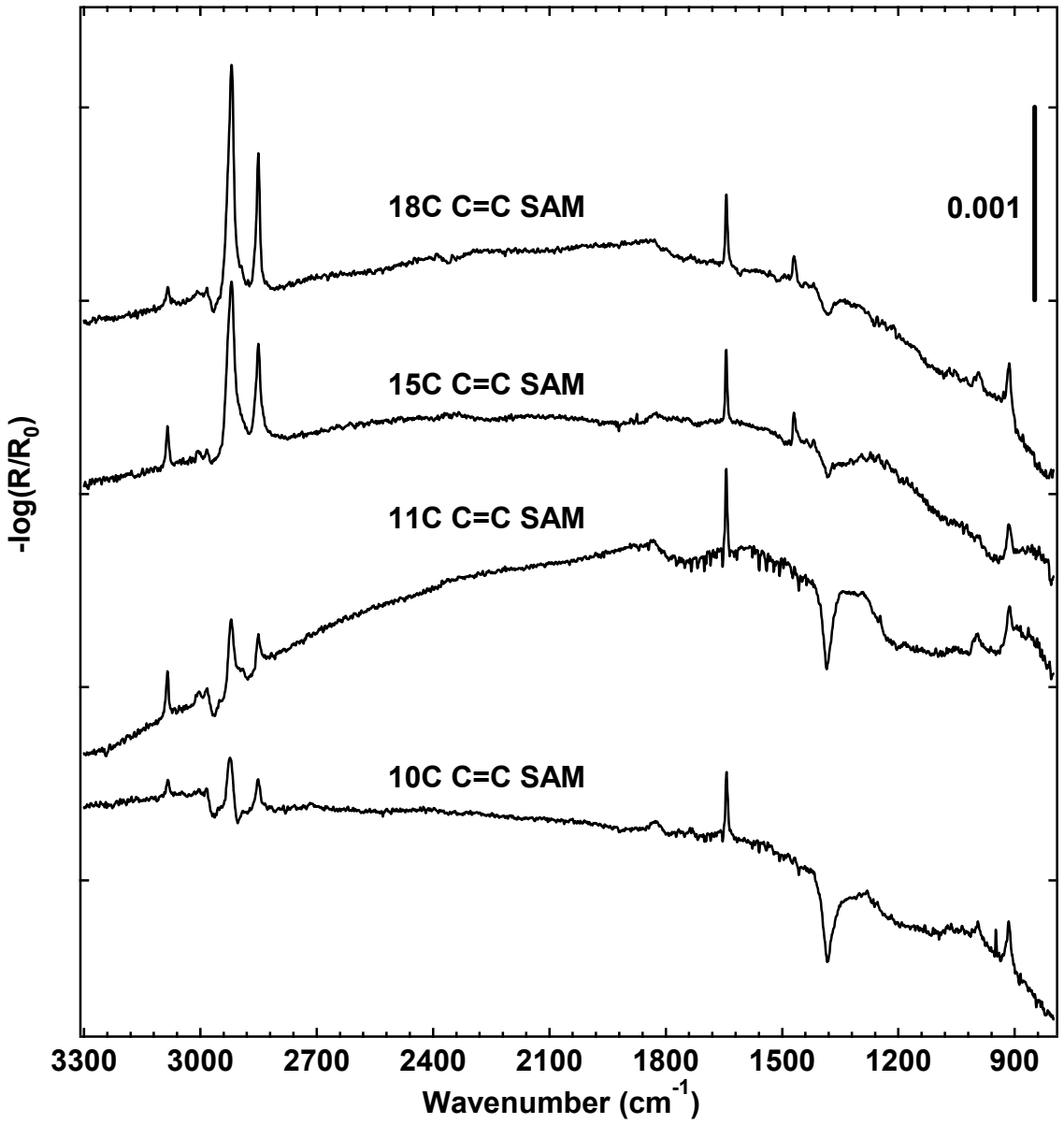

Figure 4.3. Reflection-absorption infrared spectra of 10,11,15, and 18C C=C SAMs. Spectra offset for clarity.

Although we have not performed a quantitative orientation analysis on the vinyl terminated SAMs,[68,98,117,128] relative infrared peak intensities enable one to make some qualitative estimates about the monolayers orientation.[112] In RAIRS, only molecules on the surface that have a transition dipole moment that is aligned normal to the surface will

be observable. Therefore, the RAIR intensities allow one to determine how a molecule is oriented relative to the surface normal.

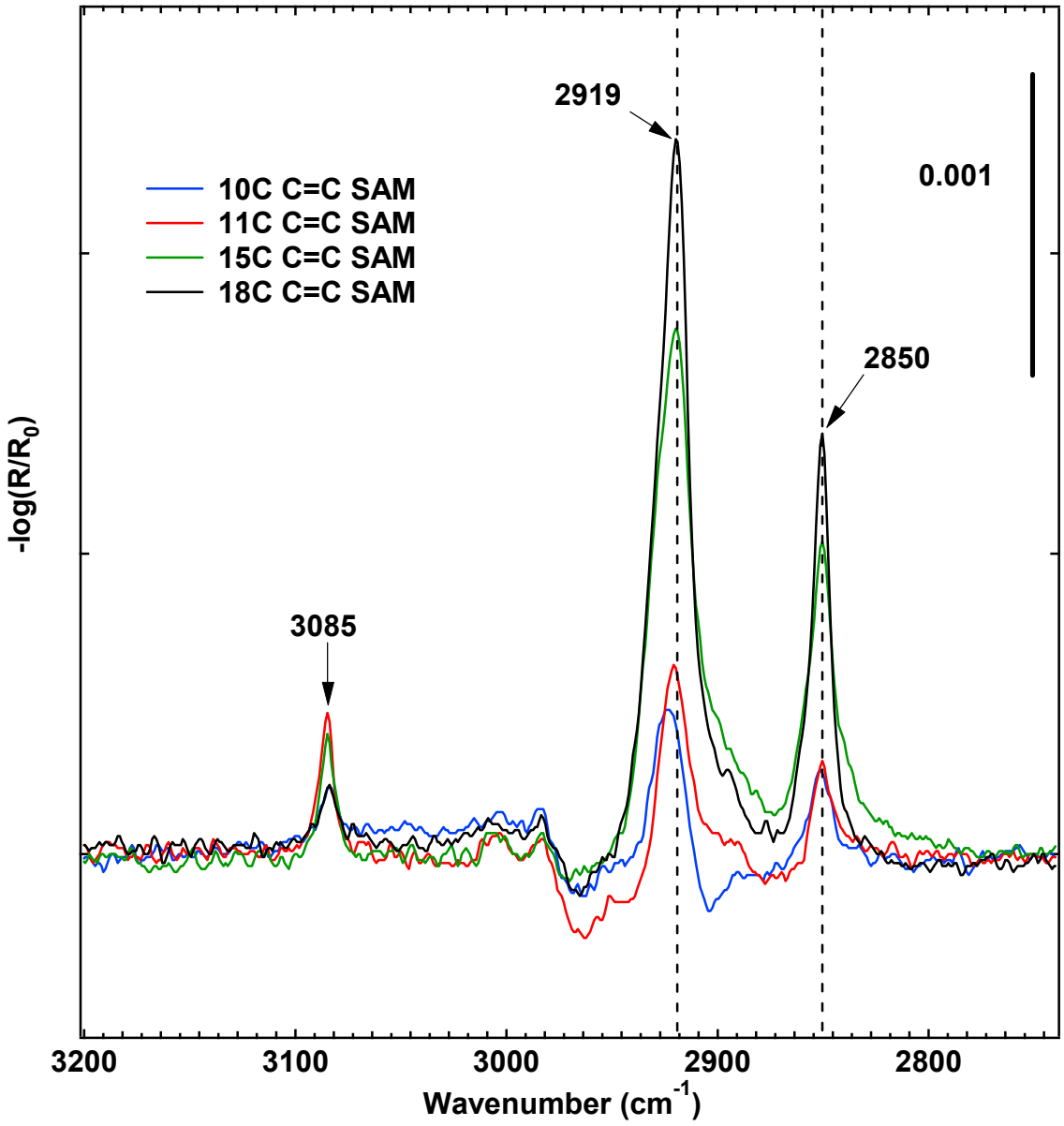

Figure 4.4. Reflection-absorption infrared spectra of 10,11,15, and 18C C=C SAMs in the hydrocarbon region of the spectrum.

The hydrocarbon region of the RAIR spectra for the 10, 11, 15, and 18C C=C SAMs is shown in Figure 4.4. No offset is included in the ordinate axis; therefore, all intensities

can be directly compared between each spectrum. Two interesting trends are observed. First, as the chain length of the vinyl terminated monolayer increases, the band from the $\nu_a(CH_2)$ stretch shifts towards lower wavenumbers, approaching 2919 cm^{-1} for the longest chain. Shifting of the band from the $\nu_a(CH_2)$ stretch toward lower wavenumbers indicates that the chains of the monolayers are becoming a more well-order system as the length increases.[99,100] The band from the $\nu_s(CH_2)$ stretch does not change upon increasing the chain length and is found at 2851 cm^{-1} for all vinyl terminated monolayers analyzed. Second, the peak assigned to the $\nu_a(=CH_2)$ stretch shows a dependence upon the odd or even total number of carbons within the hydrocarbon chain. When the total number of carbons in the chain is odd, the intensity of this band is nearly a factor of two greater compared to when the total number of carbons in the chain is even, see Figure 4.4. Because the intensities of both the $\nu_a(=CH_2)$ and $\nu(C=C)$ modes are significant in the RAIRS spectrum and the transition dipole moments of these stretches are orthogonal (see Figure 4.5), the H-C-H plane of the vinyl group must be tilted away from the surface normal.[112] Furthermore, because the $\nu(C=C)$ stretch shows no dependence upon the odd or even number of carbons within the chain, the H-C-H plane of the vinyl group cannot contain the C-C-C plane of the hydrocarbon backbone. This implies that there must be a rotation along the second to last C-C axis. The H-C-H plane of the vinyl group must be tilted away from the surface normal similar amounts for both the odd and even chain lengths since the $\nu(C=C)$ mode shows little dependence upon chain length.

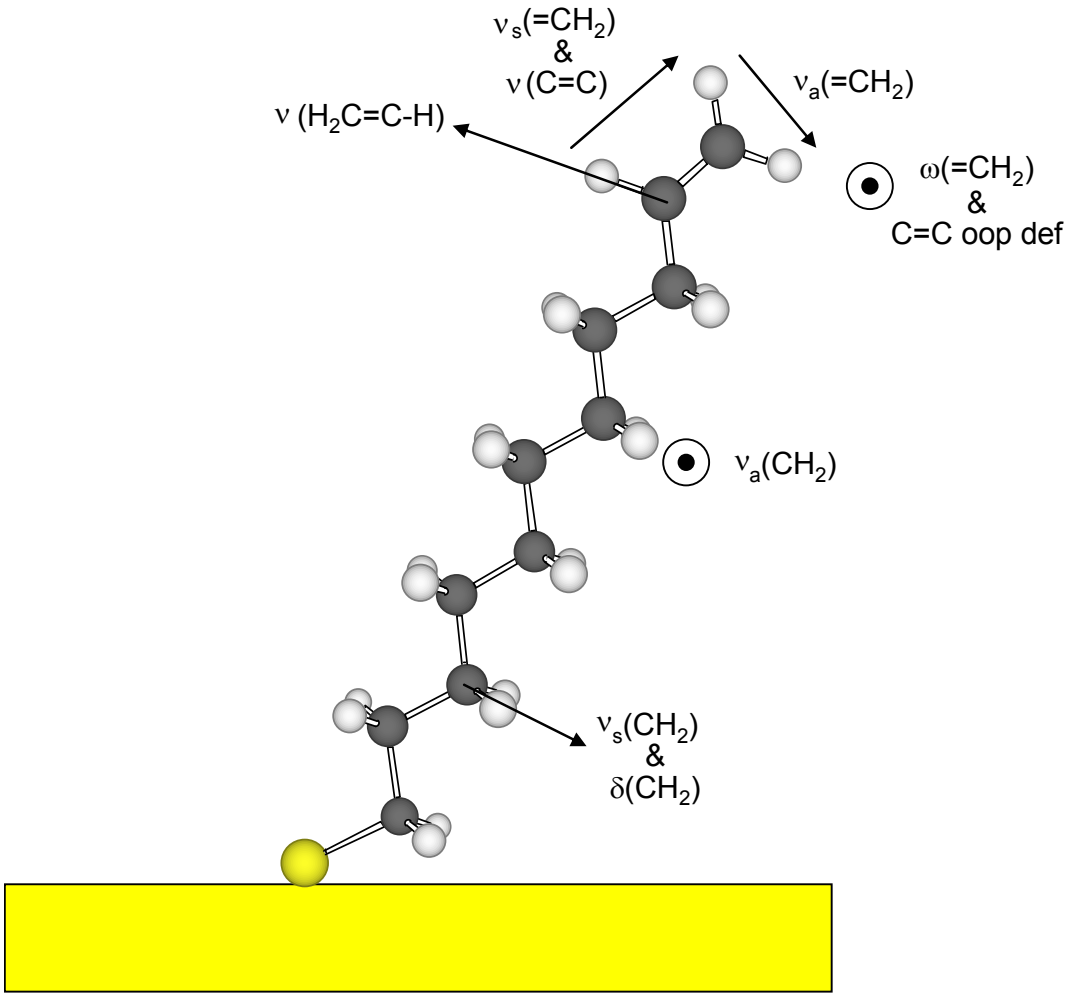

Figure 4.5. Schematic representation indicating the direction of the transition dipole moments for a vinyl terminated monolayer.

If we assume that the hydrocarbon backbone is tilted by an angle (α) ~30° away from the surface normal and that the chain is twisted by a rotation (β) ~49° (a fair assumption base on previous IR work on ω-substituted thiols),[97] the observations noted in Figure 4.4 are consistent with a model in which the vinyl group is rotated by an angle (γ) ~61° around the second to last C-C axis in the clockwise direction. A schematic representation of this model is shown in Figure 4.6. Vinyl terminated chains like the ones shown in Figure 4.6 would show no chain length dependence for the intensity of the band from the

ν(C=C) mode because the orientation is independent of the length of the chain, but would show a chain length dependence for the intensity of the band from the $\nu_a(=CH_2)$ mode. The transition dipole moment of the $\nu_a(=CH_2)$ stretch, for both chains, is shown in Figure 4.6. Notice the difference in the tilt of the transition dipole moments relative to the surface normal for the even versus odd chain lengths. In Figure 4.6, the vinyl group is coming out of the plane of the page for the odd chain length, and going into the plane of the page for the even chain length. This model is consistent with a model proposed by Peanasky et al. for an odd chain length vinyl terminated monolayers, 11C C=C SAMs.[112]

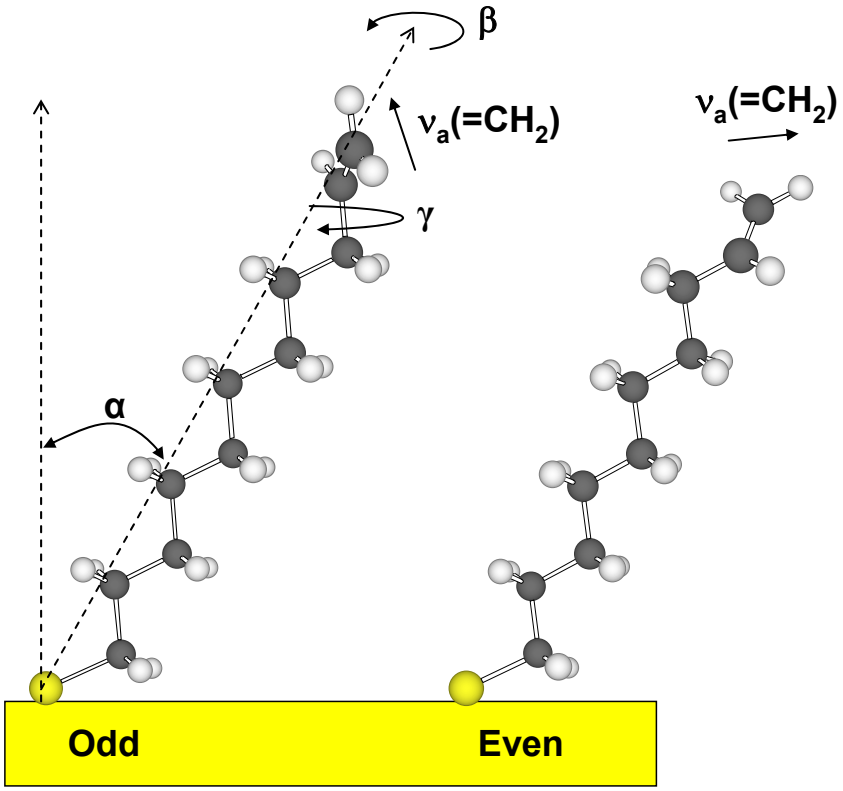

Figure 4.6. A schematic representation of an odd chain length and even chain length vinyl terminated thiolate absorbed to an Au surface, demonstrating the direction relative to the surface normal of the transition dipole moments of the $\nu_a(CH_2)$ stretch.

4.3.1.2 XPS

Further characterization of the vinyl terminated monolayers was performed with X-ray photoelectron spectroscopy (XPS). A typical survey spectrum of the 18C C=C SAM is shown in Figure 4.7. This spectrum is representative of all vinyl terminated monolayers that were analyzed. The primary feature in Figure 4.7 is the presence of signal from the C 1s photoelectron at 285 eV. Gold photoelectrons (4s, 4p, 4d, 4f, and 5p) from the substrate are also present in the spectrum. Nearly indistinguishable above the noise, at the resolution used for the survey spectrum, is a signal from the S(2p) photoelectrons at 162 eV. No other peaks or features due to contamination of the samples were observed. Information about the binding environments of the elements can be realized by further analysis at higher resolution. Representative high resolution spectra of the S(2p), C(1s) , and O(1s) regions of a 18C C=C SAM are shown in Figures 4.8–4.10. A high resolution XP spectrum was recorded for the Au 4f region (data not shown) and was used as a reference for the binding energy of all spectra reported. The Au 4f spectrum consisted of a well-resolved doublet (Au $4f_{(7/2,5/2)}$) at 83.8 and 87.4 eV.

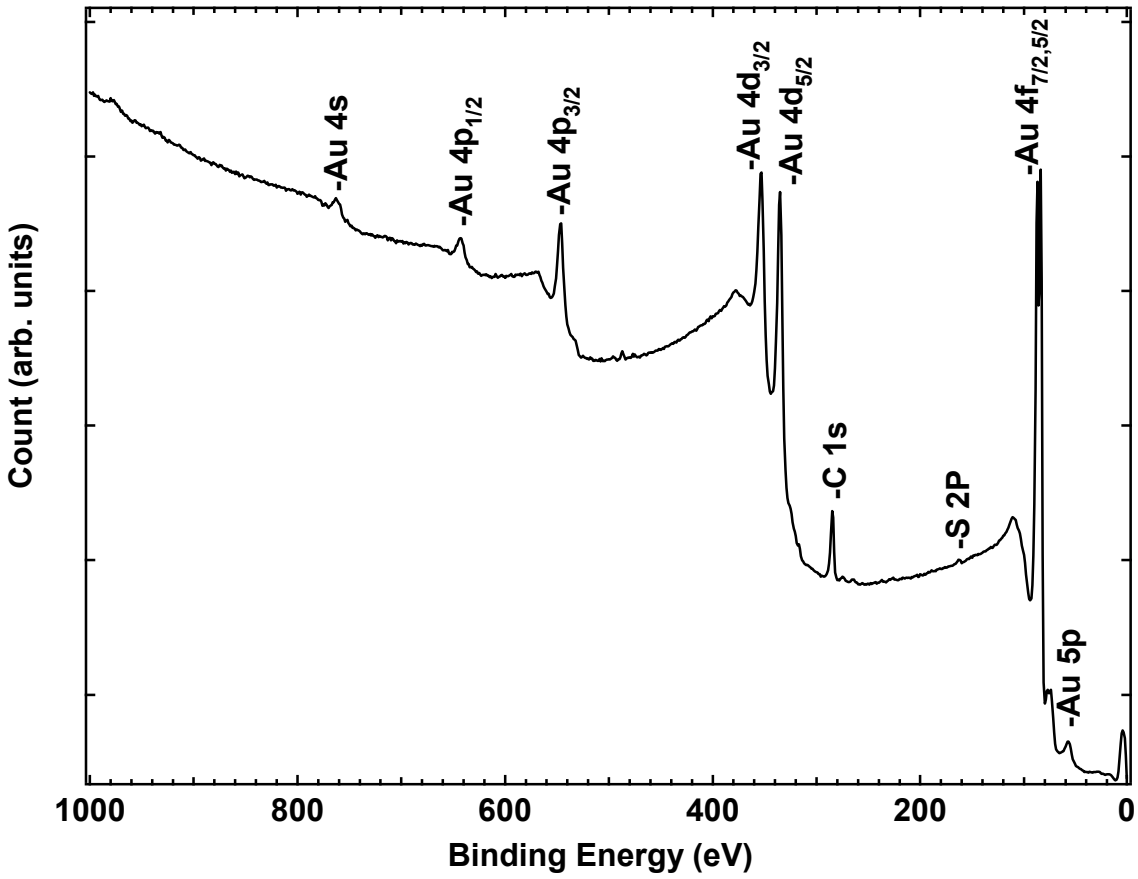

Figure 4.7. X-ray photoelectron survey spectrum of an 18C C=C SAM.

The S 2p region of the 18C C=C SAM, Figure 4.8, is well fit by a pair of spin-orbit doublets. Each doublet was fit with a fixed $2p_{3/2}/2p_{1/2}$ area ratio of 2:1 and a spin-orbit splitting of 1.2 eV.[92,129] In Figure 4.8, the raw XPS data (solid circles) has been fitted to a composite (thick solid line) of two S 2p ($2p_{3/2}/2p_{1/2}$) Gaussian peaks with S $2p_{3/2}$ peaks positioned at 162.0 eV (thin solid line) and 164.4 eV (dashed line). The full-width at half-maximum was set equal for all peaks and was a fitted parameter. The S 2p doublet with the S $2p_{3/2}$ peak located at 162.0 eV is consistent with sulfur atoms bound to the gold substrate as thiolate species.[92,101,103,130,131] Additional intensity above 163 eV required a second spin-orbit doublet at 164.4 eV, see Figure 4.8. Previous researchers

using polymer monolayers bound to gold substrates with alkyl disulfide side chains have shown S $2p_{3/2}$ binding energies of 164 eV for unbound disulfides.[132,133] In a study by Castner et al., researchers detected the presence of two sulfur species in XPS studies of various length thiols and disulfides on Au substrates.[101] The researchers assigned the two species to bound thiolates (162 eV) and unbound thiols or disulfides (163.5 to 164 eV). Castner et al. found that the use of a poor solvent for thiol absorption solutions and the lack of a rinsing step both resulted in unbound thiols present at the surface of the monolayers. X-ray induced damage from low-energy secondary electrons has also been shown to transform native thiolate head groups of alkanethiol SAM into new irradiation induced sulfur species,[92,103,134] but the reported binding energies of the irradiation induced sulfur species are all less then 163.3 eV. Due to the higher binding energy of the second S 2p doublet (>164 eV) in Figure 4.8, we assign the S 2p doublet at 164.4 eV (S $2p_{3/2}$ position) to unbound thiols that are present at the surface of the substrate. The presence of unbound thiols may prove that hexanes is a poor choice of solvents for assembling and rinsing 18C C=C SAMs. When the vinyl terminated monolayers are removed from the thiol solution after 48 hours of incubation, the monolayers are "rinsed" by dipping into a solution of fresh hexanes. A procedure that involves rinsing the monolayers in a stream of fresh hexanes or another solvent (isooctane or hexadecene) from a squirt bottle may remove the unbound thiols.[101]

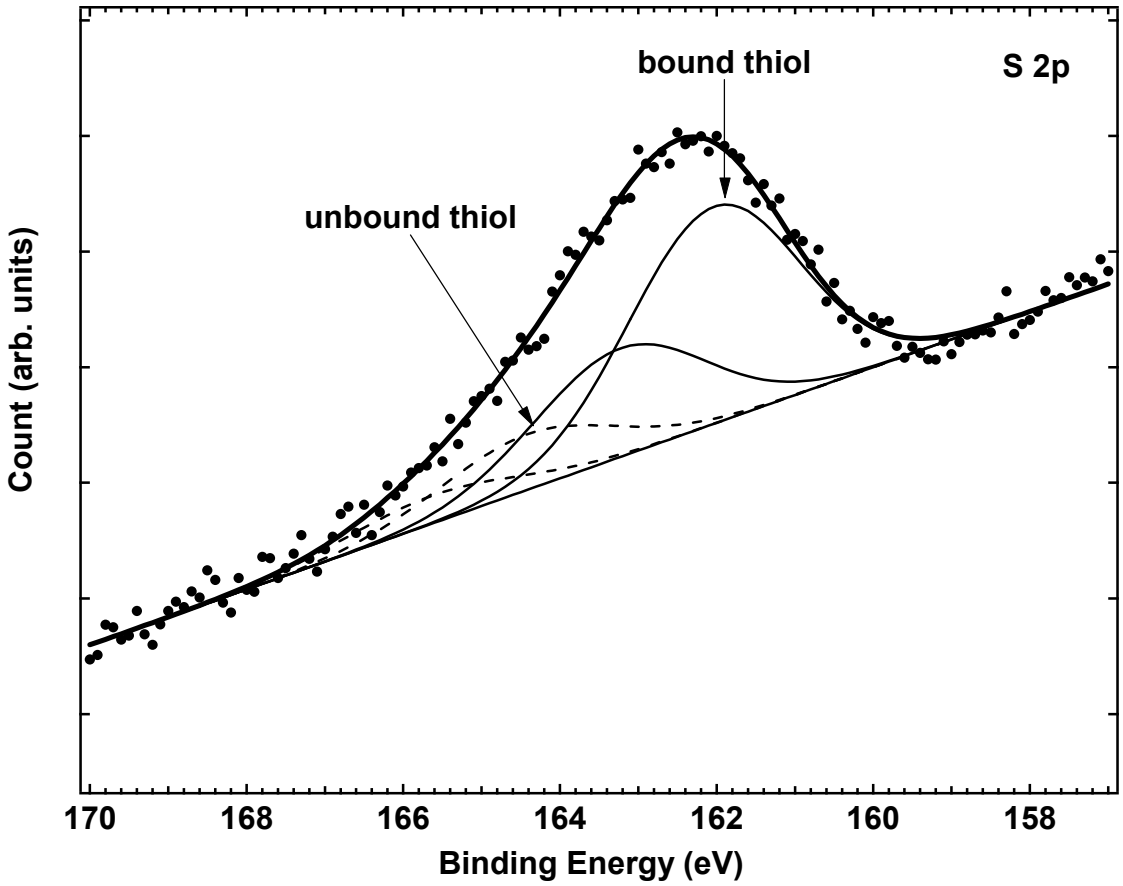

Figure 4.8. High-resolution X-ray photoelectron spectrum of the S(2p) region for a 18C C=C SAM. The raw XPS data (solid circles) have been fitted to a composite (thick solid line) of two spin-orbit doublets S(2p) Gaussian peaks and a linear baseline.

A high resolution X-ray photoelectron spectrum of the C 1s region of an 18C C=C SAM is shown in Figure 4.9. The raw data (solid circles) is reasonably fit with two Gaussian peaks (dashed lines). The composite of the baseline (thin solid line) and Gaussian peaks is shown as a thick solid line. The largest Gaussian peak is centered at 284.7 eV, and this binding energy is consistent with methylene (284.9 eV) and terminal vinyl (284.4 eV) carbon atoms.[134-136] A second Gaussian peak is need for a reasonable fit of the C 1s XP data, which is centered at 287.5 eV. Previous researchers analyzing monolayers with XPS have assigned C 1s peaks at 286-287.1 eV to carbon atoms bound

to sulfur atoms (C-S).[130,137] We suggest that the Gaussian peak at 287.5 eV in Figure 4.9 could be reasonably assigned to the C atoms bound to the thiolates of the monolayer, but may also appear from surface contamination of C-O or C=O species (contamination discussed below).[97,102,138]

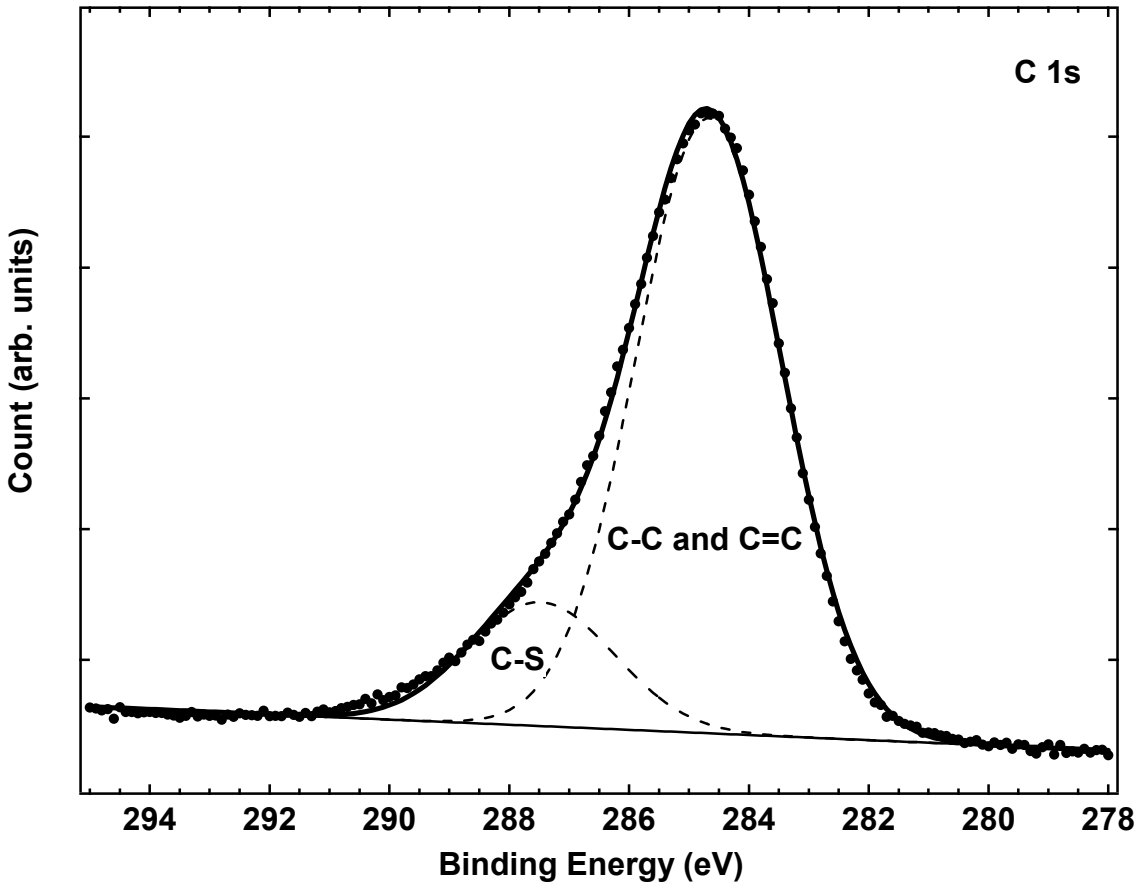

Figure 4.9. High-resolution X-ray photoelectron spectrum of the C(1s) region for a 18C C=C SAM. The raw XPS data (solid circles) have been fitted to a composite (thick solid line) of two C(1s) Gaussian peaks (dashed lines) and a linear baseline (thin solid line).

For a thorough characterization of the vinyl terminated monolayers, a high resolution spectrum of the O 1s region of the 18C C=C SAM was recorded and is shown in Figure 4.10. While the vinyl terminated monolayers should show no signal above the noise for O 1s photoelectrons, we note a small signal (solid circles) that is fit with the

sum of a linear baseline (thin solid line) and a single Gaussian peak (thick solid line) positioned at 532.4 eV. This signal is relatively small and is probably caused by the presence of a surface contamination either from air exposure or some adventitious impurity in the thiol solution.

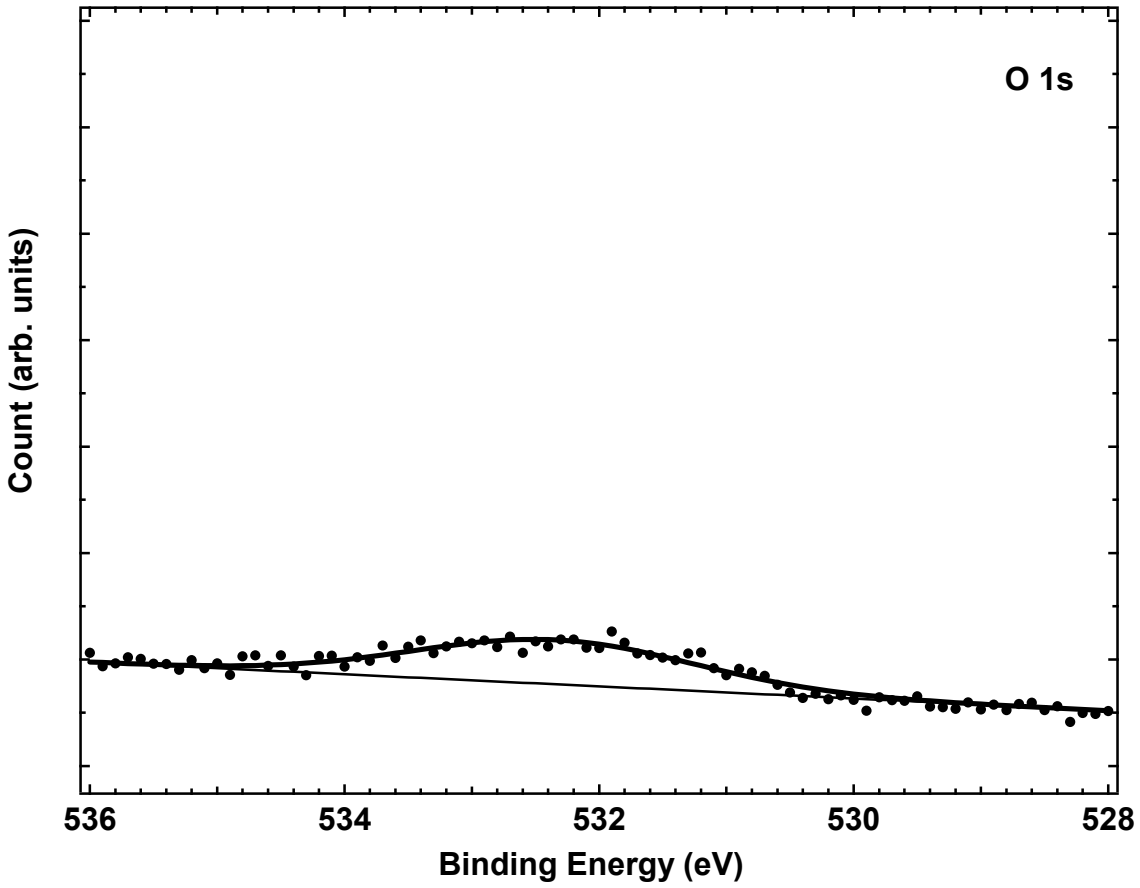

Figure 4.10. High-resolution X-ray photoelectron spectrum of the O(1s) region for a 18C C=C SAM. The raw XPS data (solid circles) have been fitted to a composite (thick solid line) of a O(1s) Gaussian peak and a linear baseline (thin solid line). The small signal from oxygen is most likly due to the presence of a surface contamination (see text for details).

4.3.2 Ozone Exposure

4.3.2.1 RAIRS

We monitored the oxidation of the vinyl terminated SAMs using RAIRS. A subset of the RAIR difference spectra of an 18C C=C SAM during ozone exposure is shown in Figure 4.11. The background for the spectra in Figure 4.11 is the absorbance spectrum of the monolayer before exposure to ozone. The bottom spectrum in Figure 4.11 is the monolayer before exposure to ozone. For all other spectra from the bottom toward the top of the graph, exposure of the monolayer to ozone increased by ~1890 L per spectrum with the uppermost spectrum receiving a total of ~6.2×10^4 L of ozone. The noise in each spectrum at ~1100 cm^{-1} is caused by instruments attached to the FTIR spectrometer and does not seem to interfere with the analysis of the oxidation of the 18C C=C SAM.

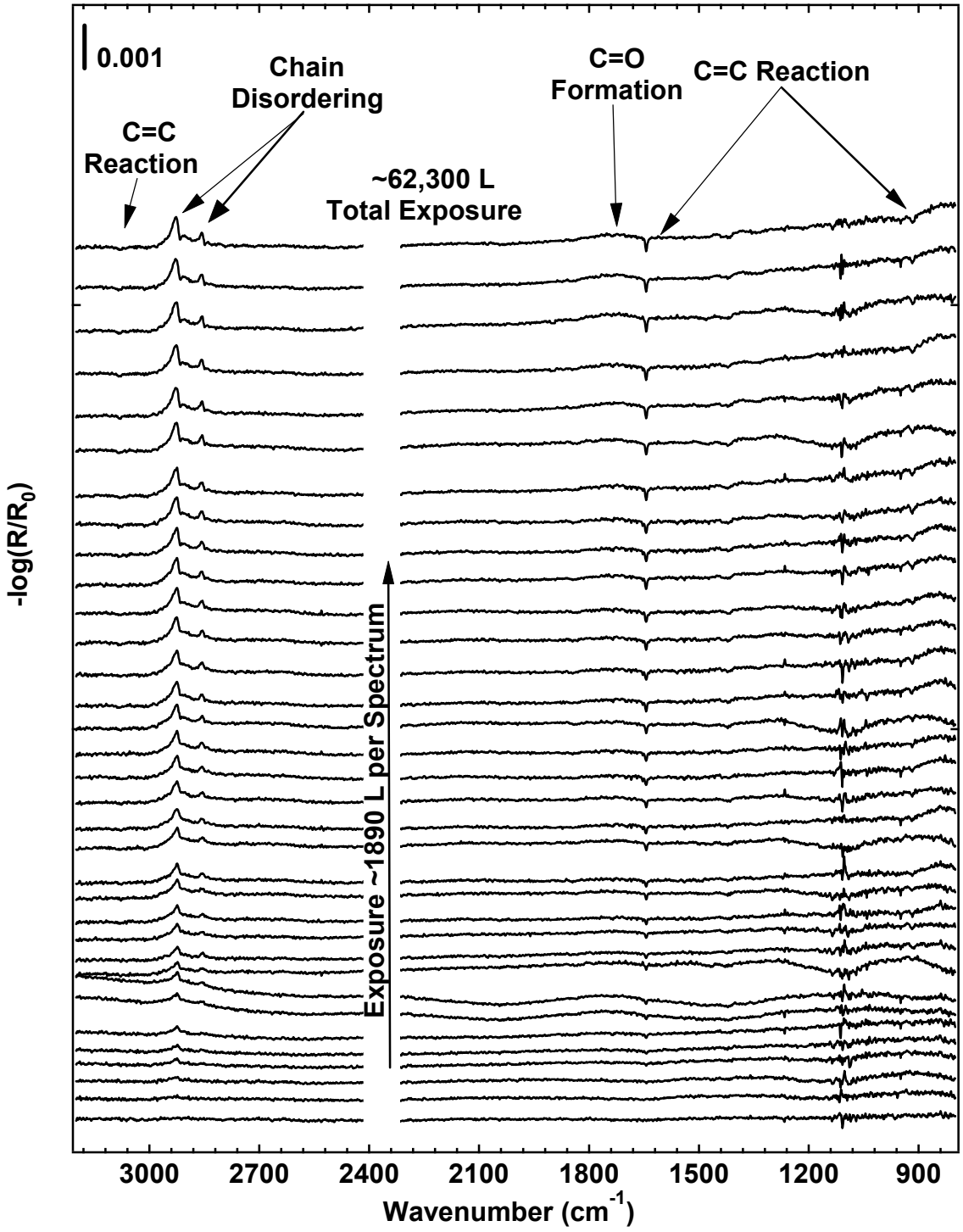

Figure 4.11. Reflection-absorption infrared difference spectra of an 18C C=C SAM during exposure to pure ozone. The bottom spectrum is the monolayer with no exposure to ozone, and the exposure increases ~1890 L per spectrum from bottom to top with the upper-most spectrum receiving a total dose of ~62,300 L of ozone.

The first observable changes in the RAIR spectrum of the 18C C=C SAM upon exposure to ozone appear after ~3780 L, see the third spectrum from the bottom in Figure 4.11. The most significant change noticed is an increase in signal in the hydrocarbon region of the spectrum. The increase is caused by the asymmetric and symmetric methylene bands broadening and shifting to higher wavenumbers upon exposure to ozone. This is a consequence of the surface orientation changing such that more transition dipole moments of the methylene stretches align in directions that can be observed in RAIRS. Because the position of the peaks from the $\nu_a(CH_2)$ and $\nu_s(CH_2)$ stretches has been shown to be a sensitive indicator of the ordering of the alkyl chain,[79,94-98] the shifting to higher wavenumbers of both the asymmetric and symmetric methylene bands is indicative of disordering within the monolayer upon exposure to ozone. In a polyethylene crystal,[99,100] the $\nu_a(CH_2)$ and $\nu_s(CH_2)$ stretches are found at 2920 and 2850 cm^{-1}, respectively; whereas, in the liquid phase, the values shift to 2928 and 2856 cm^{-1}.

At the same time that the bands of the $\nu_a(CH_2)$ and $\nu_s(CH_2)$ stretches broaden and shift to higher wavenumbers, negative peaks emerge at ~3081, 1644, and ~916 cm^{-1}, see Figure 4.11. Upon continuous exposure to ozone, these bands continue to decrease in conjunction with the broadening and shifting of the bands of the $\nu_a(CH_2)$ and $\nu_s(CH_2)$ stretches. The negative features that appear at ~3081, 1644, and ~916 cm^{-1} are indicative of a reaction occurring with the terminal C=C moiety removing this species from the monolayer.

The only other change observed in the spectra of Figure 4.11 is the formation of a weak signal from a broad band centered at ~1724 cm^{-1}, see the uppermost traces in

Figure 4.11. Signal at 1724 cm^{-1} most likely indicates that the reaction of ozone with vinyl terminated monolayers forms a species containing a carbonyl or carboxylic acid.

The changes detect in the spectra of Figure 4.11 are also displayed in the spectra of Figure 4.12, which shows the RAIR spectra of an 18C C=C SAM before and after exposure to ozone. In contrast to the spectra in Figure 4.11, a clean gold background was used for each spectrum shown in Figure 4.12. The bottom spectrum is that of the monolayer before exposure to ozone, while the top spectrum is that of the monolayer after exposure to ~62,300 L of ozone. The broadening of the band from the $\nu_a(CH_2)$ and $\nu_s(CH_2)$ stretches is most noticeable when examining the before and after exposure spectra of the monolayer in Figure 4.12. The spectra in Figure 4.12 have been offset along the ordinate axis for clarity. Also observed in Figure 4.12 is a decrease in signal from the $\nu_a(=CH_2)$ stretch at 3085 cm^{-1}, the $\nu(C=C)$ stretch at 1644 cm^{-1}, and the $\omega(=CH_2)$ deformation at 914 cm^{-1}, all indicating that a reaction is occurring at the double bond. A new broad feature is also formed at ~1724 cm^{-1} in the upper trace in Figure 4.12. The spectrum of the monolayer before exposure to ozone also shows a larger negative feature at 1381 cm^{-1} than the spectrum after exposure to ozone. This minor effect could be caused by a change in the refractive index of the sample or the formation of a gold oxide overlayer, see section 4.3.1.1.

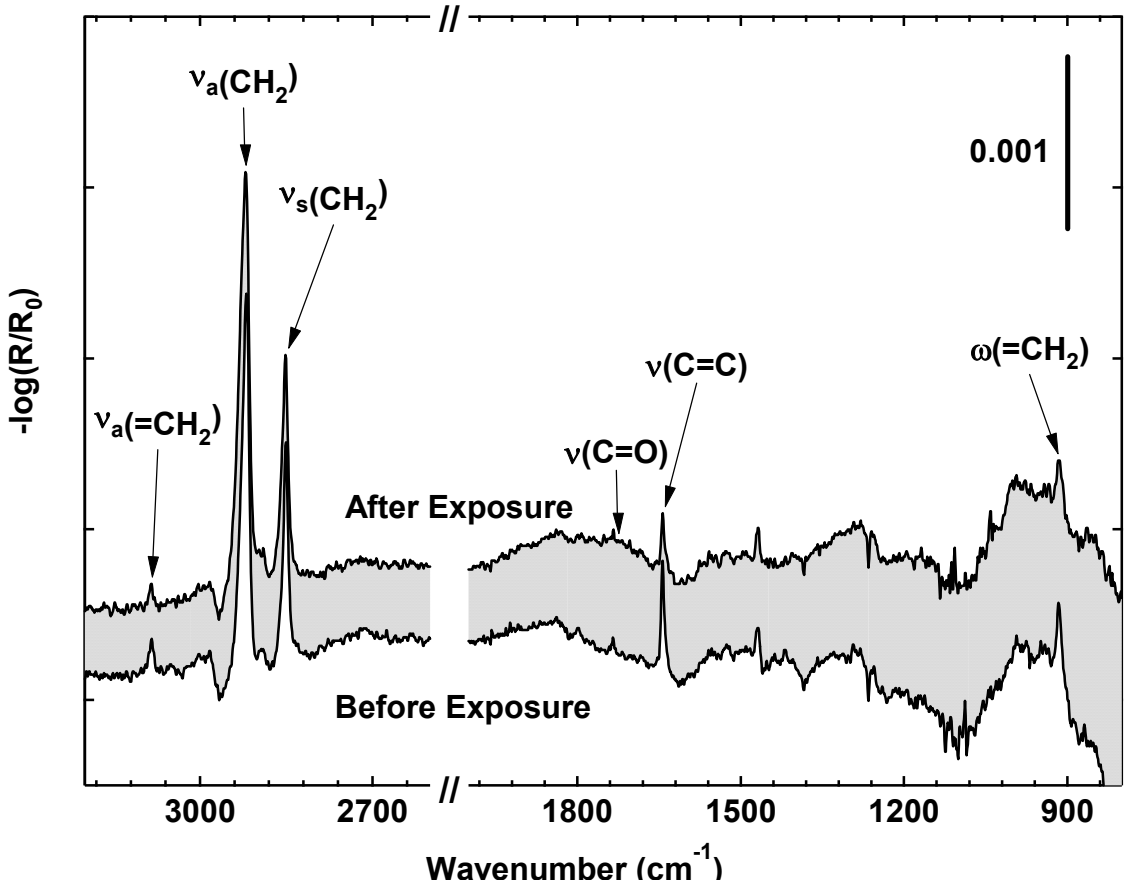

Figure 4.12. Reflection-absorption infrared spectra of an 18C C=C SAM before and after exposure to ozone. The bottom spectrum is that of the monolayer before exposure to ozone and the top spectrum is the monolayer after exposure to 62,300 L of ozone.

To learn about the kinetics of the heterogeneous oxidation of vinyl terminated self-assembled monolayers, we analyzed the data by plotting the position of the band from the $\nu_a(CH_2)$ stretch verses exposure time to ozone in Figure 4.13. Inspection of Figure 4.13 reveals that the position of the band from the $\nu_a(CH_2)$ stretch begins at ~2921 cm^{-1} and continues to shift to higher wavenumbers during exposure to ozone. The position of the band for the $\nu_a(CH_2)$ stretch reaches a value that is greater than 2926 cm^{-1}. The shifting to higher wavenumbers of the band from the $\nu_a(CH_2)$ is indicative of a transition from a highly-ordered crystalline environment to a disordered liquid-like state.[99,100]

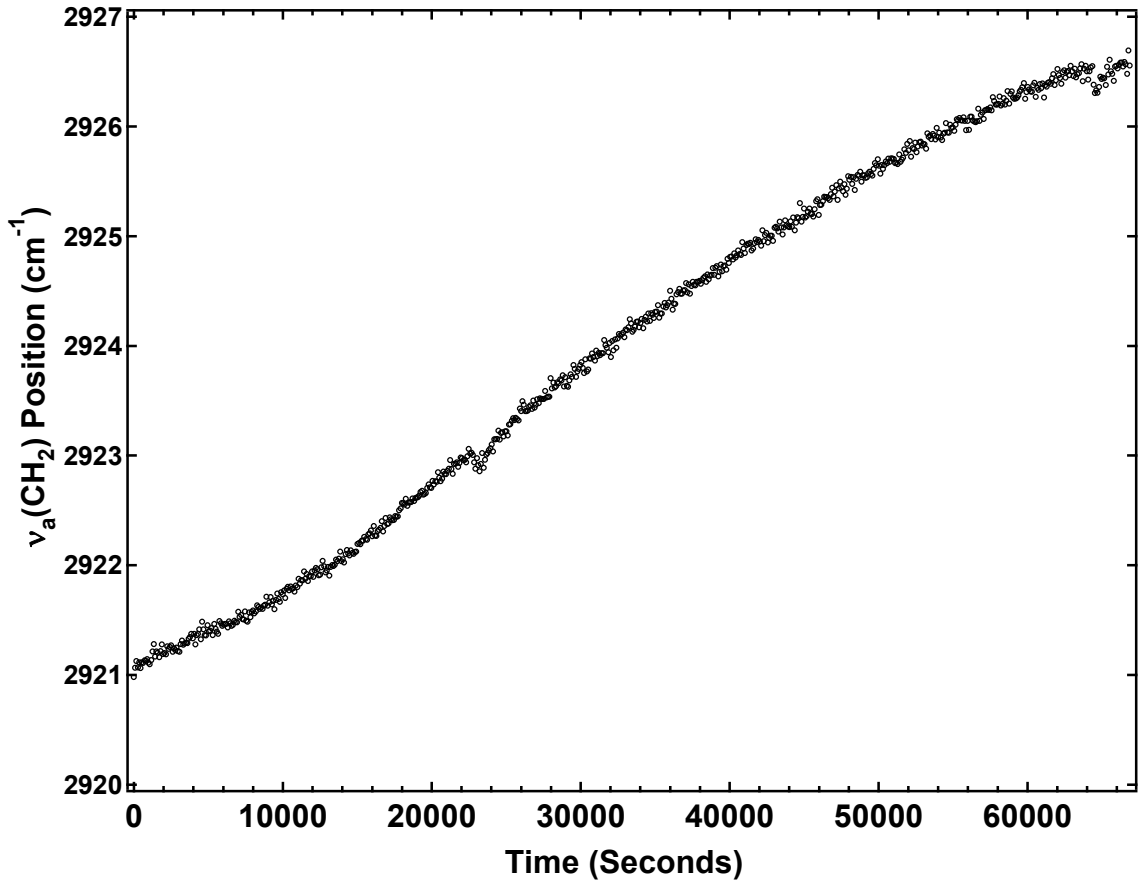

Figure 4.13. A graph of the position of the $\nu_a(CH_2)$ band versus the time of exposure to ozone.

To probe the kinetics of the disordering event, we graphed the change in the integrated area of the band from the asymmetric methylene stretch of an 18C C=C SAM during exposure to ozone in Figure 4.14 (open circles). As observed in Figure 4.14, the change in area of the peak from the $\nu_a(CH_2)$ stretch (ΔA) increase exponentially during exposure to ozone. Assuming that the disordering event, which causes the increase in area of the band from the $\nu_a(CH_2)$ stretch, follows first-order kinetics, we can fit a single exponential of the form shown in Equation 4.1 to the ΔA vs. time traces, see solid red line in Figure 4.14.

$$\Delta A(t) = A_0(1 - e^{(-k_{obs}t)}) \qquad (4.1)$$

In Equation 4.1, A_0 is the initial area of the band from the $\nu_a(CH_2)$ stretch; k_{obs} is an observed rate constant for the disordering event occurring in the monolayer upon oxidation; and t is the time of exposure to ozone. Equation 4.1 was fitted to the data by the non-linear least-squared fitting procedure described in Chapter 3. Because active surface sites are consumed during the reaction, only early reaction times were fitted, and an observed rate constant of 3.1×10^{-5} s^{-1} was obtained.

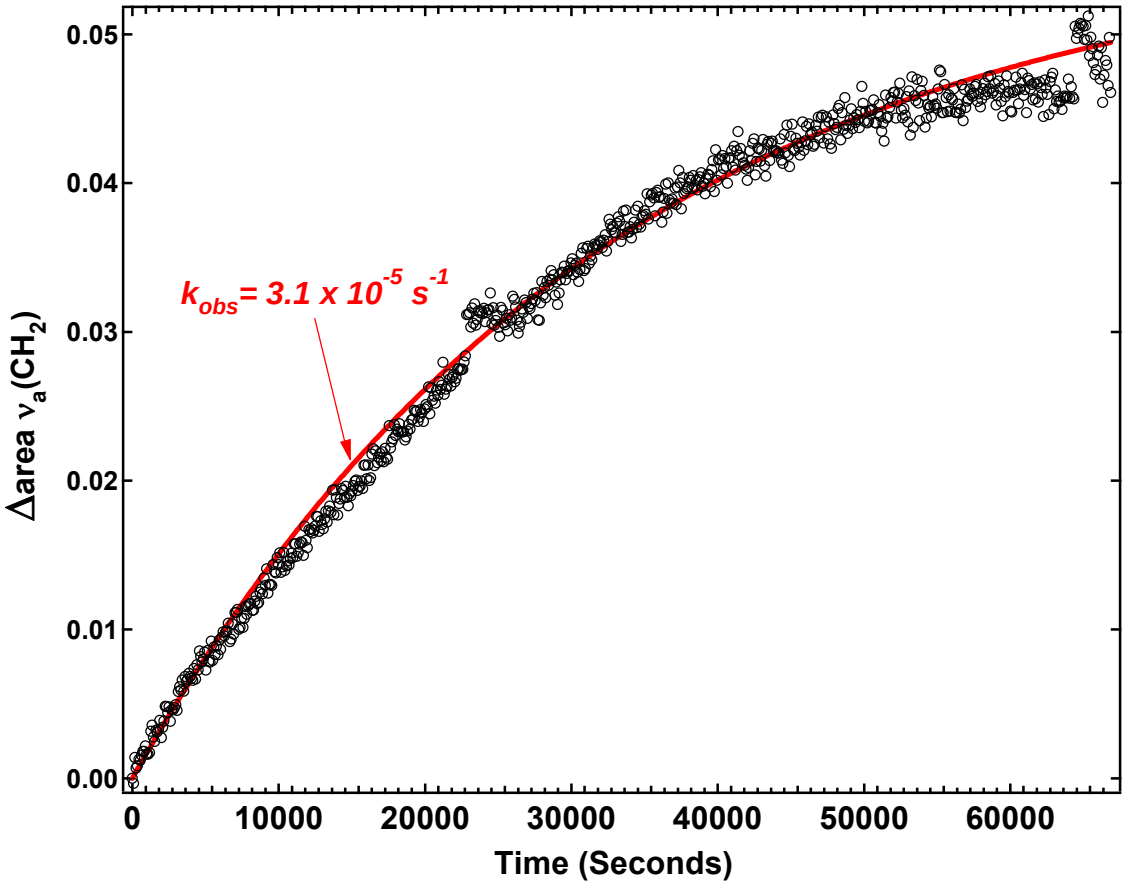

Figure 4.14. A graph of the Δarea of the $\nu_a(CH_2)$ band (open circles) versus the time of exposure to ozone. The solid red line has been fitted to the data to determine observed rate constants (see text for details).

Two interesting observations are noted about the change in area of the peak from the $\nu_a(CH_2)$ stretch. First, the observed rate constant is an order of magnitude lower than the observed rate constant of the oxidation of an 18C CH_3 SAM (6.1×10^{-4} s^{-1}), see

Chapter 3. This difference, in observed rate constants, implies that the reactions proceed via two different mechanisms. Second, the area of the peak from the $\nu_a(CH_2)$ stretch exponentially increases and reaches a maximum, but never decreases during exposure to ozone. This continual increase of area is significantly different from the changes observed in the oxidation of methyl terminated SAMs, see Chapter 3 (Figure 3.16). The area of the band from the $\nu_a(CH_2)$ stretch of CH_3 SAMs initially increases, reaches a maximum, and then decreases, approaching zero. In fact, the CH_3 SAMs, upon oxidation, lose most of the hydrocarbon chains as indicated by RAIRS and XPS data, see Chapter 3. In contrast, the vinyl terminated monolayers do not seem to have a significant loss of the methylene units during oxidation.

We note that an exponential function does not fit the data perfectly. This may imply that the reaction causing the change in area of the asymmetric methylene stretch is not a first-order process. There may be competing reaction channels. For example, radicals from a Criegee intermediate may be reacting with carbon-carbon double bonds instead of just the reactions of the double bonds with ozone.

To further explore the kinetics of the reaction of ozone with an 18C vinyl terminated monolayer, we graphed the intensity of the band from the ν(C=C) stretch at 1644 cm^{-1} vs. exposure time in Figure 4.15. Because the position of this band does not shift during oxidation (data not shown), the change in intensity of the band is most likely proportional to the change in concentration of the C=C bonds. The intensity of the band from the ν(C=C) stretch decreases exponentially during exposure to ozone. The decrease in intensity of the band from the ν(C=C) stretch indicates that a reaction is consuming the carbon-carbon double bond. If we assume that the reaction consuming the C=C bonds

follows pseudo-first-order kinetics, we can model the reaction with an equation of the functional form shown in Equation 4.2:

$$I(t) = \mathrm{I}_0 e^{(-k_{obs}t)} \tag{4.2}$$

Here, I(t) is the intensity of the band from the ν(C=C) stretch at any time, and I_0 is the initial intensity of the same band. k_{obs} is the observed rate constant for the consumption of the C=C moiety, and t is the time of exposure to ozone in seconds. As stated earlier in Chapter 4, the flux of ozone molecules was ~1.7×10^{15} molecules s^{-1} cm^{-2} during the reaction. Only the initial exposure times were considered when fitting Equation 4.2 to the data. The solid red line in Figure 4.15 is the non-linear least-squares fit to the data with k_{obs} as the only optimized parameter. For this particular data set, the fit yields an observe rate constant of 3.1×10^{-5} s^{-1}.

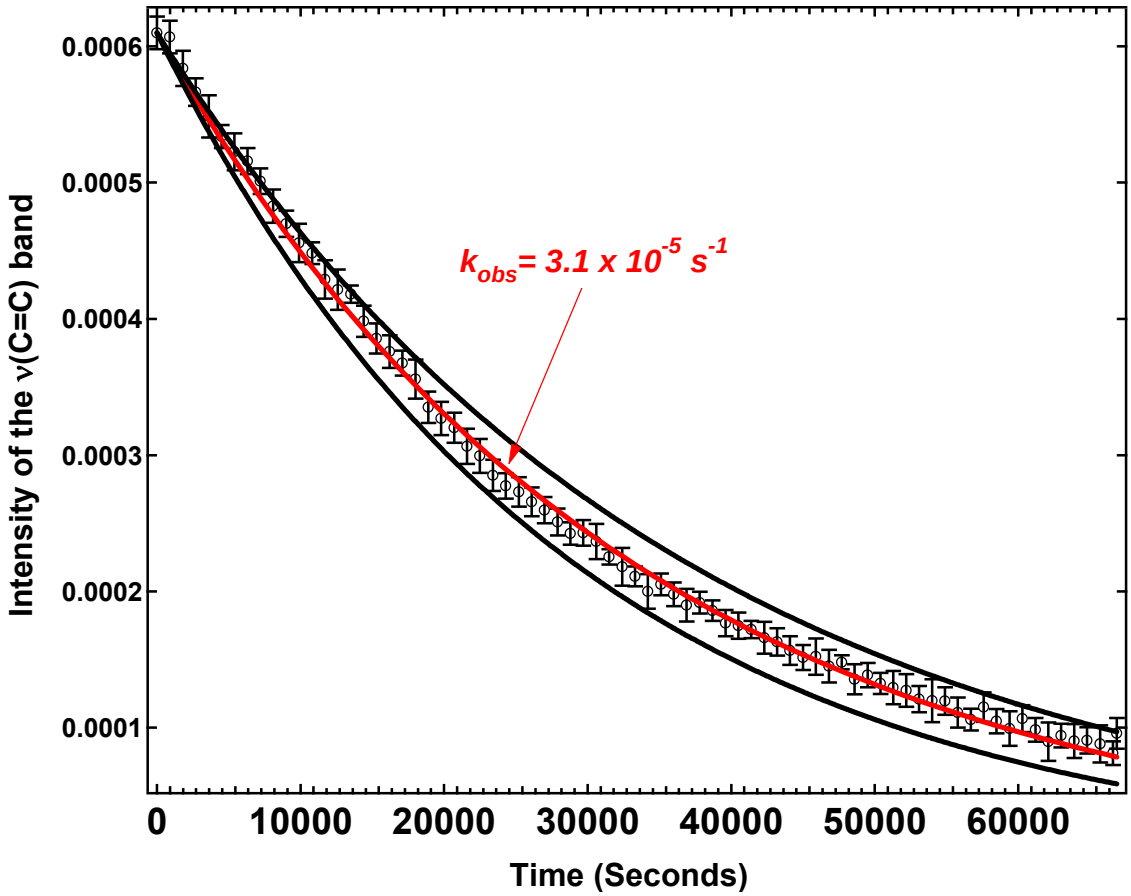

Figure 4.15. A graph of the intensity (open circles) of the ν(C=C) band at 1644 cm^{-1} versus the time of exposure to ozone. The solid red and black lines are fits to the data to determine observed rate constants (see text for details).

To demonstrate the sensitivity of our data when determining the rate constant, we show two other exponential functions with the data in Figure 4.15. Both the upper and lower solid black lines are exponentials with the functional form shown in Equation 4.2. The upper solid black line is displayed with a rate constant of 2.7 × 10^{-5} s^{-1} and clearly overestimates most of the raw data points. The lower solid black line is displayed with a rate constant of 3.5 × 10^{-5} s^{-1} and clearly underestimates most of the raw data points. We determined the average rate constant for three independent experiments of (2.5 ± 0.5) × 10^{-5} s^{-1}.

4.3.2.2 XPS

To further understand the products and mechanism of the reaction between vinyl-terminated monolayers and ozone, we examined the monolayers after exposure to ozone with X-ray photoelectron spectroscopy. The monolayers were analyzed only after consumption of the C=C bond as determined by RAIRS (no signal above the noise at 1644 cm^{-1}). XPS allowed us to identify elemental composition and oxidation state of the molecules on the surface. Figure 4.16 is a high-resolution spectrum of the S (2p) region of an 18C C=C SAM after exposure to ~1.4×10^6 L of ozone. The raw XPS data (solid circles) have been fitted to a composite (thick solid line) of two spin-orbit doublets S(2p) Gaussian peaks and a linear baseline. Each doublet was fit with a fixed $2p_{3/2}/2p_{1/2}$ area ratio of 2:1 and a spin-orbit splitting of 1.2 eV.[92,129] The S(2p) doublet with the S $2p_{3/2}$ peak located at 161.9 eV (line solid line) is consistent with sulfur atoms bound to the gold substrate as thiolate species.[92,101,103,130,131] To fit the composite to the raw data, it was necessary to include a small contribution from an S(2p) Gaussian peak (S $2p_{3/2}$) centered at 166.1 eV (dashed line). Previous researchers have assigned peaks at 167 eV to sulfonate species formed by oxidation.[45,51,58] However, this peak centered at 166.1 eV is consistent with literature values reported for surface sulfite species $(SO_3)^{2-}$.[139] It is reasonable to assume that minor oxidation of the sulfur head group forms an SO_x moiety. In contrast to the methyl terminated monolayers, most of the sulfur on the surface of the 18C C=C SAM remains in the unoxidized form.

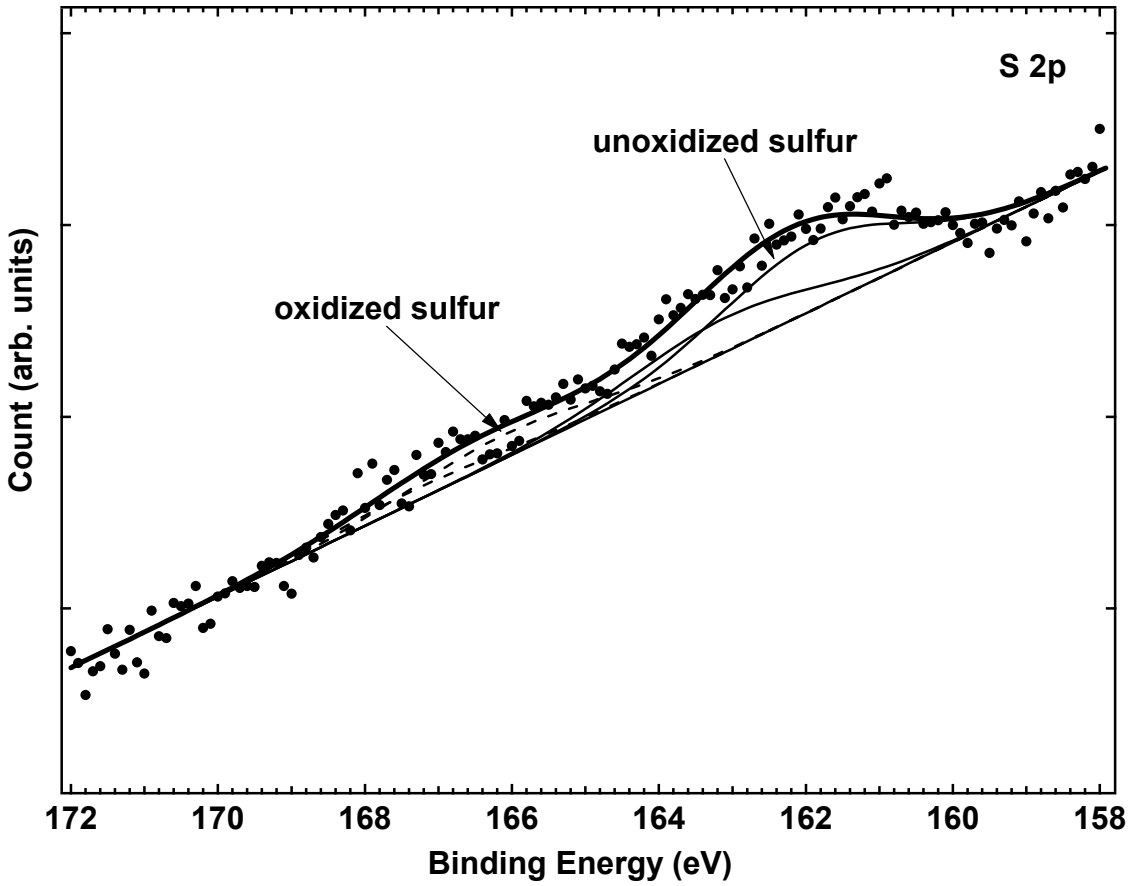

Figure 4.16. High-resolution X-ray photoelectron spectrum of the S(2p) region of an 18C C=C SAM after exposure to ~1.4×10^6 L of ozone. The raw XPS data (solid circles) have been fitted to a composite (thick solid line) of two spin-orbit doublets S(2p) Gaussian peaks and a linear baseline (see text for details).

We also examined the C(1s) region of the spectrum of the 18C C=C SAM after exposure to ~1.4×10^6 L of ozone. The raw data are shown as solid circles in Figure 4.17, and a composite (thick solid line), consisting of two individual Gaussian peaks (dashed lines) and a linear baseline (thin solid line), has been fitted to the data. The two Gaussian peaks are positioned at 284.4 and 287.6 eV. These data are consistent with the monolayer before exposure to ozone, indicating that the carbon species within the monolayer has undergone little change. The peak at 284.4 eV is caused by methylene

carbon atoms, [134-136] while the peak centered at 287.6 eV is consistent with carbon atoms bound to sulfur atoms (C-S).[130,137]

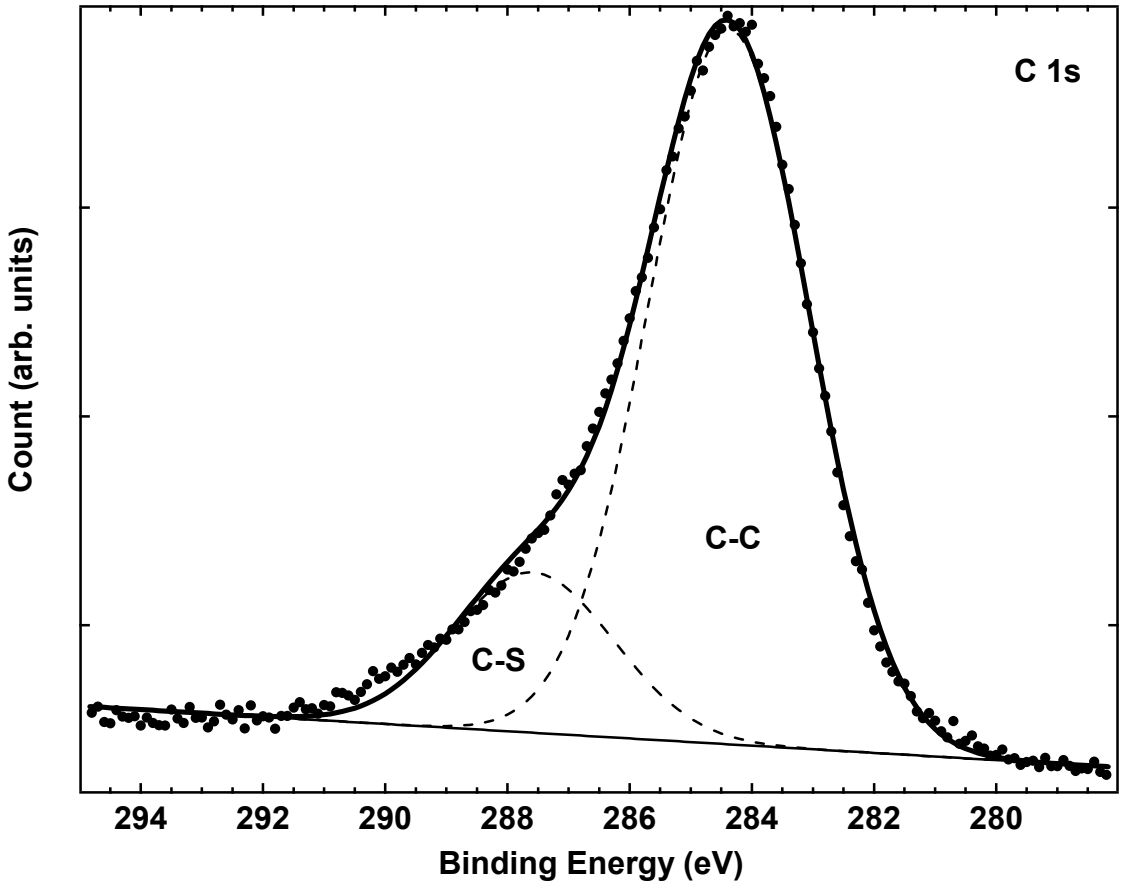

Figure 4.17. High-resolution X-ray photoelectron spectrum of the C(1s) region for a 18C C=C SAM after exposure to ~1.4 × 10^6 L of ozone. The raw XPS data (solid circles) have been fitted to a composite (thick solid line) of two C(1s) Gaussian peaks (dashed lines) and a linear baseline (thin solid line).

In contrast to the negligible changes in the C(1s) or S(2p) signals, significant addition of oxygen to the surface is observed in the high-resolution spectrum of the O(1s) region, as seen in Figure 4.18. These data were obtained after the 18C C=C SAM was exposed to ~1.4 × 10^6 L of ozone. A composite was fit to the raw data (solid circles) and consists of a single Gaussian peak (thick solid line) and a linear baseline (thin solid line). The Gaussian peak is centered at 533.7 eV. O(1s) binding energy at 533.7 eV has been

previously proposed to be due to the oxygen of an anhydride species (C-O-C).[137] This is a reasonable assignment since previous research in our laboratory has shown the formation of carboxylic acid anhydrides when 11C C=C SAM where exposed to ozone under high vacuum conditions.[24]

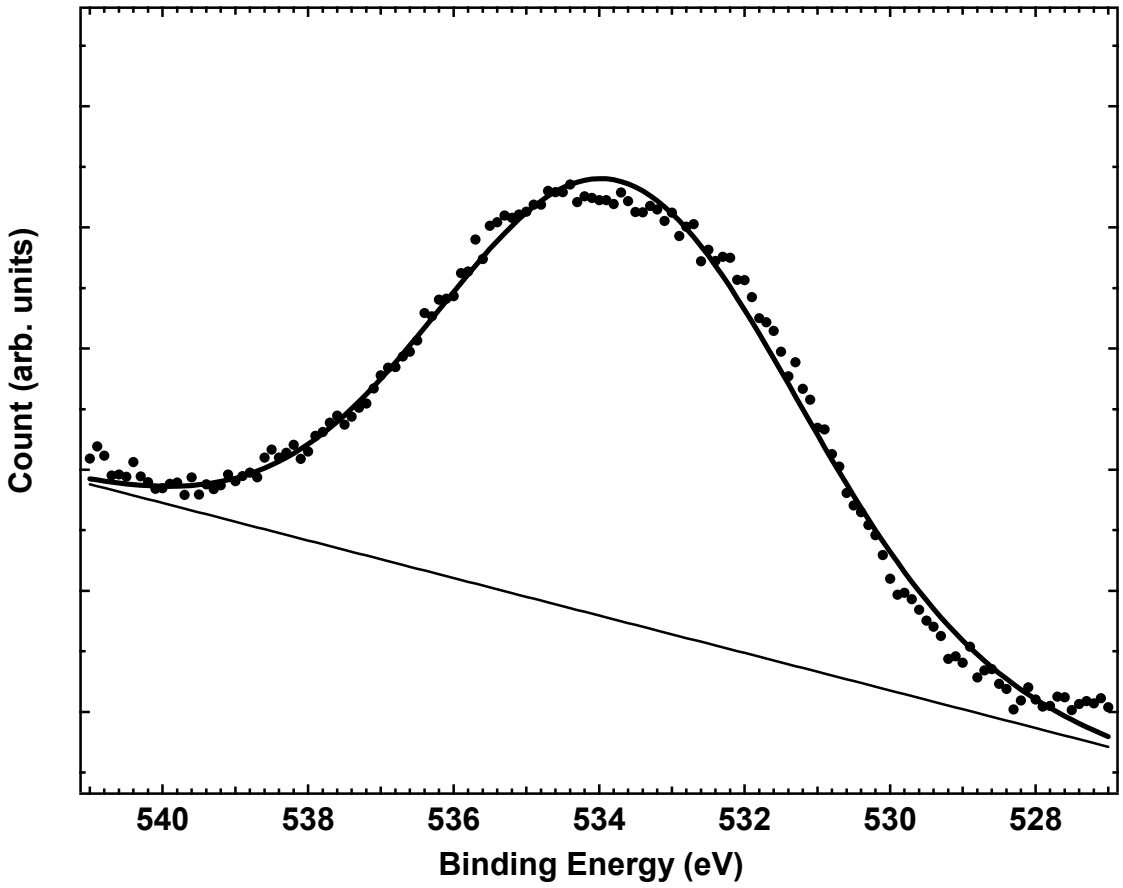

Figure 4.18. High-resolution X-ray photoelectron spectrum of the O(1s) region for a 18C C=C SAM after exposure to ~1.4×10^6 L of ozone. The raw XPS data (solid circles) have been fitted to a composite (thick solid line) of an O(1s) Gaussian peak and a linear baseline (thin solid line).

4.4 Discussion

We investigated the heterogeneous reaction of ozone with vinyl terminated organic thin films as proxies for atmospheric aerosols. The objective of this research was to develop a fundamental understanding of the reactions of ozone with vinyl terminated

interfaces, both from a mechanistic and kinetic perspective. We sought to understand how the unsaturated organic surface reacts with pure ozone when it is isolated in ultrahigh vacuum from interfering reactions of background gases.

4.4.1 Ozone Exposure

4.4.1.1 Mechanism

Similar to gas-phase and solution experiments, the reaction of ozone with surface-bound terminal alkenes is expected to proceed by the initial insertion of ozone to the carbon-carbon double bond to form a primary ozonide on the surface, as illustrated in Figure 4.19.[4,6] Previous researchers have proposed that the primary ozonide is unstable and will decompose in one of two pathways.[4,6] In the first pathway, the primary ozonide decomposes by breaking the carbon-carbon bond, originally belonging to the vinyl group, and rupturing the O-O bond labeled (1) in Figure 4.19. This pathway leads to the formation of a surface aldehyde species and a gas-phase diradical. The surface aldehyde can be further oxidized by ozone to form a surface-bound carboxylic acid. The gas-phase diradical can undergo a series of rearrangements yielding gas-phase products such as HCOOH, CO_2, H_2, H_2O, and CO. If the primary ozonide decomposes as illustrated in the second pathway, the carbon-carbon bond will break but the O-O bond labeled (2) in Figure 4.19 will rupture instead. Pathway 2 leads to the formation of formaldehyde in the gas phase and a diradical species on the surface. The surface diradical species is also unstable and can rearrange in numerous pathways. One possible rearrangement forms a surface methyl group and gas-phase CO_2.[6] Another possible rearrangement forms a surface bound carboxylic acid. As suggested by McIntire et al., the diradical species

could also react with neighboring vinyl, aldehyde, or carboxylic acid groups.[140] Reactions of this type will cause the chains of the monolayer to crosslink.

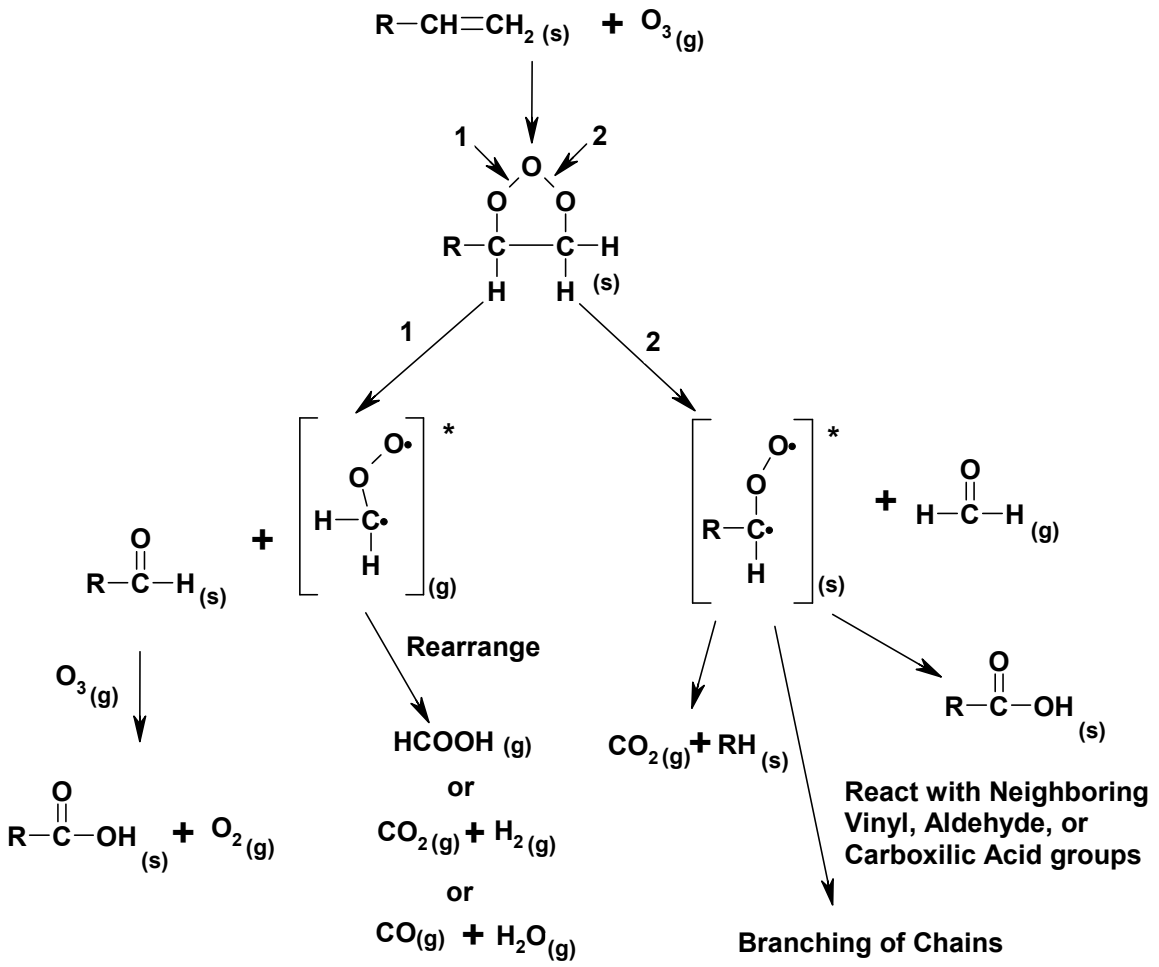

Figure 4.19. Overall scheme demonstrating the possible mechanistic pathways in which ozone can oxidize a terminal vinyl group bound to a surface. The subscripts (s) and (g) represent surface and gas-phase species, respectively.

When we monitored the heterogeneous oxidation of the vinyl terminated monolayers in real-time using RAIRS, we observed two significant changes to the monolayers. The first change, as displayed in Figure 4.11, was a shift toward higher wavenumbers of the bands from the $\nu_a(CH_2)$ and $\nu_s(CH_2)$ stretches of the hydrocarbon chains in the monolayer. Because the position of peaks from the $\nu_a(CH_2)$ and $\nu_s(CH_2)$ stretches are sensitive indicators of the ordering of the alkyl chain,[79,94-98] the shifting to higher

wavenumbers of both the asymmetric and symmetric methylene bands indicates a disordering event occurring within the monolayer. The disordering of the monolayer occurred concurrently with the second significant change to the monolayer observed in the RAIR spectra. The second change observed was the disappearance of IR signal from the C=C bond. The disappearance of the bands associated with the C=C bond implies that this species was consumed during the oxidation. We also observed the formation of a small broad band at ~1724 cm^{-1}, see Figure 4.12. The broad band at ~1724 cm^{-1} is most likely caused by a ν(C=O) stretch, possibly from a carboxylic acid. During the oxidation experiments, we observed no signal in the RAIR spectra from the formation of a methyl or aldehyde surface species. We cannot rule out the initial formation of an aldehyde species, because the aldehyde could be quickly oxidized to a surface carboxylic acid group. If this secondary reaction is extremely fast, we would likely not observe a mode corresponding to the aldehyde species, which is expected to appear at ~2720 cm^{-1}.

The trends in the time-resolved IR data could be explained by a mechanism that follows pathway (2) in Figure 4.19. Pathway (2) leads to the direct formation of a carboxylic acid on the surface; however, the formation of a carboxylic acid group is not necessarily responsible for the disordering observed in the RAIRS data. Pure carboxylic acid SAMs have been previously synthesized in our group (data not shown), and these monolayers are extremely well-ordered.[97] Another explanation for the observed trends could be that the oxidation of vinyl terminated monolayers leads to the formation of a surface diradical. The diradical could react with neighboring vinyl, aldehyde, or carboxylic acid groups (see Figure 4.19). A mechanism that includes this pathway would cause branching of the hydrocarbon chains within the monolayers. Branching of the

chains, in principle, could lead to disordering of the monolayer. Previous researchers have proposed similar mechanisms of the oxidation of SAMs leading to the formation of polymers or cross-linked hydrocarbon chains.[24,140] In these studies, the authors suggest that ozone oxidation of vinyl terminated SAMs lead to the agglomeration of organic material in the original SAM into large features observed by atomic force microscopy, scanning electron microscopy, and Auger electron spectroscopy.

Our XPS data suggest that the vinyl terminated monolayer resists significant oxidation of the sulfur head group, even after prolonged exposure to ozone. This surprising result also supports the hypothesis that the ends of the hydrocarbon chains react with each other to form a stable cross-linked film, which prevents the diffusion of ozone to the sulfur binding site. We observed the addition of oxygen to the monolayer upon oxidation using XPS. The binding energy of the O(1s) peak suggests the formation of an anhydride species. We have previously shown the formation of carboxylic acid anhydrides when 11C C=C SAMs were oxidized by ozone under high vacuum conditions.[24] It is reasonable to believe that some of the cross-linked networks could contain carboxylic acid anhydrides.

4.4.1.2 Kinetics

Recently, the kinetics and mechanisms of the surface oxidation of unsaturated hydrocarbons in thin films, as models for organic aerosols, have received significant attention.[4,6,9,14,18-22] The underlying goal of many of these studies is determining the reaction probability of ozone with the unsaturated hydrocarbons.[2] In general, atmospheric models use reaction probabilities; however, most of the reaction probabilities known are derived from gas-phase reaction data.[2] Previous researchers have shown that surface-

absorbed vinyl groups react with ozone faster than expected based on analogous gas-phase data.[4] With the objective of determining a reaction probability for the oxidation of vinyl groups at a gas-surface interface by ozone, we monitored the kinetics of the reaction of ozone with vinyl terminated monolayers.

Alkanethiol SAMS have previously been shown to display an even-odd effect in the transfer of energy in the collision of rare gases,[73] and in the chemical reactivity of the monolayer.[141] Furthermore, the tilt of methyl terminated monolayers with respect to the surface normal results in an n = even or n = odd orientation dependence to the terminal C-C bond.[90,97,142,143] Because vinyl-terminated alkanethiolates display a lattice structure indistinguishable from those of methyl-terminated SAMs,[144] we hypothesized that the vinyl terminated SAMs would display an orientation dependence to the terminal C=C bond. We also hypothesized that the orientation dependence would lead to an even–odd reactivity dependence toward ozone.

To test these hypotheses, we monitored the kinetics in the oxidation of four unique chain length vinyl terminated SAMs with RAIRS. Although we have performed detailed studies looking for even–odd effects in the reaction rate of vinyl terminated monolayer, this effect has been difficult to analyze. When studying the difference between the 10 and 11C C=C SAMs, these monolayers displayed competing reactions between the oxidation of the C=C bond and the oxidation of the sulfur head groups. We continued to pursue the investigation of the even–odd chain length reaction rates by synthesizing longer chain vinyl terminated monolayers, in hopes of separating the competing reactions. Currently, the results for the oxidation of the 18C C=C SAM are consistent with the 15C C=C SAM (data not shown). As discussed in section 4.3.1.1, the consistent

data between the 15 and 18C C=C SAMs should be expected because the orientation of the C=C bond does not seem to display an even–odd orientation dependence. Further studies should be performed exploring the difference between an 18C and 19C C=C SAM, since the 18C C=C SAM shows very little competition between the reaction of ozone with the C=C bond and the oxidation of the sulfur head group.

In an effort to probe the kinetics of the oxidation of the 18C C=C SAM, we plotted the change in area of the band in the RAIR spectra, associated with the $\nu_a(CH_2)$ stretch. We observed that the area increased exponentially upon exposure to ozone, see Figure 4.14. The increase in area of the band from the $\nu_a(CH_2)$ stretch signifies a transition of the monolayer from a ordered environment toward a disordered state. If we assume that the disordering event causing the increase in area follows first-order kinetics, we could fit a single exponential of the form shown in Equation 4.1. The best fit to the data requires an observed rate constant of 3.1×10^{-5} s^{-1}. We also observed that the intensity of the band associated with the ν(C=C) stretch at 1644 cm^{-1} decreased in an exponential fashion. If we assume that the reaction consuming the C=C moieties follows pseudo-first-order kinetics, we can model the reaction with an equation of the functional form shown in Equation 4.2. The best fit to the data requires an observe rate constant identical to the rate constant determined from the change in area of the asymmetric methylene stretch, 3.1×10^{-5} s^{-1}. These rate constants yield a half-life of approximately 6.2 hours. Because the same rate constants were obtained for each set of data, the spectral changes most likely arise from the same reaction. It is possible that the mechanism discussed above, which allows the cross-linking of chains, could be responsible for both the consumption of the double bond and the disordering of the monolayers. This would only be true if the

reaction of ozone with the double bond was much slower than the reaction of the surface diradical with the neighboring chains.

To determine the initial reaction probability, we modeled the change in the intensity of the ν(C=C) stretch at 1644 cm^{-1} with a Langmuirian desorption isotherm:[145,146]

$$I(t) = I_0 e^{(-\alpha t)} \qquad (4.3)$$

where I(t) is the infrared intensity at any time and I_0 is the infrared intensity before exposure to ozone. The time of exposure to ozone in seconds is represented by t, and α is determined from Equation 4.4.

$$\alpha = (\tfrac{1}{4} \langle v \rangle \gamma_0 [O_3]_g) / L \qquad (4.4)$$

In Equation 4.4, <v> is the mean molecular velocity (cm/s) of ozone, γ_0 is the initial reaction probability, $[O_3]_g$ is the gas-phase ozone concentration adjacent to the surface, and L is the initial surface coverage of the C=C moieties. The gas-phase ozone concentration adjacent to the surface, 1.20×10^{11} molecules cm^{-3}, was estimated from the number density of ozone measured with the attached UV/Vis spectrometer and the calculated conductance through the capillary of the doser. (The conductance was calculated with the known size of the aperture in the capillary, and this calculated conductance matches the conductance calculated from the total pressure of ozone in the UHV chamber, which was measured with the cold cathode gauge.) The initial surface coverage of carbon-carbon double bonds is assumed to be the same as methyl-terminated alkanethiolate coverage, 4.7×10^{14} molecules cm^{-2}.[78,136,147] This assumption is most likely valid since vinyl-terminated thiolate SAMs display a lattice structure indistinguishable from those of methyl-terminated thiolate SAMs, as determined from scanning tunneling microscopy.[144] From the model fits, the initial reaction probability for

ozone with vinyl terminated SAMs was calculated to be $(1.1 \pm 0.5) \times 10^{-5}$. This translates to one reaction occurring in every ~77,000 gas-phase collision between ozone and the carbon–carbon double bond.

The calculated reaction probability of ozone with the vinyl terminated monolayers can be compared to the gas-phase reaction probability of ozone with a terminal alkene (1-hexene), $\sim 3 \times 10^{-8}$.[4] This value is approximately three orders of magnitude smaller than the reaction probability we obtained for ozone with C=C SAMs. The increase reactivity of the vinyl terminated monolayer clearly demonstrates that the gas-surface interface plays an important role in this reaction. The initial reaction probability that we report for vinyl terminated monolayer with ozone, $(1.1 \pm 0.5) \times 10^{-5}$, is in excellent agreement with literature values of adsorbed alkenes at solid interfaces;[7,14] however, our value is approximately an order of magnitude larger than previously reported reaction probabilities of ozone with unsaturated phospholipids absorbed at an air-liquid interface.[148] The increased reaction probability of vinyl SAMs compared to unsaturated phospholipids is most likely caused by the fact that the reactive site, C=C bond, is positioned precisely at the interface for the vinyl SAMs.

The larger reaction probability for vinyl terminated monolayers, as compared to analogous gas-phase terminal alkenes, can be explained when one considers the collision rate of ozone with the double bond. In the gas-phase reaction, ozone will collide with many of the saturated sites of the linear alkene before colliding with the unsaturation site; these collisions will not result in a reaction. This is in contrast to the situation in which the unsaturated site is positioned precisely at the gas-surface interface, as in our C=C SAMs. In this circumstance, all ozone molecules must initially collide with an

unsaturation site, first. Furthermore, each ozone molecule could potentially collide with more than one double bond before desorbing from the surface. This will necessarily increase the reaction probability since each collision provides an opportunity for the reaction.

4.5 Summary

In summary, we have synthesized vinyl terminated self-assembled monolayers of four unique chain lengths. Each monolayer was characterized by reflection absorption infrared spectroscopy and X-ray photoelectron spectroscopy. These analytical techniques prove that the C=C SAMs assemble into highly ordered domains. We postulate that the vinyl terminated monolayer show no even/odd orientation dependence of the ν(C=C) mode as displayed by RAIRS.

The heterogeneous oxidation of vinyl terminated monolayers with pure ozone was monitored in situ with reflection absorption infrared spectroscopy. The surface bond products were monitored during the reaction. Disordering of the monolayers was observed concurrently with the disappearance of the vinyl group. Formation of carbonyl functionalities was observed during the reaction. We proposed a mechanism involving cross-linking of the hydrocarbon chains.

Using RAIRS, we tracked the kinetics of the oxidation of an unsaturation site positioned precisely at the gas-surface interface. We were able to determine an observed rate constant for this reaction, and used the rate constant to determine an initial reaction probability, important in climate models, of ozone with a vinyl moiety at a gas-solid interface. The initial reaction probability determined is approximately three orders of magnitude larger than an analogous gas-phase reaction probability of ozone with 1-

hexene. The increased reaction probability can be explained when considering the percentage of collisions between ozone and the unsaturation site in each system. When ozone collides with the C=C SAMs, the initial collision must be with an unsaturation site since these sites are at the gas-solid interface. This collision is a potential reaction; however, when ozone collides with the gas-phase terminal alkene, the initial collision does not necessarily involve the carbon-carbon double bond. Collisions with the saturated hydrocarbons do not lead to reactions. This work allowed us to calculate reaction probabilities of ozone with surface bound vinyl moieties position precisely at the gas-surface interface. These reaction probabilities could prove to be useful when modeling atmospheric chemistry involving aerosol particles containing organic films.

Chapter 5

Summary and Concluding Remarks

5.1 Summary of Results

The main focus of my research was to develop a better understanding of the interfacial reaction of ozone with vinyl-containing organic thin films. Heterogeneous reactions of atmospheric species at gas/surface or gas/liquid interfaces have recently received significant attention in the literature because of their influence on many atmospheric processes. An important example of a heterogeneous reaction at a gas/surface interface, prevalent in the atmosphere, is the reaction of ozone with organic aerosols. Reactions with ozone can change the aerosol's chemical properties, affecting the particle's hygroscopic nature, cloud condensation nuclei activity, and optical properties. Constructing a detailed understanding of the reaction pathways and kinetics will enable scientists to predict the fate of atmospheric gases and the particles with which they interact.

In an effort to develop a more complete understanding of the reaction of ozone with atmospheric particles containing unsaturation sites, we developed proxies for this system using SAMs. The monolayers provided a method to precisely control the chemical identity, density, and orientation of the vinyl groups at the interface. To perform these experiments, I designed and constructed an ultrahigh vacuum surface analysis system capable of exposing the proxies to controlled amounts of gas-phase analytes. A system was also developed to synthesis, purify, store, and deliver pure ozone to the surface analysis chamber for extended periods of time. The surface analysis system is capable of three major analytical techniques to monitor reactions in situ. Reactions can be

monitored in real time with reflection absorption infrared spectroscopy to determine the kinetics of the reaction as well as monitor the products that form on the surface. Chemical identity and oxidation state determination of the surface bound molecules can be realized with X-ray photoelectron spectroscopy before or after exposure of the surface, and gas-phase products can be monitored during a reaction with mass spectrometry (although this capability was not utilized during the course of these studies).

We synthesized vinyl terminated monolayers of four unique chain lengths as proxies for atmospheric aerosols, and characterized each with RAIRS and XPS. The monolayers assembled into well-ordered systems that demonstrated an increase in order as the hydrocarbon chains lengthened. The heterogeneous reaction of pure ozone with the vinyl terminated SAMs was monitored in situ with RAIRS. We observed disordering of the monolayers concurrently with the disappearance of the vinyl functional group. We also observed new bands within the RAIR spectra that we attribute to the formation of carbonyls or carboxylic acids bound to the surface. Using XPS, we observed no significant loss of carbon and little oxidation of the sulfur head groups during the reaction. We proposed a mechanism that includes the cross linking of the hydrocarbon chains within the monolayer, which impedes further oxidation of the head groups and stops desorption of the hydrocarbon chains.

Using RAIRS, we tracked the kinetics of the oxidation of the vinyl groups that were positioned precisely at the gas/surface interface, and we monitored the changes in order of the system. We determined the rate constant for the disordering of the hydrocarbon chains using the change in area of the absorption band from the $\nu_a(CH_2)$ stretch. We also determined an observed rate constant for the oxidation of the vinyl group by monitoring

the changes in IR absorbance of the ν(C=C) stretch. We report identical rate constants for both reactions of 3.1×10^{-5} s^{-1}. We suggest that the equality of the rate constants implies a mechanism that includes the disordering of the monolayer during the consumption of the double bond. Using the observed rate constant, we determined an initial reaction probability of $(1.1 \pm 0.5) \times 10^{-5}$, which translates to one reaction occurring for every ~77,000 collision of ozone with the vinyl group. This reaction probability is approximately three orders of magnitude greater than the reaction probability for an analogous gas-phase reaction. The increase in reactivity of the vinyl terminated system clearly demonstrates that the gas/surface interface plays an important role in this reaction.

As a control for the reactions mentioned above, we also studied the reaction of methyl terminated SAMs with pure ozone in the ultrahigh vacuum system. The reaction of ozone with a methyl terminated monolayer is also important because these model systems have shown potential use in applications such as chemical sensors, molecular electronic devices, corrosion inhibitors, and biomaterials; and the environmental stability of these monolayers is critical to the success of such devices.[43] Reactions of the methyl terminated monolayers with ozone were monitored in situ with RAIRS. We observed the formation of a sulfonate species during the oxidation of the monolayer. Continuous exposure of the sulfonate species yielded the formation of a sulfate moiety that remained on the surface even after prolonged exposure to ozone. During the oxidation of the sulfur head group, we observed changes in the absorbance of the $\nu_a(CH_2)$ and $\nu_S(CH_2)$ stretches that were consistent with a transition from an ordered system to a highly disordered system. Upon further exposure to ozone, we detected almost complete removal of the hydrocarbon chains from the surface. XPS also confirmed the changes in the system

mentioned above; we observed facile oxidation of the sulfur head group with concomitant loss of carbon from the surface.

We also performed a kinetic analysis of the oxidation of a series of n-alkanethiols with increasing chain length. We determined an observed rate constant for the disordering of the hydrocarbon chains during the oxidation of the monolayers by monitoring the changes in absorbance of the $\nu_a(CH_2)$ stretch. We observed an exponential decrease in the rate constant as the length of the hydrocarbon chains increased. From these data, we hypothesized that the initial site of attack of ozone with SAMs is at defects within the film. The knowledge gained in this study could help predict the rate of oxidation of alkanethiols and guide in the design of more robust monolayers.

5.2 Atmospheric Implications

The reaction probability that we measured for the reaction of ozone with a vinyl terminated monolayer, $(1.1 \pm 0.5) \times 10^{-5}$, agrees extremely well with other reported reaction probabilities of ozone with unsaturated surfaces in the literature. Dubowski et al. reported an initial reaction probability for vinyl terminated alkylsilane monolayers of 10^{-5}.[4] Voges et al. reported an initial reaction probability for surface bound terpenes of 1×10^{-5},[14] and Moise and Rudich reported an initial reaction probability for frozen oleic acid of $(5.2 \pm 0.1) \times 10^{-5}$.[19] The fact that our reported reaction probability agrees extremely well with the above mentioned reports is a surprising result considering the varied reaction conditions of each experiment. For each of the above mentioned reports, the experiments were carried out at pressures between 10–760 Torr with ozone concentrations at ppm levels. In each of these experiments, significant amounts of background gases (H_2O, O_2, and CO_2) were present at the pressures reported. Because

ozone could react with the background gases at high pressures to form more reactive species, one may have predicted that the reaction probability would be different under ultrahigh vacuum conditions, where the partial pressures of the background gases are negligible. For example, ozone and water react to form the hydroxyl radical.[58,149,150] The hydroxyl radical is extremely reactive and has been shown to have a reaction probability near unity when reacting with vinyl terminated monolayers.[151] The surprising result that the reaction probability at atmospheric conditions is the same under ultrahigh vacuum conditions implies that the reactions of ozone with atmospheric background gases do not play a significant role in the oxidation of vinyl terminated organic thin films. Furthermore, the structure of the monolayer must not play a significant role.

During the oxidation of vinyl-terminated surfaces as proxies for atmospheric aerosols, we observed the formation of carbonyl or carboxylic acid species on the surface. The carbonyl or carboxylic acid species formed by the ozone reaction with unsaturated surfaces are far more polar than the original vinyl functionalities. Consequently, atmospheric aerosols, which contain unsaturation sites, can react with ozone to form carbonyl or carboxylic acid species that contribute to their cloud nucleation activity from the aerosol's enhanced water affinity.[6] In addition, the cross-linking that we have observed could change the permeability of the organic particles. Further studies in our group will use thermal desorption techniques to determine the extent to which cross-linking competes with oxidation up to a carboxylic acid.

5.3 Future Research

Future work utilizing the UHV surface analysis chamber should include studies that monitor gas-phase products that desorb from the surfaces during ozone exposure. The

future work should also include temperature program desorbtion (TPD) analysis for further surface characterization. These studies could help identify the gas-phase products and further elucidate the mechanisms of the oxidation of both methyl and vinyl terminated monolayers by ozone.

5.4 Concluding Remarks

Vinyl terminated SAMs have proven to be useful proxies for exploring the reactions of organic atmospheric particles containing unsaturation sites. Investigations of the heterogeneous reactions of ozone with these proxies in ultrahigh vacuum conditions are a valuable tool for separating the chemistry of numerous oxidizing background gases within the atmosphere. The results presented in this thesis should help develop a more detailed understanding of the interfacial reactions of ozone at surfaces.

6. Appendix

6.1 Non-Linear Least Squares Fitting in Fortran 77

Main.f

```
!
!   This code optimizes parameters.
!   It examines the RMSD of the analytic and "true" values
!   and minimizes the RMSD calling minpack routines.
!
!   Larry Fiegland 01 February 2007
!
!   N is the number of parameters
!   M is the number of wavenumbers
!
      IMPLICIT DOUBLE PRECISION(A-H,O-Z)
      CHARACTER*5 ANAME(20),ASYMB(20)
      INTEGER INFO,M,N,J
      INTEGER IWA(664157)
      DOUBLE PRECISION TOL
      DOUBLE PRECISION FVEC(3371),WA(16865),X(14)
      DOUBLE PRECISION EAB(3371),FREQ(3371),WAVENUMBER(320,3371)
      EXTERNAL FCN
      COMMON /IRE/ IREAD
      COMMON /ABINITIO/ EAB, FREQ,RMSD
!
      OPEN(7,FILE='params.initial')
      !file that initial parameter are read in from
      OPEN(8,FILE='baselineflattened.dat')
      !file in which the actual data is read in from
      OPEN(9,FILE='parametersvstime.dat')
      !file that is written that contains the final parameters
      N = 14 !number of parameters
      M = 3371 !number of wavenumbers
      NCOLUMNS = 135 !number of experiments
      TOL = 0.0001 !convergence parameter
      LWA = 26865
!
!     Read in the starting parameters from params.initial
!
      DO I=1,N
        READ(7,*) X(I)
      END DO
!
!     Read in the "true" values from  baselineflattened.dat
!     (Read the data only once and store them in WAVENUMBER)
```

```
!
      IF(IREAD.EQ.0) THEN
       DO I=1,M
         READ(8,*) FREQ(I),(WAVENUMBER(J,I),J=1,NCOLUMNS)
       END DO
       IREAD=1
      END IF
      DO J=1,NCOLUMNS
        DO I=1,M
          EAB(I)=WAVENUMBER(J,I)
        END DO
!
!     Call to the minpack subroutines
!
      CALL LMDIF1(FCN,M,N,X,FVEC,TOL,INFO,IWA,WA,LWA)
      WRITE(6,*) 'Final parameters',(X(I),I=1,N)
      WRITE(9,*) J,(X(I),I=1,N)
      CALL FLUSH(9)
!
      END DO
      END
!     This subroutine gives you an array of parameters (X(I))
!     and asks you for an array of residues (differences between
!     the "true" values and the analytic ones), FVEC(I).
!
      SUBROUTINE FCN(M,N,X,FVEC,IFLAG)
      IMPLICIT DOUBLE PRECISION(A-H,O-Z)
      INTEGER M,N,IFLAG,I,NATOMS,J,IREAD,K
      DOUBLE PRECISION X(N),FVEC(M)
      DOUBLE PRECISION RAC(M),CLJ(6,3),E
      DOUBLE PRECISION AC,AF,BC,BF,CC,CF,DC,DF,E1(M)
      DIMENSION FREQ(3371),EAB(3371)
      CHARACTER*5 ANAME(40),ASYMB(40)
      CHARACTER*50 AINFO
      COMMON /IRE/ IREAD
      COMMON /ABINITIO/ EAB,FREQ,RMSD
!
!     **********
!
!
      RMSD=0.0
      DO I=1,M
!the following is a function that is the sum of 5 Lorentzian functions
!with one linear term. it also fixes the position and width of one of
!the Lorentzian functions
! this is where one would change the functions that was being fit
```

```
      Y=(X(1)+((X(2)*(0.31830988618379067153776752674503*(X(3)/
     .(((FREQ(I)-X(4))**2)+X(3)**2))))
     .+(X(5)*(0.31830988618379067153776752674503*(X(6)/
     .(((FREQ(I)-X(7))**2)+X(6)**2))))
     .+(X(8)*(0.31830988618379067153776752674503*(X(9)/
     .(((FREQ(I)-X(10))**2)+X(9)**2))))
     .+(X(11)*(0.31830988618379067153776752674503*(3.954515/
     .(((FREQ(I)-2936.58)**2)+(3.954515)**2))))
     .+(X(12)*(0.31830988618379067153776752674503*(X(13)/
     .(((FREQ(I)-X(14))**2)+X(13)**2))))))
!
          FVEC(I)=EAB(I)-Y
          RMSD=RMSD+FVEC(I)**2
!
!       the following is used to weight the fit
          IF(FREQ(I).LT.2825.0.OR.FREQ(I).GT.2987.0) FVEC(I)=0.0
      END DO
      RMSD=SQRT(RMSD/REAL(M-1))
      RETURN
!
!     LAST CARD OF INTERFACE SUBROUTINE FCN.
!
      END
```

6.2 Ultrahigh Vacuum Chamber Interlock Program in Labview

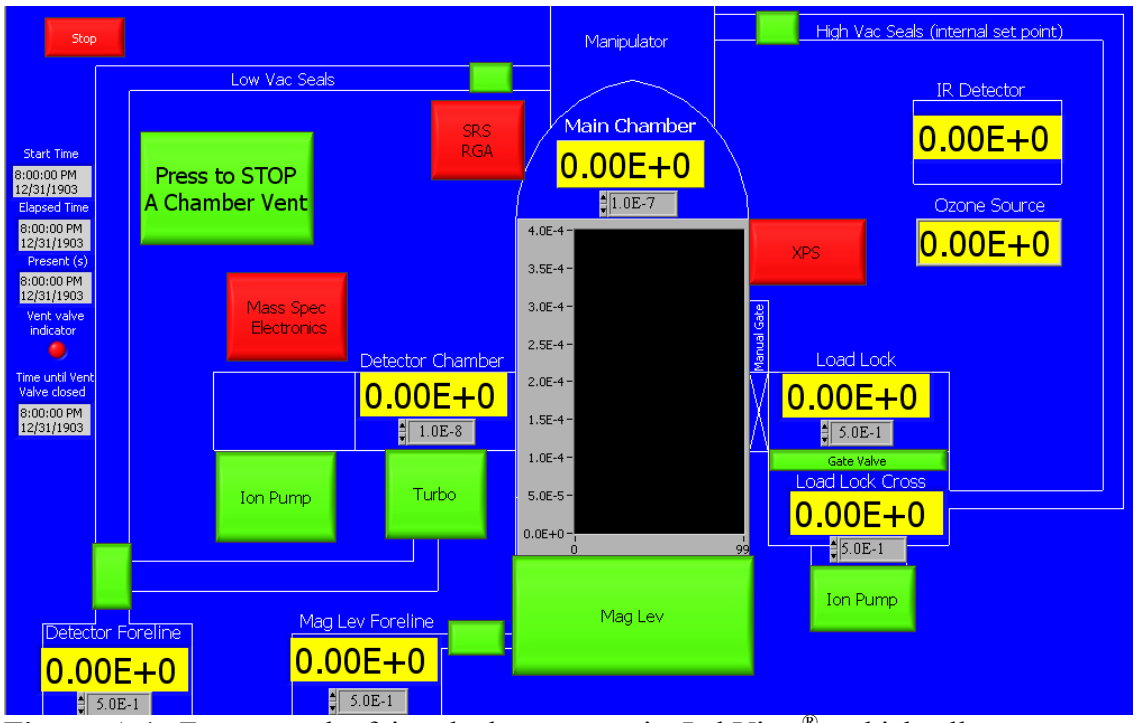

Figure A.1. Front panel of interlock program in LabView®, which allows a user to manually control the pumps, set points, gate valves and instrumentation.

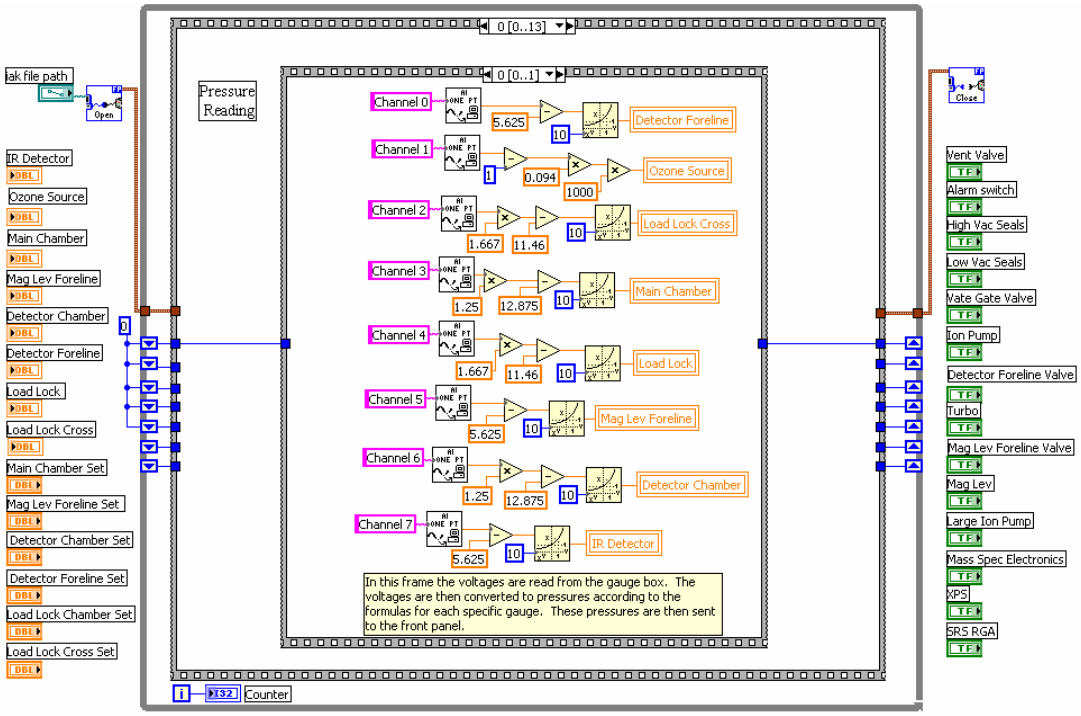

Figure A.2a.

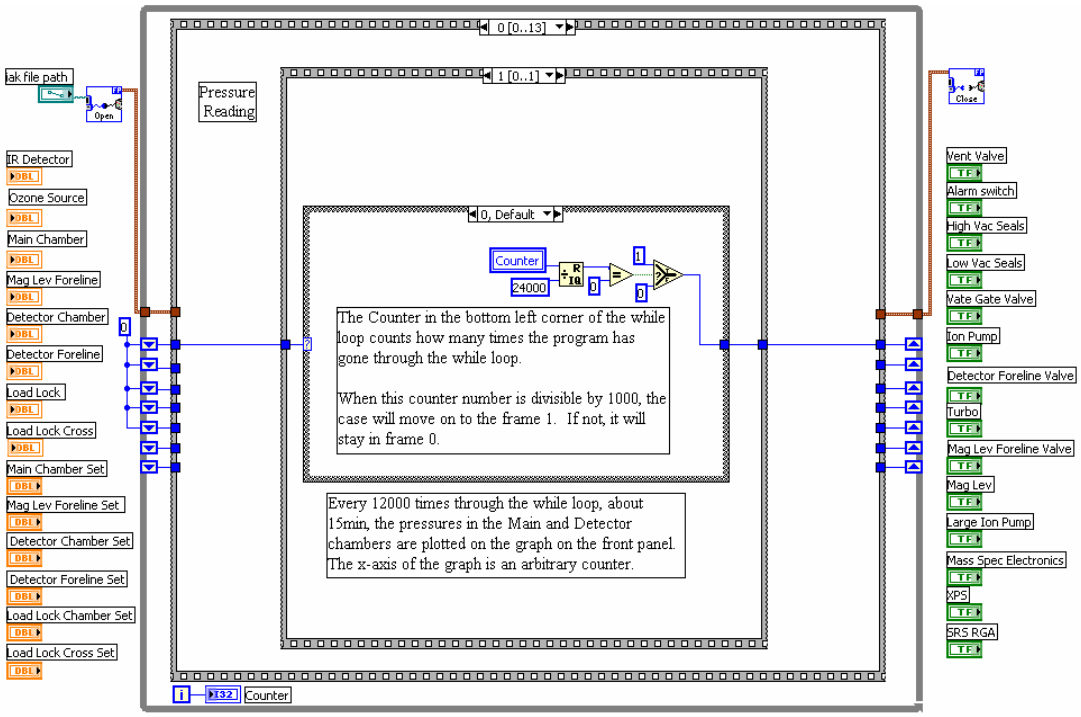

Figure A.2b.

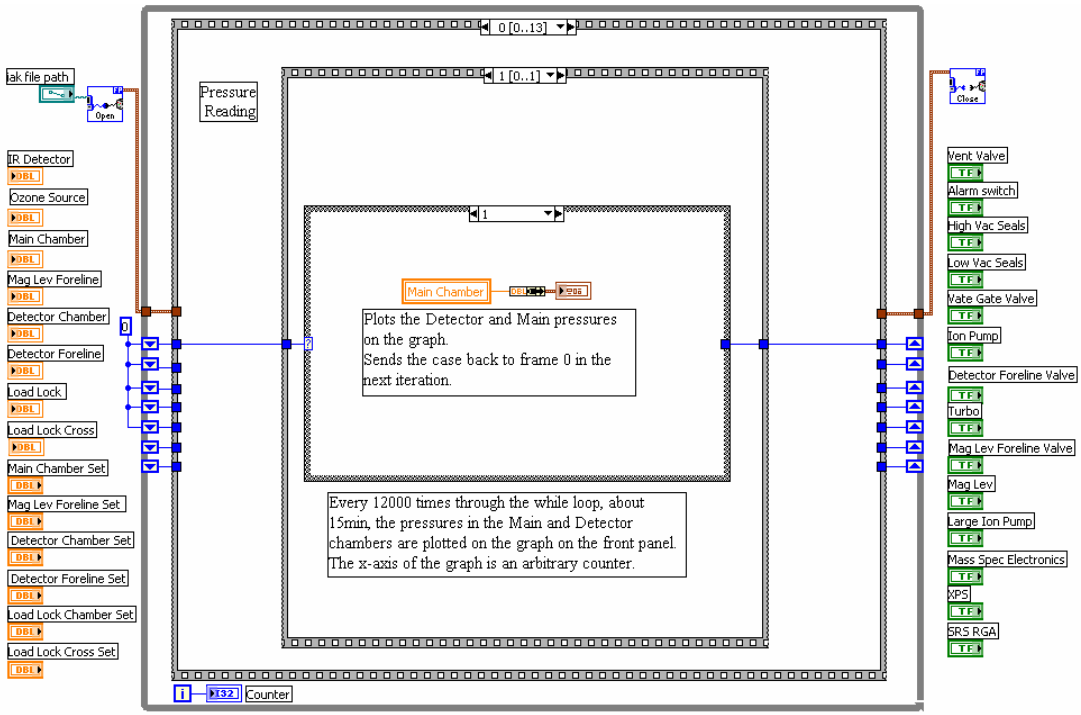

Figure A.2c. The first sequence structure within the while loop that records the voltage signal from the pressure gauges and outputs the pressures to the front panel. The main pressure is also plotted on the front panel every 15 minutes.

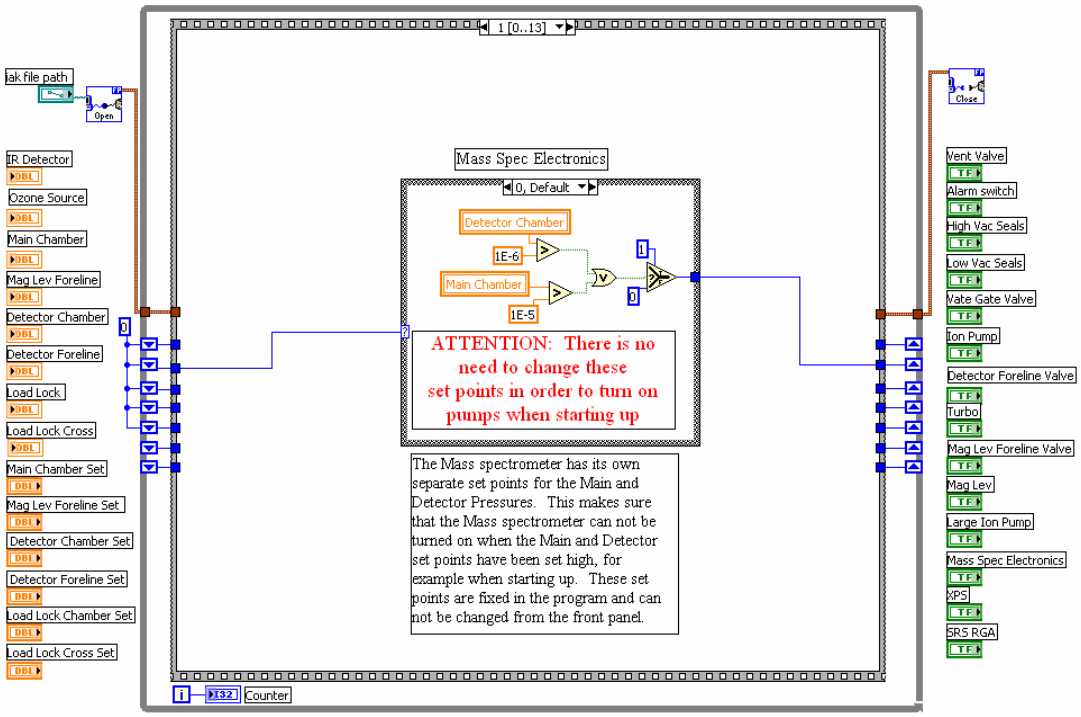

Figure A.3a.

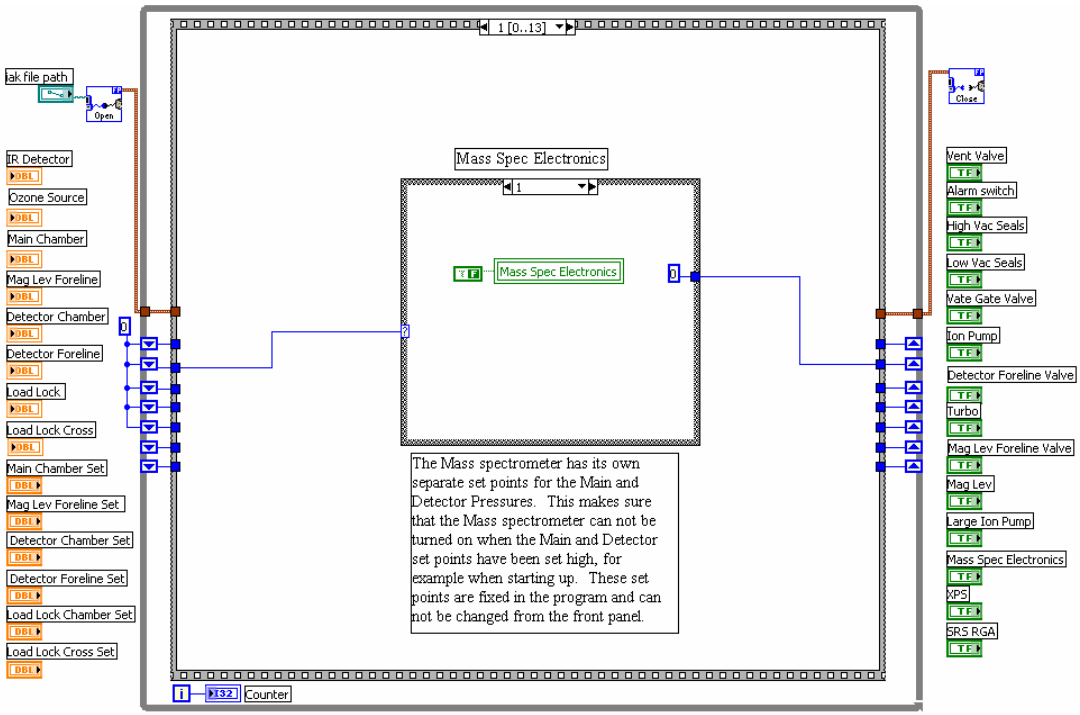

Figure A.3b. The second sequence structure in the while loop. This sequence sets the internal set points for the Extrel mass spectrometer's electronics. The electronics are turned off if the pressure in the detector chamber is above the set point.

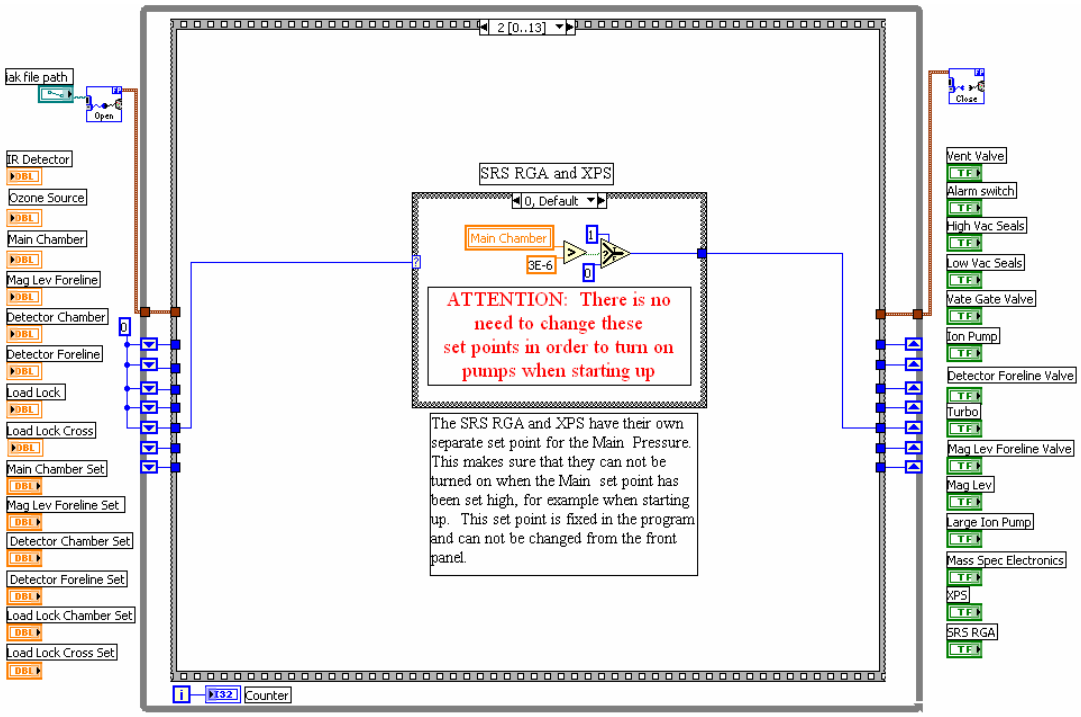

Figure A.4a.

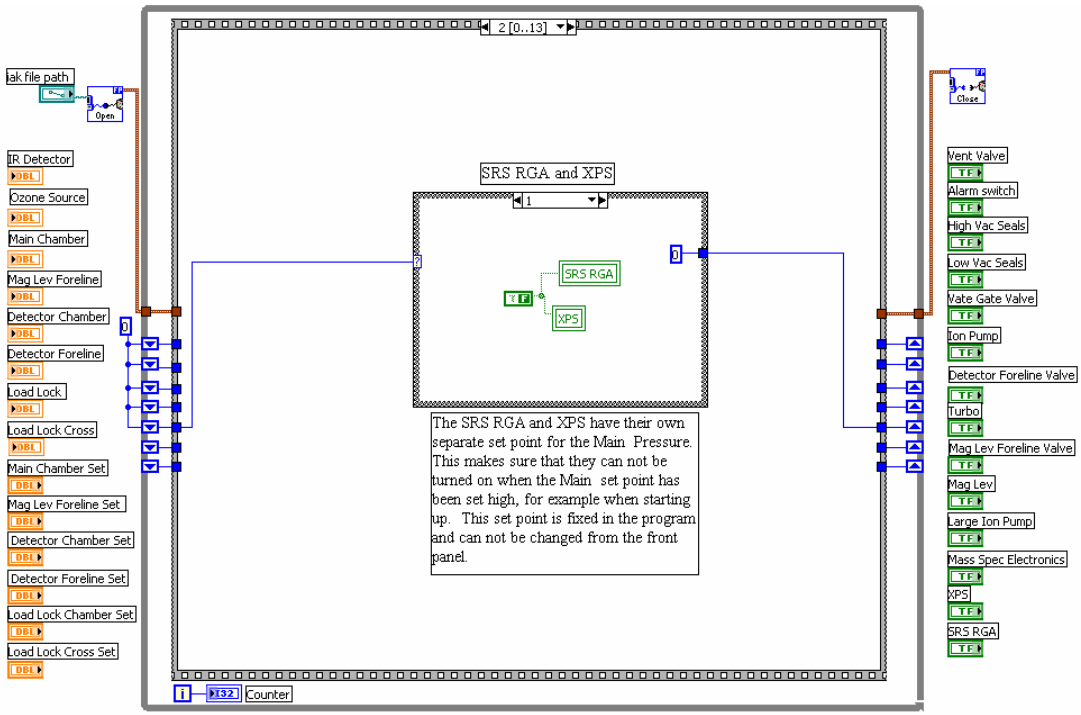

Figure A.4b. The third sequence structure in the while loop. This sequence sets the internal set points for the SRS mass spectrometer and the XP spectrometer. Both the mass spectrometer and the x-ray photoelectron spectrometer are turned off if the pressure in the main chamber is above the set point.

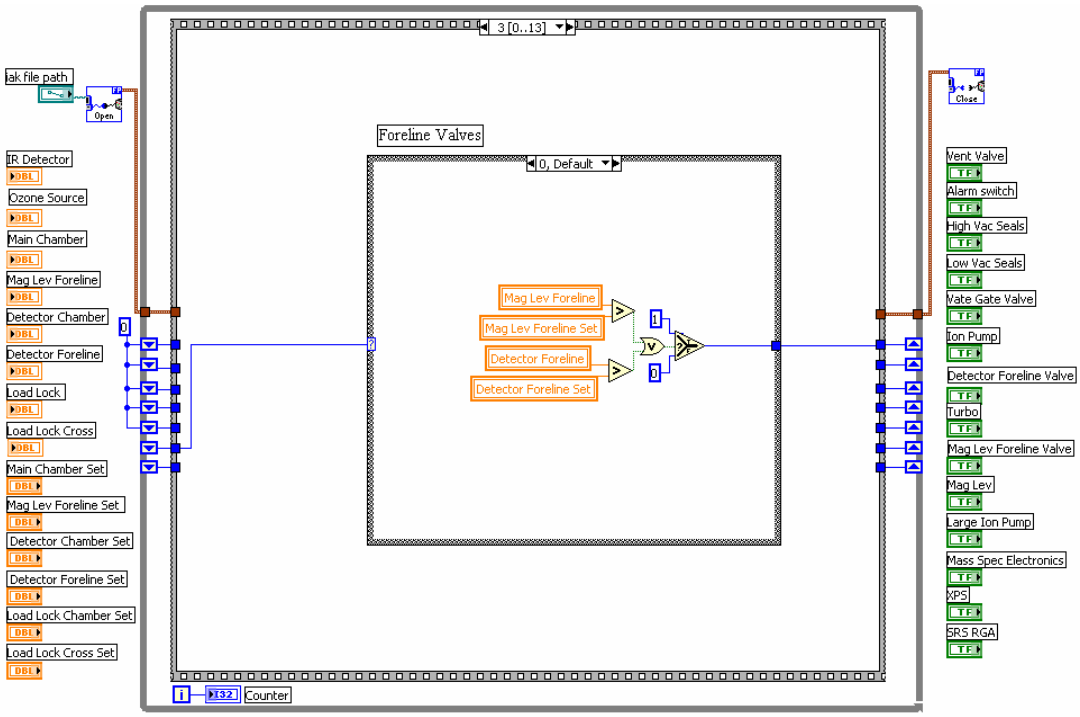

Figure A.5a.

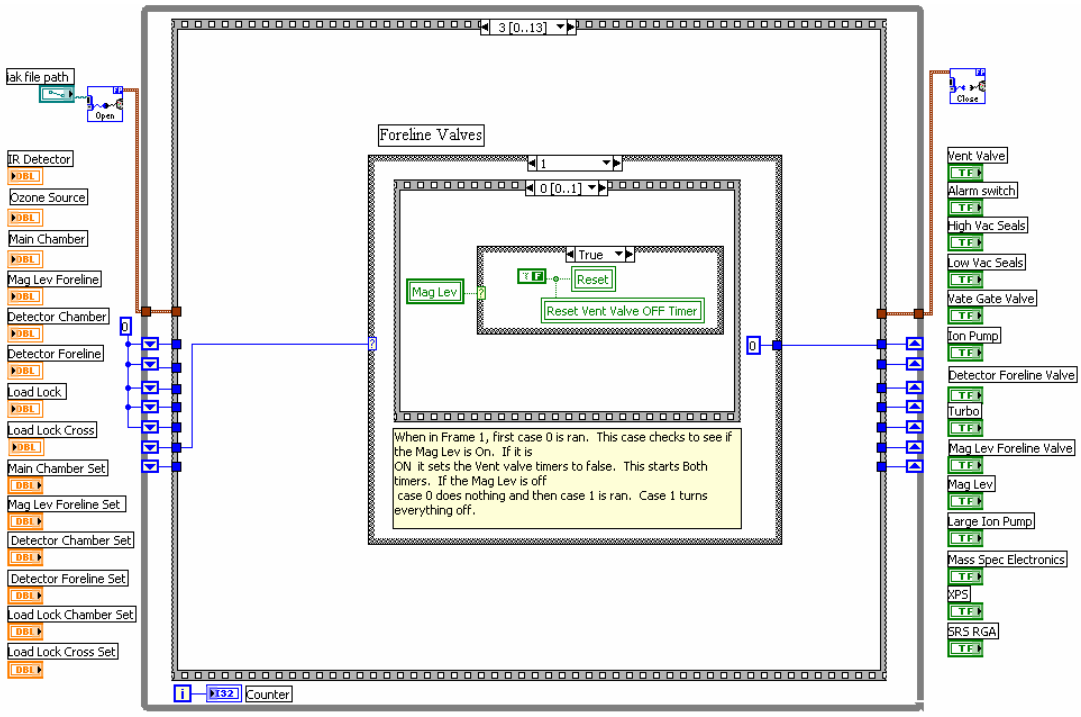

Figure A.5b.

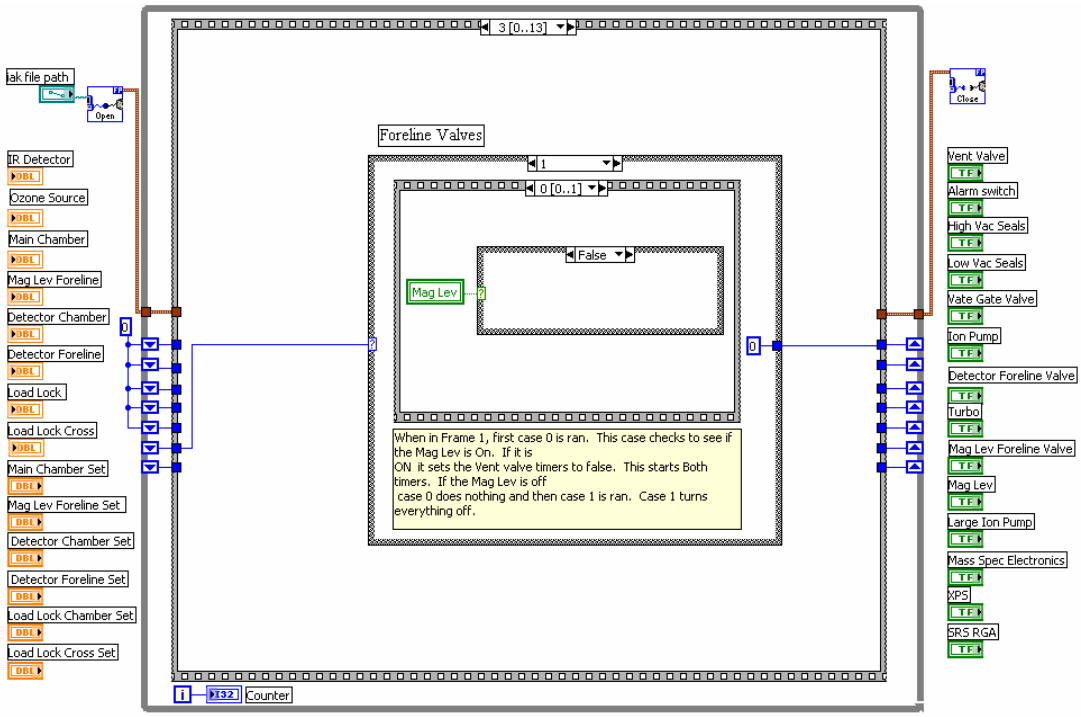

Figure A.5c.

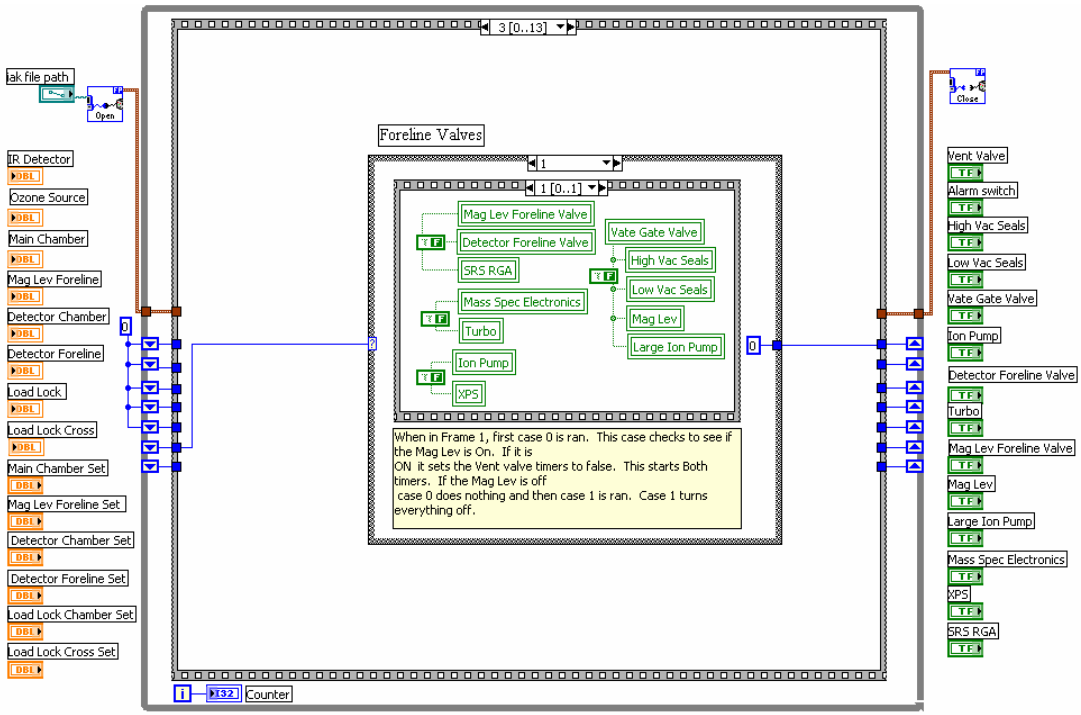

Figure A.5d. The fourth sequence structure of the while loop checks the front panel set points of the main and detector chamber's forelines. If the pressures are higher then the set points, all equipment is turned off and all valves are closed. The chamber vent timers are also started.

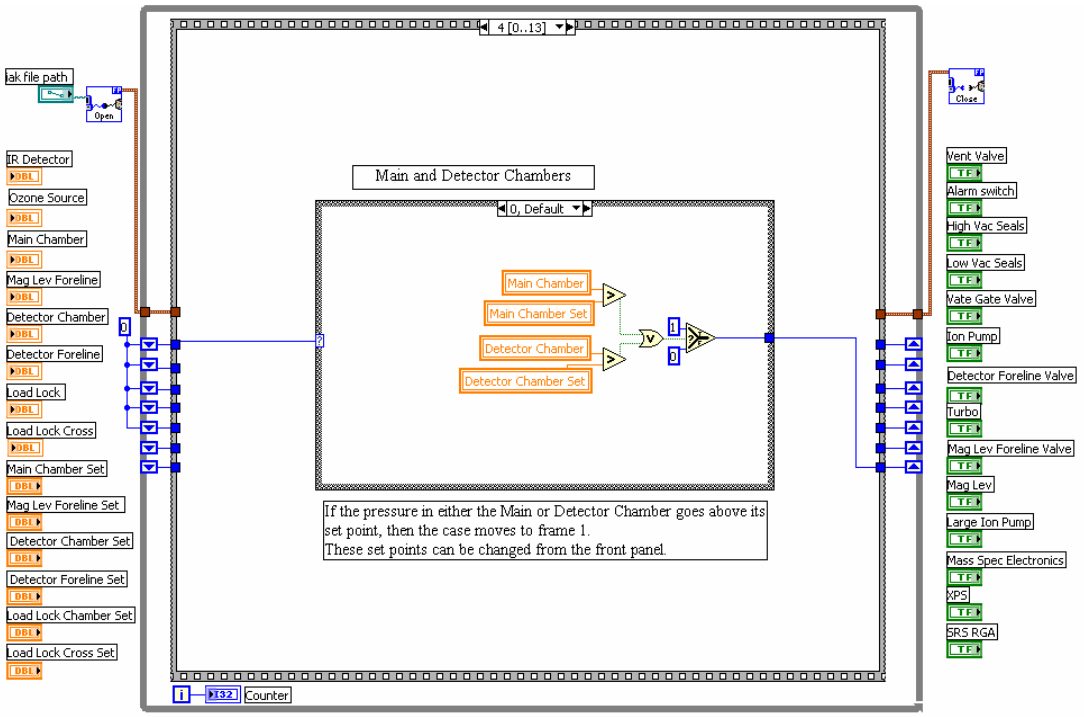

Figure A.6a.

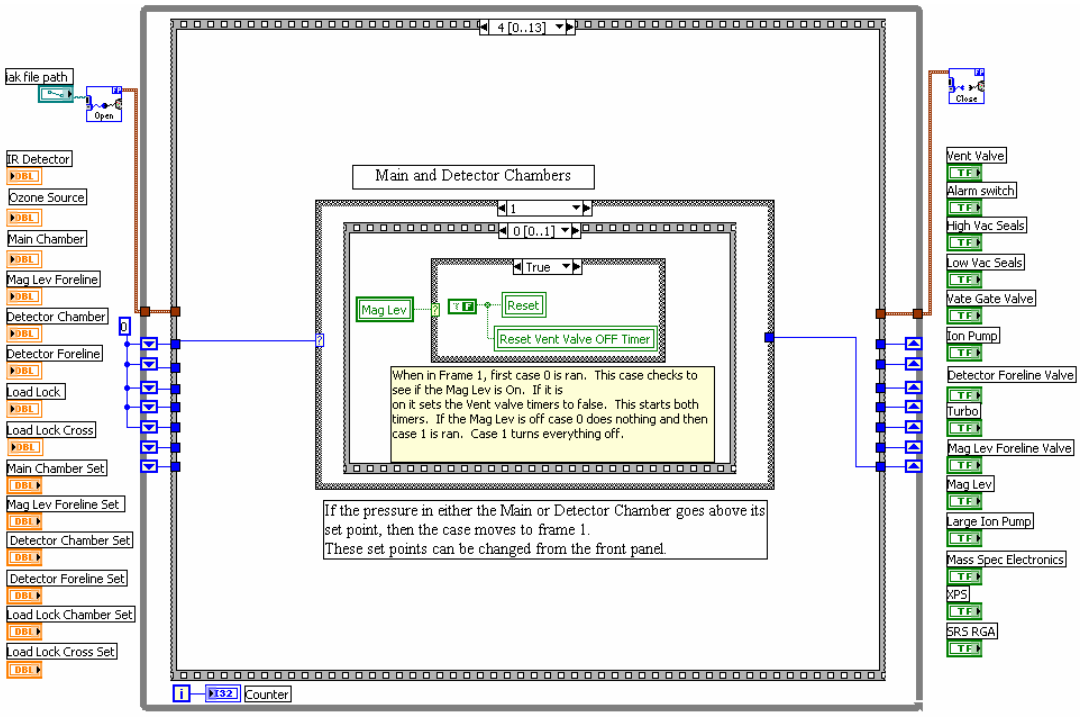

Figure A.6b.

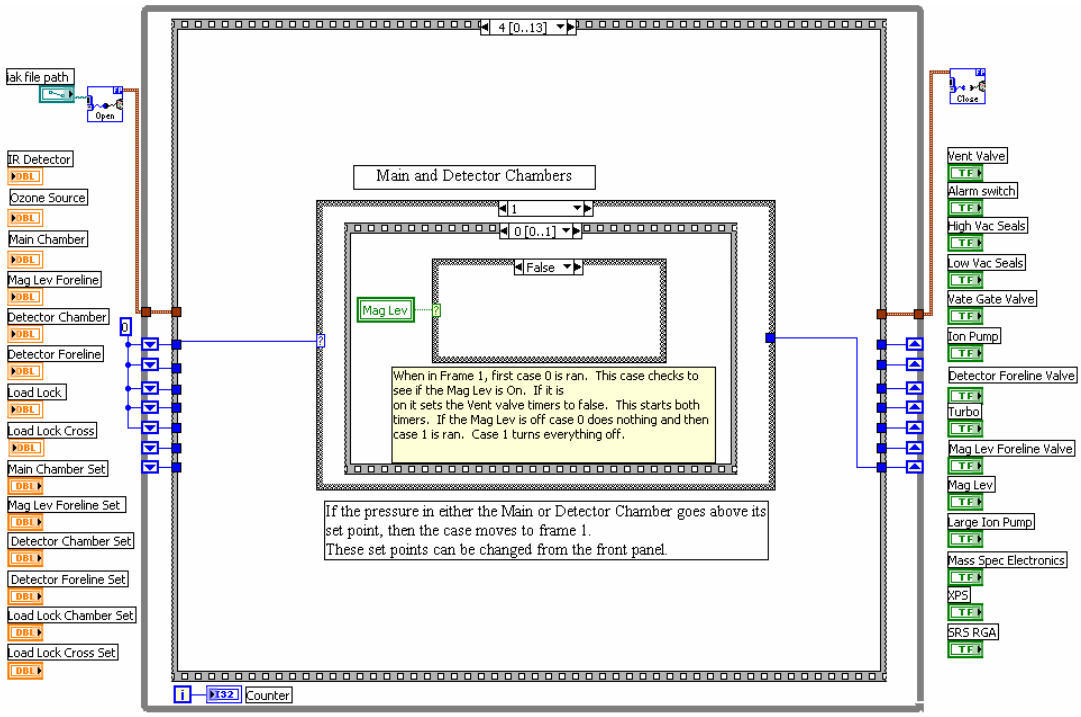

Figure A.6c.

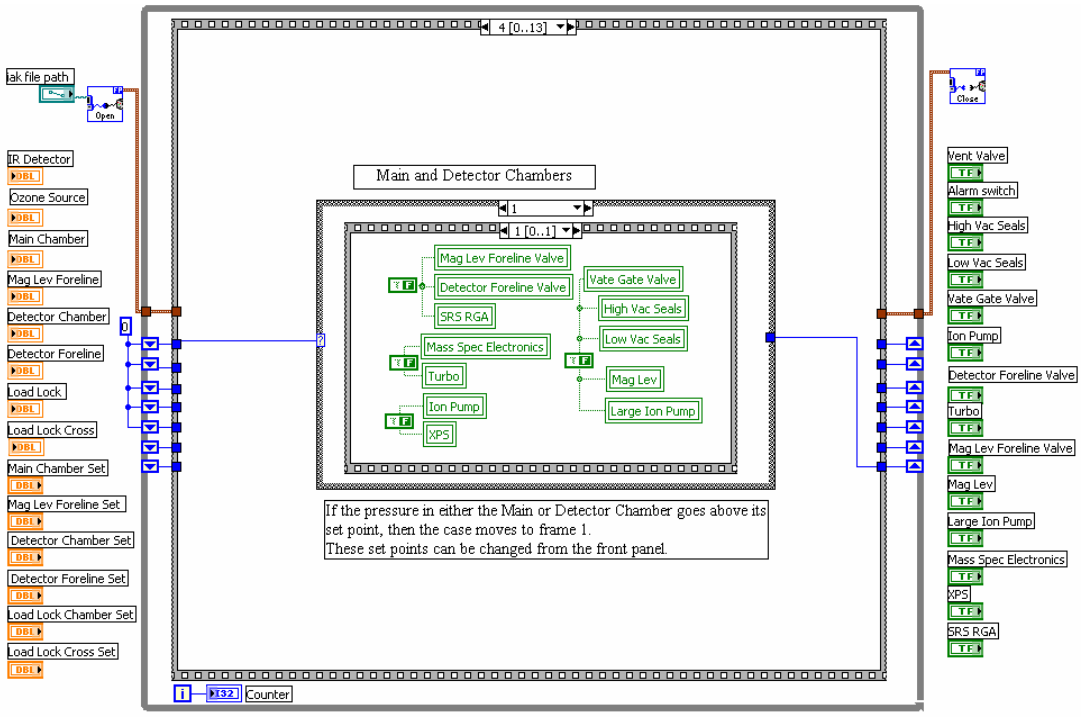

Figure A.6d. The fifth sequence structure of the while loop checks to ensure that the main chamber and detector chamber pressure's are below their individual set points. If either pressure is too high, all equipment is turned off and all valves are closed and the vent timers are activated.

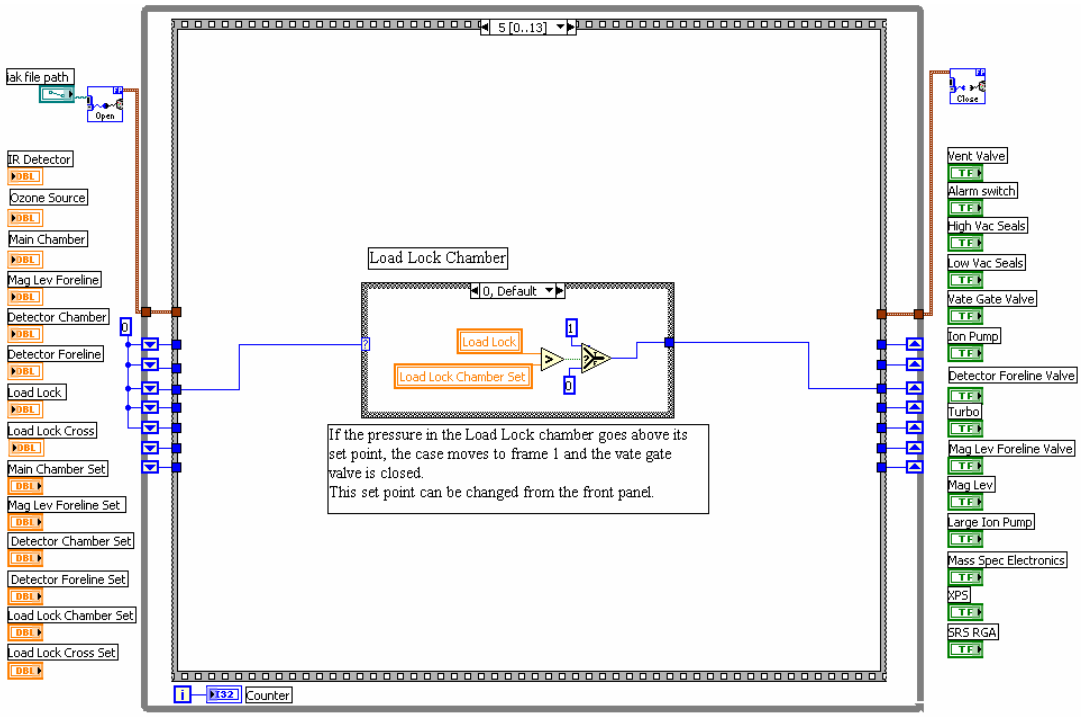

Figure A.7a.

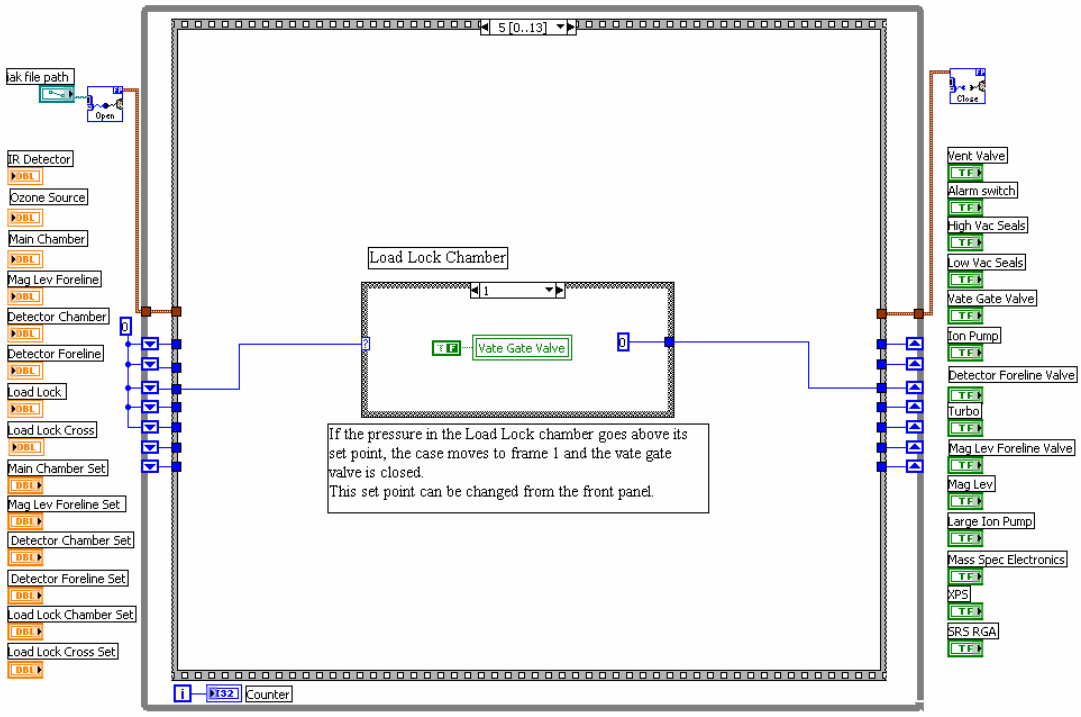

Figure A.7b. The sixth sequence structure of the while loop checks to ensure the pressure of the load lock chamber is below the load lock chamber's set point. If the pressure is too high, the UHV gate valve is closed

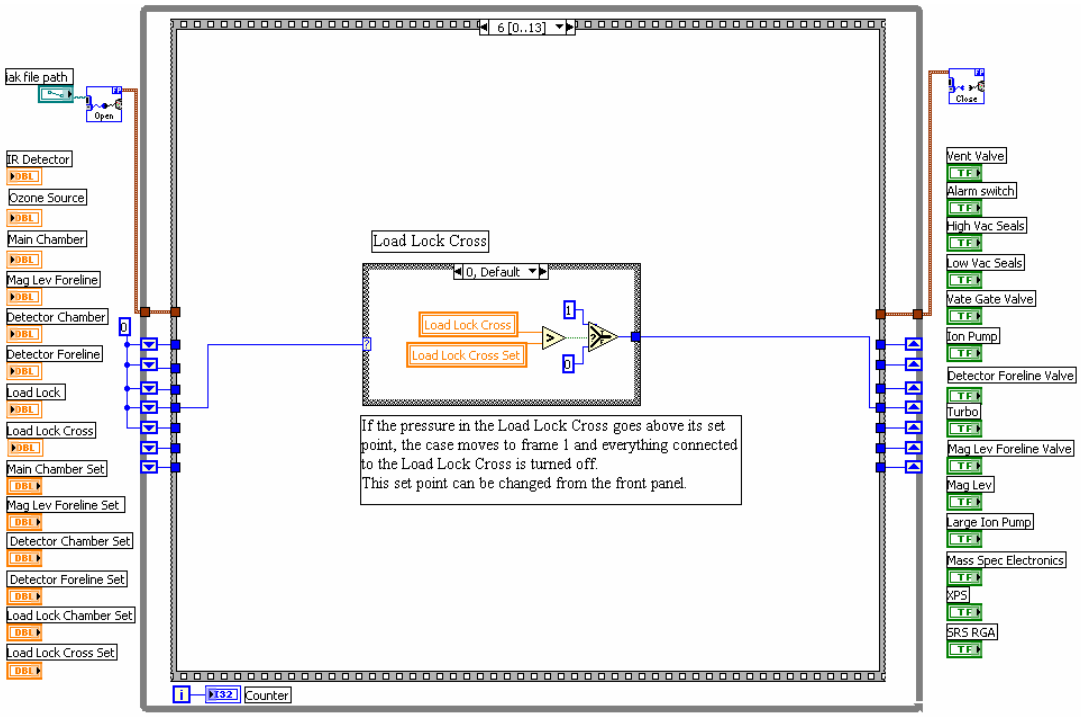

Figure A.8a.

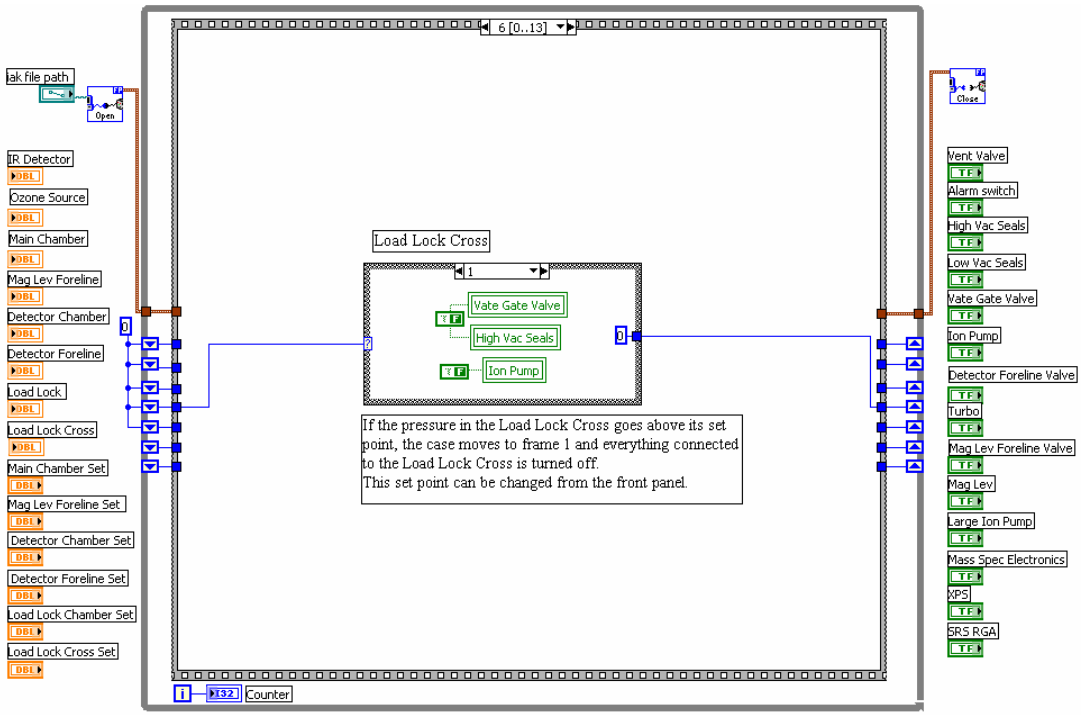

Figure A.8b. The seventh sequence structure of the while loop checks to ensure the pressure of the load lock cross is below the load lock cross' set point. If the pressure is too high, the UHV gate valve and the high-vacuum seal valve are closed and the ion pump is turned off.

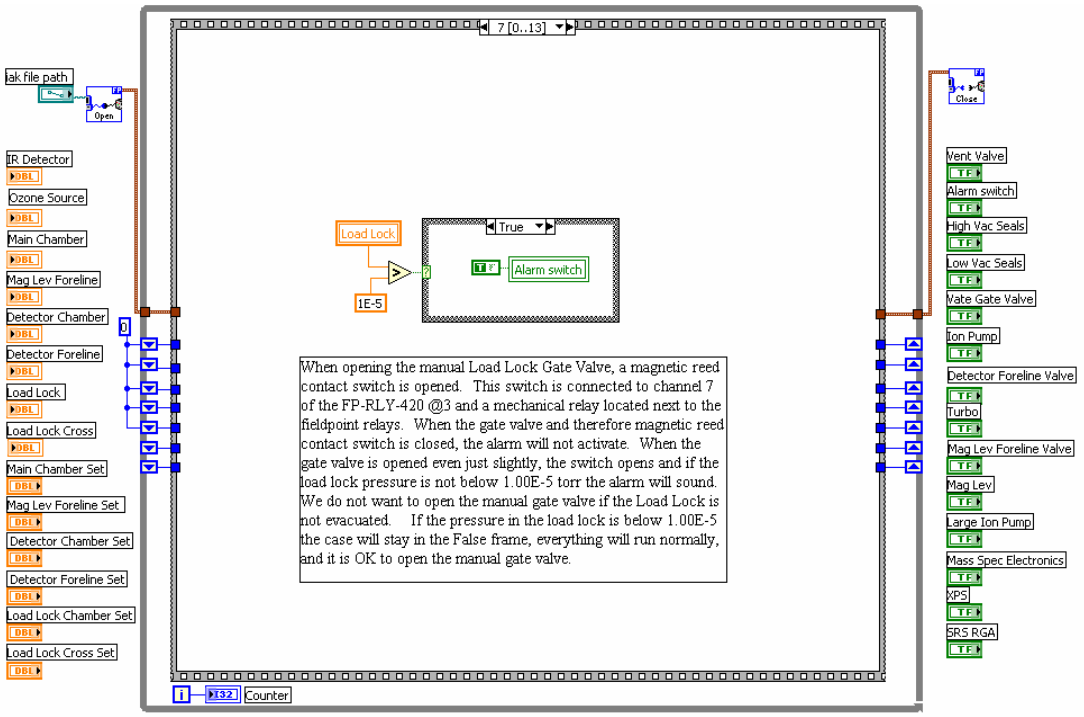

Figure A.9a.

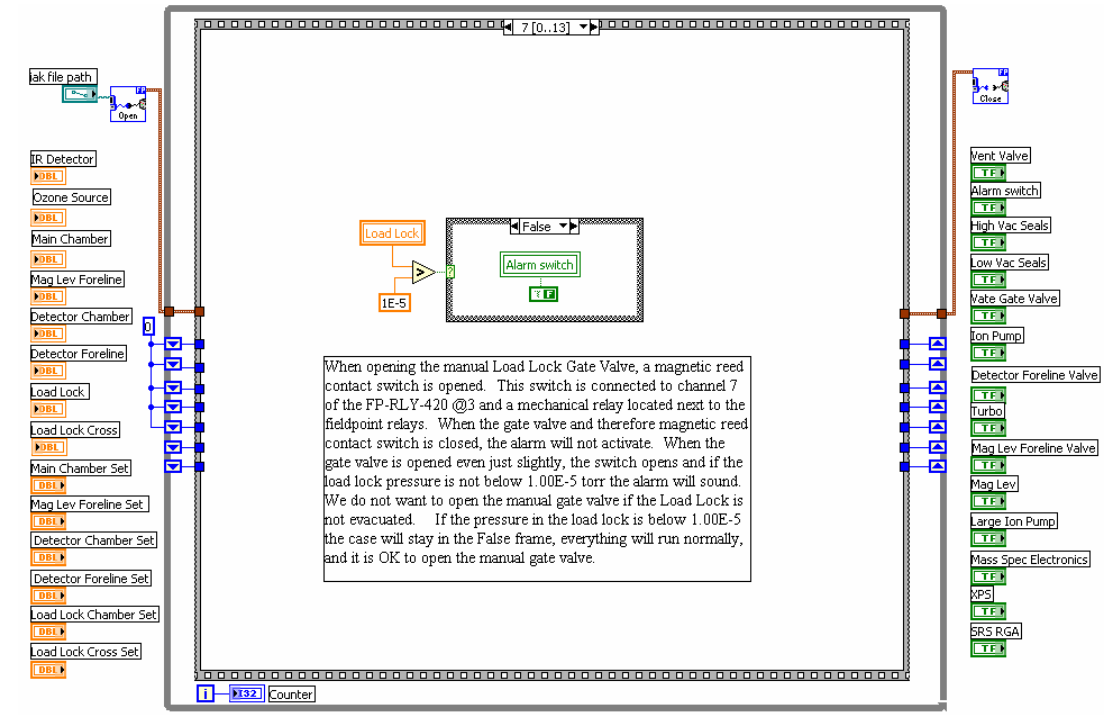

Figure A.9b. The eighth sequence structure of the while loop activates an alarm if the manual gate valve is opened and the pressure in the load lock is above 1.0×10^{-5}.

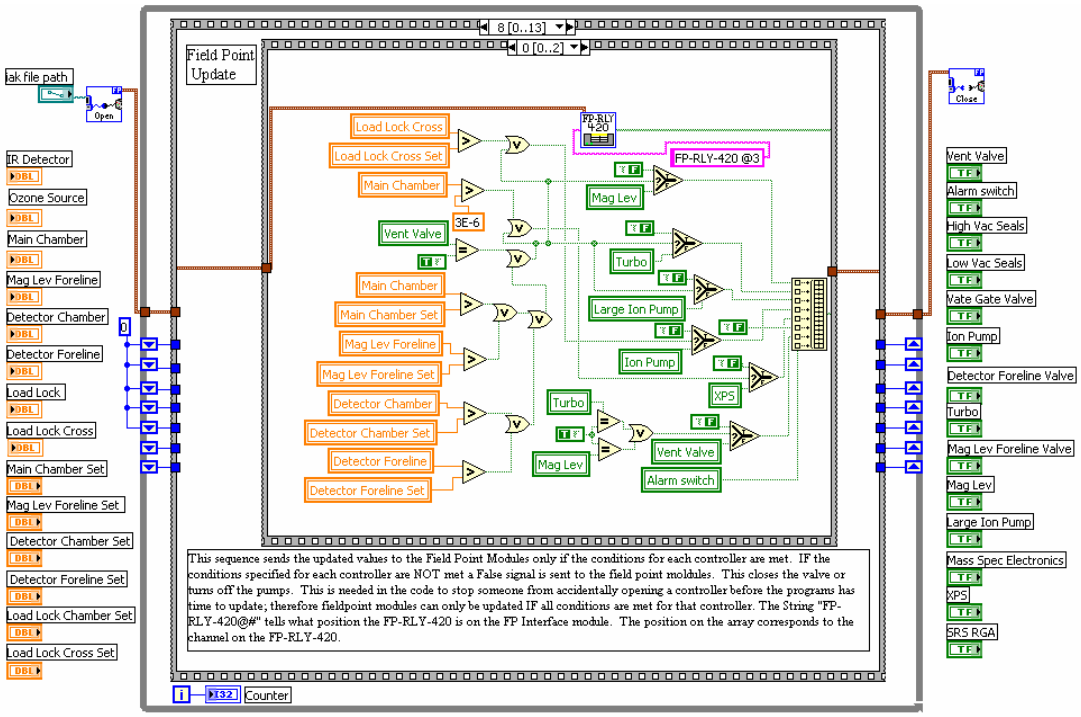

Figure A.10a.

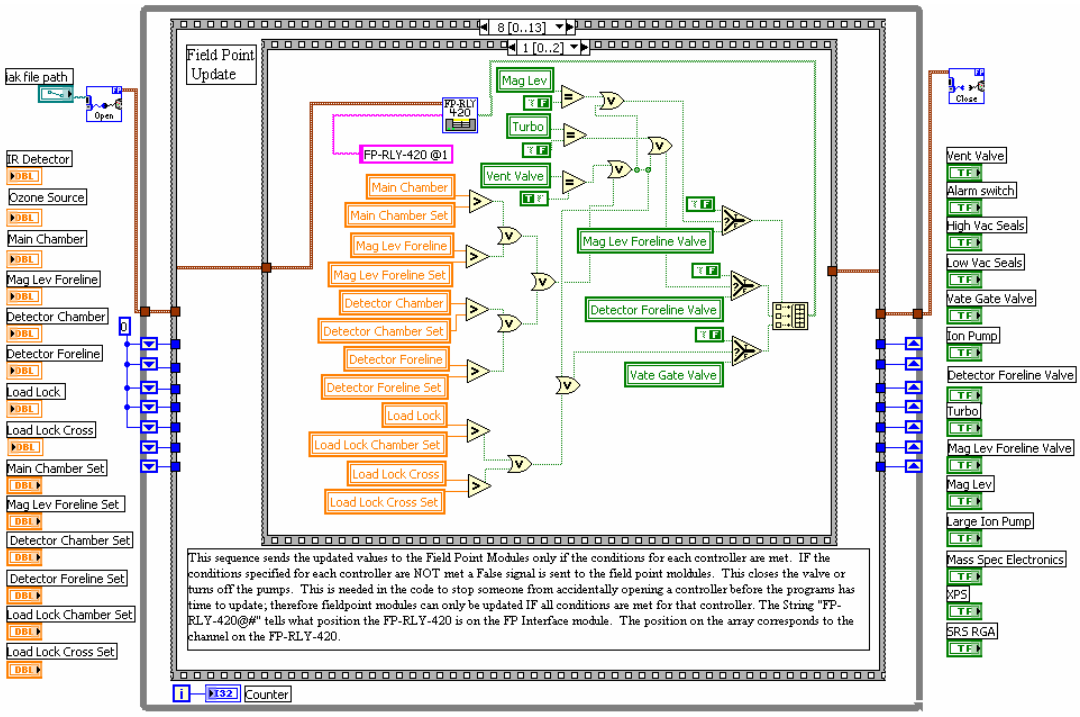

Figure A.10b.

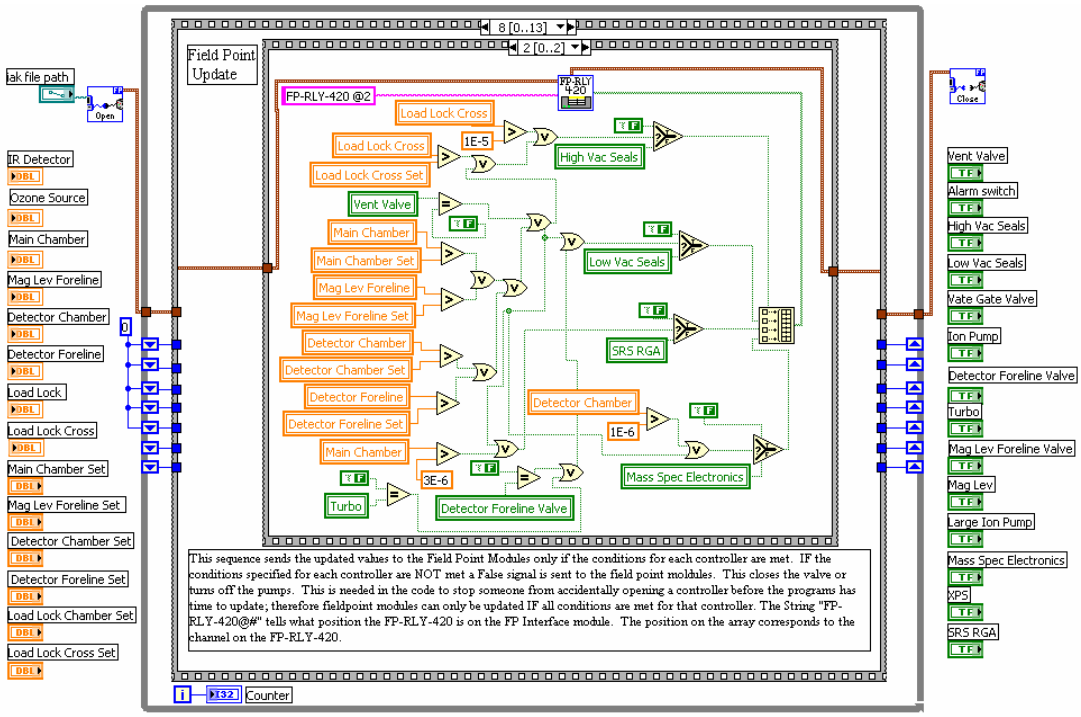

Figure A.10c. The ninth sequence structure of the while loop sends the updated Boolean valves to the FieldPoint™ relays if specific conditions for each controller are met.

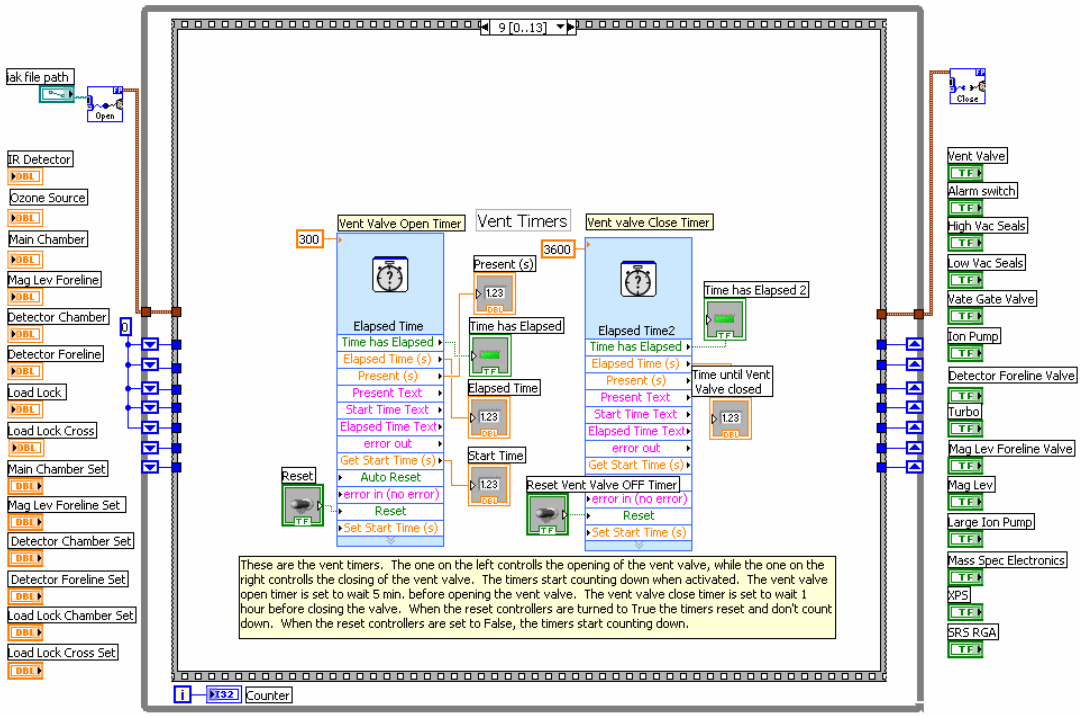

Figure A.11. The tenth sequence structure of the while loop activates the chamber vent timers if the pressures in the main chamber, detector chamber, or either of their forelines go above its corresponding set point.

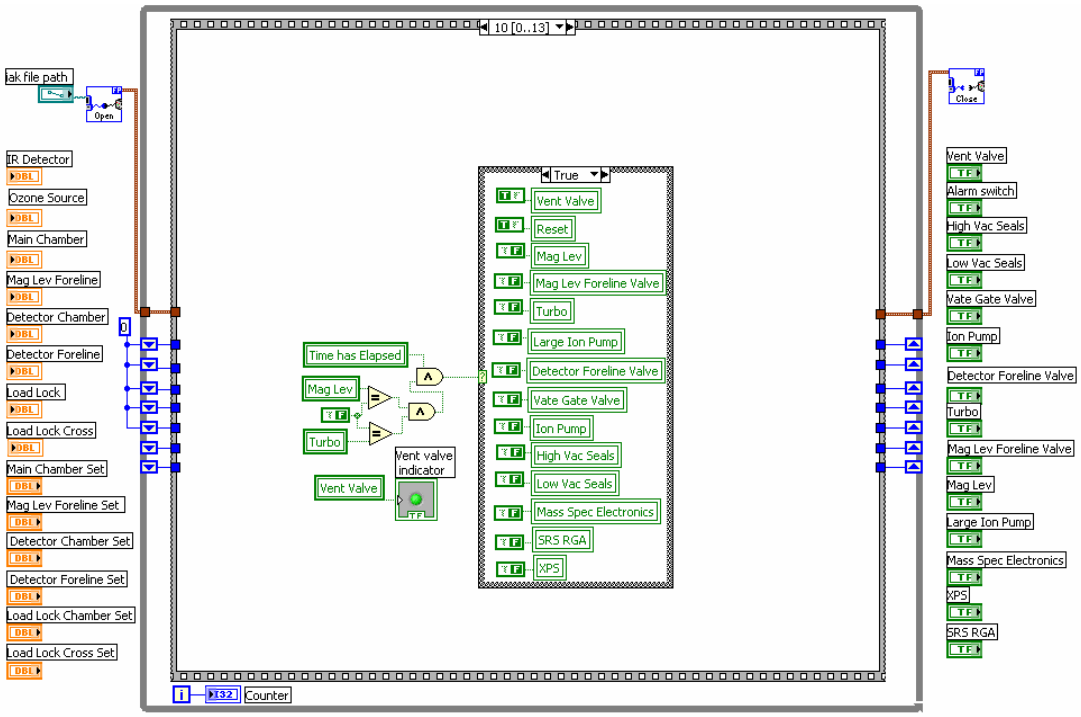

Figure A.12a.

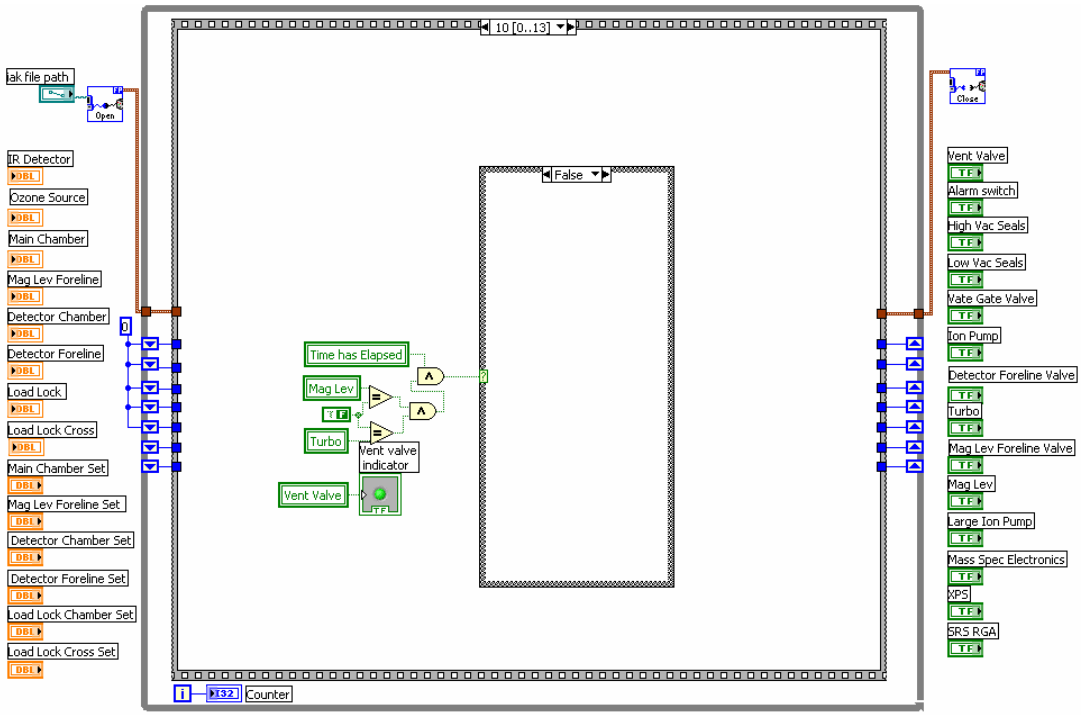

Figure A.12b. The eleventh sequence structure in the while loop opens the chamber vent valve, five minutes after the chamber vent timers are started.

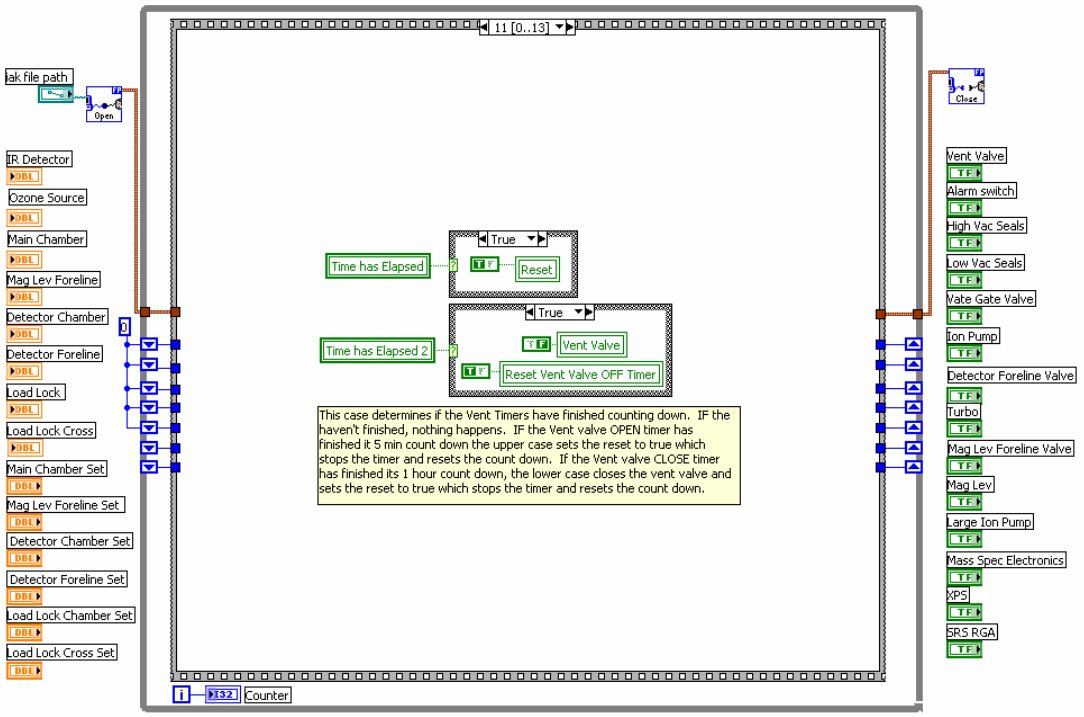

Figure A.13a.

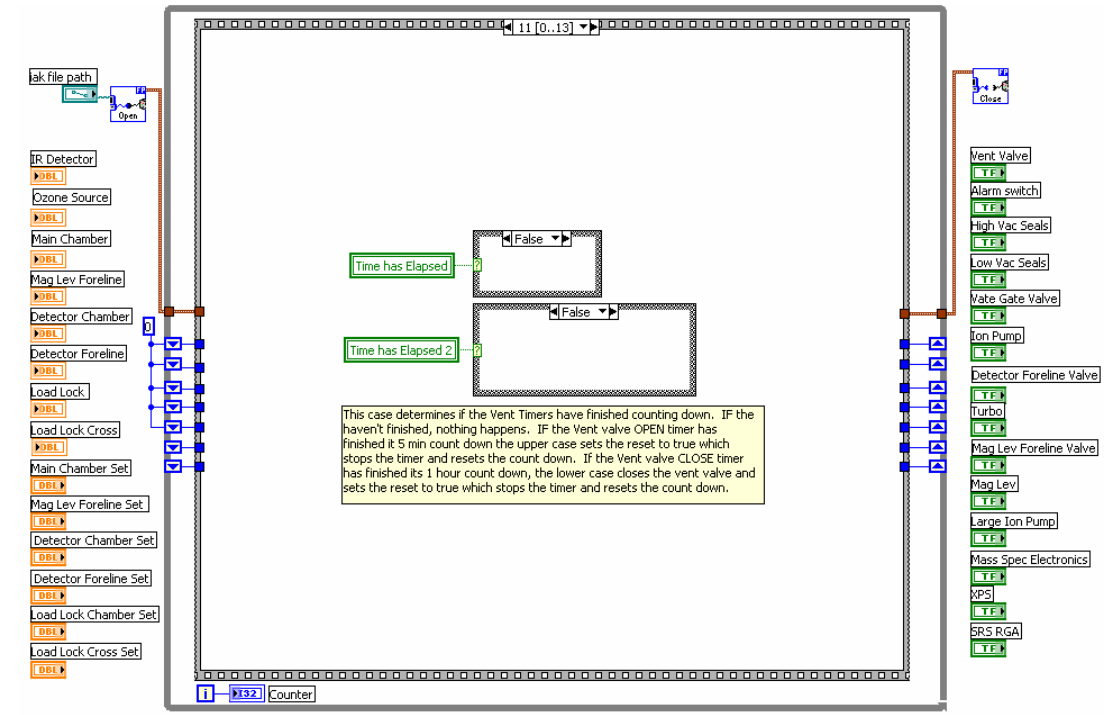

Figure A.13b. The twelfth sequence structure in the while loop closes the chamber vent valve, one hour after the chamber vent timers are started. This sequence also resets the chamber vent timers.

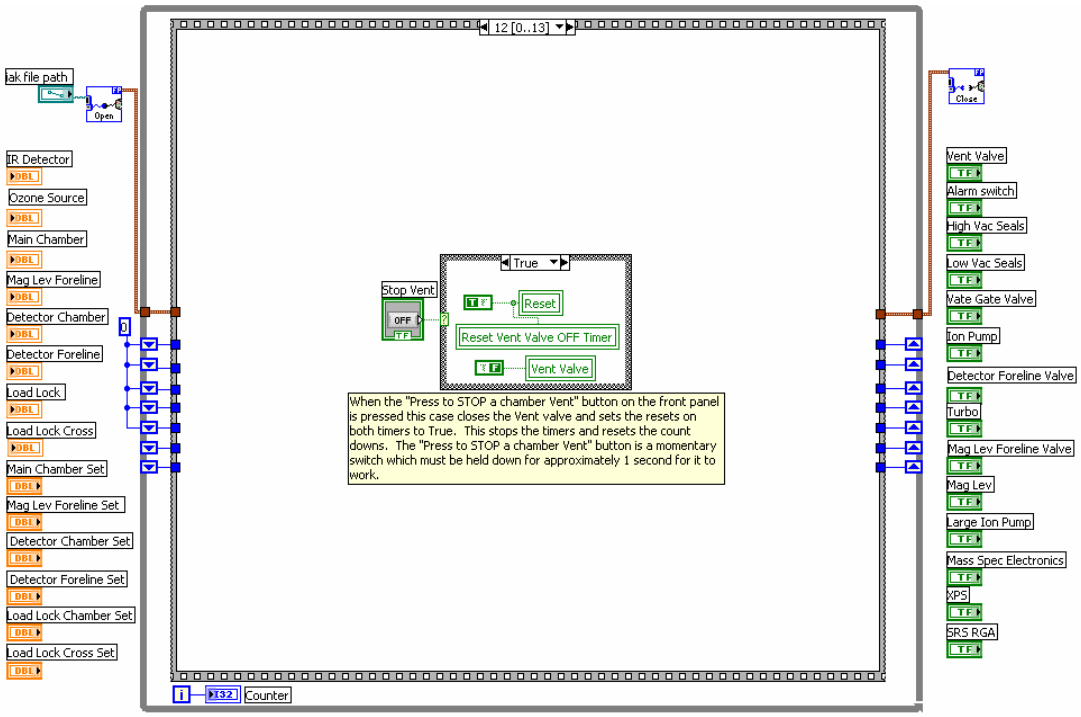

Figure A.14a.

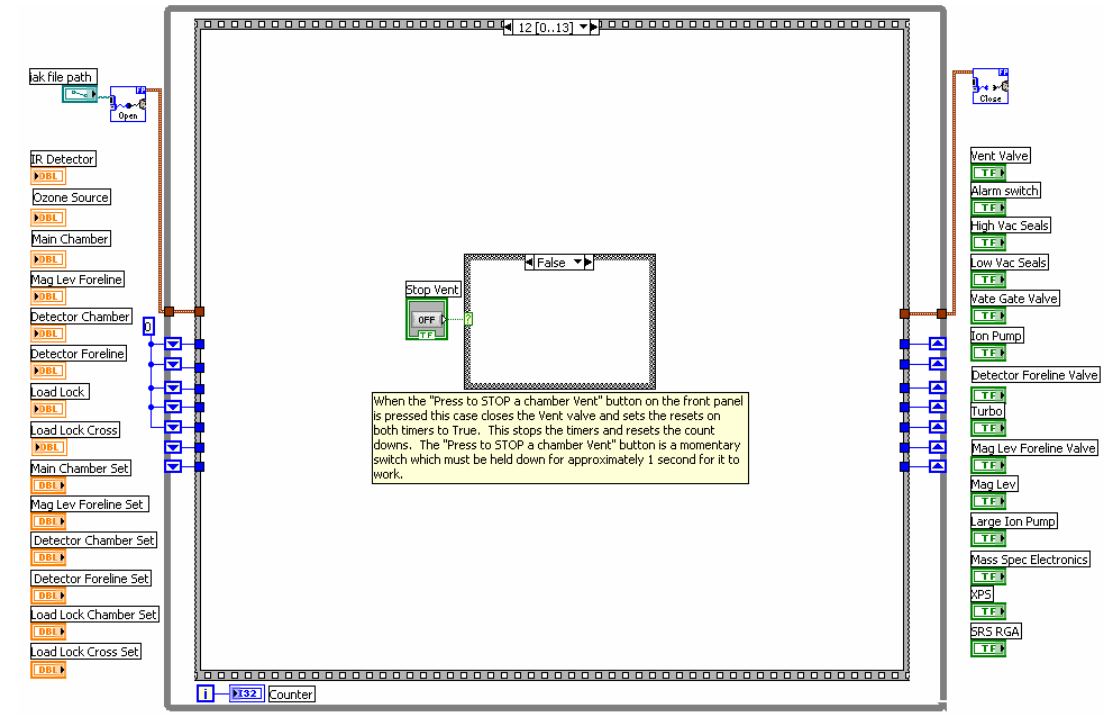

Figure A.14b. The thirteenth sequence structure of the while loop controls the "Press to STOP A Chamber Vent" button on the front panel. This button can be pressed at any time and will stop and reset the chamber vent timers and close the chamber vent valve.

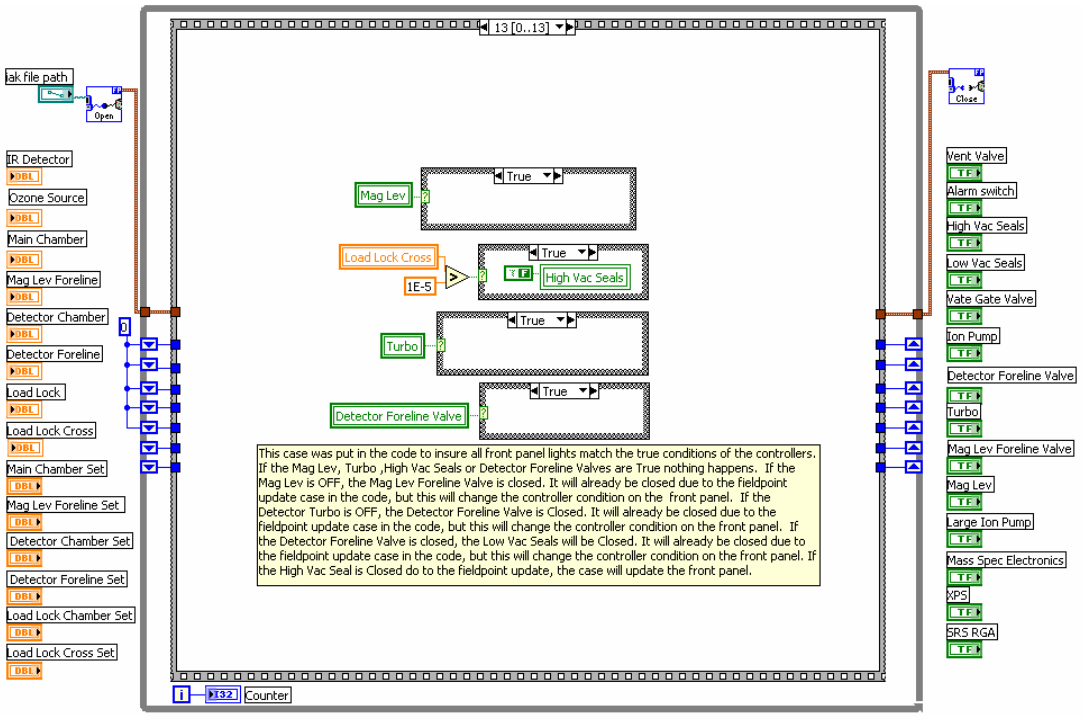

Figure A.15a.

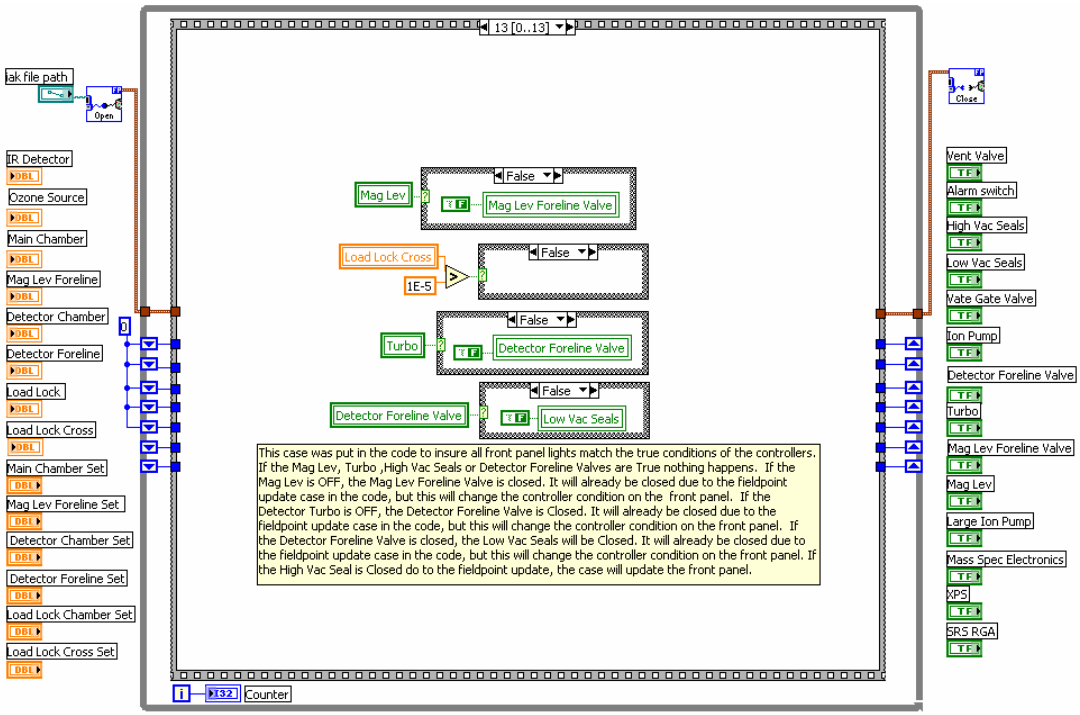

Figure A.15b. The last sequence structure of the while loop ensures that the color of the Boolean switches on the front panel match their actual conditions.

References

(1) Molina, M. J.; Molina, L. T.; Kolb, C. E. *Annual Review of Physical Chemistry* **1996**, *47*, 327-367.
(2) Ravishankara, A. R. *Science* **1997**, *276*, 1058-1065.
(3) Usher, C. R.; Michel, A. E.; Grassian, V. H. *Chemical Reviews* **2003**, *103*, 4883-4940.
(4) Dubowski, Y.; Vieceli, J.; Tobias, D. J.; Gomez, A.; Lin, A.; Nizkorodov, S. A.; McIntire, T. M.; Finlayson-Pitts, B. J. *Journal of Physical Chemistry A* **2004**, *108*, 10473-10485.
(5) Ellison, G. B.; Tuck, A. F.; Vaida, V. *Journal of Geophysical Research* **1999**, *104*, 11633-11641.
(6) Thomas, E. R.; Frost, G. J.; Rudich, Y. *Journal of Geophysical Research* **2001**, *106*, 3045-3056.
(7) Usher, C. R.; Michel, A. E.; Stec, D.; Grassian, V. H. *Atmospheric Environment* **2003**, *37*, 5337-5347.
(8) Smith, G. D.; Woods, E.; Baer, T.; Miller, R. E. *Journal of Physical Chemistry A* **2003**, *107*, 9582-9587.
(9) Moise, T.; Rudich, Y. *Journal of Geophysical Research* **2000**, *105*, 14667-14676.
(10) Middlebrook, A. M.; Murphy, D. M.; Thomson, D. S. *Journal of Geophysical Research* **1998**, *103*, 16475-16483.
(11) Novakov, T.; Penner, J. E. *Nature* **1993**, *365*, 823-826.
(12) Novakov, T.; Hegg, D. A.; Hobbs, P. V. *Journal of Geophysical Research* **1997**, *102*, 30023-30030.
(13) Finlayson-Pitts, B. J.; Pitts, J. N., Jr. *Chemistry of the Upper and Lower Atmosphere: Theory Experiments, and Applications*; Academic Press: San Diego, CA, 2000.
(14) Voges, A. B.; Stokes, G. Y.; Gibbs-Davis, J. M.; Lettan, R. B.; Bertin, P. A.; Pike, R. C.; Nguyen, S. T.; Scheidt, K. A.; Geiger, F. M. *Journal of Physical Chemistry C* **2007**, *111*, 1567-1578.
(15) Atkinson, R.; Tuazon, E. C.; Aschmann, S. M. *Environmental Science and Technology* **1995**, *29*, 1860-1866.
(16) Atkinson, R.; Arey, J. *Atmospheric Environment* **2003**, *37*, 197-219.
(17) Atkinson, R.; Arey, J. *Chemical Reviews* **2003**, *103*, 4605-4638.
(18) Gonza´lez-Labrada, E.; Schmidt, R.; DeWolf, C. E. *Chemical Communications* **2006**, 2471-2473.
(19) Moise, T.; Rudich, Y. *Journal of Physical Chemistry A* **2002**, *106*, 6469-6476.
(20) Morris, J. W.; Davidovits, P.; Jayne, J. T.; Jimenez, J. L.; Shi, Q.; Kolb, C. E.; Worsnop, D. R.; Barney, W. S.; Cass, G. *Geophysical Research Letters* **2002**, *29*, 71-1-71-4.
(21) Park, J.; Gomez, A. L.; Walser, M. L.; Lin, A.; Nizkorodov, S. A. *Physical Chemistry Chemical Physics* **2006**, *8*, 2506-2512.
(22) Thornberry, T.; Abbatt, J. P. D. *Physical Chemistry Chemical Physics* **2004**.
(23) Lai, C. C.; Finlayson-Pitts, B. J.; Willis, W. V. *Chemical Research in Toxicology* **1990**, *3*, 517-523.

(24) Fiegland, L. R.; McCorn Saint Fleur, M.; Morris, J. R. *Langmuir* **2005**, *21*, 2660-2661.
(25) Bailey, P. S. *Ozonation In Organic Chemistry*; Academic Press, Inc.: New York, 1978.
(26) Rubin, M. B. *Bulletin for the History of Chemistry* **2001**, *26*, 40-56.
(27) Schönbein, C. F. *Philos. Mag. (III)* **1840**, *17*, 293-294.
(28) Hughes, R. H. *The Journal of Chemical Physics* **1956**, *24*, 131-138.
(29) Trambarulo, R.; Ghosh, S. N.; Burrus, J. C. A.; Gordy, W. *The Journal of Chemical Physics* **1953**, *21*, 851-855.
(30) Yates, J. J. T. *Experimental Innovations in Surface Science*; Springer-Verlag: New Youk, 1998.
(31) Jenkins, A. C.; Birdsall, C. M. *The Journal of Chemical Physics* **1952**, *20*, 1158-1161.
(32) Brown, C.; Berger, A. W.; Hersh, C. K. *Journal of Chemical Physics* **1954**, *22*, 1151-1152.
(33) Horvath, M.; Bititzky, L.; Huettner, J. *Ozone*; Elsevier: New York, 1985.
(34) Ichimura, S.; Nonaka, H.; Morikawa, Y.; Noyori, T.; Nishiguchi, T.; Kekura, M. *Journal of Vacuum Science & Technology A: Vacuum, Surfaces, and Films* **2004**, *22*, 1410-1414.
(35) Koike, K.; Inoue, G.; Fukuda, T. *Journal of Chemical Engineering of Japan* **1999**, *32*, 295-299.
(36) Koike, K.; Nifuku, M.; Izumi, K.; Nakamura, S.; Fujiwara, S.; Horiguchi, S. *Journal of Loss Prevention in the Process Industries* **2005**, *18*, 465-468.
(37) Zhukov, V.; Popova, I.; Yates, J. J. T. *Journal of Vacuum Science & Technology A: Vacuum, Surfaces, and Films* **2000**, *18*, 992-994.
(38) Schönbein, C. F. *Journal fuer Praktische Chemie (Weinheim, Germany)* **1868**, *105*, 232-239.
(39) Rudolf, C. *Justus Liebigs Annalen der Chemie* **1953**, *583*, 1-36.
(40) Pryor, W. A.; Das, B.; Church, D. F. *Chemical Research in Toxicology* **1991**, *4*, 341-348.
(41) Vieceli, J.; Ma, O. L.; Tobias, D. J. *Journal of Physical Chemistry A* **2004**, *108*, 5806-5814.
(42) Laibinis, P. E.; Whitesides, G. M. *Journal of the American Chemical Society* **1992**, *114*, 9022-9028.
(43) Ulman, A. *Chemical Reviews* **1996**, *96*, 1533-1554.
(44) Camillone III, N.; Chidsey, C. E. D.; Eisenberger, P.; Fenter, P.; Li, J.; Liang, K. S.; Liu, G. Y.; Scoles, G. *The Journal of Chemical Physics* **1993**, *99*, 744-747.
(45) Schoenfisch, M. H.; Pemberton, J. E. *Journal of the American Chemical Society* **1998**, *120*, 4502-4513.
(46) Huang, J.; Hemminger, J. C. *Journal of the American Chemical Society* **1993**, *115*, 3342-3343.
(47) Huang, J.; Dahlgren, D. A.; Hemminger, J. C. *Langmuir* **1994**, *10*, 626-628.
(48) Hutt, D. A.; Leggett, G. J. *Journal of Physical Chemistry* **1996**, *100*, 6657-6662.
(49) Lee, M. T.; Hsueh, C. C.; Freund, M. S.; Ferguson, G. S. *Langmuir* **1998**, *14*, 6419-6423.

(50) Lewis, M.; Tarlov, M.; Carron, K. *Journal of the American Chemical Society* **1995**, *117*, 9574-9575.
(51) Tarlov, M. J.; Burgess, D. R. F.; Gillen, G. *Journal of the American Chemical Society* **1993**, *115*, 5305-5306.
(52) Zhang, Y.; Terrill, R. H.; Bohn, P. W. *Chem. Mater.* **1999**, *11*, 2191-2198.
(53) Zhang, Y.; Terrill, R. H.; Tanzer, T. A.; Bohn, P. W. *Journal of the American Chemical Society* **1998**, *120*, 2654-2655.
(54) Horn, A. B.; Russell, D. A.; Shorthouse, L. J.; Simpson, T. R. E. *Journal of the Chemical Society, Faraday Transactions* **1996**, *92*, 4759-4762.
(55) Li, Y.; Huang, J.; McIver, R. T.; Hemminger, J. C. *Journal of the American Chemical Society* **1992**, *114*, 2428-2432.
(56) Scott, J. R.; Baker, L. S.; Everett, W. R.; Wilkins, C. L.; Fritsch, I. *Analytical Chemistry* **1997**, *69*, 2636-2639.
(57) Tarlov, M. J.; Newman, J. G. *Langmuir* **1992**, *8*, 1398-1405.
(58) Poirier, G. E.; Herne, T. M.; Miller, C. C.; Tarlov, M. J. *Journal of the American Chemical Society* **1999**, *121*, 9703-9711.
(59) Nix, Roger M. *Why is UHV required for surface studies?* 2003, viewed 8 December 2007, <http://www.chem.qmul.ac.uk/surfaces/scc/scat4_2.htm>.
(60) M^{c}Pherson, M. K. Doctor of Philosophy, Virginia Polytechnic Institute and State University, 2005.
(61) Hosokawa, S.; Ichimura, S. *Review of Scientific Instruments* **1991**, *62*, 1614-1619.
(62) Nishiguchi, T.; Morikawa, Y.; Kekura, M.; Miyamoto, M.; Nonaka, H.; Ichimura, S. *Review of Scientific Instruments* **2002**, *73*, 1217-1223.
(63) Ichimura, S.; Hosokawa, S.; Nonaka, H.; Arai, K. *Journal of Vacuum Science & Technology A: Vacuum, Surfaces, and Films* **1991**, *9*, 2369-2373.
(64) Stevens, R. E.; Hsiao, C. W.; Linh, L.; Curro, N. J.; Monton, B. J.; Chang, B. Y.; Kung, C. Y.; Kittrell, C.; Kinsey, J. L. *Review of Scientific Instruments* **1998**, *69*, 2504-2509.
(65) Yagi, S.; Tanaka, M. *Journal of Physics D: Applied Physics* **1979**, *12*, 1509-1520.
(66) Sponholtz, D. J.; Walters, M. A.; Tung, J.; BelBruno, J. J. *Journal of Chemical Education* **1999**, *76*, 1712-1713.
(67) Cohen, Z.; Varkony, H.; Keinan, E.; Mazur, Y. *Organic Syntheses* **1988**, *Coll. Vol. 6*, 43.
(68) Greenler, R. G. *The Journal of Chemical Physics* **1966**, *44*, 310-315.
(69) Greenler, R. G. *The Journal of Chemical Physics* **1969**, *50*, 1963-1968.
(70) Trenary, M. *Annual Review of Physical Chemistry* **2000**, *51*, 381-403.
(71) Einstein, A. *Annalen der Physik* **1905**, *17*, 132-148.
(72) Day, B. S.; Shuler, S. F.; Ducre, A.; Morris, J. R. *The Journal of Chemical Physics* **2003**, *119*, 8084-8096.
(73) Day, B. S.; Morris, J. R. *Journal of Physical Chemistry B* **2003**, *107*, 7120-7125.
(74) Day, B. S.; Morris, J. R. *The Journal of Chemical Physics* **2005**, *122*, 234714-10.
(75) Ferguson, M. K.; Lohr, J. R.; Day, B. S.; Morris, J. R. *Physical Review Letters* **2004**, *92*, 073201-4.
(76) Chidsey, C. E. D.; Liu, G.-Y.; Rowntree, P.; Scoles, G. *The Journal of Chemical Physics* **1989**, *91*, 4421-4423.
(77) Schreiber, F. *Progress in Surface Science* **2000**, *65*, 151-257.

(78) Strong, L.; Whitesides, G. M. *Langmuir* **1988**, *4*, 546-558.
(79) Dubois, L. H.; Nuzzo, R. G. *Annual Review of Physical Chemistry* **1992**, *43*, 437-463.
(80) Petrovykh, D. Y.; Kimura-Suda, H.; Opdahl, A.; Richter, L. J.; Tarlov, M. J.; Whitman, L. J. *Langmuir* **2006**, *22*, 2578-2587.
(81) Sohn, S.; Schröder, M.; Lipinsky, D.; Arlinghaus, H. F. *Surface and Interface Analysis* **2004**, *36*, 1222-1226.
(82) Worley, C. G.; Linton, R. W. *Journal of Vacuum Science & Technology A: Vacuum, Surfaces, and Films* **1995**, *13*, 2281-2284.
(83) Garrell, R. L.; Chadwick, J. E.; Severance, D. L.; McDonald, N. A.; Myles, D. C. *Journal of the American Chemical Society* **1995**, *117*, 11563-11571.
(84) Norrod, K. L.; Rowlen, K. L. *Journal of the American Chemical Society* **1998**, *120*, 2656-2657.
(85) Sandhyarani, N.; Pradeep, T. *Chemical Physics Letters* **2001**, *338*, 33-36.
(86) Sun, L.; Gardella, J. A. *Langmuir* **2002**, *18*, 9289-9295.
(87) Cooper, E.; Leggett, G. J. *Langmuir* **1998**, *14*, 4795-4801.
(88) Molina, L. T. M., M. J. *Journal of Geophysical Research* **1986**, *91*, 14501-14508.
(89) Bensebaa, F.; Ellis, T. H.; Badia, A.; Lennox, R. B. Proceedings of the 41st National Symposium of the American Vacuum Society, Denver, Colorado (USA), 1995; p 1331-1336.
(90) Laibinis, P. E.; Whitesides, G. M.; Allara, D. L.; Tao, Y. T.; Parikh, A. N.; Nuzzo, R. G. *Journal of the American Chemical Society* **1991**, *113*, 7152-7167.
(91) More', J.; Garbow, B.; Hillstrom, K. Chicago, 1999.
(92) Wagner, A. J.; Carlo, S. R.; Vecitis, C.; Fairbrother, D. H. *Langmuir* **2002**, *18*, 1542-1549.
(93) Wagner, C. D.; Riggs, W. M.; Davis, L. E.; Moulder, J. F.; Muilenberg, G. E. *Handbook of X-ray Photoelectron Spectroscopy*; Perkin-Elmer Corporation, 1979.
(94) Bain, C. D.; Whitesides, G. M. *Angewandte Chemie International Edition* **1989**, *28*, 506-512.
(95) Hostetler, M. J.; Stokes, J. J.; Murray, R. W. *Langmuir* **1996**, *12*, 3604-3612.
(96) Nuzzo, R. G.; Fusco, F. A.; Allara, D. L. *Journal of the American Chemical Society* **1987**, *109*, 2358-2368.
(97) Nuzzo, R. G.; Dubois, L. H.; Allara, D. L. *Journal of the American Chemical Society* **1990**, *112*, 558-569.
(98) Porter, M. D.; Bright, T. B.; Allara, D. L.; Chidsey, C. E. D. *Journal of the American Chemical Society* **1987**, *109*, 3559-3568.
(99) Snyder, R. G.; Strauss, H. L.; Elliger, C. A. *Journal of Physical Chemistry* **1982**, *86*, 5145-5150.
(100) Snyder, R. G.; Maroncelli, M.; Strauss, H. L.; Hallmark, V. M. *Journal of Physical Chemistry* **1986**, *90*, 5623-5630.
(101) Castner, D. G.; Hinds, K.; Grainger, D. W. *Langmuir* **1996**, *12*, 5083-5086.
(102) Bain, C. D.; Troughton, E. B.; Tao, Y. T.; Evall, J.; Whitesides, G. M.; Nuzzo, R. G. *Journal of the American Chemical Society* **1989**, *111*, 321-335.
(103) Gorham, J.; Smith, B.; Fairbrother, D. H. *Journal of Physical Chemistry C* **2007**, *111*, 374-382.
(104) Detoni, S.; Hadzi, D. *Spectrochim. Acta* **1957**, *17*, 601-608.

(105) Paulson, G.; Bakke, J.; Giddings, J.; Simpson, M. *Biological Mass Spectrometry* **1978**, *5*, 128-132.
(106) Perov, P. A.; Savrasov, A. S.; Tember, G. A.; Bez'yazychnaya, L. A.; Gerasimova, N. T. *Journal of Applied Spectroscopy* **1982**, *37*, 1018-1021.
(107) Bellamy, L. J. *The Infrared Spectra of Complex Molecules*; 3rd ed.; Halsted: New York, N.Y., 1975.
(108) Barnard, D.; Fabian, J. M.; Koch, H. P. *Journal of the Chemical Society* **1949**, 2442 - 2454.
(109) Ham, N. S.; Hambly, A. N.; Laby, R. H. *Australian Journal of Chemistry* **1960**, *13*, 443-455.
(110) Bellamy, L. J.; Williams, R. L. *Journal of the Chemical Society* **1957**, 863-868.
(111) Evans, S. D.; Goppert-Berarducci, K. E.; Urankar, E.; Gerenser, L. J.; Ulman, A.; Snyder, R. G. *Langmuir* **1991**, *7*, 2700-2709.
(112) Peanasky, J. S.; McCarley, R. L. *Langmuir* **1998**, *14*, 113-123.
(113) Alemozafar, A. R.; Madix, R. J. *The Journal of Chemical Physics* **2005**, *122*, 214718-8.
(114) Pace, R. J.; Chan, S. I. *The Journal of Chemical Physics* **1982**, *76*, 4241-4247.
(115) Ramanathan, V.; Crutzen, P. J.; Kiehl, J. T.; Rosenfeld, D. *Science* **2001**, *294*, 2119-2124.
(116) Hu, J.; Fox, M. A. *Journal of Organic Chemistry* **1999**, *64*, 4959-4961.
(117) Allara, D. L.; Nuzzo, R. G. *Langmuir* **1985**, *1*, 52-66.
(118) Maroncelli, M.; Qi, S. P.; Strauss, H. L.; Snyder, R. G. *Journal of the American Chemical Society* **1982**, *104*, 6237-6247.
(119) Snyder, R. G. *The Journal of Chemical Physics* **1967**, *47*, 1316-1360.
(120) Socrates, G. *Infrared and Raman Characteristic Group Frequencies: Tables and Charts*; 3rd ed.; John Wiley & Sons, Inc.: New York, 2001.
(121) Kurth, D. G. *Langmuir* **1998**, *14*, 6987-6991.
(122) Greenler, R. G.; Rahn, R. R.; Schwartz, J. P. *Journal of Catalysis* **1971**, *23*, 42-48.
(123) Berreman, D. W. *Physical Review* **1963**, *130*, 2193-2198.
(124) Andersson, S. K.; Niklasson, G. A. *Journal of Physics: Condensed Matter* **1995**, *7*, 8507-8518.
(125) Grosse, P.; Harbecke, B.; Heinz, B.; Meyer, R.; Offenberg, M. *Applied Physics A* **1986**, *39*, 257-268.
(126) Zhizhin, G. N.; Moskaleva, M. A.; Nazin, V. G.; Yakovlev, V. A. *Soviet Physics, Solid State* **1977**, *19*, 1352-1355.
(127) Lee, J. K.; Lee, K. B.; Kim, D. J.; Choi, I. S. *Langmuir* **2003**, *19*, 8141-8143.
(128) Allara, D. L.; Nuzzo, R. G. *Langmuir* **1985**, *1*, 45-52.
(129) Salaneck, W. R.; Lipari, N. O.; Paton, A.; Zallen, R.; Liang, K. S. *Physical Review B* **1975**, *12*, 1493.
(130) Vogt, A. D.; Han, T.; Beebe, T. P. *Langmuir* **1997**, *13*, 3397-3403.
(131) Yang, Y. W.; Fan, L. J. *Langmuir* **2002**, *18*, 1157-1164.
(132) Sun, F.; Castner, D. G.; Grainger, D. W. *Langmuir* **1993**, *9*, 3200-3207.
(133) Sun, F.; Grainger, D. W.; Castner, D. G. The 40th National Symposium of the American Vacuum Society, Orlando, Florida (USA), 1994; p 2499-2506.
(134) Zharnikov, M.; Geyer, W.; Gz.oumllzhz.aumluser, A.; Frey, S.; Grunze, M. *Physical Chemistry Chemical Physics* **1999**.

(135) Heister, K.; Zharnikov, M.; Grunze, M.; Johansson, L. S. O.; Ulman, A. *Langmuir* **2001**, *17*, 8-11.
(136) Robinson, G. N.; Freedman, A.; Graham, R. L. *Langmuir* **1995**, *11*, 2600-2608.
(137) Abdureyim, A.; Okudaira, K. K.; Harada, Y.; Masuda, S.; Aoki, M.; Seki, K.; Ito, E.; Ueno, N. *Journal of Electron Spectroscopy and Related Phenomena* **2001**, *114-116*, 371-374.
(138) Whelan, C. M.; Ghijsen, J.; Pireaux, J.-J.; Maex, K. *Thin Solid Films* **2004**, *464-465*, 388-392.
(139) Ferrizz, R. M.; Gorte, R. J.; Vohs, J. M. *Catalysis Letters* **2002**, *82*, 123-129.
(140) McIntire, T. M.; Scott Lea, A.; Gaspar, D. J.; Jaitly, N.; Dubowski, Y.; Li, Q.; Finlayson-Pitts, B. J. *Physical Chemistry Chemical Physics* **2005**.
(141) Tao, F.; Bernasek, S. L. *Chemical Reviews* **2007**, *107*, 1408-1453.
(142) Bryant, M. A.; Pemberton, J. E. *Journal of the American Chemical Society* **1991**, *113*, 8284-8293.
(143) Laibinis, P. E.; Nuzzo, R. G.; Whitesides, G. M. *Journal of Physical Chemistry* **1992**, *96*, 5097-5105.
(144) Gorman, C. B.; He, Y.; Carroll, R. L. *Langmuir* **2001**, *17*, 5324-5328.
(145) Gordon, W. O., Virginia Polytechnic Institute and State University, 2006.
(146) Qi, H.; Gee, P. E.; Nguyen, T.; Hicks, R. F. *Surface Science* **1995**, *323*, 6-18.
(147) Camillone III, N.; Chidsey, C. E. D.; Liu, G.-y.; Putvinski, T. M.; Scoles, G. *The Journal of Chemical Physics* **1991**, *94*, 8493-8502.
(148) Lai, C. C.; Yang, S. H.; Finlayson-Pitts, B. J. *Langmuir* **1994**, *10*, 4637-4644.
(149) Krol, M.; Leeuwen, P. J. v.; Lelieveld, J. *Journal of Geophysical Research* **1998**, *103*, 10697-10711.
(150) Ravishankara, A. R.; Hancock, G.; Kawasaki, M.; Matsumi, Y. *Science* **1998**, *280*, 60-61.
(151) DAndrea, T. M.; Zhang, X.; Jochnowitz, E. B.; Lindeman, T. G.; Simpson, C. J. S. M.; David, D.; Curtiss, T.; Morris, J. R.; Ellison, G. B. *Submitted to Journal of Physical Chemistry A* **2007**.

Vita

Larry Richard Fiegland was born August 6, 1976 to Dale and Karen Fiegland in Medina, Ohio. He moved to North Fort Myers, Florida with his parents, his older sister, Brianna, and his younger brother, Nathan, in 1980. Larry graduated as valedictorian from Evangelical Christian High School in 1994. He attended the University of Florida and received a Bachelors of Science in Chemistry in 1999. After graduation, Larry worked for Clariant Life Science Molecules in Gainesville, Fl as a chemical operator and technical writer. In 2002, Larry began his graduate studies at Virginia Tech, where he joined Professor John Morris's research group. Larry married Jessica Erin Sarisky on March 27, 2004. Larry defended his dissertation in the spring of 2008, and he will join David Nesbitt's research group at the University of Colorado at Boulder as a research scientist.